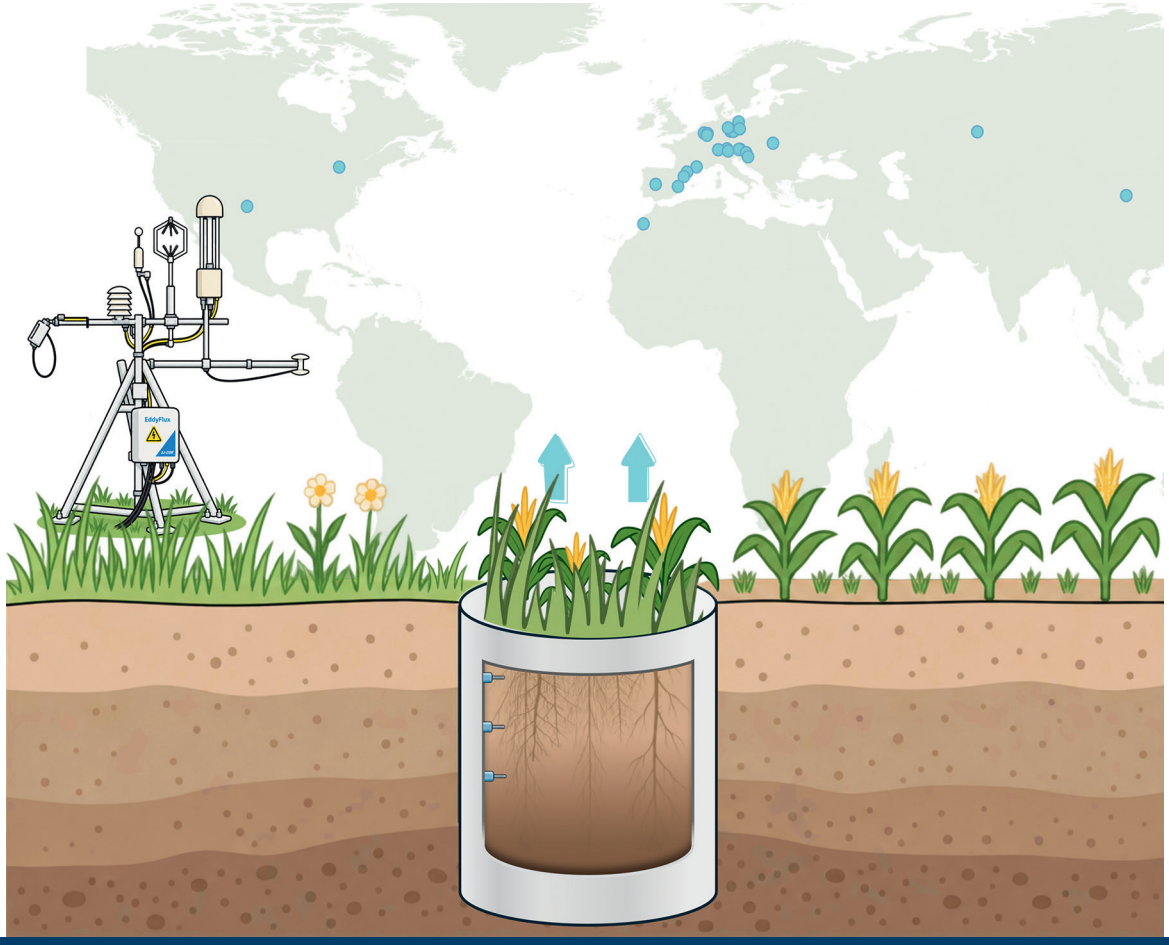


Advancing the understanding of actual evapotranspiration and critical soil moisture thresholds using lysimeter networks

Xiao Lu

Energie & Umwelt / Energy & Environment
Band / Volume 737
ISBN 978-3-69367-001-9

Mitglied der Helmholtz-Gemeinschaft

JÜLICH
Forschungszentrum

Schriften des Forschungszentrums Jülich
Reihe Energie & Umwelt / Energy & Environment Band / Volume 737

Forschungszentrum Jülich GmbH
Institut für Bio- und Geowissenschaften (IBG)
Agrosphäre (IBG-3)

Advancing the understanding of actual evapotranspiration and critical soil moisture thresholds using lysimeter networks

Xiao Lu

Schriften des Forschungszentrums Jülich
Reihe Energie & Umwelt / Energy & Environment Band / Volume 737

ISSN 1866-1793 ISBN 978-3-69367-001-9

Bibliografische Information der Deutschen Nationalbibliothek.
Die Deutsche Nationalbibliothek verzeichnet diese Publikation in der
Deutschen Nationalbibliografie; detaillierte Bibliografische Daten
sind im Internet über http://dnb.d-nb.de abrufbar.

Herausgeber und Vertrieb:	Forschungszentrum Jülich GmbH Zentralbibliothek, Verlag 52425 Jülich Tel.: +49 2461 61-5368 Fax: +49 2461 61-6103 zb-publikation@fz-juelich.de www.fz-juelich.de/zb
Umschlaggestaltung:	Grafische Medien, Forschungszentrum Jülich GmbH
Druck:	Grafische Medien, Forschungszentrum Jülich GmbH
Copyright:	Forschungszentrum Jülich 2026

Schriften des Forschungszentrums Jülich
Reihe Energie & Umwelt / Energy & Environment, Band / Volume 737

D 82 (Diss. RWTH Aachen University, 2026)

ISSN 1866-1793
ISBN 978-3-69367-000-2 (Print)
ISBN 978-3-69367-001-9 (E-Book)

Vollständig frei verfügbar über das Publikationsportal des Forschungszentrums Jülich (JuSER)
unter www.fz-juelich.de/zb/openaccess.



This is an Open Access publication distributed under the terms of the Creative Commons Attribution License 4.0, which permits unrestricted use, distribution, and reproduction in any medium, provided the original work is properly cited.

Abstract

Climate change is expected to significantly alter water availability, intensifying the frequency and severity of extreme weather events and increasing the risk of drought. Actual evapotranspiration (ET_a) is a key component in the terrestrial water cycle, linking the hydrosphere, atmosphere and biosphere by modulating a range of land surface and ecohydrological processes. ET_a is limited either by atmospheric energy supply or soil moisture (θ) availability. The shift between the energy-limited and water-limited ET_a regimes is dependent on θ and is often characterized by a threshold known as critical soil moisture (θ_{crit}). A comprehensive understanding and accurate quantification of ET_a and its regime classification marked by θ_{crit} is essential for irrigation management, drought monitoring, evaluating drought impacts and improving future projections of climate and water resources, food production, especially in the context of climate change.

Weighable lysimeters play a vital role in understanding the complex interactions within the soil-plant-atmosphere continuum and are regarded as the most precise in situ method for quantifying ET_a, but only at pedon scale due to their limited surface area. Equipped with soil moisture sensors at multiple depths, lysimeters offer a unique opportunity to assess the role of both surface, and, importantly, root zone θ on the transition between water and energy limited ET_a regimes. This thesis explores the potential of lysimeters in providing ET_a that is representative at larger scales than their surface area, as well as the surface and root zone θ_{crit} associated with ET_a regimes shifts. The scope of this thesis expands progressively, from a limited number of lysimeters in selected regions of Germany to a national network and, ultimately, incorporates an international dataset spanning multiple continents.

The first study assessed whether lysimeter ET_a measurement, despite their small surface area, can provide representative information for larger areas, such as the plot scale, landscape scale and larger regional scale. To address this, we examined the spatial correlations between ET_a measured at different locations by lysimeter (ET-LYS) and at different locations by eddy covariance (ET-EC). This was done for the period 2015 - 2020 and the analysis was made for different spatial (range: 0 to 500 km) and temporal scales (range: 1 day to 1 year) using 23 lysimeters and 4 eddy covariance towers in Germany. We found that ET-LYS is generally as representative as ET-EC with high correlations at the plot scale, and moderate to high correlations at the landscape and larger regional scale. Wavelet analysis further indicated weaker spatial correlations under drought conditions (in the year 2018) and the strongest temporal correlations at annual and sub-seasonal scales. Furthermore, combination of multiple ET-LYS from different sites improved the predictability of ET-LYS for another site, suggesting that ET-LYS can be predicted well using ET-LYS from different neighboring sites. Overall, lysimeter measurements can provide information at much larger scales compared to their small measurement area.

Using lysimeter ET_a measurements, combined with in situ θ measured inside the lysimeters, the second study focuses on the determination of θ_{crit} that separates the water- and energy-limited ET_a regimes. The quantification of θ_{crit} is subject to uncertainties due to the different methods used to evaluate the relationship between ET_a and θ, such as θ depths, definitions of ET_a and curve fitting functions. Typically, surface θ is used to identify θ_{crit} as it is easily accessible and assumed to represent root zone θ status. Alternatively, weighable lysimeter technology allows for the assessment of both surface and root zone θ_{crit} by enabling accurate determination of ET_a and in-situ θ measurements. In this study, we estimated θ_{crit} using in situ θ measurements at 10 cm depth and root zone θ by vertically integrating in situ θ (0–60 cm) observations utilizing a total of 61 lysimeters from 7 sites in Germany. In addition, we applied three different definitions of relative evapotranspiration (evaporative fraction, the ratio of ET_a to grass reference evapotranspiration and the ratio of actual ET_a to calculated potential evapotranspiration) as well as two different fitting curves to investigate their sensitivities to θ_{crit}. We found robust θ_{crit} estimates across different definitions and fitting curve methods. Our results also highlight the high correlation (0.83) between root zone θ_{crit} and surface θ_{crit}. However, the relation between both values is not unique since it depends on the actual moisture profile and plant root system and, herewith, on the soil type and previous weather conditions. We further observed that both surface and root zone θ_{crit} decreased with increasing sand fraction. Under changing climatic conditions but with identical soil and ecosystem types, both surface and root zone θ_{crit} decreased with increasing aridity. Additionally, we found that using the midpoint between field capacity and wilting point provides a reliable range of root zone θ_{crit} for a given soil texture.

By extending the lysimeter networks to a total of 179 lysimeters from 27 sites across Asia, Europe and North America, a detailed analysis was conducted for surface and root zone θ_{crit} in the third study. We compared surface and root zone θ_{crit}, assessed whether the two layers reached their respective thresholds synchronously, and investigated their environmental controls across different climates and land cover types. Surface and root zone θ_{crit} were strongly correlated ($r = 0.84$) and showed broadly similar environmental controls, with soil texture emerging as the dominant driver at both depths. However, strong agreement in θ_{crit} did not necessarily translate into synchronous transitions to water limitation. In humid and sub-humid climates and grasslands, surface and root zone soil moisture approached their respective thresholds nearly synchronously, resulting in comparable persistence of water-limited conditions. In contrast, in semi-arid climates and croplands, surface soil moisture more frequently reached its threshold while root zone soil moisture remained above θ_{crit}, resulting in delayed root-zone transitions, lower persistence of root-zone water limitation, and more frequent false alarms from surface-based classification. These results demonstrate that surface θ_{crit} contains substantial information on the spatial variability of root zone θ_{crit}, but that agreement between the two thresholds does not necessarily imply agreement in when water limitation occurs.

Overall, this thesis was carried out using weighable lysimeter measurements, which are regarded as the most reliable in situ observations for ET_a. Our results show that weighable lysimeters can provide ET_a representative of spatial scales beyond their limited surface area

and yield unique insights into root zone θ_{crit}. These findings are crucial for designing monitoring networks and improving Earth system models. Further assessment of lysimeter representativeness by including more parallel measurements could confirm their suitability for upscaling and support the development of efficient, cost-effective monitoring networks. These networks could therefore further be used to accurately quantify ET_a, θ_{crit}, and their drivers at broader scales, and thus provide essential benchmarks for model evaluation. Incorporating θ_{crit} as a multidimensional function of their drivers into models could ultimately improve predictions of water fluxes, drought responses, and land–atmosphere feedbacks under future climate scenarios.

Zusammenfassung

Der Klimawandel wird voraussichtlich die Wasserverfügbarkeit erheblich verändern, die Häufigkeit und Schwere extremer Wetterereignisse verstärken und das Risiko von Dürren erhöhen. Die tatsächliche Evapotranspiration (ET_a) ist eine Schlüsselkomponente des terrestrischen Wasserkreislaufs, die Hydrosphäre, die Atmosphäre und die Biosphäre durch die Modulation einer Reihe von Landflächen- und ökohydrologischen Prozessen miteinander verbindet. ET_a wird entweder durch die Energieversorgung der Atmosphäre oder durch die Verfügbarkeit von Bodenfeuchte (θ) begrenzt. Der Übergang zwischen energiebegrenzten und wasserbegrenzten ET_a -Regimen hängt von θ ab und wird häufig durch einen Schwellenwert charakterisiert, der als kritische Bodenfeuchte (θ_{crit}) bezeichnet wird. Ein umfassendes Verständnis und eine genaue Quantifizierung von ET_a und seiner durch θ_{crit} gekennzeichneten Regimeklassifizierung sind für die Bewässerungssteuerung, die Überwachung von Dürren, die Bewertung von Dürreauswirkungen und die Verbesserung zukünftiger Prognosen zu Klima und Wasserressourcen sowie zur Nahrungsmittelproduktion, insbesondere im Zusammenhang mit dem Klimawandel, von entscheidender Bedeutung.

Wägbare Lysimeter spielen eine wichtige Rolle für das Verständnis der komplexen Wechselwirkungen innerhalb des Boden-Pflanzen-Atmosphäre-Kontinuums und gelten als die genaueste In-situ-Methode zur Quantifizierung von ET_a, jedoch aufgrund ihrer begrenzten Oberfläche nur auf Pedon-Skala. Ausgestattet mit Bodenfeuchtesensoren in mehreren Tiefen bieten Lysimeter eine einzigartige Möglichkeit, die Rolle sowohl der Oberfläche als auch, was besonders wichtig ist, der Wurzelzone θ beim Übergang zwischen wasser- und energiebegrenzten ET_a Regimen zu bewerten. Diese Arbeit untersucht das Potenzial von Lysimetern für die Bereitstellung von ET_a, die repräsentativ für größere Skalen als ihre Oberfläche sind, sowie die mit ET_a Regimewechseln verbundenen θ_{crit} an der Oberfläche und in der Wurzelzone. Der Umfang dieser Arbeit erweitert sich schrittweise von einer begrenzten Anzahl von Lysimetern in ausgewählten Regionen Deutschlands zu einem nationalen Netzwerk und umfasst schließlich einen internationalen Datensatz, der mehrere Kontinente umfasst.

In der ersten Studie wurde untersucht, ob Lysimeter ET_a Messungen trotz ihrer geringen Fläche repräsentative Informationen für größere Gebiete liefern können, beispielsweise für die Parzellen-, Landschafts- und größere regionale Skalen. Dazu wurden die räumlichen Korrelationen zwischen ET_a-Messungen an verschiedenen Standorten mit Lysimetern (ET-LYS) und an verschiedenen Standorten mit Eddy-Kovarianz (ET-EC) untersucht. Dies geschah für den Zeitraum 2015–2020, und die Analyse wurde für verschiedene räumliche (Bereich: 0 bis 500 km) und zeitliche Skalen (Bereich: 1 Tag bis 1 Jahr) unter Verwendung von 23 Lysimetern und 4 Eddy-Kovarianztürmen in Deutschland durchgeführt. Wir haben festgestellt, dass ET-LYS im Allgemeinen genauso repräsentativ ist wie ET-EC, mit hohen Korrelationen auf Parzellenebene und moderaten bis hohen Korrelationen auf Landschafts- und größerer regionaler Ebene. Die Wavelet-Analyse zeigte außerdem schwächere räumliche Korrelationen

unter Trockenbedingungen (im Jahr 2018) und die stärksten zeitlichen Korrelationen auf jährlicher und sub-saisonaler Ebene. Darüber hinaus verbesserte die Kombination mehrerer ET-LYS-Werte von verschiedenen Standorten die Vorhersagbarkeit von ET-LYS für einen anderen Standort, was darauf hindeutet, dass ET-LYS anhand von ET-LYS-Werten aus verschiedenen benachbarten Standorten gut vorhergesagt werden kann. Insgesamt können Lysimeter Messungen im Vergleich zu ihrem kleinen Mess enbereich Informationen in viel größeren Maßstäben liefern.

Unter Verwendung von Lysimeter ET_a Messungen in Kombination mit in situ gemessenen θ Werten innerhalb der Lysimeter konzentriert sich die zweite Studie auf die Bestimmung von θ_{crit}, das die wasser- und energiebegrenzten ET_a Regime trennt. Die Quantifizierung von θ_{crit} unterliegt Unsicherheiten aufgrund der unterschiedlichen Methoden zur Bewertung der Beziehung zwischen ET_a und θ, wie z. B. θ Tiefen, Definitionen von ET_a und Kurvenanpassungsfunktionen. Typischerweise wird die Oberflächen-θ verwendet, um θ_{crit} zu identifizieren,da sie leicht zugänglich ist und angenommen wird, dass sie den θ-Status der Wurzelzone repräsentiert. Alternativ ermöglicht die wiegbare Lysimetertechnologie die Bewertung sowohl der Oberflächen- als auch der Wurzelzonen θ_{crit}, da sie eine genaue Bestimmung von ET_a und In-situ θ Messungen ermöglicht. In dieser Studie haben wir θ_{crit} anhand von In-situ θ Messungen in 10 cm Tiefe und der Wurzelzonen θ durch vertikale Integration der In-situ θ Beobachtungen (0–60 cm) unter Verwendung von insgesamt 61 Lysimetern an 7 Standorten in Deutschland geschätzt. Darüber hinaus haben wir drei verschiedene Definitionen der relativen Evapotranspiration (Verdunstungsanteil, Verhältnis von ET_a zur Referenzevapotranspiration von Gras und Verhältnis der tatsächlichen ET_a zur berechneten potenziellen Evapotranspiration) sowie zwei verschiedene Anpassungskurven verwendet, um deren Empfindlichkeit gegenüber θ_{crit} zu untersuchen. Wir fanden robuste Schätzungen von θ_{crit} über verschiedene Definitionen und Anpassungskurvenmethoden hinweg. Unsere Ergebnisse zeigen auch die hohe Korrelation (0,83) zwischen θ_{crit} in der Wurzelzone und θ_{crit} an der Oberfläche. Die Beziehung zwischen beiden Werten ist jedoch nicht eindeutig, da sie vom tatsächlichen Feuchteprofil und dem Pflanzenwurzelsystem und damit vom Bodentyp und den vorherigen Wetterbedingungen abhängt. Wir haben außerdem beobachtet, dass sowohl θ_{crit} an der Oberfläche als auch in der Wurzelzone mit zunehmendem Sandanteil abnahm. Unter wechselnden klimatischen Bedingungen, aber bei identischen Boden- und Ökosystemtypen, nahm sowohl θ_{crit} an der Oberfläche als auch in der Wurzelzone mit zunehmender Trockenheit ab. Darüber hinaus haben wir festgestellt, dass die Verwendung des Mittelwerts zwischen Feldkapazität und Welkepunkt einen zuverlässigen Bereich für θ_{crit} in der Wurzelzone für eine bestimmte Bodenbeschaffenheit liefert.

Durch die Erweiterung der Lysimeter-Netzwerke auf insgesamt 179 Lysimeter an 27 Standorten in Asien, Europa und Nordamerika wurde in der dritten Studie eine detaillierte Analyse des θ_{crit} der Oberbodenschicht und der Wurzelzone durchgeführt. Wir verglichen den θ_{crit} der Oberbodenschicht und der Wurzelzone, untersuchten, ob die beiden Schichten ihre jeweiligen Schwellenwerte synchron erreichten, und untersuchten ihre umweltbedingten Einflussfaktoren in verschiedenen Klimazonen und bei unterschiedlichen Landbedeckungstypen. Der θ_{crit} der Oberbodenschicht und der Wurzelzone korrelierten stark

miteinander (r = 0,84) und wiesen weitgehend ähnliche umweltbedingte Einflussfaktoren auf, wobei sich die Bodenbeschaffenheit in beiden Tiefen als dominierender Einflussfaktor herausstellte. Die starke Übereinstimmung beim θcrit führte jedoch nicht zwangsläufig zu synchronen Übergängen in den wasserbegrenzten Zustand. In feuchten und subhumiden Klimazonen sowie auf Grünland näherten sich die Bodenfeuchte an der Oberfläche und in der Wurzelzone ihren jeweiligen Schwellenwerten nahezu synchron an, was zu einer vergleichbaren Dauer der wasserbegrenzten Bedingungen führte. Im Gegensatz dazu erreichte die Bodenfeuchte an der Oberfläche in semiariden Klimazonen und auf Ackerflächen häufiger ihren Schwellenwert, während die Bodenfeuchte in der Wurzelzone über θcrit blieb, was zu verzögerten Übergängen in der Wurzelzone, einer geringeren Dauer der Wasserbegrenzung in der Wurzelzone und häufigeren Fehlalarmen bei der Klassifizierung auf Basis der Oberflächenwerte führte. Diese Ergebnisse zeigen, dass der Schwellenwert θ_{crit} an der Oberfläche wichtige Informationen über die räumliche Variabilität des Schwellenwerts θcrit in der Wurzelzone enthält, dass jedoch die Übereinstimmung zwischen den beiden Schwellenwerten nicht zwangsläufig bedeutet, dass auch der Zeitpunkt des Eintritts der Wasserbegrenzung übereinstimmt.

Insgesamt wurde diese Arbeit unter Verwendung von Messungen mit wiegbaren Lysimetern durchgeführt, die als die zuverlässigsten In-situ-Beobachtungen für ETa gelten. Unsere Ergebnisse zeigen, dass wiegbare Lysimeter ETa-Werte liefern können, die über ihre begrenzte Oberfläche hinaus repräsentativ für räumliche Skalen sind, und einzigartige Einblicke in θcrit im Wurzelbereich ermöglichen. Diese Erkenntnisse sind entscheidend für die Konzeption von Überwachungsnetzwerken und die Verbesserung von Erdsystemmodellen. Eine weitere Bewertung der Repräsentativität von Lysimetern durch Einbeziehung weiterer Parallelmessungen könnte ihre Eignung für eine Hochskalierung bestätigen und die Entwicklung effizienter, kostengünstiger Überwachungsnetzwerke unterstützen. Diese Netzwerke könnten daher weiter genutzt werden, um ET_a, θ_{crit} und ihre Treiber auf breiterer Ebene genau zu quantifizieren und somit wichtige Benchmarks für die Modellbewertung zu liefern. Die Einbeziehung von θ_{crit} als mehrdimensionale Funktion ihrer Einflussfaktoren in Modelle könnte letztlich die Vorhersagen von Wasserflüssen, Dürre-Reaktionen und Land-Atmosphäre-Rückkopplungen unter zukünftigen Klimaszenarien verbessern.

Acknowledgements

First and foremost, I would like to express my deepest gratitude to my supervisor, Prof. Dr. Harrie-Jan Hendricks-Franssen, for his intensive guidance and continuous support throughout my doctoral studies. Over the course of these years, we had frequent meetings and fruitful discussions. He devoted considerable time and effort to reviewing my slides, posters, reports and manuscripts with great patience. I am deeply impressed by his profound knowledge, scientific rigor, critical thinking and insightful suggestions, from which I have greatly benefited.

My sincerest thanks go to Dr. Jannis Groh for his close collaboration and the vital role he played throughout my PhD work. He not only shared with me extensive expertise in lysimeters, hydrology and soil science, but also sought to establish important collaborations in lysimeter research, which made the completion of our papers possible. He dedicated countless hours to providing data, discussing my work, offering insightful feedback, and reviewing drafts. I am truly grateful for his warm encouragement, tremendous support, and thoughtful guidance throughout my doctoral journey.

I also wish to thank Dr. Alexandar Graf for his engaging discussions and prompt constructive feedback on my queries and draft manuscripts. I am especially grateful for his thoughtful advice, not only academically but also in life including guidance on how to prioritize tasks and make effective decisions. Special thanks go to Dr. Thomas Pütz, whose knowledge, humor, encouragement, and positive attitude have inspired me and gave me confidence and motivation throughout this journey.

I would like to express my sincere appreciation to Prof. Dr. Harry Vereecken, Director of our institute, for his invaluable support and inspiring insights. His broad vision, profound knowledge, and deep love for science have been truly inspiring. I would also like to extend my gratitude to Prof. Dr. Jan Vanderborght, who provided skillful suggestions during our conversations, IKOs, PhD seminars, and other occasions.

I would like to express my heartfelt thanks to everyone who contributed their time and expertise whether by providing data, offering technical support, or reviewing my manuscript. Each suggestion and correction has played a meaningful role in the refinement of this thesis.

I would also like to sincerely thank my friends and colleagues at IBG-3 (Forschungszentrum Jülich) for their help in my study and life. The many enjoyable conversations and relaxing lunch breaks offered much-needed moments of balance and relief from the intensity of research work.

In addition, I would like to thank the China Scholarship Council (CSC) for sponsoring my work and life in Germany. Furthermore, I gratefully acknowledge the Terrestrial Environmental Observatories (TERENO) network for providing valuable data and opportunities to participate in scientific conferences and workshops.

I would also like to thank my friends, both those close by and those far away. Whether they have accompanied me for a part of the journey or stayed by my side throughout, they have all brought color and joy to my life.

Last but not least, special thanks to my families, especially my parents and my lovely sister Bei, for their constant support, encouragement, and love. Thanks to my husband Kerui for his companionship and for sharing with me both joyful and challenging moments along the way.

Contents

Abstract v
Zusammenfassung ix
Acknowledgements xiii
Contents xv
List of Figures xviii
List of Tables xxvii
List of Acronyms xxx
Chapter 1. Introduction 1
Chapter 2. Materials 9
2.1 TERENO lysimeter network and set up 9
2.2 Eddy covariance tower set up 14
2.3 Meteorological data 14
2.4 Lysimeter data 15
2.5 Eddy covariance data 17
Chapter 3. Scale-dependent spatial correlations of actual evapotranspiration measured by lysimeters…….. 19
3.1 Introduction 19
3.2 Materials and methods 22
3.2.1 Study sites 22
3.2.2 Lysimeters set up 25
3.2.3 Lysimeter data 25
3.2.4 Eddy covariance data 27
3.2.5 Pearson correlation coefficient of standardized anomalies of ET_a 28
3.2.6 Wavelet analysis 29
3.3 Results 31
3.3.1 Observations of ET-LYS and ET-EC 31
3.3.2 Pearson correlations for ET-LYS and ET-EC at different spatial scales 35
3.3.3 Wavelet coherence of ET-LYS and ET-EC 39
3.3.4 Combined ET_a measurements from multiple sites 45
3.4 Discussion 50
3.4.1 Overall assessment of correlations 50

3.4.2 Implications for lysimeter networks 52
3.5 Conclusions 53
Chapter 4. Variability and robustness of critical soil moisture: Insights from lysimeter data in Germany 55
4.1 Introduction 55
4.2 Materials and Methods 59
4.2.1 A framework for estimating critical soil moisture thresholds 60
4.2.2 Site description and lysimeter set-up 62
4.2.3 Data 66
4.2.4 Energy world (Evaporative fraction) 69
4.2.5 Water world (Ratio of actual to potential ET) 69
4.2.6 Spherical variogram fitting 70
4.2.7 Critical root zone soil moisture thresholds according FAO-56 71
4.3 Results 72
4.3.1 Consistency of θ_{crit} derived from the EF, rET_0 and $rPET_{FAO}$ definitions 72
4.3.2 Comparison between the linear-plus-plateau and spherical variogram fitting curves 76
4.3.3 Comparison between surface and root zone θ_{crit} 77
4.3.4 Comparison of root zone θ_{crit} derived from observations and FAO-56 80
4.4 Discussion 81
4.5 Conclusions 86
Chapter 5. Comparison of surface and root zone critical soil moisture from lysimeter time series 88
5.1 Introduction 88
5.2 Materials and Methods 90
5.2.1 Study sites 90
5.2.2 Data 91
5.2.3 Drydown identification 92
5.2.4 Determination of critical soil moisture 93
5.2.5 Consistency of critical soil moisture between surface and root zone layers 94
5.2.6 Drivers of θ_{crit} 95
5.3 Results 96
5.3.1 Overall evaluation of surface and root zone θ_{crit} 96

5.3.2 Comparison surface and root zone θ_{crit} across climates and land covers 97
5.3.3 Consistency between surface and root zone ET_a regime identification 99
5.3.4 Drivers of surface and root zone θ_{crit} 102
5.4 Discussion 104
5.5 Conclusion 108
Chapter 6. Conclusions and outlook 109
6.1 Conclusions 109
6.2 Outlook 110
Appendix 113
Appendix A 113
Appendix B 119
Appendix B.1 119
Appendix B.2 123
Appendix C 131
Bibliography 137

List of Figures

Figure 2.1 Locations of the four TERENO observatories in Germany. The red circles marked in each observatory indicate the location of the lysimeter stations used in this thesis (adapted from Pütz et al., 2016). The pink dashed arrow line indicates the transfer of the soil monoliths. 12

Figure 3.1 Location of TERENO observatories over Germany and locations of the four study sites (marked by red circle), as well as distances (in km) between different sites (three different shades of blue are used to indicate different spatial scales; modified from Pütz et al., 2016). RO: Rollesbroich, WU: Wüstebach, SE: Selhausen, GW: Graswang. 24

Figure 3.2 Average monthly cumulative ET-LYS, ET-EC, ET-ECc and ET_0 at different sites, calculated over the period 2015-2020. Error bars denote the standard deviations of monthly ET, calculated over the years. 35

Figure 3.3 Pearson correlation coefficient (PCC) for ET-LYS, ET-EC and ET-ECc at the landscape scale. Bars refer to PCC of standardized anomaly of ET-LYS ($SA_{ET\text{-}LYS}$, red bar), standardized anomaly of ET-EC ($SA_{ET\text{-}EC}$, green bar), or standardized anomaly of ET-ECc ($SA_{ET\text{-}ECc}$, blue bar) between different sites for the period 2015-2020. Yellow bar refers to PCC between $SA_{ET\text{-}LYS}$ from lysimeters at SE site filled with soil from RO site (SEro) and another lysimeter site. Purple bar refers to PCC between $SA_{ET\text{-}LYS}$ from lysimeters at SE site filled with soil from WU site (SEwu) and another lysimeter site. Circles denote the PCC for individual years. 38

Figure 3.4 Scatter plot of Pearson correlation coefficient (PCC) of standardized anomaly (SA) of ET-EC and ET-ECc between the different sites. ET-EC and ET-ECc refer to the ET_a measurements from EC without and with energy balance closure, respectively. Dashed line is the 1:1 line. 39

Figure 3.5 Wavelet transform coherence (WTC) and global coherence coefficient (GCC) of ET-LYS between (a) RO and WU, (b) RO and SEro, (c) RO and SEwu, (d) RO and SEse, (e) WU and SEro, (f) WU and SEwu, (g) WU and SEse. The vertical axis shows the periodicity up to 770 days. The right part of each panel demonstrates the GCC. The left part of each panel depicts WTC and the horizontal axis shows the study period (from 2015-2020 on daily basis). Thick contours indicate significant coherence at 95% confidence level. The pale region delineates the cone

of influence (COI) where edge effect might distort the results. Small arrows show the phase difference between two series (right arrows indicate in-phase (positive) relationship, left arrows indicate out-of-phase (or negative) relationship (180°), and arrows upwards (downwards) indicate the second series leading (lagging) the first by 90°). The color denotes the strength of coherence with the red being high and blue being low.....41

Figure 3.6 Wavelet transform coherence (WTC) and global coherence coefficient (GCC) of ET-EC between (a) RO and WU, (b) RO and SE, (c) WU and SE. The vertical axis shows the periodicity up to 770 days. The right part of each panel demonstrates the GCC. The left part of each panel depicts WTC and the horizontal axis shows the study period (from 2015-2020 on daily basis). Thick contours indicate significant coherence at 95% confidence levels against red noise. The pale region delineates the cone of influence (COI) where edge effect might distort the results. Small arrows show phase difference between two series (right arrows indicate in-phase relationship, left arrows indicate out-of-phase relationship (180°), and arrows upwards (downwards) indicate the second series leading (lagging) the first by 90°). The color denotes the strength of coherence. 42

Figure 3.7 Wavelet transform coherence (WTC) and global coherence coefficient (GCC) of ET-LYS between (a) WU and GW, (b) RO and GW, (c) SEse and GW, (g) SEwu and GW and (h) SEro and GW, and WTC of ET-EC between (d) WU and GW, (e) RO and GW and (f) SE and GW. The vertical axis shows the periodicity up to 770 days. The right part of each panel demonstrates the GCC. The left part of each panel depicts WTC and the horizontal axis shows the study period (from 2015-2020 on daily basis). Thick contours indicate significant coherence at 95% confidence level. The pale region delineates the cone of influence (COI) where edge effect might distort the results. Small arrows show phase difference between two time series (right arrows indicate in-phase relationship, left arrows indicate out-of-phase relationship (180°), and arrows upwards (downwards) indicate the second series leading (lagging) the first by 90°). The color denotes the strength of coherence. 44

Figure 3.8 Two-site scenario of multiple wavelet coherence (MWC) at the landscape scale. The vertical axis shows the periodicity up to 770 days, and the horizontal axis the study period (from 2015-2020 on daily basis). Thick contours indicate significant

coherence at 95% confidence level. The pale region delineates the cone of influence (COI) where edge effect might distort the results. The color denotes the strength of coherence. 47

Figure 3.9 Two-site scenario of multiple wavelet coherence (MWC) of ET-LYS at the larger regional scale. The vertical axis shows the periodicity up to 770 days, and the horizontal axis the study period (from 2015-2020 on daily basis). Thick contours indicate significant coherence at 95% confidence level. The pale region delineates the cone of influence (COI) where edge effect might distort the results. The color denotes the strength of coherence. 48

Figure 3.10 Two-site scenario of multiple wavelet coherence (MWC) of ET-EC at the larger regional scale. The vertical axis shows the periodicity up to 770 days, and the horizontal axis the study period (from 2015-2020 on daily basis). Thick contours indicate significant coherence at 95% confidence level. The pale region delineates the cone of influence (COI) where edge effect might distort the results. The color denotes the strength of coherence. 49

Figure 3.11 Three-site scenario of multiple wavelet coherence (MWC) at the larger regional scale. The vertical axis shows the periodicity up to 770 days, and the horizontal axis the study period (from 2015-2020 on daily basis). Thick contours indicate significant coherence at 95% confidence level. The pale region delineates the cone of influence (COI) where edge effect might distort the results. The color denotes the strength of coherence. 50

Figure 4.1 Schematic plot showing the assessment of fET - θ relationship, where fET represents either EF, rET_0 or $rPET_{FAO}$. θ can be soil moisture from soil surface (θ_s) or from the root zone (θ_v). Blue dots represent the data points during dry downs over the growing periods. The thick black line denotes the linear-plus-plateau fitting 58

Figure 4.2 Flow chart showing the estimation of critical soil moisture (θ_{crit}). 60

Figure 4.3 Example time series of vertically integrated (0-60 cm) soil moisture (θv) for one lysimeter (SE42) of the SEsb lysimeter group at the SE site for April-September 2019. Drydowns are highlighted in orange. θv during the drydown events are marked as red. Blue dots represent θv which are outside or excluded from the drydown events. Bars represent the daily precipitation. 61

Figure 4.4 Locations of the four TERENO observatories in Germany. The red circles marked in each observatory indicate the location of the lysimeter stations used in this study (adapted from Pütz et al. 2016). The pink dashed arrow line indicated the transfer routes of the soil monoliths.....64

Figure 4.5 Critical soil moisture thresholds (θ_{crit}) estimated from the root zone soil moisture (θ_v) for one crop lysimeter SE42 at the SE site filled with soil from the SB site using the EF, rET_0 and $rPET_{FAO}$ definitions by (a-c) linear-plus-plateau fitting and (d-f) spherical variogram fitting. In each plot, the shape of the dots indicates the crop type. The thick black line in each plot indicates the fitted curve. The red numbers in each plot indicate the estimated θ_{crit}.....74

Figure 4.6 θ_{crit} for surface soil (0-10cm) and root zone soil (0-60cm) according to the rET_0, EF and $rPET_{FAO}$ definition using (a) linear-plus-plateau fitting and (b) spherical variogram fitting. The middle line represents the median θ_{crit} estimated by a given definition based on values for individual lysimeters (indicated by dots); the box represents the upper and lower quartiles, and the whiskers represent 1.5 times the interquartile range. The color of the dots indicates the lysimeter sites. Black stars above the boxplots represent statistically significant differences of θ_{crit} between the surface soil and root zone soil using Wilcoxon test. * represents $p < 0.05$, ** represents $p < 0.01$, and *** represents $p < 0.001$. There was no significant difference in θ_{crit} estimates from different fitting curves or ET_a definitions ($p > 0.05$).....74

Figure 4.7 (a-c) Comparison between lysimeter-specific θ_{crit} estimated according EF, rET_0 and $rPET_{FAO}$ definitions using linear-plus-plateau fitting. RMSD is the root mean square deviation of θ_{crit} estimates between the definitions. The dashed line is the 1:1 line. The shape of the dots represents the soil depth and the color of the dots indicates the land cover type. (d-f) Distribution of differences in θ_{crit} according the different definitions. 76

Figure 4.8 Comparison between the linear-plus-plateau fitting (LP) and spherical variogram fitting (SV) regarding (a) θ_{crit}, (b) the plateau value of the fitting and (c) the performance of fitting based on values for individual lysimeters for each definition (EF, rET_0 and $rPET_{FAO}$) and soil depth (surface soil and root zone soil). The color indicates the definitions. Dashed line is 1:1 line and red line is the regression line.

RMSD is the root mean square deviation. (d) Distribution of differences in θ_{crit} derived from the two fitting curves. 77

Figure 4.9 (a) Scatterplot of θ_{crit} for surface soil (θ_{crit_s}) versus root zone soil (θ_{crit_v}), estimated for each lysimeter using the rET_0 definition. AI means aridity index. (b) Distribution of differences in θ_{crit} between root zone soil and surface soil. 78

Figure 4.10 Relationship between sand fraction and θ_{crit} for (a) surface soil and (b) root zone soil. The thick black line represents the linear regression of θ_{crit} to sand fraction for all lysimeter groups. Regression equations, R^2 and p-values (regression t-test) are indicated (**P < 0.01). Colored regression lines indicate the relationships between θ_{crit} and sand fraction for lysimeter groups that have the same land cover type at the same site but differ in soil texture..... 79

Figure 4.11 Relationship between aridity index and θ_{crit} for (a) surface soil and (b) root zone soil. The thick blue line represents the linear regression of θ_{crit} to aridity index for all the translocated lysimeter groups. Regression equations, R^2 and p-values (regression t-test) are indicated (*P < 0.05). Colored regression lines indicate the relationships between θ_{crit} and aridity index for translocated lysimeters which have the same soil origin but are placed at different sites..... 80

Figure 4.12 Root zone θ_{crit} for different soil textures. The middle line represents the median θ_{crit} estimated for a given soil texture on the basis of values for individual lysimeters for that soil texture; the box represents the upper and lower quartiles and the whiskers represent 1.5 times the interquartile range. The shape of the dots indicates the land cover type of the lysimeters. Red lines indicate the upper and lower θ_{crit} calculated based on FAO-56. 81

Figure 4.13 Comparison between plateau values estimated from the rET_0 and $rPET_{FAO}$ definition across all the lysimeters. The dashed line is the 1:1 line. 82

Figure 5.1 Distribution of lysimeter sites included in this study. Red, blue, orange, and gray dots indicate sites where θ_{crit} was detected for both surface and root zone layers, sites where θ_{crit} was detected for only one layer, sites that were in the water-limited regime only, and sites where no θ_{crit} was detected, respectively. A single site may have multiple lysimeters. 91

Figure 5.2 (a-b) Probability density functions (PDFs) of θ_{crit} in (a) surface layer and (b) root zone layers, respectively. (c) Comparison of lysimeter-specific θ_{crit} between surface and root zone layers using all valid estimates. (d) Relationship of lysimeter-

specific θcrit between surface and root zone layers using all paired values The solid black line represents the reduced major axis (RMA) regression and the dashed line is the 1:1 line. The RMA equation, R^2, two-sided P value for the linear regression slope (regression t-test), and sample size (N) are shown in the panel (***P < 0.001). 96

Figure 5.3 Relationship of lysimeter-specific θcrit between surface and root zone layers (a) for humid and sub-humid sites, (b) for semi-arid sites, (c) for grasslands and (d) for croplands. The solid black line represents the reduced major axis (RMA) regression and the dashed line is the 1:1 line. The RMA equation, R^2, two-sided P value for the linear regression slope (regression t-test), and sample size (N) are shown in the panels (***P < 0.001). 98

Figure 5.4 Boxplot of lysimeter-specific θ_{crit} for surface and root zone layers using all valid pairs across different (a) climates and (b) land covers. 98

Figure 5.5 Difference and relative difference between surface and root zone θcrit across (a,b) climates and (c,d) land covers. 99

Figure 5.6 Binary regime similarity (φ) between surface and root zone layer across (a) climates and (d) land covers. Scatter plot of the time spent in water-limited regime (γ) for the surface layer (γ_{surf}) against that for the root zone layer (γ_{root}) across different (b-c) climates and (e-f) land covers. The solid black line represents the reduced major axis (RMA) regression and the dashed line is the 1:1 line. The RMA equation, R^2 and two-sided P value for the linear regression slope (regression t-test) are shown in the panels (***P < 0.001). 101

Figure 5.7 (a) Relationship between root zone θ_{crit} and conditionally averaged root zone soil moisture when surface soil moisture reaches surface θ_{crit} ($E(\theta_{root} \mid \theta_{surf} = \theta_{crit,surf})$). (b,c) The differences ($\Delta_{EC\Theta}$) between root zone θ_{crit} and $E(\theta_{root} \mid \theta_{surf} = \theta_{crit,surf})$ across (b) different climates and (c) land cover types. 101

Figure 5.8 Distributions of (a,d) false alarms rate (FAR), (b,e) missed event rate (MER), and (c,f) true alarms rate (TAR) across (a-c) different climates and (d-f) different land covers. 102

Figure 5.9 Relative importance of factors influencing θcrit for (a) surface layer and (b) root zone layer. The importance was assessed with the mean absolute SHAP value. 103

Figure 5.10 Partial dependence plots of the SHAP value for surface θcrit against the seven explanatory variables in (a) sand fraction, (b) clay fraction, (c) aridity index (AI), (d) air temperature (AI), (e) wind speed (WS), (f) global radiation (Rg) and (g) vapor pressure deficit (VPD). Positive and negative SHAP values indicate contributions towards higher and lower predicted θ_{crit}, respectively. The black line shows the fitted line, providing an estimate of the general trend. The shading area indicates the 95% confidence interval. 103

Figure 5.11 Partial dependence plots of the SHAP value for root zone θcrit against the seven explanatory variables in (a) sand fraction, (b) clay fraction, (c) aridity index (AI), (d) air temperature (AI), (e) wind speed (WS), (f) global radiation (Rg) and (g) vapor pressure deficit (VPD). Positive and negative SHAP values indicate contributions towards higher and lower predicted θ_{crit}, respectively. The black line shows the fitted line, providing an estimate of the general trend. The shading area indicates the 95% confidence interval. 104

Figure A.1 Average monthly cumulative ET-LYS for different lysimeter groups, ET-EC, ET-ECc and ET_0 at Selhausen (SE) site, calculated over the period 2015-2020. Error bars denote the standard deviations of monthly ET, calculated over the years.. 116

Figure A.2 Continuous wavelet transform (CWT) for the six daily ET-LYS series and four daily ET-EC series for years 2015 – 2020. The contours indicate 95% confidence levels. Thin solid lines delineate the cones of influence. The color denotes the strength of wavelet power..... 117

Figure A.3 Budyko plots for the 4 sites during 2015-2020. This was done using the mean daily ET-LYS from multiple lysimeters at the same site. 118

Figure B.1 Scatterplots comparing the measured G at 3 cm depth at the field (G_{03_obs}) and the measured G at 10 cm depth in the lysimeter (G_{10}, upper left panel) as well as the estimated G (G_{03_est}) by the four approaches for daytime from April to September for one lysimeter (RO11) at the Rollesbroich site. The dashed line is a 1:1 line. 122

Figure B.2 Critical soil moisture threshold (θ_{crit}) of the surface soil moisture (θ_s) and root zone soil moisture (θ_v) for all lysimeters using the EF and rET_0 method for the WUwu lysimeters. In each plot, the shape of the dots indicates the crop type. The thick black line in each plot indicates the fitted linear-plus-plateau regression. The red numbers in each plot indicate the estimated θ_{crit}..... 125

Figure B.3 Critical soil moisture threshold (θ_{crit}) of the surface soil moisture (θ_s) and root zone soil moisture (θ_v) for all lysimeters using the EF and rET_0 method for the ROro lysimeters. In each plot, the shape of the dots indicates the crop type. The thick black line in each plot indicates the fitted linear-plus-plateau regression. The red numbers in each plot indicate the estimated θ_{crit}.....125

Figure B.4 Critical soil moisture threshold (θ_{crit}) of the surface soil moisture (θ_s) and root zone soil moisture (θ_v) for all lysimeters using the EF and rET_0 method for the SEfr and SEsy lysimeters. In each plot, the shape of the dots indicates the crop type. The thick black line in each plot indicates the fitted linear-plus-plateau regression. The red numbers in each plot indicate the estimated θ_{crit}. 126

Figure B.5 Critical soil moisture threshold (θ_{crit}) of the surface soil moisture (θ_s) and root zone soil moisture (θ_v) for all lysimeters using the EF and rET_0 method for the SEro and SEwu lysimeters. In each plot, the shape of the dots indicates the crop type. The thick black line in each plot indicates the fitted linear-plus-plateau regression. The red numbers in each plot indicate the estimated θ_{crit}. 127

Figure B.6 Critical soil moisture threshold (θ_{crit}) of the surface soil moisture (θ_s) and root zone soil moisture (θ_v) for all lysimeters using the EF, rET_0 and $rPET_{FAO}$ method for the SEro and SEwu lysimeters. In each plot, the shape of the dots indicates the crop type. The thick black line in each plot indicates the fitted linear-plus-plateau regression. The red numbers in each plot indicate the estimated θ_{crit}.....127

Figure B.7 Critical soil moisture threshold (θ_{crit}) of the surface soil moisture (θ_s) and root zone soil moisture (θ_v) for all lysimeters using the EF, rET_0 and $rPET_{FAO}$ method for the SEdd and SEse lysimeters. In each plot, the shape of the dots indicates the crop type. The thick black line in each plot indicates the fitted linear-plus-plateau regression. The red numbers in each plot indicate the estimated θ_{crit}.....128

Figure B.8 Critical soil moisture threshold (θ_{crit}) of the surface soil moisture (θ_s) and root zone soil moisture (θ_v) for all lysimeters using the EF, rET_0 and $rPET_{FAO}$ method for the DDdd and DDhd lysimeters. In each plot, the shape of the dots indicates the crop type. The thick black line in each plot indicates the fitted linear-plus-plateau regression. The red numbers in each plot indicate the estimated θ_{crit}.....128

Figure B.9 Critical soil moisture threshold (θ_{crit}) of the surface soil moisture (θ_s) and root zone soil moisture (θ_v) for all lysimeters using the EF, rET_0 and $rPET_{FAO}$ method for the DDk and DDs lysimeters. In each plot, the shape of the dots indicates the crop type.

The thick black line in each plot indicates the fitted linear-plus-plateau regression. The red numbers in each plot indicate the estimated θ_{crit}. 129

Figure B.10 Critical soil moisture threshold (θ_{crit}) of the surface soil moisture (θ_s) and root zone soil moisture (θ_v) for all lysimeters using the EF, rET_0 and $rPET_{FAO}$ method for the SBsb lysimeters. In each plot, the shape of the dots indicates the crop type. The thick black line in each plot indicates the fitted linear-plus-plateau regression. The red numbers in each plot indicate the estimated θ_{crit}. 129

Figure B.11 Critical soil moisture threshold (θ_{crit}) of the surface soil moisture (θ_s) and root zone soil moisture (θ_v) for all lysimeters using the EF, rET_0 and $rPET_{FAO}$ method for the BLbl lysimeters. In each plot, the shape of the dots indicates the crop type. The thick black line in each plot indicates the fitted linear-plus-plateau regression. The red numbers in each plot indicate the estimated θ_{crit}. 130

Figure C.1 Example time series of (a) surface soil moisture at 10 cm depth and (b) root zone soil moisture integrated over 0-60 cm for a cropland lysimeter (SE34) at the Selhausen site, Germany, during April-September 2023. Drydowns are highlighted in orange. Soil moisture observations during the drydown events are marked as red, whereas observations outside or excluded from the drydown events are shown in blue. Bars represent the daily precipitation.Horizontal dashed line indicates the corresponding critical soil moisture estimated for this lysimeter from 2013-2023. 136

List of Tables

Table 2.1 Specifications of the TERENO-SOILCan lysimeters used in this thesis. For the lysimeter group, the first two letters represent the location of the lysimeters, and the last two letters represent the soil origin. For the lysimeter ID, the first two letters indicate the site where the lysimeter is located, the first number indicates the lysimeter hexagon and the second number indicates the lysimeter of the hexagon. T_a denotes the long-term mean annual air temperature and P is the long-term mean annual precipitation at each site. Aridity index (AI) was calculated by mean annual grass reference ET (ET_0) divided by mean annual precipitation over the study period. There are four classifications according to AI: humid ($AI \leqslant 1.3$), sub-humid ($1.3 < AI \leqslant 1.5$), semi-arid ($1.5 < AI \leqslant 5$), and arid ($5 < AI < 20$). 12

Table 3.1 Specifications of the four lysimeter (LYS) sites used for the analyses in this chapter including location, number of individual lysimeters, soil information and land use. 24

Table 3.2 Yearly sums of ET_0, ET-LYS, ET-EC and ET-ECc at different sites. "Gap-filled ET_a [%]" denotes the percentage of hourly ET_a which were gap-filled. Here, yearly ET-LYS is the mean of multiple lysimeters at the same site. The standard deviations between the lysimeters are presented in parentheses. 34

Table 3.3 Average Pearson correlation coefficient (PCC) of $SA_{ET\text{-}LYS}$, calculated between different pairs of lysimeters at the same site for the period 2015-2020. "Stdv" denotes the standard deviation of correlations. 38

Table 3.4 Average wavelet coherence (AWC) and percent area of significant coherence (PASC) values for the wavelet coherence of ET-LYS or ET-EC between two sites at the landscape scale. 42

Table 3.5 Average wavelet coherence (AWC) and percent area of significant coherence (PASC) values for the wavelet coherence of ET-LYS or ET-EC between two sites at the larger regional scale. 43

Table 3.6 Main statistics of multiple wavelet coherence (MWC) of ET-LYS (or ET-EC) between sites at the landscape scale. AWC refers to average multiple-wavelet coherence. PASC refers to the percent area of significant coherence. The symbol "&" means combination, e.g., RO - WU & SEse means the coherence between ET-

LYS at the RO site and the combination of ET-LYS from lysimeters at the WU site and SE site filled with local soil. 45

Table 3.7 Main statistics of multiple wavelet coherence (MWC) of ET-LYS (or ET-EC) between sites at the larger regional scale. AWC refers to average multiple-wavelet coherence. PASC refers to the percent area of significant coherence. The symbol "&" means combination, e.g., RO - WU & GW means the coherence between ET-LYS at the RO site and the combination of ET-LYS measured by lysimeters at the WU site and lysimeters at the GW site. 46

Table 3.8 Main statistics of multiple wavelet coherence (MWC) of ET-LYS (or ET-EC) between sites at the larger regional scale. AWC refers to average multiple-wavelet coherence. PASC refers to the percent area of significant coherence. The symbol "&" means combination, e.g., RO - WU & SEse & GW means the coherence between ET-LYS at the RO site and the combination of ET-LYS measured by lysimeters at the WU site, lysimeters at the SE site filled with local soil and lysimeters at the GW site. 46

Table 4.1 Specifications of the lysimeters used in this study. For the lysimeter group, the first two letters represent the location of the lysimeters and the last two letters represent the soil origin. For the lysimeter ID, the first two letters indicate the site where the lysimeter is located, the first number indicates the lysimeter hexagon and the second number indicates the lysimeter of the hexagon. Sand fraction for soil depth 0-60cm was weighted according the soil sample depths. Aridity index was calculated by mean annual grass reference ET divided by mean annual precipitation. There are four classifications according the aridity index: humid (Aridity index $\leqslant$ 1.3), sub-humid (1.3 < Aridity index $\leqslant$ 1.5), semi-arid (1.5 < Aridity index $\leqslant$ 5), and arid (5 < Aridity index < 20). 64

Table 4.2 Differences in mean annual grass reference ET (ET_0), mean annual precipitation (P), mean annual air temperature (T_a) and aridity index (AI, defined as the ratio of ET_0 to P) between the translocated and original sites. 66

Table 4.3 The lower and upper values for field capacity (FC) and wilting point (WP) according to FAO-56, and the range of root zone critical soil moisture thresholds (θ_{crit_FAO56}) calculated from the midpoint of FC and WP. *Note:* values for Sandy clay loam are based on values from Raes et al. (2023). 72

Table 4.4 Number of θ_{crit} estimates for surface or/and root zone soil at each site by the EF, rET_0 and $rPET_{FAO}$ definitions fitted by linear-plus-plateau curve. 72

Table A.1 Start and end of the snow cover period observed for the lysimeters at the Rollesbroich (RO) site. "/" means no records. The information is from the camera surveillance system near the lysimeters. 113

Table A.2 Start and end of the snow cover period observed for the lysimeters at the Wüstebach (WU) site. The information is from the camera surveillance system near the lysimeters. 113

Table A.3 Start and end of the snow cover period observed on the lysimeters at the Graswang (GW) site. 114

Table A.4 The percentage of gap-filled hourly data for each month over 2015-2020. The units are "%". 114

Table A.5 The percentage of gap-filled hourly data during daytime and nighttime for each year over 2015-2020. Daytime and nighttime defined based on sunrise and sunset. . 115

Table A.6 Crop information for the lysimeters in Selhausen filled with soil from Selhausen (SEse). 115

Table A.7 Crop information for the EC field at Selhausen (SE). 116

Table B.1 Overview of the approaches 121

Table B.2 Summary of approach performance indicated by the statistical metrics. RO11 to RO16 indicate the statistical metrics for each lysimeter. Mean and Sd refer to the average and standard error for NEM or RMSE for all the lysimeters, respectively. The unit for NME is % and for RMSE is W m^{-2}. 122

Table B.3 Summary of sowing dates of crops at lysimeter sites and the information of similar crop in FAO-56. 123

Table B.4 Site-specific crop information including the recorded crop types, sowing dates, harvest dates as well as the estimated start and end dates of the mid-season stage at the Selhausen (SE) site from 2012-2023. 123

Table B.5 Same as Table B.4, but for the Dedelow (DD) site from 2014-2023. 124

Table B.6 Same as Table B.4, but for the Bad-Lauchstädt (BL) site from 2014-2018. 124

Table B.7 Same as Table B.4, but for the Sauerbach (SB) site from 2012-2020. 124

Table C.1 Summary of lysimeters details and corresponding critical soil moisture thresholds for both surface and root zone soil. 131

Table C.2 Summary of availability of critical soil moisture. 136

List of Acronyms

AP	Air pressure
EC	Eddy covariance
EF	Evaporative fraction
ET	Evapotranspiration
ET_a	Actual evapotranspiration
ET_0	Grass reference evapotranspiration
G	Soil heat flux
H	Sensible heat flux
LE	Latent heat flux
P	Precipitation
PCC	Pearson correlation coefficient
PET	Potential evapotranspiration
RH	Relative humidity
Rg	Global radiation
R_n	Net radiation
rET_0	Ratio of actual evapotranspiration to grass reference evapotranspiration
rPET	Ratio of actual evapotranspiration to potential evapotranspiration
T_a	Air temperature
TERENO	TERrestrial ENvironmental Observatories
Ts	Soil temperature
VPD	vapor pressure deficit
WS	wind speed
θ	Soil moisture
θ_{crit}	Critical soil moisture
θ_s	Surface soil moisture
θ_v	Root zone soil moisture

Chapter 1. Introduction

The water cycle plays a crucial role in Earth's climate system, particularly in the context of climate change, which intensifies the water cycle, leading to more frequent and severe extreme weather events such as floods and droughts (Denissen et al., 2022; Ficklin et al., 2022; Newman et al., 2006; Odorico et al., 2018; Zaitchik et al., 2023). Hence the demand to investigate the water cycle has increased. Evapotranspiration (ET), a major component of the terrestrial water cycle, typically accounts for a greater proportion of water than runoff and for more than 60% of global precipitation (Maxwell & Condon, 2016; Oki & Kanae, 2006; Trenberth et al., 2006). ET also serves as a unique link between energy, water and carbon cycles. It accounts for more than 50% of the total solar energy in the form of latent heat flux, facilitating the phase change of water from liquid (or ice) to vapor (Trenberth et al., 2009; Wang & Dickinson, 2012). Commonly, ET refers to the combination of evaporation from the surface (in some cases including evaporation from water intercepted on plant leaves), and transpiration by the plant, the latter of which is coupled with carbon uptake through photosynthesis (Fisher et al., 2017). Potential ET (PET) is the amount of water that can be evaporated and transpired by a plant under sufficient water supply, whereas actual ET (ET_a) refers to the ET that actually occurs, affected by possible water scarcity. A better knowledge of ET_a is essential across multiple disciplines, including climatology, hydrology, and agricultural science, as it underpins accurate drought prediction, efficient agricultural water management, and the sustainable use of water resources in the face of growing environmental and socioeconomic pressures (Allen et al., 1998; Kool et al., 2014).

Despite significant advances in ET science and applications over the past decades, there is still a knowledge gap regarding the accurate quantification of ET_a. This is because ET_a involves a phase change of water from liquid (or ice) to gas and with transport from the land to the air (Wang & Dickinson, 2012), making it a variable that is difficult to measure and parametrize (Cuxart & Boone, 2020). Nevertheless, precise determination of ET_a is crucial for drought monitoring (Fisher et al., 2017), especially vital for water management practices which need precise ET information associated with daily irrigation decision and scheduling (Raoult et al., 2022). Typical approaches to measure or estimate ET_a include ground-based observations or satellite remote sensing products. Although satellite remote sensing is advanced and promising, retrieval algorithms or models are needed to estimate ET from other variables observed by satellite remote sensing as ET cannot be directly measured by sensors from space (Tran et al.,

2023). This results in various sources of uncertainty in ET estimates, including inaccuracies in input data, such as the mismatches between finer vegetation data and coarser meteorological forcings (Karbalaye et al., 2025; Long et al., 2014; Tran et al., 2023), as well as limitations in retrieval algorithms and models such as uncertainties in parameterization (Cao et al., 2021; Zhang et al., 2023). More importantly, they require ground validation data (Mu et al., 2011; Sun et al., 2012). Therefore, ground-based observations remain the most established reference measurements for ET_a. Two main techniques are the eddy covariance (EC) technique established in micrometeorology and the lysimeter technique commonly used in hydrology.

The EC technique is a prevalent micrometeorological technique for ground-based ET_a measurements with relative low operational costs (Dhungel et al., 2021; Ding et al., 2010). It is based on the detection of turbulent eddies of varying sizes and frequencies that transport energy and matter both vertically and horizontally across the atmosphere-surface interface (Baldocchi, 2003; Callejas-Rodelas et al., 2024). The calculation of the turbulent properties within an eddy is simplified using Reynolds averaging which decomposes each measurement into a mean value and a fluctuating component at a given point in time (Reba et al., 2009). This finally allows for the estimation of latent heat of ET_a based on the covariance between vertical wind velocity and specific humidity. EC system can therefore provide field-scale ET_a estimates related to the measurement footprint of the installed EC tower, typically covering approximately 100 m to several kilometers in radius around the towers (Chu et al., 2021; Levy et al., 2022; Zhu et al., 2023). However, the EC technique is subjected to several limitations. The size and shape of the flux footprint are not fixed but vary temporally depending on observation height, wind speed and direction, and atmospheric stability (Finnigan, 2004; Kljun et al., 2015). EC measurements are also difficult to interpret during periods of weak turbulence, such as nighttime conditions (Peltola et al., 2025). Moreover, EC cannot directly account for advective fluxes in areas with significant heterogeneity or complex terrain, limiting its applicability in certain locations (Wilson et al., 2001). Most importantly, a widespread and persistent issue is the energy imbalance problem, wherein the sum of latent and sensible heat fluxes falls short of the available energy (Franssen et al., 2010). A lack of energy balance closure on the order of 20–30% is commonly observed at EC sites (Foken, 2008), resulting in the underestimation of ET_a (Stoy et al., 2013).

Alternatively, weighable lysimeters are widely regarded as the most accurate instruments to directly measure ET_a in situ (Gebler et al., 2015; Peters et al., 2017; Schrader et al., 2013).

They contain isolated soil columns that are separated from the surrounding soil, enabling the weight of the column to be determined gravimetrically. Changes in weight are used to quantify the water fluxes across the soil - vegetation - atmosphere interface with high accuracy (Unold & Fank, 2008). Recent developments in lysimeter technology have not only enhanced the precision and temporal resolution of the measurements, but also enabled the implementation of a more dynamic tension controlled lower boundary condition based on field tension measurements. This allows mimicking the soil water dynamics observed in the field at the bottom of the lysimeter, which includes also an influx at the bottom during upward water flow conditions in field. This offers a more realistic representation of ET processes under conditions influenced by shallow groundwater tables or upward movement from deeper soil layers during the growing season (Groh et al., 2016). The ability of weighable lysimeters to accurately detect small water fluxes, including dew and hoarfrost formation (Groh et al., 2018; Xiao et al., 2009), as well as nighttime ET_a (Groh et al., 2019), further demonstrated their high precision. As a result, lysimeter-based ET_a measurements are often used as a reference to address the energy balance closure problem and to correct EC-derived ET_a estimates (Ding et al., 2010; Gebler et al., 2015; Hirschi et al., 2017; Mauder et al., 2018).

However, weighable lysimeters also have several disadvantages. They are often complex and costly to install and operate. A major limitation is their relatively small footprint, typically representing only a pedon-scale area due to their limited surface area. It remains poorly understood whether lysimeter measurements capture ET_a information that is representative of areas beyond their surface area. Several studies have pointed to the fact that lysimeter ET_a contain information applicable to larger areas, e.g., they are comparable with measurements within EC footprint or even can be representative for a catchment (Denager et al., 2020; Evett et al., 2012; Hirschi et al., 2017; Seneviratne et al., 2012; Teuling, 2018; Widmoser & Michel, 2021). However, this has never been analyzed in a systematic manner at different spatial scales, such as a field scale, landscape scale and larger regional scale. Addressing this gap forms one of the objectives of this PhD work.

In addition to the challenges regarding quantification of ET_a, it is important to consider the ET_a regime, which reflects the dynamic interactions within the soil-vegetation-atmosphere continuum. ET_a regimes are characterized as either water-limited or energy-limited (Budyko, 1974). Depending on the availability of soil moisture (θ), the transition between the two regimes is characterized by a threshold known as critical soil moisture (θ_{crit}). In the water

limited regime ($\theta < \theta_{crit}$), ET_a is mainly controlled by θ. As the soil dries out, plants stomata progressively close to conserve water, thereby reducing transpiration. This reduces evaporative cooling and increase surface sensible heat flux, resulting in a warmer and drier overlying atmosphere (Humphrey et al., 2021; Koster, Guo, et al., 2009). Such positive interactions between the land surface and the atmosphere can lead to the persistence of drought and heatwaves (Miralles et al., 2019). On the contrary, when θ exceeds θ_{crit} ($\theta > \theta_{crit}$), ET_a enters the energy-limited regime and is primarily governed by energy supply. In this regime, the stomata of the plants do not need to close to conserve water and ET_a approaches the upper limitation bounded by the atmospheric evaporative demand depending on other environmental conditions such as temperature, radiation and wind (Xiang et al., 2020). The increased θ doesn't necessarily increase ET_a and may even decline ET_a. This is because very wet soils may show saturated conditions with limited oxygen supply to the plant roots, which affects transpiration and ecosystem productivity (Garcia-Vila et al., 2025). Therefore, knowledge of θ_{crit} associated with this regime shift is crucial for its wide use in terrestrial and atmosphere research communities, such as understanding the hydroclimatic extremes and assessing agricultural and crop yield risks.

θ_{crit} can be estimated based on the relationship between θ and a variable derived from ET_a, which can be the evaporative fraction (EF, the ratio of latent heat flux to the available energy) representing the energy partitioning, or the evaporative factor (the ratio of ET_a to PET, hereafter rPET) describing the degree of water stress. This functional relationship is implicitly assumed and parameterized in Earth system models (Pitman, 2003). While some model-based analyses used the concept of critical soil water potential (Cowan, 1965; Eagleson, 1978), current land surface models use θ rather than soil water potential (Dirmeyer et al., 2000). Therefore, θ_{crit} is an important parameter or emergent property in land surface and Earth system models. Yet, the dependency of ET_a on θ remains poorly captured in current land surface and Earth system models (Green et al., 2024). Moreover, θ_{crit} is not a fixed universal constant, but depends on soil properties and is affected by vegetation and climate conditions (Wankmüller et al., 2024). This results in its value varying across different conditions. As such, a deeper understanding of θ_{crit} and its controlling factors is essential for improving the models to better predict the interaction between land surface and atmosphere and improve the accuracy of predictions of the future climate.

Earlier studies explored the relationship between θ and ET_a without explicitly quantifying θ_{crit} (Cowan, 1965; Dirmeyer et al., 2000; Eagleson, 1978; Ford, Wulff, et al., 2014; Gu et al., 2006; Yao, 1974). In recent years, however, the direct estimation of θ_{crit} has gained increasing attention. For example, Schwingshackl et al. (2017) estimated θ_{crit} on a global scale using two reanalysis datasets and one combination dataset that uses remote sensing data and gridded station observations. Their results revealed notable discrepancies between their θ_{crit} estimates and the θ_{crit} values implemented in the models for the datasets. Haghighi et al. (2018) focused on bare soil condition and provided physically based estimates of θ_{crit}, highlighting the dominant influence of soil properties, wind speed and air temperature on θ_{crit}. Feldman et al. (2019) used satellite data to assess θ_{crit} in Africa and found that vapor pressure deficit and incoming solar radiation have influence on θ_{crit}. In addition, they suggested to use finer spatiotemporal resolutions to detect the effects of factors on θ-energetic partitioning relationships. Denissen et al. (2020) introduced a correlation-difference metric to assess θ_{crit} over the European continent using satellite data and found that soil texture, climate conditions and vegetation characteristics are of similar importance for θ_{crit}. But they also pointed out a key limitation that the depth of the surface layer in the soil moisture product used is shallow and poorly defined, which can introduce uncertainty in θ_{crit} and not fully represent the vegetation-accessible θ. Meng et al. (2022) identified θ_{crit} in the humid central Amazon, implying that even tropical rainforests in water-abundant regions can be rapidly driven out of their hydraulic safety margins and become water-limited during extreme droughts. Dong et al. (2023) used remotely sensed θ data to identify θ_{crit} based on soil loss function across the globe. Hsu & Dirmeyer (2023) compared the global patterns of existing and projected ET_a regimes using climate models and found that the transition zone between energy limited and water limited ET, which is associated with a strong land-atmosphere coupling, is expanding under global warming. They pointed out that this shift of the ET_a regime is not only due to the shift in θ distribution but also to the shift of θ_{crit}. Fu et al. (2022a) employed Fluxnet station data to quantify θ_{crit} in Europe. This work was later extended to the global scale by Fu et al. (2022b). Building on these efforts, Fu et al. (2024) combined systematic satellite observations and Fluxnet station data to generate a global map of θ_{crit}.

Unfortunately, these studies rely on model- and reanalysis-based data, and satellite-derived data, as well as eddy covariance (EC) towers and in situ soil moisture sensors, or a combination of these sources, which inherently show uncertainty with respect to ET_a or θ. More importantly,

past efforts to evaluate θ_{crit} focused primarily on surface θ (typically limited to the top ~ 5 cm, particularly for remote sensing) (Akbar, Gianotti, et al., 2018). However, plants are capable of drawing water from much deeper layers to sustain transpiration (Oliveira et al., 2005). As surface θ becomes limited, plants can increase their water uptake from deeper soil layers at much higher rates than would be expected based on root density (Green & Clothier, 1995). This highlights the importance of considering root zone θ when estimating θ_{crit} to more accurately capture the full ET_a dynamics. Although surface and root zone θ are generally hydraulically connected (Akbar, Short Gianotti, et al., 2018; Feldman et al., 2023), several studies showed that this coupling weakens with depth and under extreme heat conditions (Capehart & Carlson, 1997). For example, Mahmood & Hubbard (2007) reported a decline in the correlation and cross-correlation between surface and deeper θ with increasing depth across various land use types. Likewise, Hirschi et al. (2014) showed that extreme hot conditions could lead to progressive decoupling between surface and root zone θ dynamics. These findings indicate that ET_a regimes as well as θ_{crit} values can differ between surface and root zone θ. Indeed, Buitink et al. (2020) observed lower surface θ_{crit} values compared to root zone θ_{crit} across soil moisture networks in the Netherlands, but they did not examine the relationship between surface and root zone θ_{crit}. A more recent global-scale study using ERA5 reanalysis data explored the correlation between surface and root zone θ_{crit}. However, ERA5 root zone θ is model-derived rather than observed, and has been shown to overestimate root zone θ (Tian & Zhang, 2023) and perform poorly in some arid regions (Yang et al., 2022), which could potentially bias θ_{crit} estimates. Dong et al. (2022) also compared surface and root zone θ_{crit} using flux tower observations and in situ θ data, but their study was limited to the continental United States. Moreover, these studies did not systematically investigate how soil, vegetation and climate influence both surface and root zone θ_{crit}, nor whether the two layers reach their respective thresholds synchronously across different conditions, leaving critical gaps in our understanding of both the controls on θ_{crit} and the temporal dynamics of water limitation.

Lysimeters offer a unique opportunity to address these gaps. Soil moisture sensors installed at multiple depths in the lysimeters, together with accurate in situ ET_a measured by lysimeters, provide accurate θ and ET_a data pairs. These observations enable θ_{crit} to be identified at different soil depths and allow the timing of the associated transitions to water-limited ET_a regimes to be directly compared. Moreover, such pedon-scale lysimeters enable detailed characterization of soil, vegetation and climate conditions, facilitating a more precise

investigation of the drivers of surface and root zone θ_{crit}. Given that θ_{crit} is not a fixed value but varies spatially and is influenced by multiple processes and factors within and between the land and atmosphere (Feldman et al., 2019; Haghighi et al., 2018; Hsu & Dirmeyer, 2023b), disentangling these drivers is essential for parameterizing θ_{crit} as a function of multiple factors. Such parameterization could be incorporated into future model iterations to improve the representation of land surface-atmosphere coupling and its spatial variations.

In addition to comparing θ_{crit} between different θ depths (surface vs. root zone), the uncertainty in θ_{crit} regarding the methodology is also assessed in this PhD work. The widely used approach to determine θ_{crit} relies on a well-established conceptual framework that defines ET_a regimes as a function of θ during extensive periods without rain (i.e., drydowns, Budyko, 1974; Seneviratne et al., 2010). Typically, this involves fitting a linear-plus-plateau function to the relationship between θ and a variable derived from ET_a (EF or rPET). However, the robustness of this framework in determining θ_{crit} with respect to ET_a-derived variables and fitting functions remains uncertain. As such, one of the objectives of this PhD work is to systematically test the robustness of θ_{crit} estimation across different methodological approaches within this framework.

In summary, this PhD work is centered on lysimeter-based measurements and aims to explore the potential of lysimeter in quantifying ET_a at larger scale and θ_{crit} related to ET_a regimes. The scope of this PhD work expands progressively, from a limited number of lysimeters in selected regions of Germany to a national network and, ultimately, incorporates an international dataset spanning multiple continents. The objectives of this PhD work are to:

(1) investigate whether lysimeter ET_a measurements provide, despite their small surface area, representative information for larger areas such as the plot scale, landscape scale and larger regional scale by examine the spatial correlations between ET_a measured at different locations by lysimeter and at different locations by EC in eastern and western Germany.

(2) conduct a thorough and detailed analysis of lysimeter-specific θ_{crit} using the lysimeter network in Germany, focusing on the robustness of θ_{crit} across different ET_a-derived variables and fitting functions, as well as comparing θ_{crit} derived from surface and root zone θ.

(3) offer a comprehensive evaluation of surface and root zone θ_{crit} along climate gradients using lysimeters located at multiple continents, focusing on evaluating the degree of consistency between surface and root zone θ_{crit} and the associated ET_a regime transitions across diverse

climate regions and land covers, examining how soil, vegetation and climate influence both surface and root zone θ_{crit}.

This thesis is structured as follows:

Chapter 2 provides a brief overview of the lysimeters and study sites used in this work.

Chapter 3 investigates whether lysimeter ET_a measurements, despite their small surface area, can provide representative information for larger areas. In this chapter, the spatial correlations of standardized anomalies of ET_a between different lysimeters are compared with spatial correlations of standardized anomalies of ET_a between different EC stations, at the same measurement sites. The spatial correlations are further analyzed with wavelet transform coherence and multiple wavelet coherence methods across different temporal scales.

Chapter 4 focuses on the estimation of surface (10 cm) and root zone (0-60 cm) θ_{crit} and assessment of the robustness of θ_{crit} for different methodological approaches using lysimeter-based measurements. A total of 61 lysimeters from 7 sites in Germany are employed for this analysis, including different soil texture and land cover types (grassland and arable land).

Chapter 5 extends the analysis by investigating surface (above 30cm) and root zone (0-50 to 0-80 cm) θ_{crit}, with a particular focus on their environmental controls and the temporal synchrony of the associated transitions to water limitation. A total of 179 lysimeters across 27 sites located in Europe, Asia and North America are employed for this analysis, covering a wide range of soil texture, climate types and land cover types.

Finally, chapter 6 concludes with final remarks and provides an outlook for future research based on the findings and developments of this thesis.

Chapter 2. Materials

2.1 TERENO lysimeter network and set up

The German TERrestrial ENvironmental Observatories (TERENO) network comprises four observatories that aims to observe and document the long-term ecological, social, and economic impact of global change at site to regional scales, spanning from the North German lowlands to the Bavarian Alps. The TERENO SOILCan lysimeter network was initiated in 2010, and high-precision weighable lysimeters across key monitoring sites were installed. In this thesis, Chapter 3 analyzed data from 23 lysimeters across four TERENO sites. Chapter 4 expanded the scope to 61 lysimeters at seven sites, and Chapter 5 further included 68 lysimeters from the same seven TERENO sites along with additional lysimeters outside the TERENO network. Figure 2.1 displays the location of the TERENO sites and Table 2.1 provides further information on the sites and the different lysimeters used from the sites.

The following seven TERENO-SOILCan sites were used: Bad Lauchstädt (BL), Dedelow (DD), Graswang (GW), Rollesbroich (RO), Sauerbach (SB), Selhausen (SE), and Wüstebach (WU). The sites RO, SE, and WU belong to the Eifel/Lower Rhine Valley Observatory which is located along the western border of Germany and covers a total area of 2354 km² (Bogena et al., 2018). GW belongs to the Bavarian Alps/pre-Alps observatory (Kiese et al., 2018) and Dedelow (DD) is part of the Northeast German Lowland Observatory (Heinrich et al., 2018), while BL and SB are located in the Harz/Central German Lowland Observatory (Figure 2.1, Wollschläger et al., 2017).

RO, WU, and GW are classified as humid sites according to aridity index (Table 2.1). The RO site (50.62°N, 6.30°E; 515 m a.s.l.) is an extensively managed grassland with a mean annual air temperature of 7.7 °C and 1006 mm of precipitation (1981–2010), dominated by *Lolium perenne* L., *Ranunculus repens* L., *Rumex acetosa* L., *Taraxacum officinale* L., *Dactylis glomerata* L. and *Trifolium repens* L. The vegetation on the lysimeter and the surrounding field is subjected to extensive management, including 3~4 cuts and 2~3 liquid manure applications (~1.6 L/m^2) per growing season following the local agricultural management (Groh et al., 2019). The dominant soils are Cambisols in the southern part and Stagnosols in the northern part of the site (Bogena et al., 2018). The WU site (50.50°N, 6.33°E; 625 m a.s.l.) is a forest site that has a mean annual precipitation of 1209 mm and a mean temperature of 7.0°C (1981–2010). The vegetation at this forest site is dominated by spruce trees (Norway spruce, *Picea abies* L.

and amended by Sitka spruce (*Picea sitchensis*). The vegetation on and around the lysimeters corresponds to a natural forest meadow with no active land use (Groh et al., 2019). On the hillslopes the major soils are Cambisols and Planosols, whereas in the riparian zone the main soils are Gleysols and Histosols (Bogena et al., 2018). The GW site (11.03°E, 47.57°N; 870 m a.s.l.) is a typical pre-alpine grassland ecosystem, with a mean annual precipitation of 1347 mm and a mean annual temperature of 6.9°C (2012 to 2018). The vegetation is composed of grass and herbs, with a small proportion of clover. The site is subjected to extensive management consisting of 3 cuts and 1 manure application per year following local farmers' practices (Fu et al., 2019). The soil is classified as Fluvic Calcaric Cambisol with a clay texture (Fu et al., 2017).

The SE site (50.87°N, 6.45°E; 104 m a.s.l.) is characterized as a sub-humid site (Table 2.1) and is situated in the plain of the lower Rhine Valley. The mean annual precipitation and temperature are 718 mm and 10.5 °C (1981-2010), respectively. The site is surrounded by extensively used arable land, primarily used for the production of winter cereals (mainly winter wheat), sugar beet and maize (Bogena et al., 2018). The dominant soils are (Gleyic) Cambisol and (Gleyic) Luvisol, with a high content of coarse alluvial deposits on a former river terrace in the eastern part (Korres et al., 2010).

The DD, SB, BL sites are semi-arid sites (Table 2.1). The three sites have similar precipitation and temperature. Among the three sites, the BL site (51.39°N, 11.88E°; 118 m a.s.l.) has the least amount of mean annual precipitation (503 mm) and the highest annual air temperature of 9.6°C for the period from 1981 to 2010. In contrast, DD site has the highest annual precipitation (522 mm) and the lowest annual air temperature of 8.9°C (1981-2010). The DD site (53.37°N, 13.80°E; 441 m a.s.l.) is located in the region of the younger moraines in northeastern Germany, which is an intensively cultivated hummocky arable soil landscape (Herbrich & Gerke, 2017). The SB site (52.08°N, 11.28°E; 143 m a.s.l.), located in the Magdeburger Börde region, has a mean annual air temperature of 9.5°C and annual precipitation of 520 mm (1981-2010). It is a fertile and intensively used agricultural lowland area (Wollschläger et al., 2017).

At each site of the TERENO-SOILCan lysimeter network, at least a set of six individual lysimeters (UMS GmbH, Munich, Germany) are arranged in a standardized hexagonal design centered around a service well, which hosts the measurement equipment and data loggers (Pütz et al., 2016). All lysimeters are identical in design and are made of stainless steel with a surface

area of 1.0 m^2 and a depth of 1.5 m. To avoid thermal regime difference between the lysimeter and the surrounding field, the spatial gap between lysimeter and surrounding soil was minimized. In addition, the lysimeters have a dynamically controlled bottom boundary. Here, differences between matric potential measured in the field at 1.4 m soil depth and in the lysimeter at the same depth are minimized based on an adjustable algorithm that controls the water flux rate and direction via a bi-directional pumping system (Pütz et al., 2016). This dynamic bottom boundary control ensures that the soil water dynamics of the lysimeter match field conditions in terms of their water flux direction and rate (Groh et al., 2016). The lysimeter weighing system and the high-resolution (1-minute) monitoring of the leachate tank allow tracking water fluxes at a resolution of 10 g (0.01 mm) and 1 g (0.001 mm), respectively. Soil moisture is measured using time domain reflectometry probes (TDR100, Campbell Scientific) at soil depths of 10, 30, and 50 cm. Further technical specifications of the lysimeter used in this study are found in Pütz et al. (2016).

A total of 26 grassland lysimeters with and without management and 42 arable land lysimeters managed with a cereal crop rotation were used in this thesis (Table 2.1). Based on the "space for time" concept, some local excavated lysimeters were translocated in space within and across TERENO observatories instead of remaining at their original locations to wait for changes in climatic conditions in time (Groh et al., 2020; Pütz et al., 2016). Unlike the standard "space-for-time" substitution approach in ecological or hydrological studies (e.g., Blois et al., 2013; Troch et al., 2015) which suggests gradual ecosystem changes over time, the climatic shift experienced by these translocated lysimeters was abrupt. In this thesis, lysimeters at the sites RO, WU, SB and GW always contain the local soil (Table 2.1). At each of these sites, six lysimeters were used, except for GW, where only two well-managed lysimeters from the hexagonal set were used. In contrast, at the sites SE, DD and BL, one lysimeter group contains the local soil, and other groups contain the soil from other sites (Table 2.1). It should be noted that some of the soil monoliths transferred to the site DD (i.e., DDhd, DDck, DDcs, DDgk, DDgs, DDhk, DDhs, see Table 2.1) had a different purpose than those transferred to the sites SE and BL. Here the soils representing a typical catena of hummocky ground moraines were transferred to DD to investigate the impact of past erosion processes on the soil ecosystem (Groh et al., 2020b), rather than the change in climatic conditions.

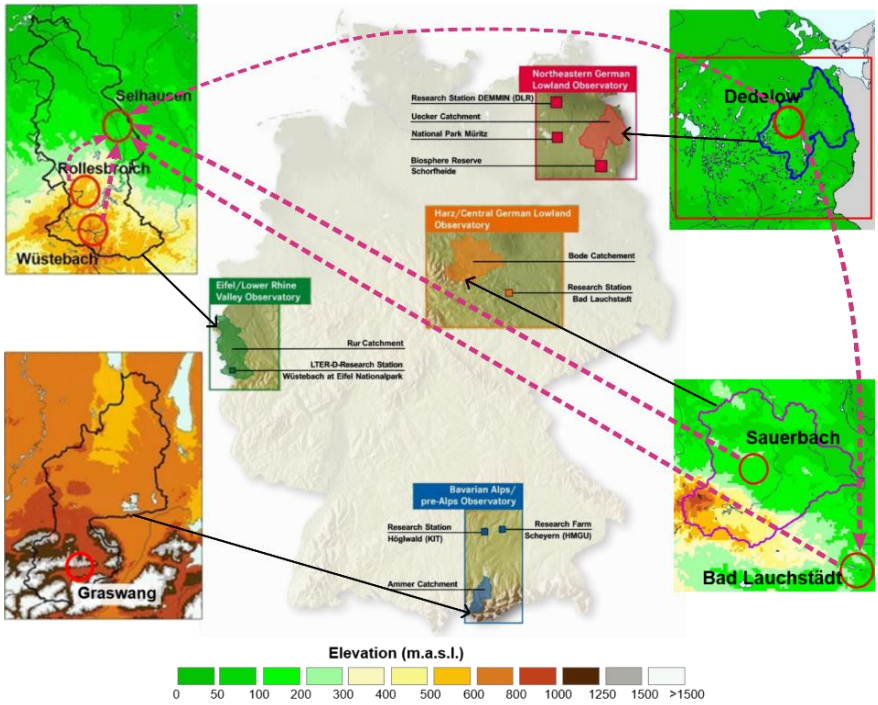


Figure 2.1 Locations of the four TERENO observatories in Germany. The red circles marked in each observatory indicate the location of the lysimeter stations used in this thesis (adapted from Pütz et al., 2016). The pink dashed arrow line indicates the transfer of the soil monoliths.

Table 2.1 Specifications of the TERENO-SOILCan lysimeters used in this thesis. For the lysimeter group, the first two letters represent the location of the lysimeters, and the last two letters represent the soil origin. For the lysimeter ID, the first two letters indicate the site where the lysimeter is located, the first number indicates the lysimeter hexagon and the second number indicates the lysimeter of the hexagon. T_a denotes the long-term mean annual air temperature and P is the long-term mean annual precipitation at each site. Aridity index (AI) was calculated by mean annual grass reference ET (ET_0) divided by mean annual precipitation over the study period. There are four classifications according to AI: humid ($AI \leqslant 1.3$), sub-humid ($1.3 < AI \leqslant 1.5$), semi-arid ($1.5 < AI \leqslant 5$), and arid ($5 < AI < 20$).

Site abbreviations: GW – Graswang; WU – Wüstebach; RO – Rollesbroich; SE – Selhausen; BL - Bad Lauchstädt; SB – Sauerbach; DD – Dedelow.

Site	Soil origin	Lysimeter Group	Lysimeter number	Lysimeter ID	T_a (℃)	P (mm)	AI	Ecosystem
GW	GW	GWgw	2	GW13,15	6.9[a]	1347[a]	0.62	grassland
WU	WU	WUwu	6	WU11-WU16	7.0[b]	1209[b]	0.46	grassland
RO	RO	Roro	6	RO11-RO16	7.7[b]	1006[b]	0.78	grassland
SE	French Technosol	Sefr	3	SE11,15,16	10.5[c]	718[c]	1.43	grassland
	Scheyern	SEsy	3	SE12,13,14				grassland
	RO	SEro	3	SE21,25,26				grassland
	WU	Sewu	3	SE22,23,24				grassland
	BL	SEbl	3	SE31,35,36				arable land
	SE	SEse	3	SE32,33,34				arable land
	DD	SEdd	3	SE41,45,46				arable land
	SB	SEsb	3	SE42,43,44				arable land
BL	SE	Blse	3	BL11,13,15	9.6[c]	503[c]	2.19	arable land
	SB	BLsb	3	BL12,14,16				arable land
	DD	BLdd	3	BL21,23,25				arable land
	BL	BLbl	3	BL22,24,26				arable land
SB	SB	SBsb	6	SB11-SB16	9.5[c]	520[c]	2.07	arable land
DD	DD	DDdd	3	DD11,13,15	8.9[c]	522[c]	1.7	arable land
	Holzendorf	DDhd	3	DD12,14,16				arable land
	Christianshof (exposed hilltops)	DDck	1	DD21				arable land
	Christianshof (topographic depressions)	DDcs	1	DD22				arable land
	Grünow (exposed hilltops)	DDgk	1	DD23				arable land
	Grünow (topographic depressions)	DDgs	1	DD24				arable land
	Holzendorf (exposed hilltops)	DDhk	1	DD25				arable land
	Holzendorf (topographic depressions)	DDhs	1	DD26				arable land

[a]For the GW site, mean annual values were calculated over 2012-2018.

[b]For the RO and WU sites, long-term means were calculated over 1991-2010. Firstly, annual P and T_a were derived from a nearby weather station (Kall-Sistig) from the German Weather Service (DWD, https://www.dwd.de). Then the annual P and T_a were adjusted using linear regression with in-situ observations at the study sites based on overlapping years to correct for site-specific values.

[c] Long-term means at the sites (SE, DD, BL and SB) were reported by Groh et al. (2016) for the period 1981-2010.

2.2 Eddy covariance tower set up

Eddy-covariance (EC) measurements are conducted near each lysimeter station at the sites RO, WU, SE and GW. Measurement heights of the EC instruments range from 2.0 to 37 m, depending on the expected maximum vegetation height at each site (Bogena et al., 2018). The instrumentation at all EC stations is essentially identical. This comprises a sonic anemometer (CSAT-3, Campbell Scientific, Inc., Logan, USA) to measure wind for all three dimensions, and an open-path gas analyzer (LI7500, LI-COR Inc., Lincoln, NE, USA) to measure CO_2 concentration and absolute humidity. In addition to the anemometer and gas analyzer, a four-component net radiometer (Eifel: NR01, Hukseflux Thermal Sensors, Delft, Netherlands; Pre-Alpine: CNR4, Kipp & Zonen, Delft, Netherlands) and soil heat flux plates (HFP01-SC, Hukseflux Thermal Sensors, Delft, Netherlands) are equipped to measure radiative fluxes and ground heat flux. Air temperature and humidity are measured by HMP45 (Vaisala Inc., Helsinki, Finland). Further details on the EC stations can be found in Bogena et al. (2018) and Kiese et al. (2018).

2.3 Meteorological data

Standard meteorological data including air temperature, air humidity, wind speed, air pressure and global radiation were collected at each site from the lysimeter weather station (WXT510, Vaisala Oyj, Helsinki, Finland) at 10-minute resolution. Precipitation was recorded with a weighable gauge (Pluvio², Ott Hydromet, Kempten, Germany) at the sites RO, WU, and SE, and with a tipping bucket gauge (GW: WXT520, Vaisala; DD and SB: ecoTech Umwelt-Meßsysteme GmbH, Bonn, Germany; and BL: LAMBRECHT meteo, Göttingen, Germany) at the sites GW, DD, SB and BL.

As the observations contain data gaps, a stepwise gap-filling strategy was employed using auxiliary data from nearby TERENO stations accessible via the TERENO-portal (http://teodoor.icg.kfa-juelich.de/ibg3searchportal2/index.jsp). Firstly, a linear regression model was established between the corresponding meteorological variables at the lysimeter station and the nearby stations. Subsequently, the regression with the lowest root mean square error (RMSE) was used to fill the gaps until all the stations were used.

In addition, a net radiation sensor (LP Net07, Delta OHM S.r.L., Caselle di Sevazzano, Italy) was installed above one lysimeter in each lysimeter group at each lysimeter site. Net radiation

was measured at a temporal resolution of 10 minutes and aggregated to hourly data. The missing hourly net radiation were gap-filled using the similar stepwise linear regression procedure as described above, but using net radiation (R_n) measurements from different lysimeter groups at the same site or from the corresponding EC station nearby.

The gap-filled hourly meteorological data were used to estimate hourly ET_0 according to the FAO Penman-Monteith equation (Allen et al., 2006):

$$ET_0 = \frac{0.408\Delta(R_n - G) + \gamma\frac{37}{T_h + 273}u_2(e^o(T_h) - e_a)}{\Delta + \gamma(1 + C_d u_2)} \quad (2.1)$$

where Δ is the slope of the vapor pressure curve (kPa $^oC^{-1}$), R_n is net radiation at the surface (MJ m^{-2} h^{-1}), G is soil heat flux density (MJ m^{-2} h^{-1}), T_h is mean hourly air temperature at 2 m height (^oC), $e^o(T_h)$ is hourly saturation vapor pressure (kPa), e_a is hourly actual vapor pressure (kPa), γ is psychrometric constant (kPa $^oC^{-1}$), C_d is the coefficient set to 0.24 s m^{-1} when R_n > 0 and 0.96 s m^{-1} when R_n < 0, and u_2 is wind speed at 2 m height (m s^{-1}).

2.4 Lysimeter data

Lysimeter raw data are recorded at 1-minute intervals, enabling the high-resolution determination of precipitation (P) including non-rainfall water (i.e., dew, rime, and fog), and actual evapotranspiration (ET_a), based on weight changes using the soil water balance approach (Schrader et al., 2013). However, lysimeter data are prone to wind or other external disturbances. Thus, lysimeter and leachate weights were processed by a four-step pre- and post-processing routine to reduce external errors and noise to separate P and ET_a (Schrader et al., 2013).

Firstly, the raw lysimeter data underwent a manual and automatic plausibility check (Schneider et al., 2021). Outliers were removed from the data by limiting the maximum weight difference between two consecutive time steps to 5 kg for the lysimeter weight and to 0.1 kg for the leachate weight.

Secondly, the adaptive window and threshold filter was applied (AWAT; Peters et al., 2014; Peters et al., 2017) on the minute-wise lysimeter weight time series to reduce the impact from external errors and noise on the determination of P and ET_a. This filter has shown to be able to identify precisely even small water fluxes from dew formation, soil water vapor adsorption, or nighttime ET_a (Groh et al., 2019; Kohfahl et al., 2019; Paulus et al., 2022).

In a third step, processed data was used to calculate ET_a and atmospheric water inputs (AWI). The latter includes precipitation as well as water from non-rainfall events. It is assumed that there is no ET_a and AWI occurring simultaneously during a 1-min time interval. Therefore, after subtracting the weight change caused by pumping water in and out, any further increase or decrease in lysimeter mass change can be attributed to ET_a or AWI. The following soil water balance equations were applied:

$$\Delta W = \Delta W_{lys} + \Delta W_{drain} \tag{2.2}$$

$$\Delta AWI = \begin{cases} \Delta W, & \Delta W > 0 \\ 0, & \Delta W \leq 0 \end{cases} \tag{2.3}$$

$$\Delta = \begin{cases} 0, & \Delta W > 0 \\ \Delta W, & \Delta W \leq 0 \end{cases} \tag{2.4}$$

where ΔW_{lys} and ΔW_{drain} (kg) are the mass change of the lysimeter and leachate between two consecutive time steps, respectively. ΔAWI (kg) represents the total mass of AWI that hit the lysimeter and vegetation surface during the time interval and ΔET is the corresponding ET_a, including interception loss. Time series of AWI and ET_a were subsequently aggregated to hourly values.

Finally, ET_a data were checked for plausibility and data gaps were filled in a post-processing step (Schrader et al., 2013). Missing hourly values were gap-filled using linear regression with parallel ET_a values from other available lysimeters (same site and same soil) or with the grass reference ET (ET_0) for a grass reference vegetation with an albedo of 0.23. The use of ET_0 for gap-filling is justified because it provides a standardized, physically based estimate of atmospheric evaporative demand that is independent of site-specific measurement errors.

However, lysimeter data during snow cover and freezing conditions are often prone to larger errors due to the formation of snow bridges and ice on the lysimeter surface (Schnepper et al., 2023). At the alpine site GW, such conditions frequently led to longer gaps during winter and spring (from December to March). In this case, hourly $ET_{0,snow}$ were used to replace the missing hourly ETa values for these gaps. $ET_{0,snow}$ was calculated using Equation 2.1 but with the actual albedo measurements instead of the albedo for grass (0.23). Actual albedo was measured using the sensor CNR4 (Kipp & Zonen, Delft, Netherlands) at the height of 1.9 m at the GW site.

2.5 Eddy covariance data

The EC raw measurements were logged at a frequency of 20 Hz, and fluxes were calculated for intervals of 30 min. The flux calculation and quality assurance were performed according to the standardized strategy proposed by Mauder et al. (2013) using the TK3 software package (Mauder & Foken, 2011). This strategy involves applying site-specific plausibility limits, removing spikes based on median absolute deviation of raw data and performing a planar fit coordinate rotation uniformly across all wind directions (Foken & Wichura, 1996). Processed half-hourly fluxes and statistics were evaluated with a three-level quality flagging system which classifies data as high, moderate, or low quality based on stationarity and integral turbulence tests.

Only high or moderate quality data were used in this thesis, while low-quality data were excluded. The gaps were filled using a zero-intercept linear regression approach between ET_a and the predictor ET_0 with a flexible time window following Graf et al. (2014). The regression was applied within a flexible time window, starting at a minimum length of 60 days and gradually increasing in 1-hour increments to find the minimum root mean square error (RMSE). The window length was extended until either (1) the RMSE started to rise as the time window expanded or (2) the maximum allowable window length of 120 days was achieved. Eventually, the regression coefficient (the slope of ET_a versus ET_0 values) associated with the chosen time window was used to fill the missing values. More specifications can be found in Graf et al. (2014).

Energy imbalance is a common issue at almost every EC site, where the sum of the turbulent fluxes (sensible plus latent heat flux) is typically less than the measured available energy (net radiation minus ground heat flux) (Twine et al., 2000; Foken et al., 2011). To correct for this discrepancy, the turbulent fluxes can be adjusted using the Bowen-ratio forced closure method. In this thesis, the energy balance deficit (EBD) was calculated on a daily scale:

$$\mathrm{EBD} = \mathrm{R_n} - (\mathrm{G} + \mathrm{LE} + \mathrm{H}) \tag{2.5}$$

where R_n is net radiation (W m^{-2}), G is ground heat flux (W m^{-2}), LE is latent heat flux (W m^{-2}), and H is sensible heat flux (W m^{-2}).

The Bowen ratio (β) is defined as:

$$\beta = \frac{\mathrm{H}}{\mathrm{LE}} \tag{2.6}$$

The energy-balance-corrected latent heat flux (LE_c) was then determined by redistributing the latent heat according to the calculated Bowen ratio:

$$LE_c = LE + EBD \times \frac{1}{1+\beta} \quad (2.7$$

Chapter 3. Scale-dependent spatial correlations of actual evapotranspiration measured by lysimeters

*adapted from: Lu, X., Groh, J., Graf, A., Pütz, T., Schneider, K., Si, B., Vereecken, H., & Franssen, H. J. H. (2024). Analysis of scale-dependent spatial correlations of actual evapotranspiration measured by lysimeters. Agricultural and Forest Meteorology, 359(October), 110288. https://doi.org/10.1016/j.agrformet.2024.110288

3.1 Introduction

Evapotranspiration (ET) is a central component of the terrestrial water cycle and links the hydrosphere, atmosphere and biosphere (Fisher et al., 2017), which includes evaporation from soil, transpiration by vegetation and evaporation of water on vegetation (Hanson, 1991; Kool et al., 2014). Potential evapotranspiration (ET_0) is the ET amount for a specific reference vegetation if there are no limitations on water availability. Actual evapotranspiration (ET_a) refers to the ET which really takes place, affected by possible water scarcity. The precise assessment of ET_a is essential for a broad range of scientific disciplines including agricultural water management, drought monitoring as well as sustainable use of water resources (Negm et al., 2017; Awada et al., 2019; Li et al., 2022).

Unfortunately, the accurate determination of ET_a remains a challenge, as it is a variable that is difficult to measure and parametrize (Cuxart & Boone, 2020). Typical approaches to determine ET_a include in situ stations like eddy covariance (EC) stations and lysimeters or estimates via remote sensing. Remote-sensing based ET_a estimates, though promising and widespread, have large uncertainties and require ground validation (Mueller et al., 2011; Seneviratne et al., 2012; Tran et al., 2023). Therefore, ground-based observations remain the most established reference measurements (Hirschi et al., 2017). EC is a prevalent micrometeorological technique for ground-based ET_a measurements with relative low operational expenses (Ding et al., 2010; Dhungel et al., 2021; Han et al., 2021). An EC system can capture field-scale ET_a information within the measurement footprint of the installed EC tower, covering approximately 100 meters to few kilometers in radius around the towers (Zhang et al., 2014; Chu et al., 2021; Levy et al., 2022; Zhu et al., 2023), but are subjected to systematic measurement errors (e.g., Wilson et al., 2001; Franssen et al., 2010; Mauder et al., 2020; Zhang et al., 2022) and random measurement errors (Hollinger & Richardson, 2005; Kessomkiat et al., 2013; Post et al., 2015).

Weighable lysimeters are another common ground-based observation technique, and are considered the best mean to directly measure ET_a in situ (Allen et al., 2011; Schrader et al., 2013; Gebler et al., 2015; Peters et al., 2017; Sánchez et al., 2019). They contain soil columns that are separated from the surrounding soil and can determine the weight of the column gravimetrically. The information on the weight changes can be used to determine the water fluxes across the soil – vegetation – atmosphere interface with high precision (Unold & Fank, 2008). Since the construction of the first weighable lysimeter in Germany in 1902, the technology has improved a lot to assess the changes in the soil water storage of the soil column that fills the lysimeter (Goss & Ehlers, 2009). An example are the lysimeters of the German TERrestrial ENvironmental Observatories (TERENO) SOILCan network which are of high accuracy and high temporal resolution and provide the opportunity for in-depth long-term investigations of the different components of the soil water cycle (Zacharias et al., 2011; Pütz et al., 2016). The ability to successfully quantify small water fluxes such as dew and hoar frost formation as well as nighttime ET_a demonstrates the high precision of the lysimeters (Groh et al., 2018; Groh et al., 2019). In addition, Gebler et al. (2015) carried out a study with one lysimeter site of this network to compare ET_a estimated by EC and lysimeter. The study illustrated that a lysimeter can measure ET_a in a reliable manner and does not suffer from some of the drawbacks of EC systems. Trigo et al. (2018) used the ET_a data from the same site for a follow-up period and showed that ET_a was underestimated by the EC technique and required a correction factor of 1.15 when compared to ET_a data from weighable lysimeters. Similarly, Mauder et al. (2018) took lysimeter measurements at two grassland ecosystems from TERENO-SOILCan as a reference to evaluate the energy balance problem for EC measurements and found EC-based ET_a was generally underestimated.

However, weighable lysimeters also have several disadvantages, such as their small footprint (pedon-scale) due to limited surface area and their limitation in quantifying ET_a from forested land. A main question is therefore how informative the precise ET_a-measurements by weighable lysimeters are. Evett et al. (2012) evaluated several methods for quantifying ET_a at different spatial scales with the same soil and crop over one growing season and found that ET_a derived from weighable lysimeters sufficiently represents the surrounding field ET_a throughout the season. They also pointed out that differences in plant height and width would result in a mismatch between ET_a from the lysimeters and the surroundings. Seneviratne et al. (2012) reported that lysimeter measurements are representative of a small catchment (3.31 km^2)

although a scale discrepancy existed by comparing 32-year data sets of lysimeter seepage with the discharge from the small catchment. They pointed out that the most significant differences between lysimeter seepage and catchment runoff occurred in March. This variation was likely associated with a greater spatial variability of hydrological processes during that month, which could be attributed to factors such as snowmelt and the initiation of the growing season. For the same research catchment in Switzerland, Hirschi et al. (2017) revealed that the long-term lysimeter measurements corresponded well with catchment water-balance evaluations of ET_a. This emphasizes that lysimeter measurements can be representative for the entire catchment, despite the relatively small source areas (typically about 3 m^2) and the diverse land use and topography within the catchment. Teuling (2018) found that ET_a from four different lysimeter stations in three countries with contrasting vegetation and climate are in line with ET_a estimates from catchment-scale water balance studies. Widmoser & Michel (2021) compared concurrent lysimeter and EC measurements across four grassland sites. In this study, they applied a partial energy closure method to correct EC measurements, wherein they evaluated the correction factor for latent heat flux by regressing the difference between the lysimeter and EC latent heat fluxes and used this weight to correct the EC latent heat flux. In contrast to this, Denager et al. (2020) found a good agreement and no statistical difference between uncorrected ET_a measured by EC and ET_a estimated by the water balance method where recharge was measured by non-weighable percolation lysimeters. They attributed this agreement to the fact that the spatial scale of the water balance method in this study was compatible with the EC measurement scale. They pointed out that in other studies EC-estimated ET_a was always underestimated compared with ET_a measured by weighable lysimeters, possibly because weighable lysimeters were not representative for the entire field. In addition, Denager et al. (2023) emphasized again that the total surface area of the lysimeters is quite small compared to the footprint of the EC system. Although these studies point to the fact that lysimeter ET_a contain information for larger areas, e.g., they are comparable with measurements within EC footprint or even can be representative for a catchment, this has never been analyzed in a systematic manner.

The core objective of this study is to provide systematic evidence that lysimeter ET_a measurements provide, despite their small surface area, representative information for larger areas such as the plot scale, landscape scale (10 ~ 50 km) and larger regional scale (500 km). To this end, we analyzed daily ET_a measurements by a total of 23 lysimeters at four study sites across Germany (separation distances from 0 to 500 km) for six consecutive years (2015 to

2020). As EC estimates at the field scale, we compare spatial correlations of standardized anomalies of ET_a between different lysimeters with spatial correlations of standardized anomalies of ET_a between different EC stations, at the same measurement sites. If the lysimeter ET_a is more affected by random fluctuations (i.e., measurement errors and small scale variability which cannot be attributed to any specific pattern or trend), related to the small footprint, we would expect smaller spatial correlations of lysimeter ET_a between the measurement sites than spatial correlations of EC derived ET_a. The spatial correlations are analyzed further, also on different temporal scales, with wavelet transform coherence (WTC) analysis, which overcomes the limitations of Fourier transform in analyzing nonstationary time series, not only to identify the scale and frequency of temporal patterns in a time series, but also to identify coherence between two time series at different scales and frequencies (Bravo et al., 2020). Compared to a single correlation coefficient, WTC allows to identify how correlations vary between years and seasons. Furthermore, measuring the correlation of two ET_a time series will not fully capture all the features of ET_a processes given the complex space-time links between climate, soil and vegetation (Rodriguez-Iturbe, 2000; Kim et al., 2022). Thus, it is essential to study multiple ET_a time series at multiple space-time domains to better reveal the relationship of ET_a among different locations. The multiple wavelet coherence (MWC) approach has been shown to be suitable to untangle a range of multivariate relationships in the field of geosciences (Hu & Si, 2016; Hu et al., 2017; Su et al., 2019; Cheng et al., 2021). MWC is therefore conducive to proper characterization of the temporal scale specific multivariate relationships between ET_a measurements under different climate, soil and vegetation conditions. A good understanding of these relationships is important for optimizing the prediction of ET_a for a given site using the measurements at other sites, and also for determining the number of lysimeter needed to be representative for a given spatial scale and thus optimizing the design of a lysimeter network.

3.2 Materials and methods

3.2.1 Study sites

The four study sites are part of the TERENO network in Germany. Figure 3.1 displays the location of the sites, together with the spatial distances between the sites. Table 3.1 provides further information on the sites and the different lysimeters used from the sites. The Selhausen (SE), Rollesbroich (RO) and Wüstebach (WU) sites belong to the Eifel/Lower Rhine Valley

Observatory which is located along the western border of Germany and covers a total area of 2354 km² (Bogena et al., 2018). Among these three sites, the Selhausen site (SE) has the least amount of mean annual precipitation (700 mm/y) and the highest mean annual air temperature (10°C) for the period from 1961 to 2014. The crops on this arable land are dominated by winter cereals (mainly winter wheat), sugar beet and maize. The prevalent soils are (Gleyic) Cambisol and (Gleyic) Luvisol, both of which are characterized as silty loam textures (Korres et al., 2015). The grassland site RO has a mean annual air temperature of 7.7°C and a mean annual precipitation of 1033 mm/y for the period 1981-2001. Stagnosol is the major soil type in the northern part, whereas Cambisol (Gleyic) dominates the soil in the southern part of the site. The plant community is mainly comprised of *Lolium perenne* and *Trifolium repens* (Forstner et al., 2021). During the study period, the vegetation on the lysimeter and the surrounding field is subjected to extensive management, including 3~4 cuts and 2~3 liquid manure applications (~1.6 L/m^2) per growing season following the local agricultural management (Groh et al., 2019). The mean annual air temperature and precipitation for the Wüstebach site (WU) are 8.2°C and 1310 mm/y (1991 to 2013), respectively. The vegetation at this forest site is dominated by spruce trees (Norway spruce, *Picea abies* L.) and amended by Sitka spruce (*Picea sitchensis*). The vegetation on and around the lysimeter corresponds to a forest meadow and the plant community consists of *Agrostis capillaris* and *Galium saxatile* (Groh et al., 2019). On the hillslopes the major soils are Cambisols and Planosols, whereas in the riparian zone the main soils are Gleysols and Histosols. The soil texture is clay loam with coarse material inclusions. Graswang (GW) is approximately 500 km away from the aforementioned three sites and belongs to the Bavarian Alps/pre-Alps observatory (Kiese et al., 2018). This site is situated in grassland ecosystems primarily used for fodder and hay production in the Ammer catchment of southern Germany (Zeeman et al., 2017). It has a temperate oceanic climate with a mean annual precipitation of 1347 mm/y and a mean annual temperature of 6.9°C (2012 to 2018). The soil in GW is classified as Fluvic Calcaric Cambisol and the soil texture is clay (Fu et al., 2017). The vegetation is composed of grasses and herbs, with a small proportion of clover. Main species are *Festuca pratensis, Poa pratensis, Prunella vulgaris, Plantago lanceolate, Knautia arvensis and Pimpinella major* (Fu et al., 2019). The site GW underwent extensive management consisting of 3 cuts and 1 manure application per year following local farmers' practices (Fu et al., 2019).

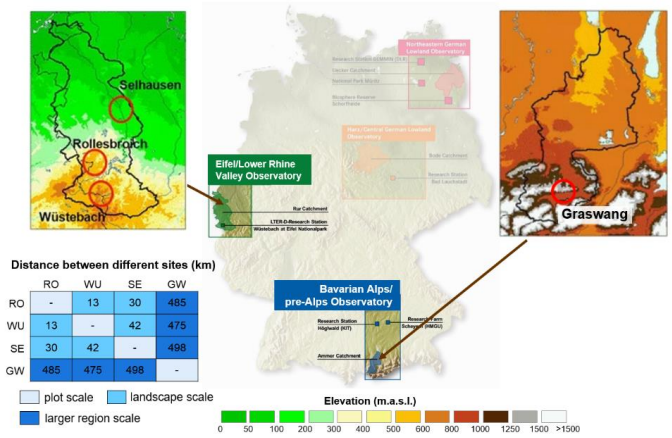


Figure 3.1 Location of TERENO observatories over Germany and locations of the four study sites (marked by red circle), as well as distances (in km) between different sites (three different shades of blue are used to indicate different spatial scales; modified from Pütz et al., 2016). RO: Rollesbroich, WU: Wüstebach, SE: Selhausen, GW: Graswang.

Table 3.1 Specifications of the four lysimeter (LYS) sites used for the analyses in this chapter including location, number of individual lysimeters, soil information and land use.

Site	location	Elevation (m a.s.l.)	Abbr.	No. of LYS	LYS ID	Soil origin	Soil location	Soil texture*	Vegetation (LYS)	Ecosystem (EC)
			SEse	3	SE32,33,34	SE	SE	silty loam	crop	
SE	50°52'8"N 6°26'59"E	104	SEro	3	SE21,25,26	RO	SE	clay loam	grass	crop
			SEwu	3	SE22,23,24	WU	SE	clay loam	grass	
RO	50°37'18"N 6°18'15"E	515	RO	6	RO11,12,13, 14,15,16	RO	RO	clay loam	grass	grass
WU	50°30'10"N 6°19'42"E	625	WU	6	WU11,12,13, 14,15,16,	WU	WU	clay loam	grass	forest
GW	47°34'15"N 11°01'57"E	864	GW	2	GW13,15	GW	GW	clay	grass	grass

*Classification of soil texture is based on the texture triangle developed by the USDA (United States Department of Agriculture).

3.2.2 Lysimeters set up

At each site of the TERENO-SOILCan lysimeter network, at least a set of six individual lysimeters (UMS GmbH, Munich, Germany) with a surface area of 1.0 m^2 and a depth of 1.5 m are arranged in a standardized hexagonal design. The distance between the lysimeters at the same site is only a few meters (about 3 - 6 m). The lysimeter stations have equal experimental and monitoring conditions. The highly precise (resolution of 10 g) and resolved (1-minute measurements) lysimeters have a dynamic control bottom boundary. Here, differences between matric potential measured in the field at 1.4 m soil depth and in the lysimeter at 1.4 m depth are minimized based on an adjustable algorithm that controls the water flux rate and direction via a bi-directional pumping system (Pütz et al. 2016). This dynamic bottom boundary control ensures that the soil water dynamics of the lysimeter match field conditions regarding their water flux direction and rate (Groh et al., 2016). Further technical specifications of the lysimeter used in this study are found in Pütz et al. (2016).

In our study, we used a total of 23 high-precision weighable lysimeters. The lysimeters from RO, WU and GW always contain local soil, while for SE there are three lysimeters with local soil, three lysimeters with soil from WU and three lysimeters with soil from RO. In detail, nine lysimeters were excavated at RO, whereby six of them remained in RO and the other three (SE21, SE25, and SE26) were transferred along an altitudinal gradient to SE in winter 2010. These soils are denoted by “SEro” in this paper. At WU, similar to RO, six out of nine lysimeters are located at WU, and the other three (SE22, SE23, and SE24) were transferred to SE and are referred as “SEwu”. Three lysimeters in SE (SE32, SE33, and SE34) are filled monolithically with local soil and were managed with a cereal crop rotation and named as “SEse” in this study. At GW, two well-managed lysimeters (GW13 and GW15) were used for this work. They both contain the local intact soil monoliths and are subject to the same extensive management as the surrounding field.

3.2.3 Lysimeter data

Lysimeter raw data were recorded at 1-minute intervals, which allows to directly determine precipitation (P) including non-rainfall water (i.e., dew, rime, and fog), and ET_a from lysimeter weight changes using the soil water balance equation (Schrader et al., 2013). This soil water balance equation takes weight changes related to water fluxes across the lysimeter bottom (percolation, capillary rise) into account. In this study, we didn’t separate between rain and non-rainfall events, thus P stands for all incoming atmospheric moisture which also includes

water inputs from non-rainfall events. The amount of P is determined from the increase of lysimeter weight after correcting the weight changes for the water fluxes across the lysimeter bottom. The procedure assumes that only P or ET_a can occur within a 1-minute period.

Lysimeter data are prone to wind or other external disturbances. Thus, lysimeter weight data were processed by a pre- and post-processing routine to reduce external errors and noise to the determination and separation of water fluxes over the land surface. In a first step, the raw lysimeter data from 2015 until 2020 underwent a manual and automatic plausibility check (Schneider et al., 2021). During the automated data control process, outliers or other disturbances in the lysimeter and tank weight data were eliminated. In a second step, the adaptive window and threshold filter was applied (AWAT; Peters et al., 2014; Peters et al., 2017) to reduce the impact from external errors and noise on the determination of P and ET_a. Typically, the high frequency of lysimeter weight measurements in combination with the AWAT-filter allowed to precisely estimate ET_a or P rates, including small water fluxes from dew formation, soil water vapor adsorption, or nighttime ET_a (Groh et al., 2019; Kohfahl et al., 2019; Paulus et al., 2022). In the next step, the lysimeter ET_a data (ET-LYS) were aggregated to hourly values. Missing hourly values were gap-filled using linear regression with parallel ET_a values from other available lysimeters (same site and same soil) or the potential ET (ET_0) for a grass reference vegetation with an albedo of 0.23. The hourly ET_0 is calculated with the FAO Penman-Monteith equation (Allen et al., 2006):

$$ET_0 = \frac{0.408\Delta(R_n - G) + \gamma\frac{37}{T_h+273}u_2(e^o(T_h) - e_a)}{\Delta + \gamma(1 + C_d u_2)} \quad (3.1)$$

where Δ is the slope of the vapor pressure curve (kPa $^oC^{-1}$), R_n is net radiation at the surface (MJ m^{-2} h^{-1}), G is soil heat flux density (MJ m^{-2} h^{-1}), T_h is mean hourly air temperature at 2 m height (^oC), $e^o(T_h)$ is hourly saturation vapor pressure (kPa), e_a is hourly actual vapor pressure (kPa), γ is psychrometric constant (kPa $^oC^{-1}$), C_d is the coefficient set to 0.24 s m^{-1} when R_n > 0 and 0.96 s m^{-1} when R_n < 0, and u_2 is wind speed at 2 m height (m s^{-1}).

However, lysimeter data during snow cover and freezing conditions are often prone to larger errors due to the influence of snow bridges and ice formation (Schnepper et al., 2023). Thus, longer gaps during winter and spring (December to March, Table A.3) due to snow or ice cover on the top of the lysimeters existed at the alpine site GW. We used hourly $ET_{0,snow}$ to replace the missing hourly values for these gaps. $ET_{0,snow}$ is the potential ET calculated with the actual albedo measurements instead of the albedo for grass (0.23). Actual albedo was measured using

the sensor CNR4 (Kipp & Zonen, Delft, Netherlands) at the height of 1.9 m at the GW site. Finally, the hourly data were aggregated to daily values.

3.2.4 Eddy covariance data

Eddy-covariance measurements are conducted near each lysimeter station. The equipment used at the different EC-stations is basically identical. The EC instrumentation consists of a CSAT-3 sonic anemometer (Campbell Scientific, Inc., Logan, USA) to measure wind for all three dimensions, and an LI7500 open-path gas analyzer (LI-COR Inc., Lincoln, NE, USA) for acquisition of H_2O and CO_2 contents of the air. Along with the anemometer and gas analyzer, a four-component net radiometer (Eifel: NR01, Hukseflux Thermal Sensors, Delft, Netherlands; Pre-Alpine: CNR4, Kipp & Zonen, Delft, Netherlands) and soil heat flux plates (HFP01-SC, Hukseflux Thermal Sensors, Delft, Netherlands) are installed to measure radiative fluxes and ground heat flux. Air temperature and humidity are measured by HMP45 (Vaisala Inc., Helsinki, Finland). More information about the EC station can be found for the individual sites in Bogena et al. (2018) and Kiese et al. (2018).

The EC raw data were obtained at a frequency of 20 Hz, followed by the aggregation of fluxes to 30-min intervals. The EC data calculation and quality assurance were conducted in accordance with the standardized strategy proposed by Mauder et al. (2013) using the TK3 software package (Mauder & Foken, 2011). Only flux data with quality flags 0 and 1 were used in this study; other poor quality data were excluded. To fill the gaps, a zero-intercept linear regression approach between ET_a and the predictor ET_0 with a flexible time window was applied according to Graf et al. (2014). The window length starts at a minimum of 60 days and then increases by 1 hour increments to find the minimum root mean square error (RMSE). We continued to increase the window length until either (1) the RMSE started to rise as the time window expanded or (2) the maximum allowable window length of 120 days was achieved. Eventually, the regression coefficient (the slope of ET_a versus ET_0 values) associated with the chosen time window was used to fill the missing values. More specifications can be found in Graf et al. (2014).

We mainly focused on the estimation of ET_a without correction of the energy balance deficit. However, energy imbalance is a common issue at almost every EC site, where the sum of the turbulent fluxes (sensible plus latent heat flux) is generally less than the measured available energy (net radiation minus ground heat flux) (Twine et al., 2000; Foken et al., 2011). To

address this discrepancy, the turbulent fluxes can be recalculated using the Bowen-ratio forced closure method. In this study, the energy balance deficit (EBD) was determined on a daily scale:

$$\mathrm{EBD} = \mathrm{R_n} - (\mathrm{G} + \mathrm{LE} + \mathrm{H}) \tag{3.2}$$

where R_n is net radiation (W m^{-2}), G is ground heat flux (W m^{-2}), LE is latent heat flux (W m^{-2}), and H is sensible heat flux (W m^{-2}).

The Bowen ratio (β) is defined as:

$$\beta = \frac{\mathrm{H}}{\mathrm{LE}} \tag{3.3}$$

The energy-balance-corrected latent heat flux ($\mathrm{LE_c}$) was then determined by redistributing the latent heat according to the calculated Bowen ratio:

$$\mathrm{LE_c} = \mathrm{LE} + \mathrm{EBD} \times \frac{1}{1+\beta} \tag{3.4}$$

Both uncorrected and corrected ETa measurements from EC (ET-EC and ET-ECc, respectively) were used in this study to assess whether the closure of the energy balance from EC measurements affects the correlations of ETa between sites.

3.2.5 Pearson correlation coefficient of standardized anomalies of ET_a

Pearson correlation coefficient (PCC) is a classic metric of the strength and direction of a linear relationship between two variables. For a sample size larger than 30, the absolute values of PCC ranging between 0-0.1 indicate no correlation, 0.1-0.3 small correlation, 0.3-0.5 moderate correlation and 0.5-1.0 strong correlation (Cohen, 1988; Fraenkel & Wallen, 1990).

If ET_a values are known over a long time period, long term averages of ET_a can be calculated, and anomalies can be deduced from this. For example, it is expected that under conditions of sufficient water supply and higher availability of energy than normal (sunny and warm weather conditions) ET_a will show a positive anomaly, whereas under conditions of very low soil moisture content, ET_a will be below normal. The anomaly for a given period is calculated by comparing with the historical mean for the same period so that surplus or deficit can be calculated (Tadesse et al., 2015). ET_a anomaly (ΔET_a) is defined as ETa for the day i ($ET_{a,i}$) minus the long-term average ET_a for that day ($\overline{ET_{a,i}}$):

$$\Delta \mathrm{ET}_a = ET_{a,i} - \overline{ET_{a,i}} \tag{3.5}$$

ΔET_a is calculated on a daily basis. As the time series of ET_a in this study are still relatively short, average ET_a shows still considerable day-to-day variations. Therefore, the yearly cycle of average daily ET_a is smoothed with help of a fourth order polynomial regression. For the subsequent statistical analysis of the ET_a, it is also important to standardize for time dependent standard deviation (e.g., the standard deviation of ET_a is in general smaller in winter than in summer). SA_{ET_a} were calculated as follow:

$$SA_{ET_a} = \frac{\Delta ET_a}{\sigma_{ET_a,i}} \tag{3.6}$$

where $\sigma_{ET_a,i}$ is the long-term standard deviation of daily ET_a for that day of the year, which is obtained from a fourth order polynomial regression. Standardized anomalies eliminate the role of seasonality (Grumm & Hart, 2001). The SA_{ET_a} are then subjected to statistical analysis focusing on spatial correlations between different sites evaluated by PCC. This calculation procedure was followed for ET-LYS, ET-EC and ET-ECc.

3.2.6 Wavelet analysis

The behavior of ET_a can differ across various temporal scales. The correlation for ET_a between sites can be positive at some temporal scales, whereas at other scales it can be negative. In order to analyze the correlations into time-frequency domain as well as for lagged responses, wavelet transform coherence (WTC) was employed. Furthermore, multivariate relationships of ET_a at multiple scales are also an interesting investigation for our better understanding of ET_a measurements and are important to improve the accuracy of ET_a predictions for a specific location based on data from different locations. With the combination of different ET_a time series, more climate conditions, vegetation types and soil types are taken into consideration. We applied multiple wavelet coherence (MWC) which is able to disentangle a range of multivariate relationships.

3.2.6.1 Continuous wavelet transform

Continuous wavelet transform (CWT) analyzes a time series in time-frequency domain (Torrence & Compo, 1998; Grinsted et al., 2004). Before WTC and MWC can be calculated, it is essential to first compute the CWT.

For a time series X of length N (X_n, n = 1, 2, ..., N) with uniform sample spacing δt (one day in this study), the CWT can be computed as:

$$W_n^X(s) = \sum_{n'=1}^{N} x_{n'} c_s \psi_0 \left(\frac{(n'-n)\delta t}{s} \right) \tag{3.7}$$

where n is the localized time index, n' is the time variable, N is the number of points in the time series, s is the wavelet scale, $c_s = \sqrt{\frac{\delta t}{s}}$ is the normalization factor and $\psi_0(\,)$ is the mother wavelet function. In this study, the Morlet wavelet was selected as the mother wavelet which has been widely used in hydrometeorological studies (Labat, 2005; Charlier et al., 2015; Su et al., 2019; Cheng et al., 2021; Wu et al., 2021). The Morlet wavelet function is expressed as $\psi_0(\eta) = \pi^{-1/4} e^{i\omega_0\eta} e^{-\eta^2/2}$, where i is the imaginary operator ($i = \sqrt{-1}$), η is the dimensionless time and ω_0 is the dimensionless frequency localization. The value of ω_0 is commonly recommended as 6 which can provide a good balance between time and frequency localization for feature extraction purposes (Grinsted et al., 2004).

3.2.6.2 Wavelet transform coherence

WTC is a correlation coefficient in the time - frequency space and can quantify the intensity of linear relationship between two time series. Given time series X and Y, with wavelet transforms $W_n^X(s)$ and $W_n^Y(s)$, the WTC between X and Y can be expressed as:

$$R_n^2(s) = \frac{\left|S(s^{-1}W_n^{XY}(s))\right|^2}{S\left(s^{-1}\left|W_n^X(s)\right|^2\right)\cdot S\left(s^{-1}\left|W_n^Y(s)\right|^2\right)} \tag{3.8}$$

where $W_n^{XY} = W_n^X(s)\cdot W_n^{Y*}(s)$ is the cross-wavelet spectrum, * denotes the complex conjugate and S is a smoothing operator (for detailed information, see Torrence & Compo, 1998). The value of $R_n^2(s)$ ranges from 0 to 1, with 0 indicating no correlation and 1 indicating the perfect linear relationship between the two time series at the given frequency and time.

3.2.6.3 Multiple wavelet coherence

MWC is a special case of wavelet analysis extended from the relationship of binary time series to multivariate time series at different time scales and frequencies (Hu & Si, 2016; Hu et al., 2017; Su et al., 2019). Given a response variable Y and multiple predictor variables X ($X = \{X_1, X_2, \dots, X_L\}$), the MWC at scale s and location τ, $\rho_m^2(s,\tau)$, can be expressed as:

$$\rho_m^2(s,\tau) = \frac{\overleftarrow{W}^{Y,X}(s,\tau)\overleftarrow{W}^{X,X}(s,\tau)^{-1}\overleftarrow{W}^{Y,X}(s,\tau)^*}{\overleftarrow{W}^{Y,Y}(s,\tau)} \tag{3.9}$$

where $\overleftarrow{W}^{X,X}(s,\tau)$ and $\overleftarrow{W}^{Y,Y}(s,\tau)$ are the matrix of smoothed auto- and cross-wavelet power spectra among multiple predictor variables X and the matrix of smoothed wavelet power spectrum of the response variable Y, respectively. $\overleftarrow{W}^{Y,X}(s,\tau)$ is the matrix of the smoothed cross-wavelet power spectra between the response variable Y and predictor variables X. $\overleftarrow{W}^{Y,X}(s,\tau)^*$ denotes the complex conjugate of $\overleftarrow{W}^{Y,Y}(s,\tau)$.

For both WTC and MWC, statistical testing was done against red noise as the null hypothesis, which can be modeled by a first-order autoregressive process requiring more than 1000 random realizations (Grinsted et al., 2004). The Monte Carlo method was adopted in this study to determine the 5% significance of WTC and MWC, which is commonly applied for hydrological and ecological data sets (Maraun & Kurths, 2004; Carey et al., 2013). Because the time series are not cyclical, edge artifacts exist. The region of the wavelet spectrum in which edge effects become important is defined as the Cone of Influence (COI), which is marked as lighter shade in the wavelet plots in this paper. For each scale, the significance level was assessed using only the values outside the COI. The global coherence coefficient (GCC), which is the time-averaged value of the WTC at a certain scale (Torrence & Compo, 1998; Liu et al., 2017) was analyzed in this study. The average wavelet coherence (AWC) and the percent area of significant coherence (PASC) relative to the whole wavelet scale-location (out of COI, Hu & Si, 2021) was also calculated. Higher overall AWC and PASC suggest greater dominance (Hu et al., 2017; Cheng et al., 2021). Although inclusion of additional ET_a measurements from other sites might increase the coherence with the ET_a at a given site, an increase in the PASC value by at least 5% should be observed before it can be concluded that the additional ET_a measurements have practical significance (Hu et al., 2017; Cheng et al., 2021). The wavelet analyses were conducted through Matlab program adopted or adapted from Torrence and Compo, Grinsted and Hu and Si from the website

https://doi.org/10.6084/m9.figshare.13031123.

3.3 Results

3.3.1 Observations of ET-LYS and ET-EC

Yearly cumulative ET-LYS, ET-EC and ET_0 for the years 2015-2020 are presented in Table 3.2. Here, the yearly sum of ET-LYS is the average over multiple lysimeters at the same site and with the same soil type, because the standard deviation between lysimeters at the same site and same soil was small. Among all sites, the lysimeters at the Selhausen site filled with Rollesbroich soil (SEro) had on average the largest cumulative ET-LYS (701.6 mm/y), while for the Rollesbroich site (RO) and the Graswang site (GW) ET-LYS were slightly smaller (676.8 mm/y and 651.4 mm/y, respectively) and for the Wüstebach site (WU) much smaller (406.1 mm/y). At the Selhausen site (SE), lysimeters with other soil types had a much lower ET-LYS than those of SEro: for lysimeters with Wüstebach soil (SEwu) 556.4 mm/y and for

lysimeters with Selhausen soil (SEse) 549.2 mm/y. The measured ET-LYS were close to ET_0 for the wet grassland RO and GW sites. In 2018 however, with a marked hot and dry summer period, both at the RO site and GW site ET-LYS was clearly smaller than ET_0 (up to 10% and 6%, respectively). On the other hand, for the drier and warmer SE site ET-LYS was in general smaller than ET_0, but strongly dependent on the soil type. For lysimeters SEse, ET-LYS was on average over the six years 27% smaller than ET_0. For SEro the difference with ET_0 was much smaller (7% on average). The largest differences between ET-LYS and ET_0 were found for the year 2018, with ET-LYS being 40% smaller than ET_0 for SEse. This shows that the ET_a in the dry year 2018 at SE was strongly limited by the lack of water, which is in line with previous investigation at SE for grassland (Forstner et al., 2021) and the crop oat (Groh et al., 2022). Finally, for WU ET-LYS was much smaller than ET_0 (37% on average over the six years) although WU is a wet site. This is because the lysimeter is located in the forest shadow and reduced sunlight reaching the grasses can result in lower rates of ET_a compared to ET_0 that was based on above-canopy radiation measurements. Among the six years, year 2020 witnessed the highest ET_0 at all the three sites in western Germany (768.1 mm/y, 706.3 mm/y and 807.3 mm/y at RO, WU, and SE, respectively), whereas the largest ET_0 was 705.8mm/y in 2018 at GW in southern Germany.

At RO and GW, the yearly sum of uncorrected ET-EC was on average 22% and 28% smaller than that of ET-LYS, respectively. This is in accordance with the findings reported by Gebler et al. (2015) and Mauder et al. (2018). For SEro, the yearly sum of ET-LYS was markedly larger than that of ET-EC (26.8%). However, for SEwu and SEse ET-LYS was only slightly larger than ET-EC at the SE site (7.7% and 6.5%, respectively). The biomass production on the lysimeters corroborate these findings with more biomass on the SEro lysimeters than the other lysimeters. These differences in ET and biomass production might be related to the soil properties, so that SEro lysimeters are less affected by drought than SEwu and SEse. We found that in July and August, ET-LYS from SEro lysimeters is much higher than that from SEse lysimeters (the difference was 37 mm on average, Figure A.1). This disparity can be explained by the fact that the SEse lysimeters were generally bare soil for most of the time during the two months which led to less transpiration by the plants (Table A.6), while on the SEro lysimeters grass was growing. In WU, the average annual ET-EC of the six years was 30% higher than ET-LYS, which agrees well with a previous investigation at the site, where ET-EC was 41 % higher than for the forest meadow (Bogena et al., 2015). This is again due to the fact that, on

the one hand, the lysimeter at the WU site is located in the forest shade, and thus has a significant lower energy input than the forest area, and, on the other hand, the ET-EC in Wüstebach measures ET_a over the forested footprint of a spruce stand (*Picea abis L.*), which has a much higher leaf area index than the local grassland.

With the correction of the energy balance deficit using the Bowen ratio method, the yearly sum of ET-ECc increased substantially (Table 3.2). The RO site had the most significant increase where the annual ET-ECc was on average 16.9% higher than ET-EC. ET-ECc is closer to ET-LYS than ET-EC, with the difference of annual ET_a measurements between EC and lysimeter on average reducing from 22% to 5.6%. Similarly, ET-ECc at the GW site also showed a clear increase and was closer to ET-LYS, but still with a difference of 17%. At the WU and SE sites, ET-ECc increased by 6.4% and 17% compared to ET-EC, respectively.

Figure 3.2 shows the average yearly cycle of ET-LYS, ET-EC, ET-ECc and ET_0 at monthly resolution for the study period. All four sites show a distinct yearly cycle. In summer (June to August) the monthly cumulative ET-LYS values for RO, WU, and GW were larger than in other seasons, with peak values in RO in June of 112.0 mm close to ET_0 (109.8 mm), in WU for July of 72.8 mm and in GW for July of 118.1 mm. ET-LYS for RO was obviously higher than ET_0 in May and June, suggesting that in these months grass heights were larger than the reference grass height of 12cm combined with ET which was not limited by soil moisture but by energy. The highest monthly ET-LYS in SE was found in May for all soils and land surface cover types, namely 105.1 mm (SEro), 86.0 mm (SEwu), and 97.3 mm (SEse). For SEse, this can be explained by the fact that in May the crops were growing and therefore ET_a was high, while in summer ET_a decreased due to the end of the growing season. For the grass, this is most likely related to the fact that in summer at the SE site ET_a is often reduced due to drought, while RO and WU are less affected by drought stress given the higher precipitation and lower ET_0, compared to SE. However, also the change in the growing season duration combined with less precipitation might affect the ET_a difference between sites. Forstner et al. (2021) demonstrated that transferring soil from RO to SE increases the length of the growing season by an average of 36 days. December witnessed the lowest average monthly cumulative ET-LYS at the RO, WU, and SE sites, but the lowest monthly ET-EC and ET-ECc was registered in January.

Over the six years, the percentage of gap-filled ET-LYS at RO, WU and SE was on average 10.2% and at GW 48.9% (Table 3.2). The higher percentage at GW is related to snow cover (with over 70% and even up to 100% of missing data in January, February, March and

December, Table A.3Table A.4) and the frequent chamber measurements performed on the lysimeters which disturbed the lysimeter ET measurements. The percentage of gap-filled ET-EC data was higher than for ET-LYS at all sites, with an average of 36.3% across the four sites, and for WU it was even up to 65.3% in 2018 (Table 3.2). More data gaps occurred during night than that during daytime (Table A.5) due to more stable conditions with lower wind speeds and reduced turbulence during night (Straaten & Weber, 2021). Given the fact that ET_a is primarily composed of daytime ET_a (Ding et al., 2010; Groh et al., 2019; Han et al., 2021), the high gap-filling percentage of nighttime ET_a does not necessarily reduce the reliability of the data. In addition, both lysimeters and EC had more missing data in winter (Table A.4), which is related to snow and frost (lysimeters, Table A.1Table A.3) and stable conditions where the EC data is not reliable.

Table 3.2 Yearly sums of ET_0, ET-LYS, ET-EC and ET-ECc at different sites. "Gap-filled ET_a [%]" denotes the percentage of hourly ET_a which were gap-filled. Here, yearly ET-LYS is the mean of multiple lysimeters at the same site. The standard deviations between the lysimeters are presented in parentheses.

Site	Year	2015	2016	2017	2018	2019	2020	Mean
RO	ET_0 [mm]	673.5	630.7	655.3	737.1	689.0	763.9	691.6
	ET-LYS [mm]	684.3 (±20.4)	642.1 (±18.3)	658.9 (±27.6)	658.3 (±34.4)	708.8 (±35.8)	708.2 (±23.9)	676.8 (±19.0)
	ET-EC [mm]	535.8	481.4	540.9	550.1	516.4	553.9	529.7
	$ET\text{-}EC_c$ [mm]	619.5	614.8	652.2	661.1	611.6	664.6	637.3
	Gap-filled ET-LYS [%]	16.2 (±2.34)	11.4 (±0.63)	12.7 (±0.41)	17.5 (±0.35)	18.5 (±9.80)	7.8 (±0.91)	14.0 (±4.11)
	Gap-filled ET-EC [%]	30.4	32.8	33.2	26.6	29.2	27.3	29.90
WU	ET_0 [mm]	628.7	592.9	598.2	691.8	648.2	694.1	642.3
	ET-LYS [mm]	469.9 (±26.6)	399.4 (±35.1)	389.9 (±29.7)	428.0 (±27.4)	376.1 (±23.8)	373.3 (±27.9)	406.1 (±25.8)
	ET-EC [mm]	507.0	543.1	550.4	528.2	516.9	532.1	529.6
	$ET\text{-}EC_c$ [mm]	553.8	581.8	557.0	577.9	555.5	584.4	568.4
	Gap-filled ET-LYS [%]	12.1 (±0.74)	16.5 (±0.83)	17.2 (±0.86)	18.8 (±1.44)	16.4 (±1.07)	13.0 (±1.99)	15.7 (±1.15)
	Gap-filled ET-EC [%]	51.5	51.1	64.2	65.3	50.9	47.9	55.2
SE	ET_0 (mm)	741.1	690.4	709.6	800.7	766.6	828.6	756.2
	ET-LYS(SEse) [mm]	733.4 (±36.6)	506.0 (±14.1)	570.4 (±46.9)	471.2 (±11.4)	533.5 (±34.1)	480.7 (±23.0)	549.2 (±9.9)
	ET-LYS(SEro) [mm]	838.0 (±23.9)	694.0 (±43.6)	681.5 (±30.1)	592.2 (±16.5)	731.5 (±33.6)	672.5 (±5.5)	701.6 (±13.2)
	ET-LYS(SEwu) [mm]	709.8 (±65.3)	611.4 (±63.8)	563.1 (±39.7)	477.1 (±19.9)	486.6 (±37.9)	490.3 (±36.3)	556.4 (±31.9)
	ET-EC [mm]	586.2	496.4	538.7	449.1	522.1	487.2	513.3
	$ET\text{-}EC_c$ [mm]	683.6	609.1	639.1	534.3	664.6	568.5	616.5
	Gap-filled ET-LYS (SEse) [%]	7.9 (±1.89)	5.5 (±0.99)	6.3 (±2.98)	5.3 (±0.58)	4.1 (±0.54)	2.9 (±0.90)	5.3 (±1.71)

	Gap-filled ET-LYS (SEro) [%]	12.4 (±4.49)	8.2 (±1.42)	5.8 (±0.40)	4.1 (±0.87)	8.2 (±0.46)	4.3 (±0.55)	7.2 (±3.15)
	Gap-filled ET-LYS (SEwu) [%]	12.7 (±6.65)	9.0 (±0.83)	5.8 (±1.18)	6.9 (±1.13)	12.4 (±2.56)	7.4 (±0.74)	9.0 (±2.89)
	Gap-filled ET-EC [%]	19.5	20.4	22.3	18.6	18.2	26.8	21.0
GW	ET_0 [mm]	674.2	623.7	666.1	705.8	681.5	666.7	669.7
	ET-LYS [mm]	637.5 (±2.9)	585.7 (±37.7)	659.2 (±50.0)	663.1 (±28.9)	665.8 (±54.8)	697.1 (±15.1)	651.4 (±31.6)
	ET-EC [mm]	462.6	446.3	507.0	492.3	459.6	465.6	472.2
	$ET\text{-}EC_c$ [mm]	572.4	506.4	546.2	556.1	474.0	495.9	525.2
	Gap-filled ET-LYS [%]	49.9 (±0.6)	41.5 (±0.6)	43.1 (±3.0)	45.2 (±1.4)	54.1 (±3.0)	59.7 (±1.7)	48.9 (±7.0)
	Gap-filled ET-EC [%]	39.3	39.2	38.4	57.3	30.4	30.7	39.2

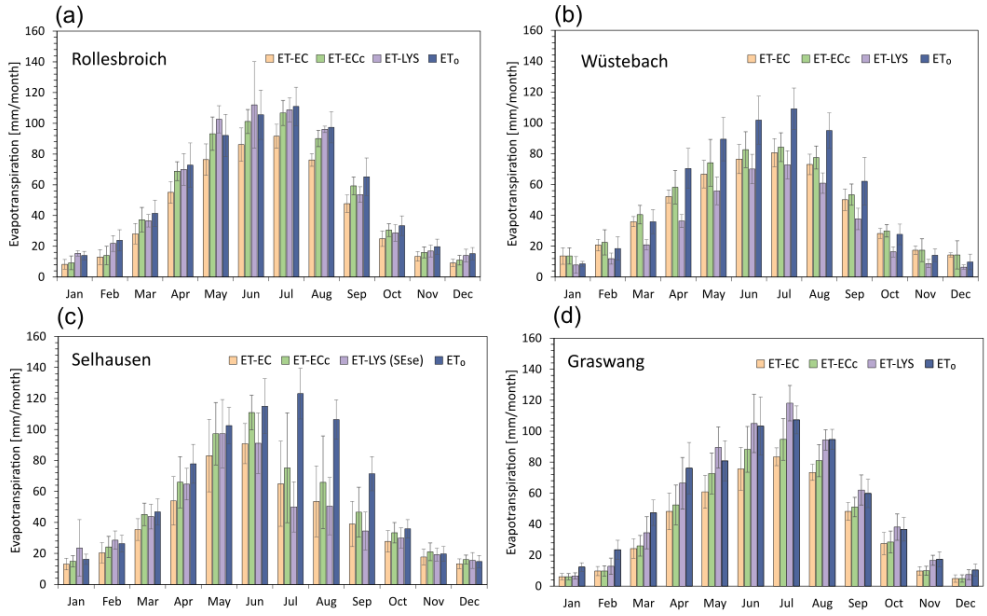


Figure 3.2 Average monthly cumulative ET-LYS, ET-EC, ET-ECc and ET_0 at different sites, calculated over the period 2015-2020. Error bars denote the standard deviations of monthly ET, calculated over the years.

3.3.2 Pearson correlations for ET-LYS and ET-EC at different spatial scales

3.3.2.1 Plot and landscape scale

Table 3.3 shows the average PCCs of $SA_{ET\text{-}LYS}$ between different individual lysimeters at the same measurement site. The lysimeters with the same soil origin at the same site showed high correlations (>0.9) and very low standard deviations (<0.08). The high PCCs indicate that the

replications of lysimeter worked well and lysimeter measurements provide representative information at the plot scale.

Given the fact that lysimeter measurements are representative at the plot scale with very high correlations among different lysimeters at the same site, we used the average ET-LYS for different lysimeters with the same soil at the same site to perform the succeeding analyses. Figure 3.3 shows PCCs for ET-LYS, ET-EC and ET-ECc between different sites. At the landscape scale (separation distances < 50 km), PCCs of $SA_{ET\text{-}LYS}$ varied between 0.32 and 0.65. The correlation between the WU and RO site was 0.65 and the two sites have a similar climate and are not separated far in space (13 km). Correlations were smaller between WU (or RO) and the SE site, which is related to differences in precipitation and potential evapotranspiration (ET_0), as well as soil type between WU or RO on one hand and SE on the other hand. The lowest correlation of 0.32 was found between WU and the lysimeters SEse. In summary, $SA_{ET\text{-}LYS}$ show moderate correlations between lysimeters which are between 10 and 50 km separated in space.

Next, we compare the PCCs of $SA_{ET\text{-}LYS}$ and $SA_{ET\text{-}EC}$ across different sites over the 6 years period at the landscape scale (Figure 3.3). The PCC between RO and WU are very similar for $SA_{ET\text{-}LYS}$ and $SA_{ET\text{-}EC}$ (0.65 and 0.66, respectively) despite the different vegetation at WU for the EC station (forest) and the lysimeters (grass). In addition, as pointed out before, the lysimeters at the WU site are located in a forest meadow which is often shaded (morning and evening hours) by the surrounding spruce stand, whereas the EC station measures ET_a above the forest canopy. The PCC was high between RO and the SEro lysimeters (0.65). This could be related to the fact that the same soil and vegetation on the lysimeters at both sites lead to a similar ET_a response. On the other hand, the PCC for ET-LYS between the lysimeters at RO and the lysimeters in SE filled with WU soil (SEwu) was slightly lower than the PCC for ET-EC (0.58) between RO and SE. Finally, PCC for ET-LYS between lysimeters in RO and lysimeters in SE filled with SE soil (SEse) was lower than PCC for ET-EC between RO and SE (0.47 versus 0.58), and showed relative high variation between years with values varying between 0.61 (2015) and 0.35 (2018). The differences between the years can be related to the different crop types and crop rotation (with different harvest times) for lysimeters and EC at the SE site (Table A.6Table A.7).

Also for WU and SE, despite the distance between the two sites of about 50 km, a moderate PCC for ET-LYS measured by lysimeter SEse was found (0.32), which was slightly smaller

than for ET-EC (0.44). The PCCs of $SA_{ET\text{-}LYS}$ between the two sites show a similar pattern as function of the different soil types as RO and SE. Lysimeters SEro showed the strongest correlation (0.44) with lysimeters in WU, closely followed by the lysimeters SEwu (0.42).

After forcing energy balance closure, the PCCs of $SA_{ET\text{-}ECc}$ were all lower than $SA_{ET\text{-}EC}$ at the landscape scale, varying between 0.41 and 0.58. The PCC of $SA_{ET\text{-}ECc}$ even became lower than PCC for $SA_{ET\text{-}LYS}$ between RO and WU sites (Figure 3.3). Overall, although the distances across the three sites vary from 10 – 50 km, PCC for ET-LYS was moderately strong, and similar to the PCC for ET-EC and ET-ECc.

3.3.2.2 Larger regional scale (~ 500km)

For the larger regional scale, the PCC was clearly lower than at the landscape scale, varying between 0.16 and 0.3 for $SA_{ET\text{-}LYS}$ and between 0.12 and 0.3 for $SA_{ET\text{-}EC}$ (Figure 3.3). At this scale, RO and GW had the highest correlations, both for $SA_{ET\text{-}LYS}$ and $SA_{ET\text{-}EC}$ (0.3). The distance between RO and GW is 485km. The strong PCC may be related to the fact that both are extensively managed grassland sites and in general not much affected by drought, as both sites are rather energy than water limited ecosystems. Between WU and GW, PCC was lower and for $SA_{ET\text{-}LYS}$ slightly lower than for $SA_{ET\text{-}EC}$, with values of 0.19 and 0.23, respectively. Between SE and GW, $SA_{ET\text{-}LYS}$ shows higher PCC than $SA_{ET\text{-}EC}$ (0.12) irrespective of soil and vegetation type, namely 0.16 (SEse), 0.22 (SEro) and 0.16 (SEwu). PCCs of $SA_{ET\text{-}EC}$ and $SA_{ET\text{-}LYS}$ between GW and the arable land SE (or lysimeter SEse) varied a lot between years.

The relationship between the PCC for ET-ECc and PCC for ET-EC was close to the 1:1 line with the R^2 of 0.94, although there was a systematically slightly lower correlation was shown for ET-ECc than for ET-EC (Figure 3.4). Interestingly, with the increase of the distance between sites, the difference between PCCs for ET-EC and PCCs for ET-ECc decreased (regardless of landscape scale or larger regional scale), with the difference reduced from 0.08 to -0.02. Though yielding different PCC values, correction of energy balance for ET-EC did not change the results of the comparison with ET-LYS at larger regional scale (Figure 3.3), indicating that the results are robust. Overall, the correlation for ET-LYS was not much smaller than that for ET-EC, suggesting that the lysimeter can provide as much information as an eddy covariance measurement. In addition, although the sites are far separated in space, still a small correlation in ET_a was found, indicating that weather systems play a role in driving ET_a.

However, given the low correlations at this separation distance of 500 km, the information content of lysimeters is quite limited for the larger regional scale.

Table 3.3 Average Pearson correlation coefficient (PCC) of $SA_{ET\text{-}LYS}$, calculated between different pairs of lysimeters at the same site for the period 2015-2020. "Stdv" denotes the standard deviation of correlations.

	RO	WU	SEro	SEwu	SEse	GW
PCC	0.96	0.94	0.92	0.91	0.94	0.95
Stdv	±0.03	±0.04	±0.02	±0.07	±0.05	\

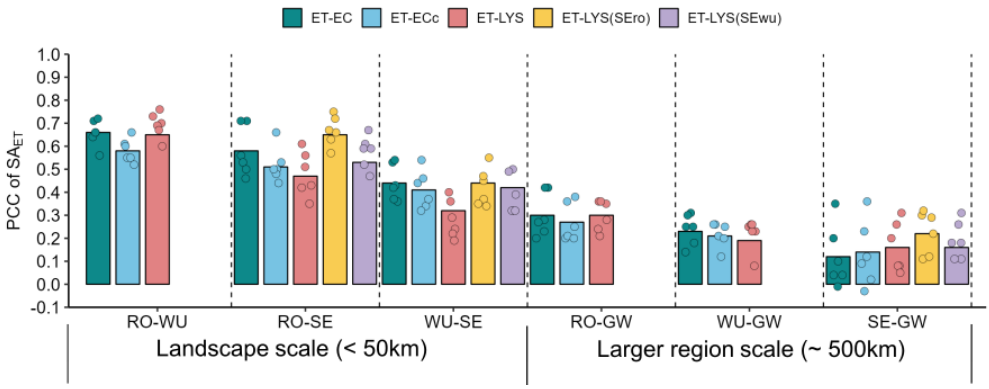


Figure 3.3 Pearson correlation coefficient (PCC) for ET-LYS, ET-EC and ET-ECc at the landscape scale. Bars refer to PCC of standardized anomaly of ET-LYS ($SA_{ET\text{-}LYS}$, red bar), standardized anomaly of ET-EC ($SA_{ET\text{-}EC}$, green bar), or standardized anomaly of ET-ECc ($SA_{ET\text{-}ECc}$, blue bar) between different sites for the period 2015-2020. Yellow bar refers to PCC between $SA_{ET\text{-}LYS}$ from lysimeters at SE site filled with soil from RO site (SEro) and another lysimeter site. Purple bar refers to PCC between $SA_{ET\text{-}LYS}$ from lysimeters at SE site filled with soil from WU site (SEwu) and another lysimeter site. Circles denote the PCC for individual years.

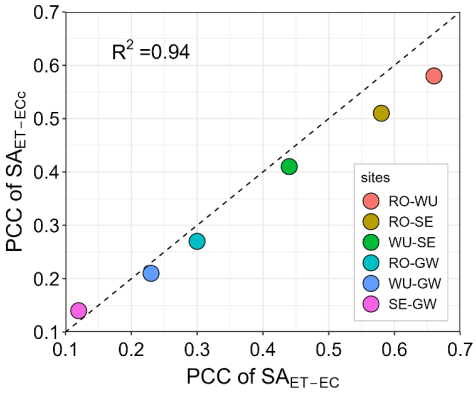


Figure 3.4 Scatter plot of Pearson correlation coefficient (PCC) of standardized anomaly (SA) of ET-EC and ET-ECc between the different sites. ET-EC and ET-ECc refer to the ET_a measurements from EC without and with energy balance closure, respectively. Dashed line is the 1:1 line.

3.3.3 Wavelet coherence of ET-LYS and ET-EC

As the similar PCC results for corrected ET-ECc, we then focused on uncorrected ET-EC. To explore the correlations for ET-LYS and ET-EC at various temporal scales, the wavelet transform coherence (WTC) was computed. Figure A.2 presents the continuous wavelet transform (CWT) ET-LYS and ET-EC for each site. Figure 3.5Figure 3.7 show the WTC results for ET-LYS and ET-EC between any two sites for the 6-year time series and at which temporal frequencies coherence of the ET_a time series appears between two sites.

When analyzing the CWT, both ET-LYS and ET-EC at each site showed significant annual cycle, and a cycle between 1 and 16 days appeared in the middle of each year (Figure A.2).

In the cross-wavelet analysis, at landscape spatial scale, from Figure 3.5Figure 3.6 it can be seen that the WTC between any two measurement sites was markedly significant both for ET-LYS and ET-EC at the semi-annual and annual scale (180 -512 days), where the GCC stayed at a consistently high value, even up to 1. This is intuitive since ET-LYS and ET-EC at each site all showed a marked annual cycle (Figure A.2). The significant WTC suggest that the semi-annual (winter to summer) trend and the between-year trend on ET_a are very similar. This is logical as the winter and summer variations on ET_a exhibit the most substantial changes, and the between-year variations can also be significant. Both lysimeter and EC can capture these distinctive features. Among these, RO exhibits perfectly in-phase (positive) correlations with

WU irrespective of ET-LYS or ET-EC, whereas RO and WU lag SE by less than 1 month for all lysimeter soils and ET-EC, as indicated by the arrows in the figures.

For the RO-WU couple, the coherence at a scale of around 1 day and 1 month was intermittent and generally in phase both for ET-LYS and ET-EC, with less coherence during winter (Figure 3.5aFigure 3.6a). But ET-EC displays more disruptions than ET-LYS at this time scale, especially in the drier years (2018-2020), when ET-EC lost coherence during summer months. Overall, the AWC and PASC for ET-LYS were similar to those for ET-EC (0.73 and 58% for ET-LYS and 0.65 and 47% for ET-EC, respectively, Table 3.4).

ET-LYS from RO and WU show similar wavelet coherence spectra with the SE lysimeters, yet RO shows greater coherence than WU. For the RO-SEse and the WU-SEse couple, the WTC results show intermittent coherence for the 1- to 16-day period and scattered coherence for the 16-day to half-year scale (Figure 3.5Figure 3.6). Most coherence is positive with varying phase shift, but at a scale of around 90 days, the coherence turns negative between May and August 2018, with arrows pointing to the left. Compared with ET-LYS, ET-EC between RO and SE has smaller AWC (0.53) and PASC (32%). For the WU-SE couple, ET-EC shows more frequent breaks at a scale <16 days compared to ET-LYS.

The RO-SEro, RO-SEwu, WU-SEro and WU-SEwu couples all show fragmentary coherence at small scales of 1 day to 1 month (Figure 3.5Figure 3.6). GCC maintained at a lower level for WU couples than RO couples. At this scale, very weak or even no coherence was found in winter due to the lower signal to noise ratio in winter, given small ET and the role of measurement errors. Coherence was also weak in spring and autumn, which may be related to the difference in beginning and end of growing season within the Eifel and at Selhausen (Forstner et al., 2021). Again, the coherence in 2018 was significantly smaller compared to other years revealed by more blue areas.

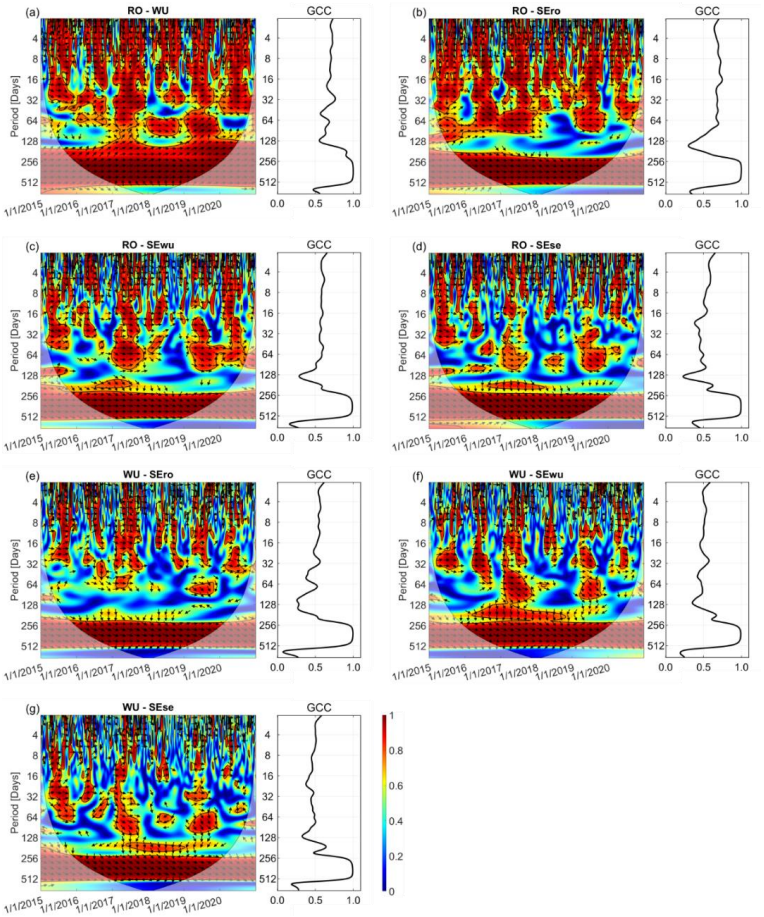


Figure 3.5 Wavelet transform coherence (WTC) and global coherence coefficient (GCC) of ET-LYS between (a) RO and WU, (b) RO and SEro, (c) RO and SEwu, (d) RO and SEse, (e) WU and SEro, (f) WU and SEwu, (g) WU and SEse. The vertical axis shows the periodicity up to 770 days. The right part of each panel demonstrates the GCC. The left part of each panel depicts WTC and the horizontal axis shows the study period (from 2015-2020 on daily basis). Thick contours indicate significant coherence at 95% confidence level. The pale region delineates the cone of influence (COI) where edge effect might distort the results. Small arrows show the phase difference between two series (right arrows indicate in-phase (positive) relationship, left arrows indicate out-of-phase (or negative) relationship (180°), and arrows upwards (downwards) indicate the second series leading (lagging) the first by 90°). The color denotes the strength of coherence with the red being high and blue being low.

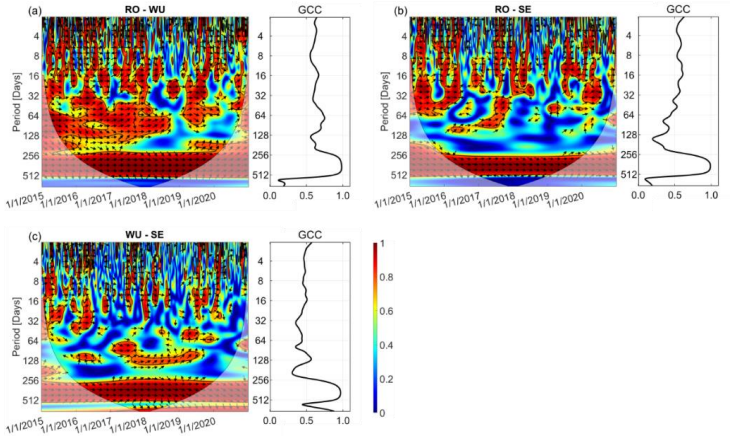


Figure 3.6 Wavelet transform coherence (WTC) and global coherence coefficient (GCC) of ET-EC between (a) RO and WU, (b) RO and SE, (c) WU and SE. The vertical axis shows the periodicity up to 770 days. The right part of each panel demonstrates the GCC. The left part of each panel depicts WTC and the horizontal axis shows the study period (from 2015-2020 on daily basis). Thick contours indicate significant coherence at 95% confidence levels against red noise. The pale region delineates the cone of influence (COI) where edge effect might distort the results. Small arrows show phase difference between two series (right arrows indicate in-phase relationship, left arrows indicate out-of-phase relationship (180°), and arrows upwards (downwards) indicate the second series leading (lagging) the first by 90°). The color denotes the strength of coherence.

Table 3.4 Average wavelet coherence (AWC) and percent area of significant coherence (PASC) values for the wavelet coherence of ET-LYS or ET-EC between two sites at the landscape scale.

ET-LYS			ET-EC		
Site	AWC	PASC (%)	Site	AWC	PASC (%)
RO - WU	0.73	58	RO - WU	0.65	47
RO - SEse	0.56	34	RO - SE	0.53	32
RO - SEro	0.68	51			
RO - SEwu	0.60	39			
WU - SEse	0.53	29	WU - SE	0.52	27
WU - SEro	0.54	30			
WU - SEwu	0.55	32			

Table 3.5 Average wavelet coherence (AWC) and percent area of significant coherence (PASC) values for the wavelet coherence of ET-LYS or ET-EC between two sites at the larger regional scale.

ET-LYS			ET-EC		
Sites	AWC	PASC	Sites	AWC	PASC
RO - GW	0.56	30	RO - GW	0.58	37
WU - GW	0.54	29	WU - GW	0.52	30
SEse - GW	0.45	20	SE - GW	0.43	18
SEro - GW	0.47	21			
SEwu - GW	0.45	20			

Compared to the landscape scale, both ET-LYS and ET-EC at the larger regional scale show less area with significant coherence (compared to Figure 3.7) and smaller AWC and PASC (Table 3.5), but there is still significant coherence at some temporal scales. Significant annual coherence prevails during the entire study period for all pairs of sites for both ET-EC and ET-LYS. RO and WU have in-phase (positive) coherence with GW, whereas the wet GW site lags the dry SE site, irrespective of the soil and vegetation type at SE, with arrows pointing slightly upwards.

ET-EC between RO and GW have the highest AWC (0.58) and PASC (37%) at the larger regional scale, followed by ET-EC between WU and GW (0.52 for AWC and 30% for PASC). The ET-LYS data show slightly less coherence than ET-EC with 30% PASC for the RO-GW couple and 29% for the WU-GW couple. ET-EC between RO (or WU) and GW displays sometimes significant coherence at a time scale around 64-128 days, more than for ET-LYS. For the WU-GW couple, ET-EC shows significant coherence at the scale around 90 days during the entire time periods, while the arrows point to the right before 2017 and pointing right down from 2018 onwards indicating that GW lags WU. On the other hand, significant coherence at the time scale around 90 days for ET-LYS between March 2018 and November 2019 shows no lag.

For the SE and GW sites, ET-LYS has higher AWC and PASC than ET-EC (Table 3.5), but both ET-LYS and ET-EC show a low significant coherence at the scales other than the annual scale.

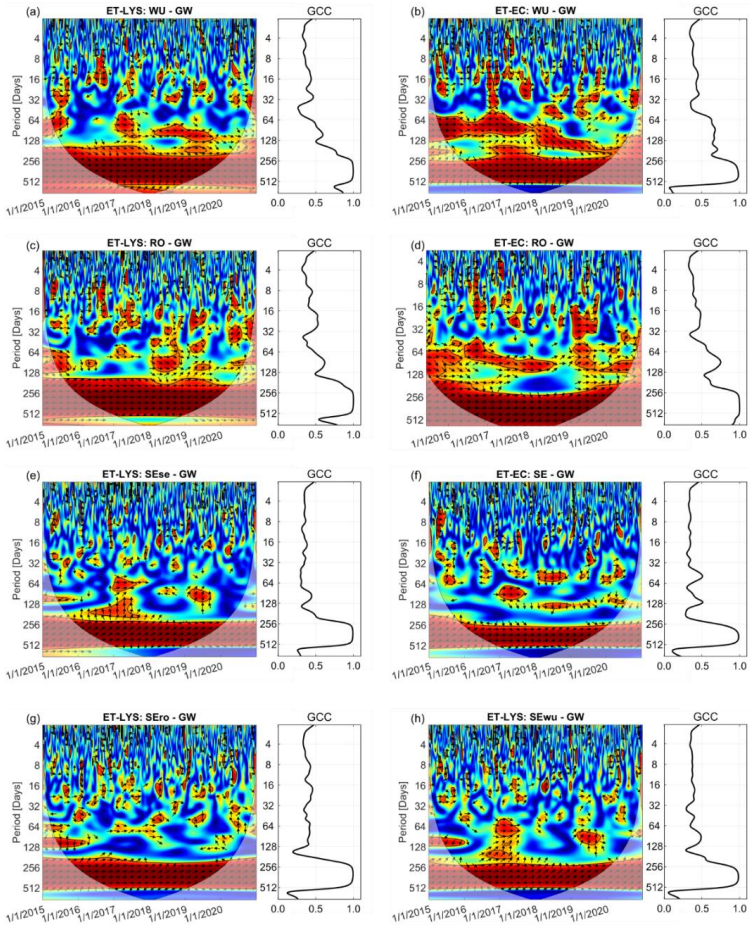


Figure 3.7 Wavelet transform coherence (WTC) and global coherence coefficient (GCC) of ET-LYS between (a) WU and GW, (b) RO and GW, (c) SEse and GW, (g) SEwu and GW and (h) SEro and GW, and WTC of ET-EC between (d) WU and GW, (e) RO and GW and (f) SE and GW. The vertical axis shows the periodicity up to 770 days. The right part of each panel demonstrates the GCC. The left part of each panel depicts WTC and the horizontal axis shows the study period (from 2015-2020 on daily basis). Thick contours indicate significant coherence at 95% confidence level. The pale region delineates the cone of influence (COI) where edge effect might distort the results. Small arrows show phase difference between two time series (right arrows indicate in-phase relationship, left arrows indicate out-of-phase relationship (180°), and arrows upwards (downwards) indicate the second series leading (lagging) the first by 90°). The color denotes the strength of coherence.

3.3.4 Combined ET_a measurements from multiple sites

In this section, we present the results of the analysis using multiple wavelet coherence across various sites. Overall, we observe significant continuous annual periodic characteristics prevailing both for ET-LYS and ET-EC at the landscape scale and larger regional scale.

At the landscape scale, compared with WTC results (on average 0.6 for ET-LYS and 0.57 for ET-EC, Table 3.4 and Table **3.5**), the two-site scenario significantly improves AWC (on average 0.86 for ET-LYS and 0.79 for ET-EC, Table 3.6). Figure 3.8 shows that the consistency and coherence for the scales of 1 day to 3 months is also notably improved compared with Figure 3.5Figure 3.6. The best combination is WU and SE sites, which account for 50% to 71% of the ET_a variation at the RO site. Conversely, the least effective combination is RO and WU sites which account only for 30% of the ET_a variation at the SE site. Interestingly, when adding one lysimeter measurement which contains the same soil and vegetation from the response site, MWC increases significantly (from 0.86 to 0.94 for the RO site and from 0.85 to 0.91 for the WU site). However, PASC does not show a significant increase (8% increase for RO and 1% decrease for WU). This could be related to the overlapping effects due to the collinearity among the lysimeter measurements at the SE site.

At the larger regional scale, two-site combination shows higher AWC than WTC, with AWC > 0.7 (Table 3.7). The highest AWC is achieved by the combination of ET-LYS from SEse, SEro and GW to predict RO (0.91). Meanwhile, the AWC for ET-LYS are not lower than for ET-EC. When adding another site, PASC for ET-LYS and ET-EC all increase, ranging from 0.84 to 0.97. However, when adding a SE site, the PASC does not improve.

Shifting from the two-site to the three-site scenario, we note a pronounced improvement in AWC both for ET-LYS and ET-EC (on average 0.91 and 0.88, respectively) and in PASC for ET-LYS (on average 52%). However, the increase of PASC for ET-EC (by 4% on average) is small. Likewise, when adding SEro or SEwu, the AWC is the highest.

Table 3.6 Main statistics of multiple wavelet coherence (MWC) of ET-LYS (or ET-EC) between sites at the landscape scale. AWC refers to average multiple-wavelet coherence. PASC refers to the percent area of significant coherence. The symbol "&" means combination, e.g., RO - WU & SEse means the coherence between ET-LYS at the RO site and the combination of ET-LYS from lysimeters at the WU site and SE site filled with local soil.

ET-LYS			ET-EC		
Two sites	AWC	PASC	Two sites	AWC	PASC
RO - WU & SEse	0.86	64	RO - WU & SE	0.82	50
RO - WU & SEse & SEro	0.94	71			
WU - RO & SEse	0.85	59	WU - RO & SE	0.81	46
WU - RO & SEse & SEwu	0.91	58			
SEse - RO & WU	0.75	35	SE - RO & WU	0.74	33

Table 3.7 Main statistics of multiple wavelet coherence (MWC) of ET-LYS (or ET-EC) between sites at the larger regional scale. AWC refers to average multiple-wavelet coherence. PASC refers to the percent area of significant coherence. The symbol "&" means combination, e.g., RO - WU & GW means the coherence between ET-LYS at the RO site and the combination of ET-LYS measured by lysimeters at the WU site and lysimeters at the GW site.

ET-LYS			ET-EC		
Two sites	MWC	PASC	Two sites	MWC	PASC
RO - WU & GW	0.86	59	RO - WU & GW	0.82	52
RO - SEse & GW	0.79	41	RO - SE & GW	0.82	51
RO - SEse & SEro & GW	0.91	56			
WU - RO & GW	0.84	59	WU - RO & GW	0.82	50
WU - SEse & GW	0.75	37	WU - SE & GW	0.76	37
WU - SEse & SEwu & GW	0.86	43			
SEse - RO & GW	0.72	31	SE - RO & GW	0.75	37
SEse - WU & GW	0.70	28	SE - WU & GW	0.70	24
GW - RO & WU	0.73	34	GW - RO & WU	0.75	40
GW - RO & SEse	0.72	29	GW - RO & SE	0.75	38
GW- WU &SEse	0.70	28	GW- WU &SE	0.71	29

Table 3.8 Main statistics of multiple wavelet coherence (MWC) of ET-LYS (or ET-EC) between sites at the larger regional scale. AWC refers to average multiple-wavelet coherence. PASC refers to the percent area of significant coherence. The symbol "&" means combination, e.g., RO - WU & SEse & GW means the coherence between ET-LYS at the RO site and the combination of ET-LYS measured by lysimeters at the WU site, lysimeters at the SE site filled with local soil and lysimeters at the GW site.

ET-LYS			ET-EC		
Three sites	AWC	PASC	Three sites	AWC	PASC
RO - WU & SEse & GW	0.93	62	RO - WU & SE & GW	0.92	57
RO - WU & SEse & SEro & GW	0.97	68			

WU - RO & SEse & GW	0.91	58	WU - RO & SE & GW	0.89	46
WU - RO & SEse & SEwu & GW	0.95	58			
SEse - RO & WU & GW	0.85	32	SE - RO & WU & GW	0.86	34
GW - RO & WU & Sese	0.84	33	GW - RO & WU & SE	0.86	39

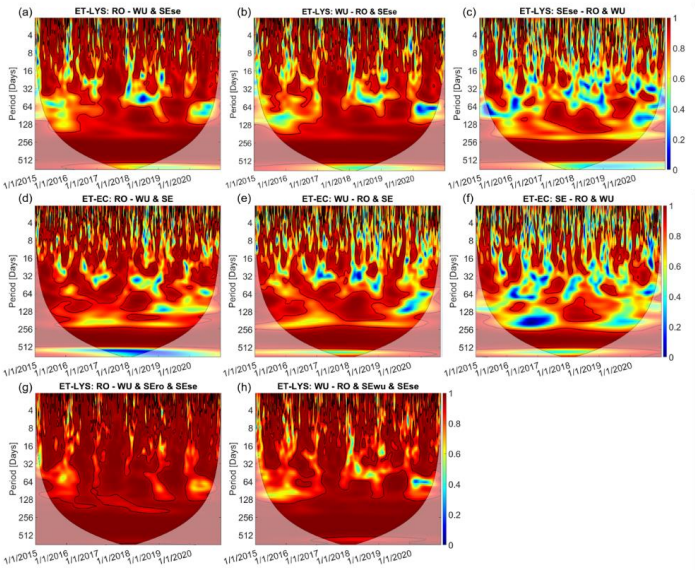


Figure 3.8 Two-site scenario of multiple wavelet coherence (MWC) at the landscape scale. The vertical axis shows the periodicity up to 770 days, and the horizontal axis the study period (from 2015-2020 on daily basis). Thick contours indicate significant coherence at 95% confidence level. The pale region delineates the cone of influence (COI) where edge effect might distort the results. The color denotes the strength of coherence.

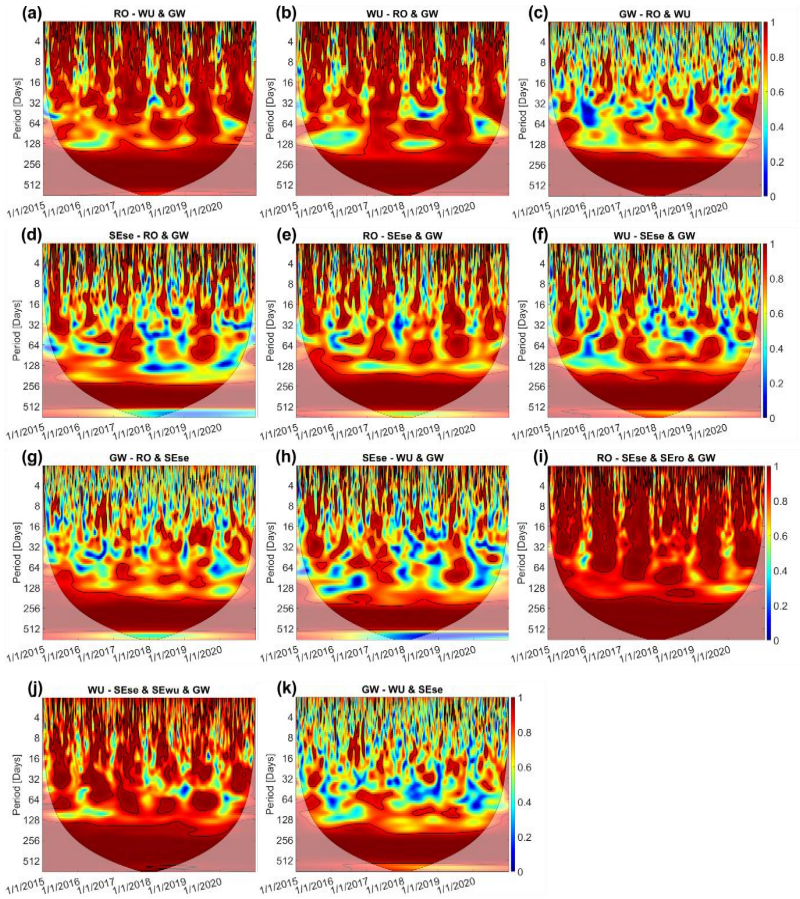


Figure 3.9 Two-site scenario of multiple wavelet coherence (MWC) of ET-LYS at the larger regional scale. The vertical axis shows the periodicity up to 770 days, and the horizontal axis the study period (from 2015-2020 on daily basis). Thick contours indicate significant coherence at 95% confidence level. The pale region delineates the cone of influence (COI) where edge effect might distort the results. The color denotes the strength of coherence.

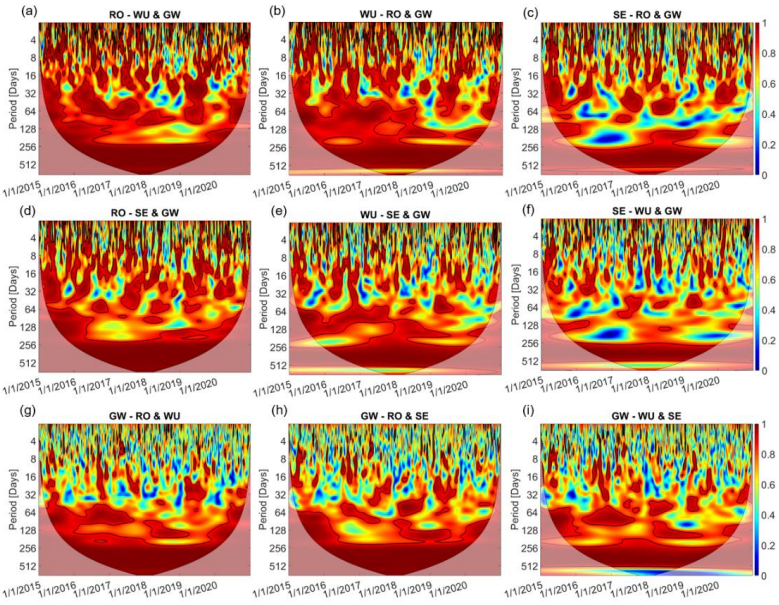


Figure 3.10 Two-site scenario of multiple wavelet coherence (MWC) of ET-EC at the larger regional scale. The vertical axis shows the periodicity up to 770 days, and the horizontal axis the study period (from 2015-2020 on daily basis). Thick contours indicate significant coherence at 95% confidence level. The pale region delineates the cone of influence (COI) where edge effect might distort the results. The color denotes the strength of coherence.

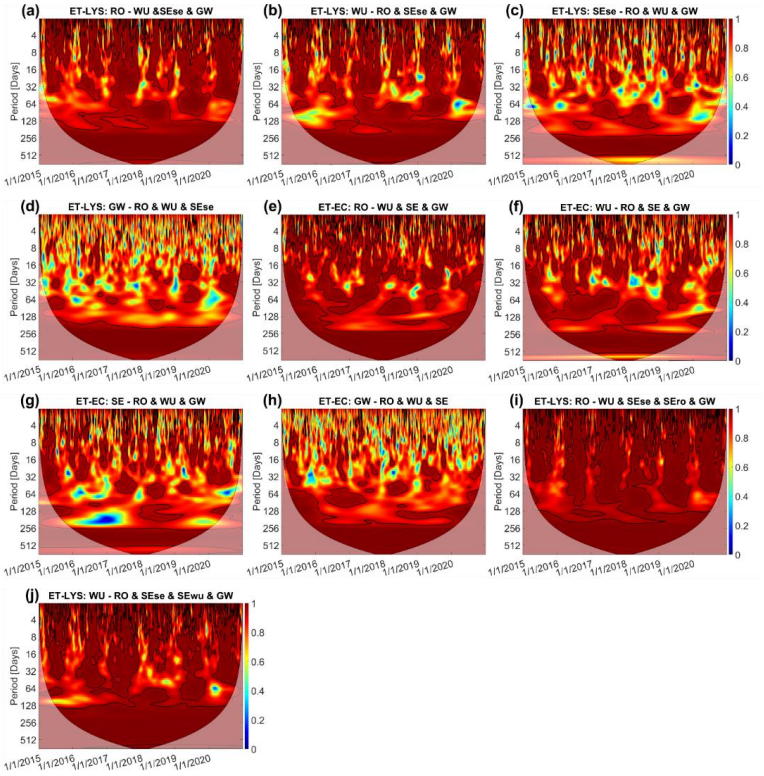


Figure 3.11 Three-site scenario of multiple wavelet coherence (MWC) at the larger regional scale. The vertical axis shows the periodicity up to 770 days, and the horizontal axis the study period (from 2015-2020 on daily basis). Thick contours indicate significant coherence at 95% confidence level. The pale region delineates the cone of influence (COI) where edge effect might distort the results. The color denotes the strength of coherence.

3.4 Discussion

3.4.1 Overall assessment of correlations

The spatial correlations of ET_a as observed are affected by the hydrological status of the system, i.e. whether ET is energy limited or water limited. This status can be characterized according to the Budyko framework, which is a widely used conceptual model by linking ET_a with ET_0 and precipitation (Akbar, Gianotti, et al., 2018; Rahmati et al., 2020). The ET_a correlations between two sites with the same hydrological status are higher than between those with different hydrological status irrespective of ET-LYS or ET-EC. For example, the RO-WU couple has the highest PCC among the lysimeter pairs at the landscape scale and the PCCs for

the RO-GW couple and the WU-GW couple are higher than for the SE-GW couple at the large regional scale (Figure 3.3). This is because RO, WU and GW are mostly energy-limited sites that are not easily affected by drought, whereas SE is a site which has sometimes water-limited conditions (Figure A.3). It would be interesting to extend the investigation further including more water limited sites to calculate also correlations between water limited sites. However, unfortunately high resolution high quality lysimeter data are scarce, especially for semi-arid and arid sites.

The vegetation and soil also affect the correlations between sites. Lysimeters for different sites have a higher correlation, and higher PASC with coherence at more temporal scales, if they contain the same soil, and the correlation is weaker if the soil in the two lysimeters has a different texture. This could be observed with the translocated lysimeters from energy-limited sites to water-limited sites (Rahmati et al., 2020), comparing for example RO-SEro vs. RO-SEse as well as WU-SEwu vs. WU-SEse (Figure 3.5 and Table 3.4).When adding an additional ET_a timeseries from the lysimeter filled with the same soil and vegetation as the response site, AWC increased significantly (Table 3.7Table 3.8).The correlations among sites for ET-LYS are not much smaller than for ET-EC, although lysimeters have a small surface area (in this study about 1 m^2) compared to the EC footprint. This can be explained by the fact that correlations for ET-EC might be unusually small or correlations for ET-LYS might be higher. The size and shape of the EC footprint vary strongly depending on wind speed and wind direction (Chu et al., 2021). If the EC field is not homogeneous, the ET_a is the spatially average over the footprint, and in combination with varying wind speed and direction this footprint might change and thus sample different areas. This footprint heterogeneity might result in lower correlations between EC sites. On the other hand, although a lysimeter has a limited surface area, it can be regarded as a large area with a homogeneous land surface, not affected by random errors due to atmospheric instabilities caused by wind gusts (Widmoser & Michel, 2021), resulting in ET_a behaving in a similar way under similar meteorological conditions and similar vegetation. In our study, the EC towers typically only sample one land use. The RO site is almost exclusively constrained to the grassland (Gebler et al., 2015). The EC tower at the WU site is centered in the forest and the footprint reaches approximately 500 m downwind (Rabbel, 2018). For the SE site, 80% of footprint climatology is within the agricultural field (Paulus et al., 2024). The flux footprint of the GW site was primarily dominated by short grass within a radius of approximately 200 meters around the EC tower (Hirschi et al., 2017). For

example, the RO and GW sites are the two sites most comparable in our study. The lysimeters have the same soil, vegetation and management as the EC field (Gebler et al., 2015; Widmoser & Michel, 2021). As a result, the correlation of $SA_{ET\text{-}LYS}$ between RO and GW is equal to the correlation of $SA_{ET\text{-}EC}$. Very weak correlations were found in winter and higher correlation in summer. This may be related to differences in the signal to noise ratio for ET_a for the different seasons, which can also be inferred from the randomly changed phase angles in winter, relatively to summer (Figure 3.5). Variability was also found across years, with less coherence in 2018, which is marked as drought year (Graf et al., 2020).

3.4.2 Implications for lysimeter networks

Given the similar spatial correlations for ET-LYS and ET-EC, we argue that the information content of lysimeter ET_a measurements is not limited by their small area. Thus, lysimeters can potentially be used to upscale measured ET_a after proper consideration of hydrological regime, land cover and other factors. This has also implications for the design of lysimeter networks. Lysimeters can estimate ET_a more precisely than EC (smaller systematic and random measurement errors, especially at nighttime the EC method is more affected by measurement problems), with a similar spatial representativity and the ability to also provide precise measurements for the other water balance components (rainfall, non-rainfall, percolation, capillary rise), but at a higher (maintenance) cost. Therefore, there is a need for a larger lysimeter network, in part collocated with the EC network, especially also in semi-arid and arid climates.

Wavelet coherence analysis is a localized spectral analysis, and thus inherent all features of spectral coherence analysis, such as revealing valuable information about the lag in ET_a signals between the sites. Additionally, wavelet analysis provides the global wavelet coherence, which is identical to spectral coherence if the two time series are stationary. These localized wavelet coherence and global wavelet coherence is particularly useful when estimating ET_a at one site based on data from neighbouring sites. Accurate prediction of ET_a requires not just an understanding of the correlation between sites, but also about the lag time between their responses. To improve these predictions, further analysis of the correlations between other driving factors, such as weather conditions and soil moisture, across sites is necessary. For example, if we want to estimate ET_a at one site but only have data from another site, understanding both the correlation and the lag time of key drivers between the two sites allows

us to predict the ET_a. This could significantly reduce the need for ET_a measurement equipment, enabling ET_a estimation at a broader scale even with a limited lysimeter or EC network.

Furthermore, examining coherence on a seasonal scale provides insight into the reliability of using lysimeter data to represent ET_a at larger spatial scales. For instance, if strong coherence is observed in the summer, we can confidently use lysimeter data to estimate ET_a over a wider area during that season. However, during winter, when coherence might be lower, more caution is needed in extending site-specific ET_a data to larger scales. This seasonal variability highlights the importance of understanding temporal coherence patterns to improve both local and regional ET_a predictions.

Due to the scarcity of parallel measurements by lysimeters and EC towers, our study sites are not abundant, particularly the lack of water-limited sites, and the land cover of EC sites and the vegetation on lysimeters are not fully compatible in this study. In addition, the study period is still not long enough, thus we do not get full insight into the correlations under different meteorological conditions. Except for these limitations, our work provides important insights to explore the potential of the in-situ ET_a lysimeter measurements.

3.5 Conclusions

This study investigates the information content of actual evapotranspiration (ET_a) measurements by lysimeters analyzing correlations of standardized anomalies of measured ET_a between four different measurement sites: Wüstebach, Rollesbroich, Selhausen and Graswang, all located in Germany. Wüstebach, Rollesbroich and Selhausen are located in North-Rhine-Westphalia, Germany with separation distances between 0 and 50km, whereas Graswang is further separated from all other sites (500km). For the same sites also the correlations of standardized anomalies of ET_a measured by the eddy covariance method are calculated. Standardized anomalies of ET_a measured by lysimeters showed at the plot scale (~10 m) very high correlations (>0.91), and at the landscape scale (distances ~50km) moderate correlations (0.3~0.7). Those correlations are not much smaller than for EC and suggest that the small lysimeter footprint gives information on ET_a comparable to EC measurements, which have a much larger footprint. In order to analyze correlations also at different spatiotemporal scales a wavelet transform coherence WTC analysis for lysimeters and EC was performed. The strongest coherence is in general found for the yearly cycle and temporal scales <3 months.

Correlations are higher in the summer half year than in winter, with variations between years and lower correlations under drought conditions (2018). High multiple wavelet coherence revealed that ET_a can be predicted for a certain point with high accuracy with help of values from multiple lysimeters located in the neighborhood of the point (separation distances 10 - 50 km). This study did not analyze in depth the drivers of the representativeness of lysimeter measurements, and how, for example, drought conditions could reduce the representativeness related to increased spatial heterogeneity of ET_a under such conditions. This will be subject of future work.

Chapter 4. Variability and robustness of critical soil moisture: Insights from lysimeter data in Germany

*adapted from: Lu, X., Groh, J., Graf, A., Pütz, T., Gerke, H. H., Javaux, M., Gründling, R., Rupp, H., Kiese, R., Hans, J., Vereecken, H., & Franssen, H. H. (2026). Robustness of critical soil moisture to curve-fitting methods and its variability with soil depth , soil texture , and climatic conditions : insights from lysimeter data in Germany. 668(November 2025). https://doi.org/10.1016/j.jhydrol.2026.134959

4.1 Introduction

Actual evapotranspiration (ET_a), as an essential component of the water, energy and carbon cycle, serves as a vital link between the land surface hydrological processes and atmospheric processes (Wang & Dickinson, 2012; Fisher et al., 2017; Corami et al., 2024). Two distinct ET_a regimes have earlier been recognized: a water-limited and an energy-limited regime (Budyko, 1974). The transition between the two regimes is associated with the soil moisture (θ) and occurs at or around a threshold value, denoted as critical soil moisture threshold (θ_{crit}; Seneviratne et al., 2010). When θ dries below θ_{crit}, ET_a falls into the water-limited regime, where plants experience water stress and ET_a is controlled by water availability. The reduction in θ causes plants to constrict the stomatal apertures to impede large leaf water potential drop and water losses, which decreases ET_a, thereby reducing evaporative cooling and increasing sensible heat flux from the land to the lower atmosphere (Koster et al., 2009; Humphrey et al., 2021). When θ is above θ_{crit}, in contrast, ET_a is mainly governed by energy supply; consequently, increased θ does not necessarily increase ET_a. In this energy-limited regime, stomatal aperture is no longer a constraint and thus ET_a reaches or approximates an upper limit bounded by atmospheric evaporative demand, commonly referred to as potential ET (PET; Xiang et al., 2020). Switching between the two regimes can potentially influence hydroclimatic extremes (e.g., floods, droughts, and heatwaves) by dampening or amplifying the land-atmosphere interactions (Berg et al., 2016; Zhang et al., 2020; Lo et al., 2021). Yet, a recent review revealed that the dependency of ET_a to θ is still badly represented in current land surface models (Green et al., 2024). Therefore, knowledge of θ_{crit} is crucial for better understanding the impacts of extreme weather events and improving land surface, hydrological and crop models to predict future climate and crop yields.

However, the quantification of θ_{crit} remains uncertain due to the lack of precise measurements on ET_a and θ. Based on the conceptual framework established by Budyko (1974) and Seneviratne et al. (2010), the most widespread determination of θ_{crit} is through the relationship between θ and a variable derived from ET_a (Figure 4.1), such as evaporative fraction (EF; the ratio of latent heat flux to the available energy) representing the energy partitioning (Ford et al., 2014a), or evaporation factor (the ratio of ET_a to PET; hereafter rPET) describing the degree of water stress (Yao, 1974; Eagleson, 1978). Such a relationship is a function of soil and plant hydraulic, and stomatal control (Wankmüller et al., 2024). Moreover, θ_{crit} is a variable rather than a constant property as it is also a function of ET_a. Past efforts to evaluate θ_{crit} dominantly rely on model- and reanalysis-based data (Schwingshackl et al., 2017; Hsu & Dirmeyer, 2023a, 2023b; Paul et al., 2025), remote sensing and satellite-based data (Feldman et al., 2019; Denissen et al., 2020; Dong et al., 2023; Koster et al., 2024), eddy covariance (EC) tower and in situ soil moisture sensors (Haghighi et al., 2018; Dong et al., 2022; Fu et al., 2022), or a combination of these sources (Buitink et al., 2020; Z. Fu et al., 2024; Y. Liu et al., 2024). However, the model representation of the coupling between θ and ET_a is highly uncertain (Dirmeyer et al., 2000), and the results regarding ET_a sensitivity to θ depend strongly on the implemented assumption in the model concerning the relationship between θ and ET_a (Schwingshackl et al., 2017). On the other hand, remote sensing data, though promising, suffer from algorithmic uncertainties in ET_a estimates (Sörensson & Ruscica, 2018). Additionally, some products have pre-defined θ and evaporation relationships (Martens et al., 2017), potentially biasing the θ_{crit}. Therefore, a purely ground-based observation analysis would have certain advantages. However, while EC towers provide in-situ observations, they often do not close the energy balance and have changing footprint sizes and shapes (Franssen et al., 2010; Kauwe et al., 2017). On top of that, the horizontal footprints of flux data vary from 100 meters to few kilometers in radius around the towers (Chu et al., 2021; Zhu et al., 2023), whereas *in situ* soil moisture sensors provide only point-scale measurements (Brown et al., 2023). The spatial variability of θ is influenced by heterogeneities in soil properties, vegetation, and topography within the flux footprint, which can pose a potential scale mismatch, leading to biases in θ_{crit} assessments (Iwema et al., 2017).

The next major challenge in understanding θ_{crit} lies in the impact of measurement depth on its estimation. Most previous studies focused primarily on surface θ (e.g., at a sampling depth of less than 5 cm for remote sensing, Escorihuela et al., 2010; Akbar et al., 2018; Feldman et al.,

2019; Denissen et al., 2020; Fu et al., 2024) or root zone θ estimated from shallow surface SM due to the lack of deeper SM measurements (Koster et al., 2024). Few studies have explicitly compared θ_{crit} derived from both surface and root zone θ. However, plants can access water stored deeply in the soil to sustain transpiration (Oliveira et al., 2005; Thompson et al., 2011). Although some studies argued that surface θ and root zone θ are closely correlated (Ford et al., 2014b), thereby implying similar surface energy balance characteristics (Qiu et al., 2016, 2020; Dong et al., 2022; Paul et al., 2025), some studies presented contrasting conclusions. For example, Mahmood & Hubbard (2007) found the correlation and cross-correlation between surface θ and subsurface θ declines rapidly with increasing depth under various land use types, suggesting estimating root zone θ based on surface θ is problematic. Likewise, Hirschi et al. (2014) pointed out that the temporal dynamics of surface SM and root zone SM decouple gradually during extreme hot conditions. Recently, Buitink et al. (2020) reported a lower θ_{crit} value for surface soil compared to root zone soil. Hence, it remains questionable whether the θ_{crit} of the surface θ is consistent with that of the root zone θ.

Alternatively, weighable lysimeters are regarded as the best method to measure in situ ET_a (Schrader et al., 2013; Gebler et al., 2015; Lu et al., 2024), which are capable of measuring the complete water balance, avoiding the underestimation of ET_a due to the energy imbalance issue present in the EC approach. Many studies regarded lysimeter-based ET_a as a reference to address the energy balance closure problem and correct EC-based ET_a (Gebler et al., 2015; Hirschi et al., 2017; Widmoser & Wohlfahrt, 2018; Mauder et al., 2021). With soil moisture sensors installed at several depths in the profile within the lysimeter, data pairs of θ and ET_a can be accurately obtained, providing a unique insight into the surface and root zone SM controls on ET_a. The German TERrestrial ENvironmental Observatories (TERENO) SOILCan network is such a lysimeter network, equipped with high-precision and high-resolution weighable lysimeters (Pütz et al., 2016; Kiese et al., 2018; Zacharias et al., 2024), offering the possibility to investigate surface and root zone θ_{crit} using precise lysimeter measurements.

As θ_{crit} is estimated from a fitting procedure based on a conceptual framework (Figure 4.1), its uncertainty can also arise from the definitions of relative ET_a (the y axis variable). As mentioned above, both EF and rPET can be used to estimate θ_{crit} using a linear-plus-plateau fit due to their same idealized structure curve as depicted in Figure 4.1. However, to our knowledge, no previous studies have examined what the impact of the definitions of relative ET_a (EF versus rPET) is on estimating θ_{crit}, as existing studies have typically focused on only

one definition of relative ET_a. Although the relationship between rPET and SM has been studied long ago (e.g., Manabe, 1969; Yao, 1974), recent studies tend to use the EF curve to determine θ_{crit} (e.g., Feldman et al., 2019; Fu et al., 2024), as EF is easier to estimate. An appropriate calculation of PET requires a series of assumptions (Koster, Schubert, et al., 2009). Therefore, alternative formulations such as grass reference ET (ET_0) and FAO-56 (The Food and Agricultural Organization (FAO) of the United Nations) based PET (PET_{FAO}) have been proposed (Allen et al., 1998). Accordingly, the ratio of ET_a to ET_0 (rET_0) and the ratio of ET_a to PET_{FAO} ($rPET_{FAO}$) can serve as alternatives to rPET (Peng et al., 2019; Qiu et al., 2020). The diversity in literature using EF, rET_0 or $rPET_{FAO}$ motivated us to analyze the impact of the chosen fitting relationship (i.e., EF-SM, rET_0-SM and $rPET_{FAO}$-SM) on estimated θ_{crit}. Additionally, linear-plus-plateau fitting curvesss likely simplify the relationship between SM and ET_a. In reality, this relationship might have a steep slope at the dry end and a more gentle slope at the wet end (Koster et al., 2024). Such consideration led us to extend the existing analyses of θ_{crit} by other functions. We aimed to investigate the sensitivity of θ_{crit} to these various fitting curves.

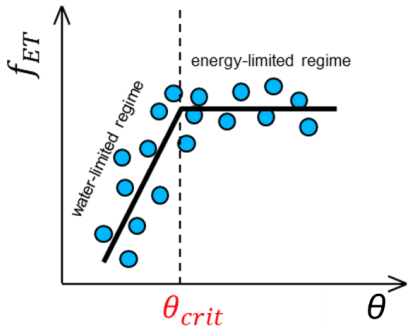


Figure 4.1 Schematic plot showing the assessment of f_{ET}- θ relationship, where f_{ET} represents either EF, rET_0 or $rPET_{FAO}$. θ can be soil moisture from soil surface (θ_s) or from the root zone (θ_v). Blue dots represent the data points during dry downs over the growing periods. The thick black line denotes the linear-plus-plateau fitting.

θ_{crit} mainly depends on soil properties and is impacted by vegetation and climate (Wankmüller et al., 2024). As the TERENO lysimeter networks span from the Northeast German lowlands to the Bavarian Alps, it enables the investigation of θ_{crit} across various soil textures, vegetation types and climatic conditions. More importantly, TERENO has implemented an observational

approach based on a modified "space-for-time" concept to capture the impacts of changing climatic conditions on the soil-plant system (Pütz et al., 2016; Groh et al., 2022). The intact soil monoliths were transferred between stations and thus exposed to different climatic regimes, which means that soils are transferred in space rather than waiting at the same location for changes in climate over time (Groh et al., 2020a). Such a crossed soil type and climate experimental setup allows for isolating the climate alone and investigating the influence of changing climatic conditions on θ_{crit}. In our study, we specifically analyzed the impact of a change in aridity index (AI) defined as the ratio of mean annual ET_0 and precipitation.

Furthermore, according to FAO-56 guidelines, θ_{crit} (θ_{crit_FAO56}) is approximated as the midpoint between field capacity (FC) and wilting point (WP), which represents the readily available water that a crop can extract from the root zone without suffering from water stress (Allen et al., 1998). As FAO-56 estimates are often used in practice, for example for irrigation scheduling, it is important to evaluate the validity of this approach using θ_{crit} values derived from lysimeter measurements.

In summary, in this study, we explore, to our knowledge for the first time, the possibility of quantifying θ_{crit} using lysimeter measurements, which enables us to examine θ_{crit} by considering root zone SM rather than only near surface SM. This is the major novelty of this work. Additionally, we evaluate the robustness of θ_{crit} by applying different curve-fitting methods and examining the impact of climatic conditions. We seek to provide a thorough and detailed analysis of lysimeter-specific θ_{crit}, with the aim of answering the following main questions: (1) Does using the rET_0 definition and $rPET_{FAO}$ definition result in comparable θ_{crit} as using the EF definition? (2) Does θ_{crit} vary when using different fitting functions? (3) How does θ_{crit} derived from surface SM differ from θ_{crit} derived from root zone θ? (4) Does θ_{crit} change for the same ecosystem under different climatic conditions?

4.2 Materials and Methods

In situ observations at lysimeter sites were used to determine the critical soil moisture thresholds (θ_{crit}), which marks the transition between the two distinguished regimes (a water-limited regime and an energy-limited regime). The analysis was performed on daytime observations over the growing seasons for each lysimeter. Daytime was defined as 9 a.m. to 5

p.m. at each site, based on the median diurnal cycle of net radiation. The growing season was defined as April to September for grass and mid-season stages for crops.

The flow chart of this study is shown in Figure 4.2. In this section, the framework we first introduced (section 4.2.1) including the detection of soil drydowns during which the transition is most likely to happen, and the estimation of θ_{crit}. Section 4.2.2 gives an overview of lysimeter sites, followed by a description of the datasets used (section 4.2.3). Next, section 4.2.4 and section 4.2.5 present the computation of EF, rET_0 and $rPET_{FAO}$, respectively. The alternative fitting function is described in section 4.2.6. Finally, section 4.2.7 introduces root zone θ_{crit} according FAO-56.

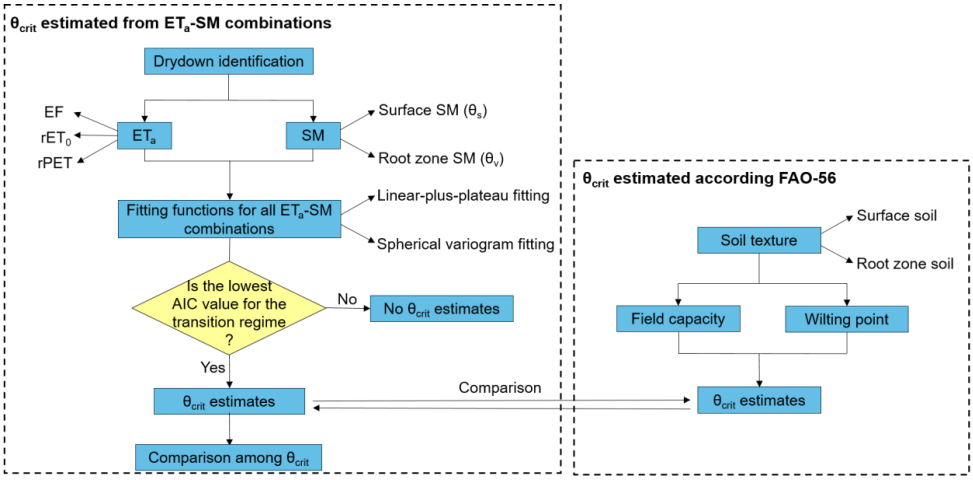


Figure 4.2 Flow chart showing the estimation of critical soil moisture (θ_{crit}).

4.2.1 A framework for estimating critical soil moisture thresholds

4.2.1.1 Drydown identification

The transition between energy-limited and water-limited regimes is most likely to occur during soil drydowns, i.e., periods when soil moisture (θ) tends to show continuous incremental decrease in the absence of precipitation. Similar to McColl et al. (2017) and Akbar et al. (2018), the drydown selection process was automated on a daytime basis according to the following logic:

1) The drydown must begin after a precipitation event stops. This means that precipitation should be zero on the first day of the drydown period.

2) During a drydown event, precipitation should not exceed 1 mm/day.

3) During a drydown event, the θ increments should be negative. However, noise can exist in observations. To avoid truncating a real drydown due to a single positive θ increment in a series of negative increments, positive θ increments less than 1% of the range of observed θ are excluded from the drydown event in order not to generate multiple drydown events. For example, in Figure 4.3 the blue dots in the orange shadows refer to the θ which have positive increments and were excluded from the real drydown event.

4) The drydown must last for at least 5 days. This minimum length was chosen as a compromise between ensuring a large sample size and focusing on drydown events of relevant impact. The results did not reveal a strong difference when compared with a 9-day period suggested in previous studies (Akbar, Gianotti, et al., 2018; Z. Fu et al., 2024; McColl et al., 2017; Shellito et al., 2018).

The drydown selection process was performed separately for surface θ (θ_s) and root zone θ (θ_v). An illustrative example of θ time series is shown in Figure 4.3 to highlight the drydowns identified by the above procedure based on observations from one lysimeter.

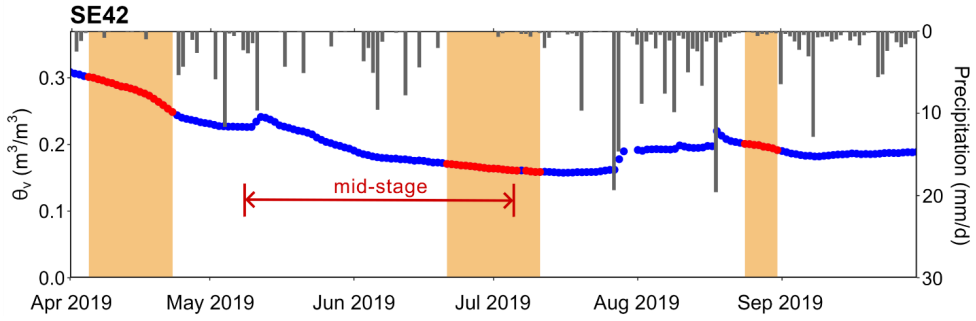


Figure 4.3 Example time series of vertically integrated (0-60 cm) soil moisture (θ_v) for one lysimeter (SE42) of the SEsb lysimeter group at the SE site for April-September 2019. Drydowns are highlighted in orange. θ_v during the drydown events are marked as red. Blue dots represent θ_v which are outside or excluded from the drydown events. Bars represent the daily precipitation.

4.2.1.2 Estimation of critical soil moisture thresholds

Figure 4.1 presents the framework of estimating θ_{crit}. The f_{ET}-θ relationship was built by using all the data pairs during drydowns over the growing seasons for each lysimeter and then fitted by a linear-plus-plateau model:

$$f_{ET} = \begin{cases} f_{max} + S(\theta - \theta_{crit}) & \text{if } \theta < \theta_{crit} \\ f_{max} & \text{if } \theta \geq \theta_{crit} \end{cases} \quad (4.1)$$

where f_{ET} represents either EF, rET_0 or $rPET_{FAO}$. θ can be either θ_s or θ_v. f_{max} is the maximum value of f_{ET} in the energy-limited stage where θ is abundant and no longer the limiting factor for ET. In the "water world", ideally, the highest ceiling of rPET must be 1, which indicates that the plants don't suffer from water stress. However, such limitation was not imposed on the maximum value of rET_0 and $rPET_{FAO,}$ since ET_0 and PET_{FAO} are not necessarily the exact value of PET. S denotes the slope of the linear increase phase, indicating the sensitivity of f_{ET} to SM and thus the impact of θ on atmospheric conditions in the water-limited regime (Schwingshackl et al., 2017; Fu et al., 2022). θ_{crit} was estimated by a global optimization that minimizes the sum of squared errors, leading to lysimeter-specific estimated values. The optimization was performed with the "minpack.lm" package in the R programming language (Elzhov et al., 2015).

Previous studies considered two other linear models, one assuming that ET_a is purely water-limited, and one assuming a purely energy-limited regime (Feldman et al., 2019; Fu et al., 2024; Hsu & Dirmeyer, 2023a). Since all sites are located in Germany where water-limited conditions are rare, the purely water-limited model is not good as a null hypothesis. Therefore, the linear-plus-plateau model was only compared with the linear model for the purely energy-limited regime. The Akaike's Information Criteria (AIC) metric (Akaike, 1974) was used to determine the optimal model with the lowest AIC value. θ_{crit} is identified only when the linear-plus-plateau model is selected.

4.2.2 Site description and lysimeter set-up

A total of 61 lysimeters from seven sites of the TERENO-SOILCan network in Germany (Figure 4.4 and Table 4.1), were selected for this study. The distances between lysimeters vary from 0 to 680 km. The aridity index (AI, mean annual ET_0 divided by mean annual precipitation) varied on average between these sites from 0.46 to 2.19, reflecting a range of climatic conditions from humid, sub-humid to semi-arid (Table 4.1). The soil texture of the surface soil and root zone soil varied and included clay, clay loam, sandy clay loam, sandy loam, silt loam

and loam (Table 4.1). The dominant land cover for the lysimeters consists of grassland (natural and managed) and arable land (crop rotation). The grassland lysimeters are mainly composed of grasses, herbs or forest meadow. Detailed information on crop types, including planting and harvest dates for the arable land, is provided in Table B.4 Table B.6.

At each site, there is at least one standardized hexagonal array of six individual cylindrical weighable lysimeters (UMS GmbH, Munich, Germany), each with a surface area of 1.0 m^2 and a depth of 1.5 m. The high-precision (resolution of 10 g, corresponding to a water depth ~0.01 mm) and high-resolution (1-minute measurements) lysimeters at the same site are situated only a few meters apart (approximately 3 - 6 m). Further technical specifications of the lysimeter used in this study are given in Pütz et al. (2016).

Based on the "space-for-time" concept, some local excavated lysimeters were transferred from their original sites to different climate regimes within and across TERENO observatories (Pütz et al., 2016). The spatial transfer of the intact soil monoliths in these lysimeters was intended to mimic changes in climatic conditions, characterized by an increased AI. This change in climatic conditions was abrupt due to the transfer of the soil monoliths in space, which differs from the standard "space-for-time" substitution approach in ecological or hydrological studies (e.g., Blois et al., 2013; Troch et al., 2015), that suggests gradual ecosystem changes over time. Instead, θ_{crit} for the same soil under different climatic conditions were compared. In this study, the lysimeters from the sites Rollesbroich (RO), Wüstebach (WU), Sauerbach (SB) and Graswang (GW) always contain the local soil, whereas for the sites Selhausen (SE), Dedelow (DD) and Bad Lauchstädt (BL), one lysimeter group contains the local soil, and other groups contain the soil from other sites (Table 4.1, Figure 4.1). It should be noted that the soil monoliths transferred to the site DD (i.e., DDhd, DDck, DDcs, DDgk, DDgs, DDhk, DDhs, see Table 4.1) investigate the impact of past erosion processes on the soil ecosystem (Groh et al., 2020b), rather than the change in climatic conditions.

The climatic conditions at the transferred site and the original site are different in terms of AI including mean annual air temperature, ET_0 and precipitation. The original sites represent a long-term climate scenario to which the soil was exposed prior to translocation, whereas after the translocation, the soil was subject to the specific meteorological conditions of the transferred sites. Therefore,

Table **4.2** summarizes the differences between the long-term climatological averages at the original site and the mean climate conditions observed during the study period at the transferred site. The AI differences ranged from 0.17 to 1.05. Additionally, the absolute differences ranged from 186 to 426 mm y^{-1} for annual ET_0, 96 to 591 mm y^{-1} for mean annual precipitation and 1.8 to 4.4 °C for mean annual air temperature.

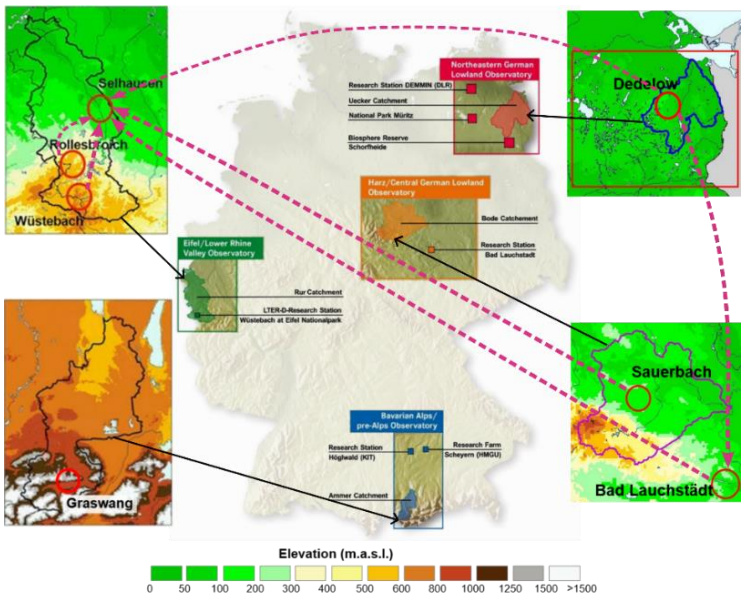


Figure 4.4 Locations of the four TERENO observatories in Germany. The red circles marked in each observatory indicate the location of the lysimeter stations used in this study (adapted from Pütz et al. 2016). The pink dashed arrow line indicated the transfer routes of the soil monoliths.

Table 4.1 Specifications of the lysimeters used in this study. For the lysimeter group, the first two letters represent the location of the lysimeters and the last two letters represent the soil origin. For the lysimeter ID, the first two letters indicate the site where the lysimeter is located, the first number indicates the lysimeter hexagon and the second number indicates the lysimeter of the hexagon. Sand fraction for soil depth 0-60cm was weighted according the soil sample depths. Aridity index was calculated by mean annual grass reference ET divided by mean

annual precipitation. There are four classifications according the aridity index: humid (Aridity index ⩽ 1.3), sub-humid (1.3 < Aridity index ⩽ 1.5), semi-arid (1.5 < Aridity index ⩽ 5), and arid (5 < Aridity index < 20).

Site	Soil origin	Lysimeter group	Lysimeter number	Lysimeter ID	Land cover type	Aridity index	Soil depth 0-10cm		Soil depth 0-60 cm	
							Sand (%)	Texture class (USDA)	Sand (%)	Texture class (USDA)
Wüstebach (WU)	WU	WUwu	6	WU11-WU16	Grassland	0.46	39	Clay loam	46	Loam
Graswang (GW)	GW	GWgw	1	GW13	Grassland	0.62	9	Clay	8	Clay
Rollesbroich (RO)	RO	ROro	6	RO11-RO16	Grassland	0.78	52	Sandy clay loam	48	Sandy clay loam
Selhausen (SE)	French Technosol	SEfr	3	SE11,15,16	Grassland	1.43	71	Sandy loam	71	Sandy loam
	Scheyern	SEsy	3	SE12,13,14	Grassland		59±3	Sany loam	58±4	Sandy loam
	RO	SEro	3	SE21,25,26	Grassland		52	Sandy clay loam	48	Sandy clay loam
	WU	SEwu	3	SE22,23,24	Grassland		39	Clay loam	46	Loam
	BL	SEbl	3	SE31,35,36	Arable land		5	Silt loam	4	Silt loam
	SE	SEse	3	SE32,33,34	Arable land		13	Silt loam	11	Silt loam
	DD	SEdd	3	SE41,45,46	Arable land		56±5	Sandy loam	54±3	Sandy loam
	SB	SEsb	3	SE42,43,44	Arable land		13	Silt Loam	15	Silt loam
Dedelow (DD)	DD	DDdd	3	DD11,13,15	Arable land	1.7	49±4	loam	50±3	Loam
	Holzendorf	DDhd	3	DD12,14,16	Arable land		57±6	Sandy loam	59	Sandy loam
	Christianenhof (exposed hilltops)	DDck	1	DD21	Arable land		55	Sandy loam	56	Sandy loam
	Christianenhof (topographic depressions)	DDcs	1	DD22	Arable land		65	Sandy loam	63	Sandy loam
	Grünow (exposed hilltops)	DDgk	1	DD23	Arable land		55	Sandy loam	54	Sandy loam
	Grünow (topographic depressions)	DDgs	1	DD24	arable land		62	Sandy loam	58	Sandy loam
	Holzendorf (exposed hilltops)	DDhk	1	DD25	arable land		61	Sandy loam	59	Sandy loam
	Holzendorf (topographic depressions)	DDhs	1	DD26	arable land		70	Sandy loam	63	Sandy loam
Sauerbach (SB)	SB	SBsb	6	SB11-SB16	Arable land	2.07	13	Silt loam	15	Silt loam
	DD	BLdd	3	BL21,23,25	Arable land	2.19	54±3	Sandy loam	52±2	Loam

Bad-Lauchstädt (BL)	BL	BLbl	3	BL22,24,26	Arable land	5	Silt loam	4	Silt loam

Table 4.2 Differences in mean annual grass reference ET (ET_0), mean annual precipitation (P), mean annual air temperature (T_a) and aridity index (AI, defined as the ratio of ET_0 to P) between the translocated and original sites.

Site abbreviations: BL - Bad Lauchstädt; DD – Dedelow; RO – Rollesbroich; SB – Sauerbach; SE – Selhausen; WU – Wüstebach.

Translocated site	Original site	ΔAI	ΔET_0 (mm y^{-1})	ΔP (mm y^{-1})	ΔT_a (°C)
SE	DD[#]	0.17	227	96	2.5
SE	BL[#]	0.18	253	115	1.8
SE	SB[#]	0.19	240	98	1.9
SE	RO[*]	0.81	254	-388	3.7
BL	DD[#]	0.93	186	-137	2.0
SE	WU[*]	1.05	426	-591	4.4

[#] Long-term means at the original sites (DD, BL and SB) were reported by Groh et al. (2016) for the period 1981-2010.

[*]For the RO and WU sites, long-term means were calculated over 1991-2010. Firstly, annual ET_0 was obtained from the grid maps from the German Weather Service (DWD, https://www.dwd.de), while annual P and T_a were derived from a nearby weather station (Kall-Sistig) from DWD. Secondly, the annual ET_0, P and T_a were adjusted using linear regression with in-situ observations at the study sites based on overlapping years to correct for site-specific values. Finally, the mean annual values for the period 1991–2010 are as follows: at the RO site, ET_0 was 633 mm y^{-1}, P 1006 mm y^{-1}, and T_a 7.70 °C; at the WU site, ET_0 was 460 mm y^{-1}, P 1209 mm y^{-1}, and T_a 7.04 °C.

4.2.3 Data

4.2.3.1 Lysimeter ET_a

Lysimeter raw data were recorded at 1-minute intervals. Firstly, the raw lysimeter data underwent a manual and automatic plausibility check (Schneider et al., 2021). Secondly, the adaptive window and threshold filter was applied (AWAT; Peters et al., 2014, 2017) to reduce the impact of noisy lysimeter mass changes on the determination of precipitation and ET_a. In

the next step, the ET_a data of the lysimeters were aggregated to hourly values. In this study, missing hourly ET_a values were partly gap-filled using linear regression with parallel ET_a values from other available lysimeters (same site and same soil). If parallel ET_a values are missing at that point in time, then ET_a at that point in time is not available and missing. Only days where ET_a was available for all daytime hours were considered in the analysis.

4.2.3.2 Soil moisture

θ was measured by the sensors (CS610 connected to a TDR100, both Campbell Scientific, North Logan, UT, USA) inside the lysimeters at 10-, 30- and 50-cm depths with a temporal resolution of 30 min (Groh et al., 2019). θ was averaged to daytime values (9 a.m. to 5 p.m.). Observations at 10 cm depth were regarded as θ_s. The 0-60 cm vertically integrated θ was considered as θ_v as most of the roots of the lysimeter plants are expected in the top 60 cm of the soil column. The θ measurements at 10, 30 and 50 cm depth were assumed to represent the soil column between 0-20, 20-40 and 40-60 cm depth respectively and were equally weighted to determine θ_v.

4.2.3.3 Meteorological data

Meteorological data including air temperature, air humidity, wind speed, air pressure and global radiation were obtained at each site from the lysimeter weather station (WXT510, Vaisala Oyj, Helsinki, Finland) for 10-min time steps. Precipitation was measured at RO, WU, and SE by a weighable gauge (Pluvio², Ott Hydromet, Kempten, Germany), and at GW, DD, SB and BL by a tipping bucket gauge (GW: WXT520, Vaisala; DD and SB: ecoTech Umwelt-Meßsysteme GmbH, Bonn, Germany; and BL: LAMBRECHT meteo, Göttingen, Germany). Precipitation was summed to daily values and other variables were averaged to hourly data prior to further computation. For those sites which have nearby stations available from the TERENO-portal http://teodoor.icg.kfa-juelich.de/ibg3searchportal2/index.jsp, the time-series were gap-filled using the data from the online database with a stepwise gap-filling procedure (Giraud et al., 2021). Firstly, a linear regression was conducted with each station for each variable. Subsequently, the regression with the lowest root mean square error (RMSE) was used to fill the gaps until all the stations were used. As a result, gaps in the hourly meteorological data were filled for all sites, except the BL site, which only had a few gaps for two days.

A net radiation sensor (LP Net07, Delta OHM S.r.L., Caselle di Sevazzano, Italy) was installed above one lysimeter in each lysimeter group at each lysimeter site. Net radiation (Rn) was

measured at a 10 min temporal resolution and aggregated to hourly data. The missing hourly R_n were gap-filled using the similar stepwise linear regression procedure as described above, but using R_n measurements from different lysimeter groups at the same site or from the corresponding eddy covariance (EC) station nearby.

4.2.3.4 Surface soil heat flux

Directly measuring surface soil heat flux (G_0) is challenging because soil heat flux plates have to be buried at a subsurface depth in the soil to avoid potential effects of soil-atmosphere processes (Gao et al., 2017). In this study, one soil heat flux plate (HFP-01, Hukseflux Thermal Sensors B.V., Delft, the Netherlands) was installed at 10 cm depth inside each lysimeter to measure the soil heat flux (G_{10}). The calorimetric method was applied to calculate G_0 according to the following equations (Ding et al., 2010; Giambelluca et al., 2009; Li et al., 2022):

$$G_0 = G_z + \Delta S \tag{4.2}$$

$$\Delta S = \frac{T_{s,i} - T_{s,i-1}}{t} z(C_{vs} + C_{vw}\theta) \tag{4.3}$$

where G_z is the soil heat flux measured at a depth of z m (W m^{-2}; here G_z is G_{10} with z equal to 0.1 m), ΔS is the heat storage between the soil surface and the heat flux plate (W m^{-2}), t is the time interval (3600s), C_{vw} is the volumetric heat capacity of water (4190 KJ m^{-3} K^{-1}), and C_{vs} is the volumetric heat capacity for the soil solid portion with a value of 1420 KJ m^{-3} K^{-1}. $T_{s,i} - T_{s,i-1}$ (K) is the soil temperature (T_s) difference between time steps i and i-1 for the soil layer above the soil heat flux plate, θ is the volumetric soil moisture content in the soil layer above the soil heat flux plate (m^3 m^{-3}).

Note that there are no sensors measuring T_s and θ in the layers between soil surface and soil heat flux plates in the lysimeters — the shallowest only at the same depth (10 cm) as the flux plates. Therefore, T_s and θ at 10 cm were utilized for the calculation for each lysimeter, except for the lysimeters at the SE site, where T_s sensors were not functioning during the study period. Thus, for the SE site, the average T_s measurements were used from three sensors at 5 cm depth from the lysimeter field which is covered by grass. Prior to the computation of G_0, G_{10}, T_s and θ were gap-filled with parallel measurements (same soil and same site) following the stepwise gap-filling procedure.

It is acknowledged that the determination of G_0 may not be highly accurate. However, a sensitivity analysis on G_0 estimation was conducted using different input data sets and

parameters and the calculated G and the measured G at 3 cm depth (G_{03}) at the RO site were compared (Supplementary Material 1). The results show that the different approaches have a similar performance and small differences between calculated G_{03} and measured G_{03}, providing confidence in the above calculation. In addition, since G_0 is a relatively small flux compared to LE and R_n during daytime, possible bias in G_0 does not have a large impact on the EF results and therefore does not affect θ_{crit}.

4.2.4 Energy world (Evaporative fraction)

EF is a non-dimensional variable that characterizes the land surface partitioning of available energy for exchange with the overlying atmosphere. EF was calculated on the same daytime basis in this analysis:

$$\mathrm{EF} = \frac{\mathrm{LE}}{\mathrm{LE+H}} \tag{4.4}$$

where LE and H are daytime mean latent and sensible heat fluxes (W m^{-2}). H was treated as the residual of the energy balance. It can be estimated as:

$$\mathrm{H} = \mathrm{R_n} - \mathrm{G_0} - \mathrm{LE} \tag{4.5}$$

H was calculated on an hourly basis in Eq. 4.5 and then aggregated to daytime values before calculating EF in Eq. 4.2. If there are missing values for LE or H during daytime, the day is excluded from the analysis. As EF shows large uncertainty, the EF was also restricted to the range of 0-1 to remove outliers, as in previous studies (Schwingshackl et al., 2017; Dong et al., 2023).

4.2.5 Water world (Ratio of actual to potential ET)

4.2.5.1 Reference ET

The ET_0 calculation is needed for both the rET_0 and $rPET_{FAO}$ methods. Hourly ET_0 was calculated with the FAO Penman-Monteith equation (Allen et al., 2006):

$$ET_0 = \frac{0.408\Delta(R_n - G_0) + \gamma\frac{37}{T_h+273}u_2(e^o(T_h) - e_a)}{\Delta + \gamma(1 + C_d u_2)} \tag{4.6}$$

where Δ is the slope of the vapor pressure curve (kPa $^oC^{-1}$), T_h is mean hourly air temperature at 2 m height (^{o}C), $e^o(T_h)$ is hourly saturation vapor pressure (kPa), e_a is hourly actual vapor pressure (kPa), γ is psychrometric constant (kPa $^oC^{-1}$), C_d is a coefficient with a value of 0.24

s m^{-1} when $R_n > 0$ and 0.96 s m^{-1} when $R_n < 0$, and u_2 is wind speed at 2 m height (m s^{-1}), and G_0 is estimated based on Equation 4.2.

4.2.5.2 Determination of mid-season stage for crops

For crops, only the mid-season stages were considered in the analysis. This is because at mid-season stages, most of the soil surface on the lysimeters is covered by the crop (crop coefficient is maximum) and water loss is mainly due to crop transpiration. Therefore, it is important to know the length of mid-season stages for each crop season. FAO-56 provided tabulated crop growing lengths (initial stage, development stage, mid-season stage and late stage) for various crops in many parts of the world. Firstly, a similar crop listed in the FAO-56 was identified (Table B.3). With the actual sowing and harvest dates recorded for the crops on each lysimeter, the total length of the crop season was determined. Then a factor, which is the ratio of the actual total length to the length specified in FAO-56, was applied to adjust the length of each plant development stage accordingly (Table B.4Table B.7). For example, winter wheat planted on 2018-11-5 at the arable land lysimeters at the SE site and harvested on 2019-7-24, had a total length of 261 days. According to FAO-56, winter wheat planted in October in Idaho, USA, has a total length of 335 days, with a mid-season stage of 75 days. Applying a factor of 0.78 (i.e. 261 divided by 335), the mid-season length for this winter wheat was determined to be 58 days, as indicated in Figure 4.3.

Such a calculation was performed for each crop and each crop season at each lysimeter site. Detailed information is provided in Table B.3Table B**.7**.

4.2.5.3 Crop coefficients

According to FAO-56, PET_{FAO} during mid-season stage is estimated from a single crop coefficient (K_{c_mid}) and ET_0 as in Eq. 4.7:

$$PET_{FAO} = K_{c_mid} ET_0 \tag{4.7}$$

Since localized K_{c_mid} values are not always available, the values of K_{c_mid} as suggested by FAO-56 are being widely used to estimated PET_{FAO}. Therefore K_{c_mid} values from FAO-56 for each lysimeter were applied (Table B.3)

4.2.6 Spherical variogram fitting

As the experimental data show a smoother curve rather than straight lines, it is worth exploring another fitting curve beyond the linear-plus-plateau fitting. The spherical variogram model which is a widely used approach in geostatistics (Mälicke et al., 2018; van Groenigen, 2000)

was selected and applied in this study to describe θ- f_{ET}. This model was chosen because its shape aligns with the relationship of θ- f_{ET} (EF, rET_0 or $rPET_{FAO}$), which exhibits a linear behavior at small θ near the origin but flattens out at larger θ values, eventually reaching a plateau, or sill. A spherical variogram curve is expressed as:

$$f_{ET} = \begin{cases} 0 & \theta = 0 \\ C_0 + C\left(\frac{3}{2}\frac{\theta}{a} - \frac{1}{2}\frac{(\theta)^3}{a^3}\right) & 0 < \theta \leq a \\ C_0 + C & \theta > a \end{cases} \quad (4.8)$$

where C_0 is the nugget constant, $C_0 + C$ is the plateau, which in this study is the maximum value of f_{ET}, and defines the range of θ in the water-limited regime. Similar to the linear-plus-plateau fitting, the parameters a, C_0 and C could be simultaneously estimated using "minpack.lm" package in R. Note that it is common practice to define an effective range where 95% of the end value is reached (Oliver et al., 2015; Wadoux et al., 2019). Therefore, θ_{crit} is not equal to a, but is defined at a point where f_{ET} reaches 95% of the plateau. Thus, the θ_{crit} can be derived from the following equation:

$$C_0 + b\left(\frac{3}{2}\frac{\theta_{crit}}{a} - \frac{1}{2}\frac{\theta_{crit}^3}{a^3}\right) = 0.95(C_0 + C) \quad (4.9)$$

This cubic equation (Equation 4.9) was solved using the "uniroot" function in software R.

The performance of the linear-plus-plateau fitting or spherical variogram fitting was evaluated using the coefficient of determination (R^2). The Wilcoxon test was applied to determine if the change of the θ_{crit} among curve-fitting methods or for different θ depths or between lysimeters is statistically significant. The root mean square deviation (RMSD) was used to assess the differences in θ_{crit} among different curve-fitting methods or θ depths.

$$RMSD = \sqrt{\frac{1}{n}\sum_{i=1}^{n}(y_i - x_i)^2} \quad (4.10)$$

where x_i and y_i are the θ_{crit} estimates from different curve-fitting methods or θ depths, and n is the total number of estimates.

4.2.7 Critical root zone soil moisture thresholds according FAO-56

FAO-56 provides a range of typical FC and WP values across various soil textures, allowing for the calculation of θ_{crit_FAO56} ranges for different soil textures. However, for sandy clay loam, no specific ranges for FC and WP were provided in FAO-56. Instead, Raes et al. (2023) reported fixed values of 0.32 m^3/m^3 for FC and 0.2 m^3/m^3 for WP. To derive a comparable

range of θ_{crit_FAO56} for sandy clay loam, the same uncertainty was assumed in FC and WP as observed for silt clay loam.

Table **4.3** presents the range of FC, WP and calculated θ_{crit_FAO56} for different soil textures.

Table 4.3 The lower and upper values for field capacity (FC) and wilting point (WP) according to FAO-56, and the range of root zone critical soil moisture thresholds (θ_{crit_FAO56}) calculated from the midpoint of FC and WP. *Note:* values for Sandy clay loam are based on values from Raes et al. (2023).

Soil texture	FC (m^3/m^3)		WP (m^3/m^3)		θ_{crit_FAO56} (m^3/m^3)	
	lower	upper	lower	upper	lower	upper
Sandy loam	0.18	0.28	0.06	0.16	0.120	0.220
Loam	0.2	0.3	0.07	0.17	0.135	0.235
Silt loam	0.22	0.36	0.09	0.21	0.155	0.285
Silt clay loam	0.3	0.37	0.17	0.24	0.235	0.305
Sandy clay loam	0.285	0.355	0.165	0.235	0.225	0.295

4.3 Results

4.3.1 Consistency of θ_{crit} derived from the EF, rET_0 and $rPET_{FAO}$ definitions

We estimated θ_{crit} using the EF, rET_0 and $rPET_{FAO}$ definitions fitted by the linear-plus-plateau curve based on soil drydowns observed during growing seasons for each lysimeter (Figure B.2Figure B.11). Out of a total of 61 lysimeters, there were 38 lysimeters with θ_{crit} estimates for surface soil and 35 for root zone soil from the EF definition (Table 4.4). The rET_0 definition provided the most estimates, with θ_{crit} determined for surface soil at 47 lysimeters and for root zone soil at 49 lysimeters. The $rPET_{FAO}$ definition had the fewest estimates, providing θ_{crit} for 30 lysimeters for the surface soil and 33 for the root zone soil, respectively. This is because the $rPET_{FAO}$ definition was performed only on crop lysimeters. Overall, more than 50% of the lysimeters had θ_{crit} values.

Table 4.4 Number of θ_{crit} estimates for surface or/and root zone soil at each site by the EF, rET_0 and $rPET_{FAO}$ definitions fitted by linear-plus-plateau curve.

Site	Surface soil			Root zone soil			All		
	EF	rET_0	$rPET_{FAO}$	EF	rET_0	$rPET_{FAO}$	EF	rET_0	$rPET_{FAO}$
GW	0	0	0	0	0	0	0	0	0
WU	1	1	0	2	1	0	3	2	0
RO	6	5	0	4	5	0	10	10	0

SE	17	21	10	16	24	12	33	45	22
BL	3	6	6	3	5	6	6	11	12
SB	0	2	2	0	4	4	0	6	6
DD	11	12	12	10	10	11	21	22	23
Sum	38	47	30	35	49	33	73	96	63

Among the sites, only for the GW site no drydown event was detected, and thus no θ_{crit} could be determined for any of the three definitions (Table 4.4). This is primarily due to the very wet conditions at this alpine site, as well as the greatly reduced number of data pairs caused by lysimeter disturbance related to chamber measurements. The SE site, which has the most lysimeters with 6 different lysimeter groups, had the highest numbers of θ_{crit} estimates. Figure 4.5(a-c) shows examples of one crop lysimeter (SE42, i.e. the second lysimeter of the fourth hexagon at the Selhausen site) for each ET definition and for both surface and root zone soil using linear-plus-plateau fitting.

For the surface soil, the mean θ_{crit} across all the lysimeters was 0.168 ± 0.058 m^3/m^3 for the EF definition, 0.170 ± 0.044 m^3/m^3 for the rET_0 definition, and 0.160 ± 0.042 m^3/m^3 for the $rPET_{FAO}$ definition (Figure 4.6a). However, the latter was only applied to lysimeters on which arable crops were grown. The highest θ_{crit} value using the EF definition was detected in the grass lysimeter WU13 at the WU site, with a value of 0.364 m^3/m^3, while the lowest θ_{crit} value was for the crop lysimeter DD14 at the DD site (0.088 m^3/m^3). For the rET_0 definition, the grass lysimeter RO13 at the RO site had the highest value of θ_{crit} (0.280 m^3/m^3), whereas the grass lysimeter SE13 showed the lowest (0.094 m^3/m^3). The $rPET_{FAO}$ definition, applied only to crop lysimeters, yielded the highest θ_{crit} value of 0.255 m^3/m^3 for the lysimeter SE35 at the SE site, and the lowest value of 0.096 m^3/m^3 for the lysimeter DD26 at the DD site.

For the root zone soil, the mean θ_{crit} across all the lysimeters was 0.206 ±0.068 m^3/m^3 for the EF definition, which was similar to the mean θ_{crit} for the rET_0 definition (0.207 ± 0.052 m^3/m^3, Figure 4.6a). The mean θ_{crit} for the $rPET_{FAO}$ definition which was only applicable to arable crops was slightly lower, with a value of 0.188 ± 0.041 m^3/m^3. The EF definition estimated the highest θ_{crit} value in the grass lysimeter WU13 at the WU site (0.355 m^3/m^3), while the lowest θ_{crit} value was for the crop lysimeter DD24 at the DD site (0.124 m^3/m^3). Both the rET_0 definition and the $rPET_{FAO}$ definition identified the lowest θ_{crit} value of 0.127 $m^3/m^3$for the lysimeter DD22 at the DD site. For the rET_0 definition, the grass lysimeter RO13 at the RO

site had the highest θ_{crit} (0.324 m^3/m^3), whereas for the $rPET_{FAO}$ definition, the highest value of θ_{crit} (0.302 m^3/m^3) was obtained from the crop lysimeter SB14 at the SB site.

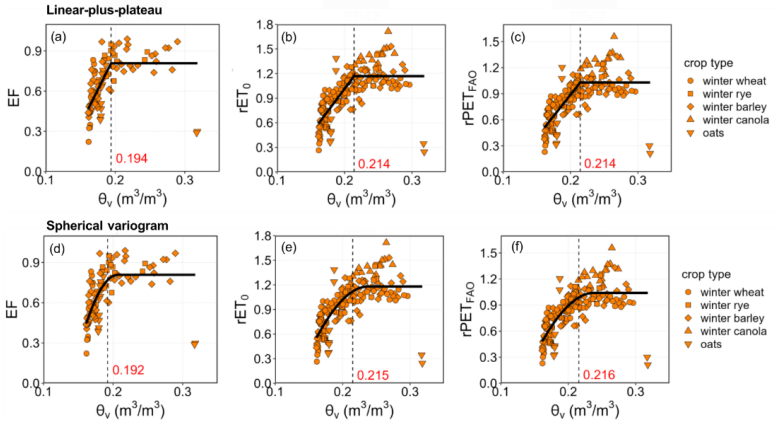


Figure 4.5 Critical soil moisture thresholds (θ_{crit}) estimated from the root zone soil moisture (θ_v) for one crop lysimeter SE42 at the SE site filled with soil from the SB site using the EF, rET_0 and $rPET_{FAO}$ definitions by (a-c) linear-plus-plateau fitting and (d-f) spherical variogram fitting. In each plot, the shape of the dots indicates the crop type. The thick black line in each plot indicates the fitted curve. The red numbers in each plot indicate the estimated θ_{crit}.

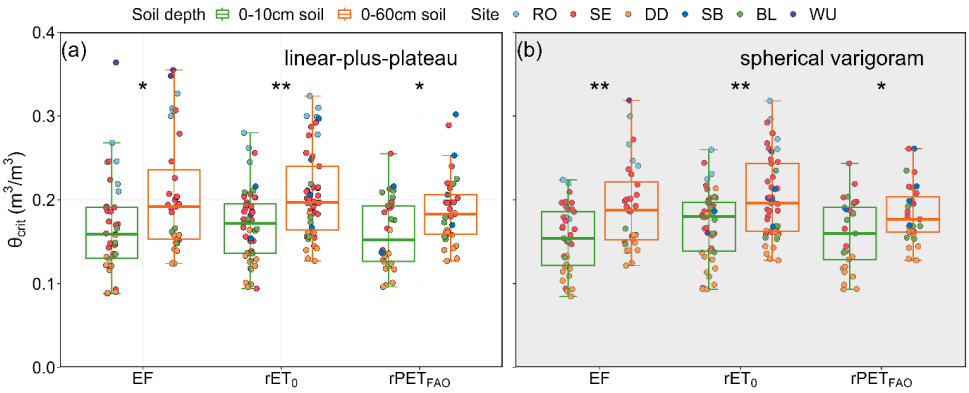


Figure 4.6 θ_{crit} for surface soil (0-10cm) and root zone soil (0-60cm) according to the rET_0, EF and $rPET_{FAO}$ definition using (a) linear-plus-plateau fitting and (b) spherical variogram fitting. The middle line represents the median θ_{crit} estimated by a given definition based on values for individual lysimeters (indicated by dots); the box represents the upper and lower quartiles, and

the whiskers represent 1.5 times the interquartile range. The color of the dots indicates the lysimeter sites. Black stars above the boxplots represent statistically significant differences of θ_{crit} between the surface soil and root zone soil using Wilcoxon test. * represents $p < 0.05$, ** represents $p < 0.01$, and *** represents $p < 0.001$. There was no significant difference in θ_{crit} estimates from different fitting curves or ET_a definitions ($p > 0.05$).

Figure 4.7 shows the comparison of lysimeter-specific θ_{crit} estimated using the three definitions (EF, rET_0, and $rPET_{FAO}$) both for surface soil and root zone soil. There was no significant difference in θ_{crit} across the three methods ($p > 0.05$), given a certain lysimeter and measurement depth (either surface θ or root zone θ). The R^2 between the rET_0 and EF definitions was 0.89 for crop lysimeters and 0.88 for grass lysimeters. The mean difference in θ_{crit} between the two definitions was 0.003 m^3/m^3 across all lysimeters, with 94% of the difference falling within the range of -0.01 and 0.01 m^3/m^3. The θ_{crit} estimates of rET_0 and $rPET_{FAO}$ definitions were nearly identical for crop lysimeters, with 97% of the difference falling between -0.01 and 0.01 m^3/m^3 and 66% of the estimates being exactly the same. This is because for crops, PET_{FAO} is ET_0 multiplied by crop coefficients during mid-season stages, so the relationship between $rPET_{FAO}$ and θ is not expected to change significantly compared to that between rET_0 and θ. The EF-$rPET_{FAO}$ relation has the lowest R^2 (0.88) for crop lysimeters, but still with a small mean difference of 0.004 m^3/m^3. Overall, most of the data points were closely distributed around the 1:1 line, with all three definitions showing consistent results ($R^2 > 0.88$, Figure 4.7), indicating the reliability of the three definitions.

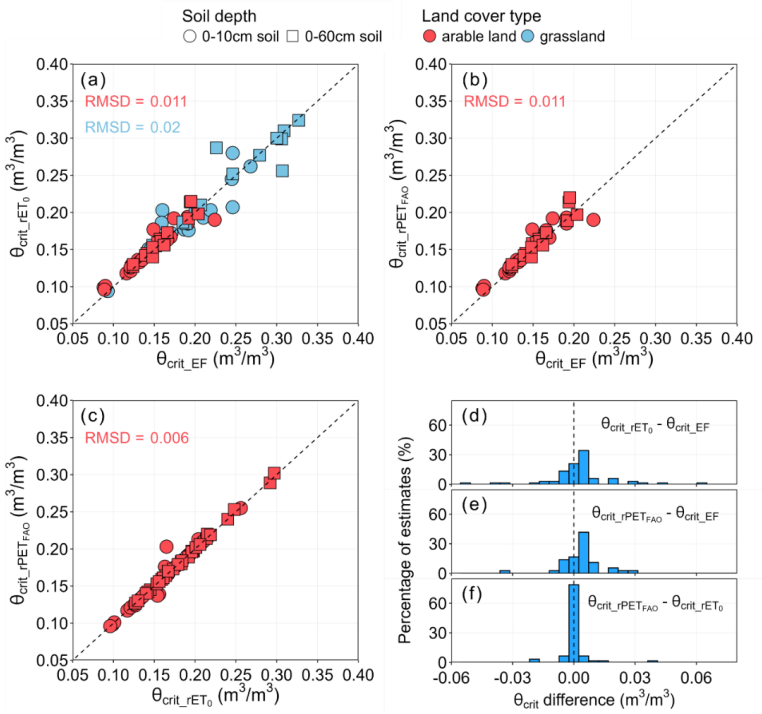


Figure 4.7 (a-c) Comparison between lysimeter-specific θ_{crit} estimated according EF, rET_0 and $rPET_{FAO}$ definitions using linear-plus-plateau fitting. RMSD is the root mean square deviation of θ_{crit} estimates between the definitions. The dashed line is the 1:1 line. The shape of the dots represents the soil depth and the color of the dots indicates the land cover type. (d-f) Distribution of differences in θ_{crit} according the different definitions.

4.3.2 Comparison between the linear-plus-plateau and spherical variogram fitting curves

Figure 4.5(d-f) shows the relationship between θ and EF, rET_0 or $rPET_{FAO}$ from the example crop lysimeter SE42 fitted by spherical variogram. Figure 4.6b presents the θ_{crit} estimated from the spherical variogram fitting for each definition and each soil depth. Figure 4.8 compares the lysimeter-specific results between linear-plus-plateau fitting and spherical variogram fitting. Though spherical variogram fitting provides a smoother fit in the water-limited regime (Figure 4.5), there was no significant difference ($p>0.05$) in the derived θ_{crit} values, plateau value or the performance of the fitting (R^2) compared to the linear-plus-plateau fitting (Figure 4.8). The data points aligned closely with the 1:1 line, suggesting that the θ_{crit} estimates are robust. This

indicates that the smoother nature of the spherical fitting does not impact the accuracy or consistency of the θ_{crit} estimates.

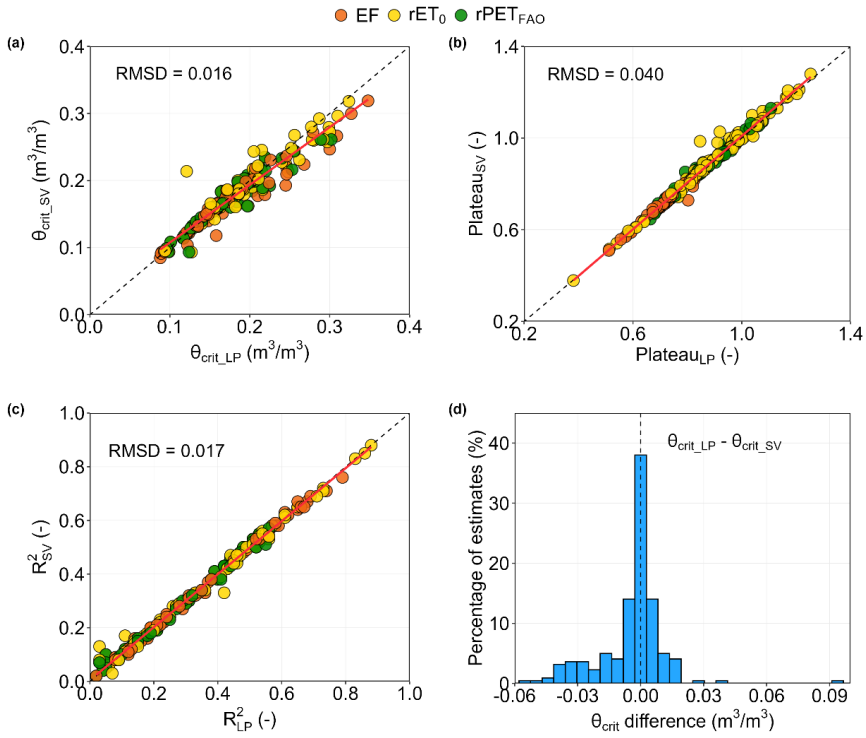


Figure 4.8 Comparison between the linear-plus-plateau fitting (LP) and spherical variogram fitting (SV) regarding (a) θ_{crit}, (b) the plateau value of the fitting and (c) the performance of fitting based on values for individual lysimeters for each definition (EF, rET_0 and $rPET_{FAO}$) and soil depth (surface soil and root zone soil). The color indicates the definitions. Dashed line is 1:1 line and red line is the regression line. RMSD is the root mean square deviation. (d) Distribution of differences in θ_{crit} derived from the two fitting curves.

4.3.3 Comparison between surface and root zone θ_{crit}

Across all the lysimeters, the θ_{crit} for the root zone soil was significantly higher than for the surface soil ($p < 0.05$), regardless of the three ET definitions or the two fitting curves (Figure 4.6). Given the robust estimates by each definition and each fitting curve, in the following, we mainly focus on the θ_{crit} detected from the rET_0 definition using the linear-plus-plateau fitting as it provided the highest number of estimates.

Figure 4.9 compares the lysimeter-specific θ_{crit} estimated using the rET_0 definition between the surface soil and root zone soil. Most of the data points were above the 1:1 line, with a RMSD of 0.046 m^3/m^3, indicating a higher θ_{crit} value for the root zone soil (Figure 4.9a). As shown in Figure 4.9b, the differences between root zone and surface θ_{crit} mostly ranged from 0 to 0.1 m^3/m^3. Despite these differences, the θ_{crit} for the surface soil and for the root zone soil showed a good correlation (r = 0.83, Figure 4.9a).

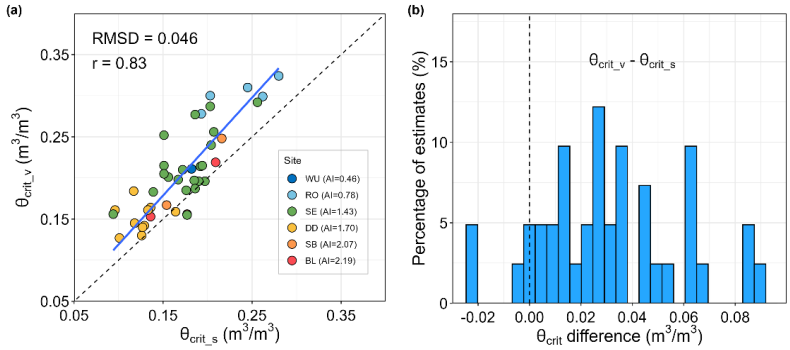


Figure 4.9 (a) Scatterplot of θ_{crit} for surface soil (θ_{crit_s}) versus root zone soil (θ_{crit_v}), estimated for each lysimeter using the rET_0 definition. AI means aridity index. (b) Distribution of differences in θ_{crit} between root zone soil and surface soil.

Figure 4.10 shows the relation between θ_{crit} and sand fraction for both surface and root zone soil. Overall, both surface and root zone θ_{crit} showed a declining trend with increasing sand fraction; however, the slope is significant only for surface θ_{crit} ($p < 0.05$). This can be explained by the fact that the hydraulic conductivity of coarser soils decreases at lower water contents (but then decreases very quickly; Wankmüller et al., 2024). At the DD, BL and SE sites, there were lysimeters containing different soils but the same vegetation type, allowing the investigation of the impact of sand fraction on θ_{crit} without confounding effects from climate and ecosystem. Under identical climate, sand fraction had a smaller influence on root zone θ_{crit} compared to surface θ_{crit} for arable land given the gentler slope. Conversely, for grassland, the effect of sand fraction on root zone θ_{crit} was more pronounced than on surface θ_{crit}.

Across the sites, some lysimeters were transferred among several sites to emulate the expected changes in climate. Figure 4.11 shows the relation between θ_{crit} and aridity index. When the lysimeters were transferred to a drier site (with higher aridity index), the θ_{crit} both for the surface

soil and root zone soil generally decreased (though not statistically significantly), except for the lysimeters with the DD soil at the SE site compared to the DD site. The reduction in θ_{crit} at drier sites could be attributed to plant self-regulation, such as adaptation of the root system or altering plant community composition to increase drought tolerance. For example, when lysimeters were moved from the humid RO site (ROro) to the sub-humid SE site (SEro), the mean surface soil θ_{crit} for the surface soil decreased from 0.245 to 0.203 m^3/m^3. In a study comparing the ROro and SEro lysimeters (Jarvis et al., 2022), it was found that the root depth was increased from ca. 56 cm at the RO site to ca. 80 cm at the SE site, and significant changes were observed in the plant community composition.

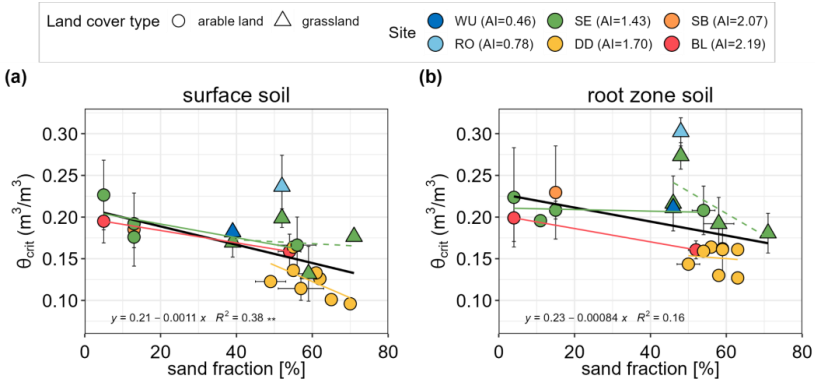


Figure 4.10 Relationship between sand fraction and θ_{crit} for (a) surface soil and (b) root zone soil. The thick black line represents the linear regression of θ_{crit} to sand fraction for all lysimeter groups. Regression equations, R^2 and p-values (regression t-test) are indicated (**P < 0.01). Colored regression lines indicate the relationships between θ_{crit} and sand fraction for lysimeter groups that have the same land cover type at the same site but differ in soil texture.

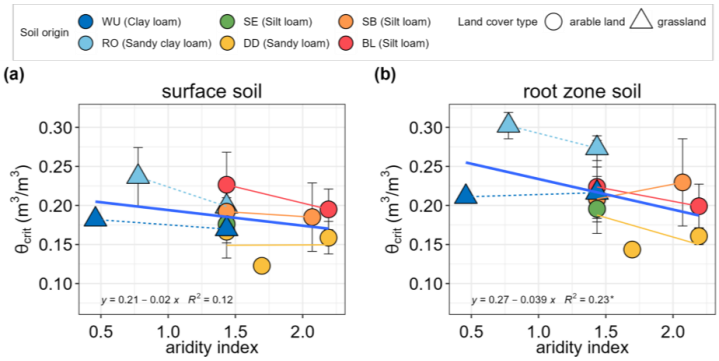


Figure 4.11 Relationship between aridity index and θ_{crit} for (a) surface soil and (b) root zone soil. The thick blue line represents the linear regression of θ_{crit} to aridity index for all the translocated lysimeter groups. Regression equations, R^2 and p-values (regression t-test) are indicated (*P < 0.05). Colored regression lines indicate the relationships between θ_{crit} and aridity index for translocated lysimeters which have the same soil origin but are placed at different sites

4.3.4 Comparison of root zone θ_{crit} derived from observations and FAO-56

The lysimeters with estimated θ_{crit} contained four different soil textures, namely sandy loam, loam, silt loam and sandy clay loam. Figure 4.12 shows the comparison of root zone θ_{crit} estimated from lysimeter observations and calculated from FAO-56 for these soil textures. Sandy loam has the lowest median θ_{crit} of 0.164 m^3/m^3, whereas sandy clay loam has the highest median θ_{crit} of 0.291 m^3/m^3. Generally, the lysimeter-specific θ_{crit} values fall within the range of θ_{crit} estimated from FAO-56, which uses the midpoint between field capacity and wilting point. However, for sandy clay loam, which is the soil from the RO site, the θ_{crit} values for some lysimeters are outside (above) the FAO-56 range. Notably, θ_{crit} for the lysimeters at the SE site (SEro lysimeters) are within the FAO-56 range, whereas θ_{crit} for the lysimeters at the RO site (ROro lysimeters) are generally above the upper limit of the FAO-56 θ_{crit} range. One possible explanation is that at the RO site, there were few cases of water-limited conditions. Although θ_{crit} values could be determined, rET_0 did not decrease significantly for θ values below θ_{crit} (Figure B.3). In contrast, the SEro lysimeter observations showed a clear transition between water-limited and energy-limited regimes (Figure B.5).

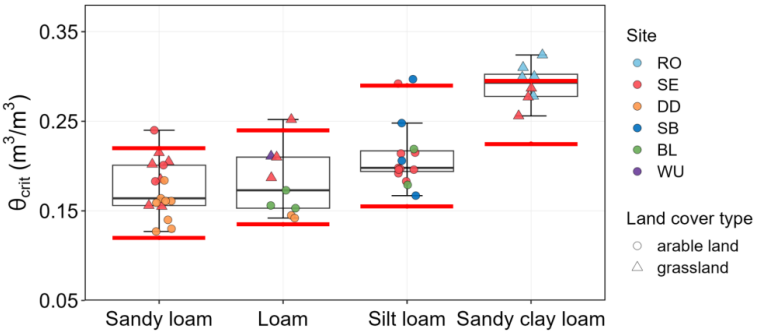


Figure 4.12 Root zone θ_{crit} for different soil textures. The middle line represents the median θ_{crit} estimated for a given soil texture on the basis of values for individual lysimeters for that soil texture; the box represents the upper and lower quartiles and the whiskers represent 1.5 times the interquartile range. The shape of the dots indicates the land cover type of the lysimeters. Red lines indicate the upper and lower θ_{crit} calculated based on FAO-56.

4.4 Discussion

Lysimeters provide a reliable means of quantifying in situ ET_a and are widely recognized as the gold standard, while also enabling SM measurements across different depths (Pütz & Groh, 2023). In this study, we applied θ_{crit} detection algorithms to a large dataset with lysimeter observations across Germany, not previously used for this purpose, and identified relationships between SM and ET_a.

We identified θ_{crit} not only from the EF-SM relationship, but also from rET_0 and $rPET_{FAO}$ definitions. The differences in lysimeter-specific θ_{crit} between the three definitions are small (Figure 4.7), suggesting that any of them can be used to identify θ_{crit}, and that studies using these different definitions can be compared. However, the rET_0 definition led to a generally higher identification of θ_{crit} values (surface: 47, root zone: 49) with the lysimeters compared to the EF (surface: 38, root zone: 35) or $rPET_{FAO}$ definition (surface: 30, root zone: 33, Table 4.4). The higher number of θ_{crit} detections for rET_0 was due to the relative simpler methodology used for ET_0, which yielded more data points compared to EF and $rPET_{FAO}$. A by-product of our analysis is the sensitivity of soil heat flux correction using calorimetric definitions, showing robustness despite varying inputs and soil parameters (Appendix B.1).

Although theoretically PET should be equal to ET_a in the energy-limited regime, the plateau values for both rET_0 and $rPET_{FAO}$ definitions fluctuated around 1 (Figure 4.13). This discrepancy is understandable because the length of mid-season stage is estimated based on sowing and harvest dates, and the crop coefficients (K_c) for each crop are assumed to be constant based on FAO-56 guidelines, so PET_{FAO} is not the exact PET, implying the information from FAO-56 differs from the local conditions. However, even when using the site-specific K_c, the plateau values still were not equal to 1. Due to the difficulty and complexity of estimating the exact PET, and the fact that θ_{crit} estimated from the rET_0 definition is consistent with that from the EF definition, we recommend the rET_0 definition rather than the $rPET_{FAO}$ definition.

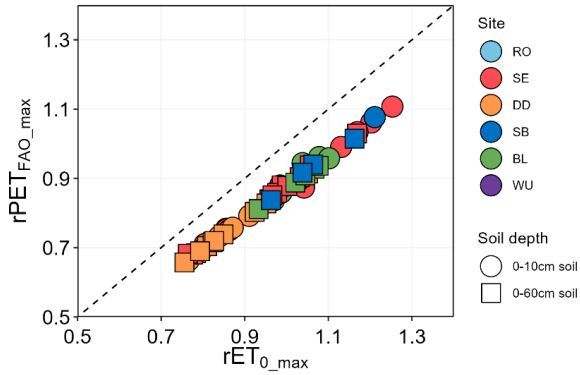


Figure 4.13 Comparison between plateau values estimated from the rET_0 and $rPET_{FAO}$ definition across all the lysimeters. The dashed line is the 1:1 line.

We also tested the impact of the fitting curves on the estimation of θ_{crit}. Very few studies fitted the relationship between θ-EF (or θ-rPET) using curves other than the linear-plus-plateau model. Dirmeyer et al. (2000) used an arctangent function to fit the relationship between root zone soil wetness index and EF, but this approach is unable to pinpoint a clear turning point. In this study, we applied the spherical variogram fitting curve to identify the θ_{crit} for the first time. We found that both linear-plus-plateau fitting and spherical variogram fitting give consistent results (Figure 4.8), suggesting that the θ_{crit} is robust. However, though the performance of spherical variogram fitting is similar to linear-plus-plateau fitting (Figure 4.8c), the spherical variogram fitting produced a smoother curve in the water-limited regime, indicating a gradual shift in the dependence of EF (or rPET) on θ. This smoother curve is

perhaps closer to the behavior in nature and could offer additional insights into changes in the θ-EF (or θ-rPET) relationship.

Taking advantage of soil moisture sensors installed at three different depths inside the lysimeters, our study estimates θ_{crit} for both surface and root zone soil. This is the advantage of the lysimeter data, as θ_{crit} for the root zone soil cannot be derived from satellite data (Purdy et al., 2018). It can be assumed that θ_{crit} estimated for the root zone is a better approximation of the true θ_{crit} as it captures better the θ control on the ET process, as also plant water uptake from deeper soil layers is considered. Plants take up water from roots, which can compensate for surface dryness and this water is transported from the deeper soil through the roots and stem to the transpiring leaves (Fan et al., 2017). Compared to the small uncertainty in θ_{crit} across different definitions and fitting curves as indicated by the low RMSD values, a much greater variability was observed in θ_{crit} between surface and root zone soil. Not surprisingly, our results show higher θ_{crit} for the root zone than for the surface soil in Germany across different climatic regimes (semi-arid to humid regimes, Figure 4.6 and Figure **4.9**), confirming results from Buitink et al. (2020) for the Netherlands and Dong et al. (2022) for the US.

While this study focused on θ, plants are known to be sensitive to water potentials, and it has been shown that the effective averaged soil water potential felt by a plant is proportional to its root distribution, when the soil hydraulic conductivity is not limiting water uptake (Couvreur et al., 2012). This implies that root spatial distribution should be used to weigh the soil water potential. However, because root spatial distribution is difficult to estimate (Zhang et al., 2023), computing an effective water potential as well as effective root zone θ is very challenging.

We then made use of different lysimeter groups to investigate the dependence of θ_{crit} on soil texture. Some lysimeters at the same site have the same land use but different soils, allowing us to isolate the effect of soil texture without confounding factors. We find that both surface and root zone θ_{crit} decrease with increasing sand fraction (Figure 4.10). Similar findings have been reported in previous studies, but only for surface soil without focusing on root zone soil (Denissen et al., 2020; Z. Fu et al., 2024; Shi et al., 2024; Wankmüller et al., 2024). The slope of the fitted regression line for surface and sand fraction (-0.0011, Figure 4.10a) is similar to that reported by Wankmüller et al. (2024), which is -0.0017. The underlying mechanism of the decreased θ_{crit} with increasing sand fraction can be attributed to the less negative matric potential in coarse-textured soils, which allows plants to access water at low water contents (Wankmüller et al., 2024). However, one limitation of this study is that we were not able to

fully characterize θ_{crit} based on hydraulic conductivity due to limited soil texture information (only sand, silt and clay fractions were available for all lysimeters). Soil hydraulic conductivity is intrinsically dependent on soil particle size distribution (PSD) and can be estimated from empirical equations based on PSD (Wang et al., 2017). Further analysis can be carried out in more detail by exploring the relationship between θ_{crit} and hydraulic conductivity, or some indices related to PSD.

We also found that under the same climatic condition, sand fraction had a relatively minor impact on root zone θ_{crit} compared to surface θ_{crit} in arable land, whereas the opposite pattern was observed for grassland. One possible reason for this difference can be due to variations in root system density. Grasslands typically develop denser root systems over time, as their roots grow and persist year after year. In contrast, crops are replanted annually, resulting in less dense root systems (Dupont et al., 2014). This high root density increases water uptake from the root zone, making the root zone θ_{crit} more sensitive to changes in soil properties, such as sand fractions. However, there are not enough data points to show that the differences in slope between surface θ_{crit} and root zone θ_{crit} for arable land on one hand and grassland on the other hand were statistically significant.

The FAO-56 guidelines propose to estimate θ_{crit} for root zone soil (θ_{crit_FAO}) as the midpoint of field capacity and wilting point for a given soil texture. The comparison between root zone θ_{crit} estimated from lysimeter time series with θ_{crit_FAO} shows that the FAO-56 provides a generally reliable range of θ_{crit} for the four soil textures (sandy loam, loam, silt loam, sandy clay loam). However, for sandy clay loam, lysimeter-specific θ_{crit} at the RO site were mostly higher than the range of θ_{crit_FAO}. This is probably due to the few cases of water-limited conditions observed at the RO site. Although the fitting curves were able to determine θ_{crit}, there was no clear decrease in rET_0 or EF when SM decreased below θ_{crit} for most of the lysimeters at the RO site (Figure B.3). It is important to note, however, that even a small decrease in EF can correspond to a substantial change in ET_a, particularly under high net radiation conditions. This warrants the need for further investigation into net radiation dynamics during soil drydown events. Overall, the general agreement between FAO-56 and curve-fitting estimates of θ_{crit} highlights the potential for the FAO-56 and the curve fitting framework to serve as complementary methods for the estimation of θ_{crit}. The FAO-56 offers a broad yet reliable range of θ_{crit}, while the framework estimates the specific values. By combining the two methods, it is possible to

cross-validate the results to obtain a more robust assessment of θ_{crit} for specific soil textures. Further study is needed to extend the analysis to a wider range of soil textures.

The impact of changing climatic conditions on θ_{crit} was examined using translocated lysimeters following the "space-for-time" concept. These lysimeters, some containing the same soil and vegetation types, were moved to sites with varying climatic conditions. We found that both surface and root zone θ_{crit} decrease with increasing aridity index (Figure 4.11). We argue that atmospheric demand and plants play a competitive role on θ_{crit}. For drier conditions with higher evaporative demand, θ_{crit} should increase as soil water conductivity will become limiting at higher SM level; in other words, water limitation would be reached while the soil is still relatively wet during drying (Feldman et al., 2019; Carminati & Javaux, 2020). Thus, the observed decrease in θ_{crit} would suggest an overcompensation by vegetation, by increasing their root length, growing roots towards wetter zones or, for grassland, changing its composition towards more drought-tolerant plant species. However, due to the limited number of lysimeters, the changes in θ_{crit} due to the aridity index are not significant, suggesting that more data is needed to fully understand the impact of these factors.

In general a high correlation (0.83, Figure 4.9a) was found between θ_{crit} for surface soil (10 cm) and for root zone soil (0-60 cm) in our study for the sites in Germany, ranging from semi-arid to humid regions. This correlation is higher than the value of 0.53 reported by Dong et al. (2022), who compared surface θ_{crit} (5 cm) and root zone θ_{crit} (0-50 cm) using AmeriFlux data from the continental United States. Furthermore, this correlation is in line with a recent global study using ERA5 reanalysis data (Paul et al., 2025). They found a correlation of 0.86 between surface θ_{crit} (0-7cm) and shallow root zone θ_{crit} (0-28cm) and a lower correlation of 0.74 between surface θ_{crit} and deeper root zone θ_{crit} (0-100cm). Interestingly, although our results only focused on 6 sites in Germany, which are fewer and with a narrower climatic gradient compared to Dong et al. (2022), we find a similar range of θ_{crit} (0.1 ~ 0.35 m^3/m^3), indicating that our sites are representative of some typical climate types. The high correlation between surface θ_{crit} and root zone θ_{crit} can be explained by the hydraulic link that governs water movement and distribution within the soil profile, suggesting both surface and root zone θ can capture comparable statistics of ET_a regime prevalence (Dong et al., 2022). However, it is worth noting that regions which may have abrupt dry and wet seasons, such as the Indian and East African Summer Monsoons (Mondal & Mishra, 2024), may exhibit much larger discrepancies in θ_{crit} between surface and root zone θ and poor correlations between them.

Under those conditions surface and root zone θ sometimes decouple with a very dry surface soil layer and still relatively elevated θ in the deeper root zone (Capehart & Carlson, 1997; Vereecken et al., 2008). In those cases, or for arid sites θ_{crit} estimated from the upper SM would not be very representative of θ_{crit}. For example, Paul et al (2025) found a greater difference between surface and root zone θ_{crit} in drier ecosystems (savannas and shrublands) than in wetter woody vegetation regions. This highlights the need for further investigation for different climate conditions, like arid and monsoon type climates.

In addition, the apparent rooting depths exhibit a broad range (even up to 25 m) across the globe (Stocker et al., 2023). We estimated root zone θ for the upper 60 cm, which might not be representative of the complete effective rooting zone. Future studies should incorporate deeper soil layers to better capture root zone SM and hence root zone θ_{crit}.

Our findings also have broader implications for the remote sensing and land surface modeling communities. Many remotely sensed products of ET_a and model-derived ET_a estimates tend to perform better under energy-limited conditions (Long et al., 2014). By providing observationally constrained estimates of θ_{crit}, our findings indicate that lysimeter-derived θ_{crit} offers possibilities to delineate ET_a regimes and identify the areas where specific remote sensing products or model simulations are expected to perform more reliably. Moreover, the lysimeter-based quantification of θ_{crit} provides valuable reference data for validating and improving the models and remote sensing products, contributing to a better understanding of land-atmosphere coupling processes under changing climatic conditions.

4.5 Conclusions

We provide estimates of critical soil moisture thresholds (θ_{crit}), the soil moisture content at which the transition from energy limited to water limited ET_a occurs, for both surface (10 cm) and root zone (0-60 cm) soil based on lysimeter data sets. Lysimeters are considered the gold standard for measuring in situ ET_a and allow concurrent in situ θ measurements at various depths. A total of 61 lysimeters from 7 sites in Germany were employed for this analysis including different soil texture and land cover types (grassland and arable land). The relationships between θ and evaporative fraction (EF), θ and the ratio of ET_a to grass reference evapotranspiration (rET_0), and θ and the ratio of ET_a to calculated potential evapotranspiration ($rPET_{FAO}$) during drydowns were fitted by a linear plus plateau function and a spherical

variogram function to determine θ_{crit}. All three definitions and two fitting functions showed good consistency, indicating the applicability of each of the three definitions or the two fitting curve frameworks. The root zone θ_{crit} was found to be higher than surface θ_{crit}. θ_{crit} for both surface and root zone soil showed a dependency on sand fraction (R^2 =0.38 for surface θ_{crit} and R^2 = 0.16 for root zone θ_{crit}). In addition, under changing climatic conditions but with identical soil and ecosystem, θ_{crit} increased when the soil monoliths moved to a drier place with higher aridity index. Overall, θ_{crit} showed a dependence on aridity index (R^2 = 0.12 for surface θ_{crit} and R^2 = 0.23 for root zone θ_{crit}). Although the difference between surface and root-zone based θ_{crit} was greater than between any of the abovementioned definitions, and cannot be ignored, we still found a good correlation between surface soil and root zone θ_{crit}. Consequently, while θ_{crit} from different measurement depths (i.e., surface vs. root zone layers) should not be directly compared, they might still serve as mutual proxies. However, we argue that it can be expected that for other climates (monsoon, arid) and (very) deep rooting vegetation this correlation may break down. This warrants further investigation with in-situ data for those sites.

Chapter 5. Comparison of surface and root zone critical soil moisture from lysimeter time series

*adapted from: Lu, X., Groh, J., Graf, A., Pütz, T., Vanderborght, J. Vereecken, H., & Franssen, H. J. H.: Comparison of surface and root zone critical soil moisture from lysimeter time series, in preparation.

5.1 Introduction

Soil moisture (θ) is a key land surface variable that regulates water and energy feedback. It determines the fraction of incoming radiative energy that is converted into actual evapotranspiration (ET_a), which in turn influences temperature and humidity in the lower atmosphere (Vereecken et al., 2008; Seneviratne et al., 2010). Depending on θ availability, two conceptual ET_a regimes are distinguished: a water-limited regime and an energy limited regime (Budyko, 1974; Seneviratne et al., 2010). The transition between the two regimes is characterized by a critical soil moisture threshold (θ_{crit}).

When θ drops below θ_{crit}, ET_a enters the water-limited regime, where ET_a is primarily constrained by θ. Reduced θ triggers progressive closure of plant stomata, limiting transpiration and thereby reducing evaporative cooling while increasing land surface temperature (Humphrey et al., 2021). Such positive land- atmosphere feedback loop can result in local warming and contributes to the persistence of drought and heatwaves (Feldman et al., 2019; Hsu & Dirmeyer, 2023a). Conversely, when θ exceeds θ_{crit}, ET_a becomes mainly governed by energy supplies rather than θ. In an energy-limited regime, stomatal conductance is no longer a limiting factor and ET_a approaches its upper bound determined by the atmospheric evaporative demand, commonly referred to as potential ET (Xiang et al., 2020). Such decoupling between ET_a and θ dampens the land-atmosphere interaction and can potentially increase the risk of flooding (Lo et al., 2021). Therefore, knowledge of θ_{crit} associated with this regime shift is crucial for its wide use in terrestrial and atmosphere research communities, such as understanding the hydroclimatic extremes and assessing agricultural and crop yield risks.

Past efforts to evaluate θ_{crit} are primarily based on surface soil moisture (e.g., typically limited to the top ~ 5 cm for remote sensing) (Akbar, Short Gianotti, et al., 2018; Denissen et al., 2020; Escorihuela et al., 2010; Feldman et al., 2019; Fu et al., 2024), but plants can access water stored much deeper in the soil to sustain transpiration (Oliveira et al., 2005). As surface θ becomes depleted, plants can compensate by increasing their water uptake from the deeper soil

layers at rates much higher than would be expected based on root density (Green & Clothier, 1995). Consequently, understanding θ_{crit} for deeper soil layers is essential for accurately characterizing total ET_a dynamics. Although the temporal dynamics of surface and root zone θ are linked through hydraulic connectivity (Akbar, Short Gianotti, et al., 2018; Feldman et al., 2023), studies show that surface θ might become decoupled from deeper θ which is more relevant for plant water uptake. For example, Mahmood & Hubbard (2007) found that both correlation and cross-correlation between surface and subsurface θ decrease rapidly with increasing depth across different land use types. Similarly, Hirschi et al. (2014) demonstrated that under extreme hot conditions, the temporal coupling between surface and root zone θ gradually weakens. These findings imply that surface and root zone soil may not exhibit similar ET_a regimes and θ_{crit} values. Indeed, Buitink et al. (2020) reported lower surface θ_{crit} values compared to root zone θ_{crit} across θ networks in the Netherlands, but they did not examine the relationship between surface and root zone θ_{crit}. A more recent study explored the correlation between surface and root zone θ_{crit} on a global scale using ERA5 reanalysis data. However, ERA5 root zone θ is model-derived rather than observed, and has been shown to overestimate root zone θ (Tian & Zhang, 2023) and perform poorly in some arid regions (Yang et al., 2022), which could potentially bias θ_{crit} estimates. Using flux tower observations and in-situ soil moisture sensors, Dong et al. (2022) also compared surface and root zone θ_{crit}, but their study was limited to the continental United States. Moreover, the aforementioned studies did not systematically compared surface and root zone θ_{crit} across climates and land covers, leaving a critical gap in our understanding of their variability and controlling factors.

Traditionally, the determination of θ_{crit} is based on a conceptual framework that relates θ to a variable derived from ET_a, such as evaporative fraction (the ratio of latent heat flux to the available energy) or evaporation factor (the ratio of ET_a to potential ET) (Eagleson, 1978; Yao, 1974). Both approaches require accurate measurements of ET_a and θ. Weighable lysimeters are regarded as the most reliable method to measure in-situ ET_a (Groh et al., 2019; Lu et al., 2024; Schrader et al., 2013; Gebler et al., 2015), as they enable the determination of a complete closed water balance. When combined with soil moisture sensors installed at multiple depths in the profile within the lysimeter, this setup allows for precise data pairs of θ and ET_a, providing a unique insight into the respective roles of surface and root zone θ in controlling ET_a. The ratio of ET_a to grass reference ET (ET_0), referred to as rET_0, has been proven to be skillful in identifying the θ_{crit} (Lu et al., 2026). Therefore, θ_{crit} can be determined by characterizing the θ-

rET_0 relationship using a linear-plus-plateau function. Despite that lysimeters typically have a small surface area (approximately 1 m^2), their ET_a measurements are valuable at larger spatial scales (Lu et al., 2024). Additionally, lysimeters enable detailed characterization of soil, vegetation and climate conditions, facilitating a more precise investigation of the drivers of surface and root zone θ_{crit}.

The objective of this study is to estimate and compare surface and root zone θ_{crit} using lysimeter measurements in a detailed and systematic manner. We collected data from a total of 179 lysimeters across 27 sites in Asia, Europe, North Africa and North America. Specifically, our comparison focuses on (a) evaluating the degree of consistency between surface and root zone θ_{crit} (b) assessing the temporal synchrony of surface and root zone ET_a-regime transitions associated with θ_{crit} and (c) identifying the drivers of surface and root zone θ_{crit}. Overall, this study attempts to offer a comprehensive evaluation of surface and root zone θ_{crit}.

5.2 Materials and Methods

5.2.1 Study sites

Data from 179 lysimeters at 27 sites were collected for this study. Figure 5.1 shows the location of the sites and Table C 1 summarizes the detailed information of the lysimeters. Among these, surface and/or root zone θ_{crit} were successfully estimated for 101 lysimeters at 20 sites (Figure 5.1, Table C 1).

Each site had one or more lysimeters. The individual lysimeters did not necessarily represent the local land cover, soil or climate. Some lysimeters were subjected to experimental climate manipulation (e.g., at the Stubai, ClimGrass, Hasselt and Montpellier sites), while some lysimeters contained soil monoliths relocated from different climate zones and ecosystems (e.g., at the Selhausen, Dedelow, Bad-Lauchstädt). In addition, several lysimeters were managed under different cropping systems (e.g., at the Soil Interpretive Health Centre Site). Therefore, the 179 lysimeters encompass 3 land cover types, 10 soil texture classes and 4 climate regimes among the lysimeters.

The dominant land cover for the lysimeters consisted of grassland and cropland, which are two major global ecosystem types, covering around 50% of the Earth's surface (Foley et al., 2011; Radolinski et al., 2025). Only a few lysimeters were covered by shrub vegetation, but no θ_{crit} were detected for these lysimeters (Table C 1). Forest land cover was not included in this

dataset due to the limited space of the lysimeters for tree roots to develop. The soil monoliths spanned a wide range of soil textures, encompassing 10 soil texture classes, seven of which had θ_{crit} identification (Table C 1).

To classify the climate dryness of each lysimeter, the aridity index (AI) defined as the ratio of mean annual grass reference ET (ET_0) to mean annual precipitation (P) was calculated. For lysimeters lacking complete annual records of ET_0 and/or P, AI values were extracted from the global aridity index dataset developed by Zomer et al. (2022), which represents AI for 1970-2000. Based on the classification from the Food and Agriculture Organization (FAO; Spinoni et al., 2015), the 179 lysimeters were divided into four categories : humid ($AI \leqslant 1.3$), sub‐humid ($1.3 < AI \leqslant 1.5$), semi‐arid ($1.5 < AI \leqslant 5$), and arid ($5 < AI < 20$) climate. Among these, 101 lysimeters with θ_{crit} estimations spanned from humid to semi-arid, with no lysimeters falling into the arid climate (Table C 1).

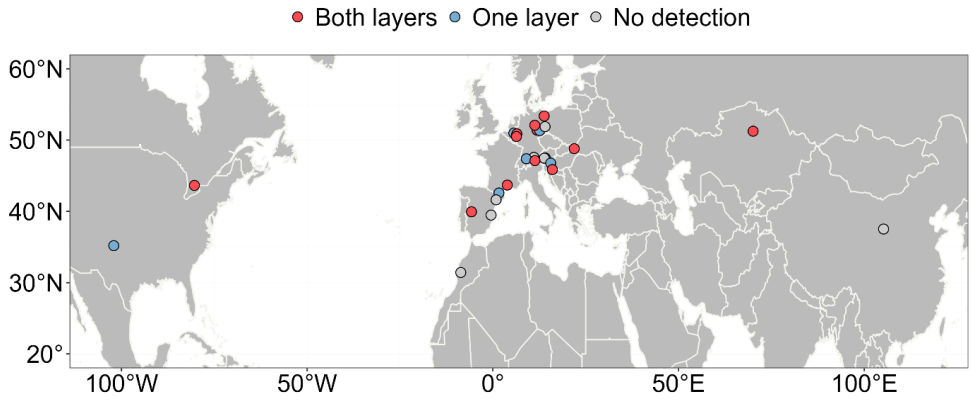


Figure 5.1 Distribution of lysimeter sites included in this study. Red, blue, orange, and gray dots indicate sites where θ_{crit} was detected for both surface and root zone layers, sites where θ_{crit} was detected for only one layer, sites that were in the water-limited regime only, and sites where no θ_{crit} was detected, respectively. A single site may have multiple lysimeters.

5.2.2 Data

In this study, ET_a was measured by lysimeters. Soil moisture (θ) was monitored at different depths within the soil monoliths. We consider the surface layer to be above 30 cm depth, while root zone layers to be vertically integrated extending from 50 to 80 cm depth.

Meteorological data were available for the lysimeters, including P, air temperature (T_a), relative humidity (RH), wind speed (WS) and global radiation (R_g). Irrigation amount was also available if irrigation was applied. For most sites, data were available at hourly or higher temporal resolution, allowing the analysis to be conducted on a daytime scale (9:00 - 17:00). For a few sites (Shapotou, Chichaoua, Montpellier and Wagna) only daily data were available, and analysis was thus performed on a daily scale to maximize data utilization.

ET_0 is estimated for a hypothetical grass reference site, assuming a fixed surface resistance of 70 s m^{-1} and an albedo of 0.23 (Allen et al., 1998; Xiang et al., 2020). ET_0 was calculated with the FAO Penman-Monteith equation (Allen et al., 2006) on an hourly basis (Equation 5.1) and then summed over the daytime or daily period.

$$ET_0 = \frac{0.408\Delta(R_n - G) + \gamma \frac{37}{T_h + 273} u_2 (e^o(T_h) - e_a)}{\Delta + \gamma(1 + C_d u_2)} \quad (5.1)$$

where Δ is the slope of the vapor pressure curve (kPa $^oC^{-1}$), R_n is net radiation at the grass surface (MJ m^{-2} h^{-1}), G is surface ground heat flux (MJ m^{-2} h^{-1}). R_n and G in this equation was estimated using a simple model based on R_g. T_h is mean hourly T_a at 2 m height (^oC), $e^o(T_h)$ is hourly saturation vapor pressure (kPa), e_a is hourly actual vapor pressure (kPa), γ is psychrometric constant (kPa $^oC^{-1}$), C_d is a coefficient set to 0.24 s m^{-1} when $R_n > 0$ and 0.96 s m^{-1} when $R_n < 0$, and u_2 is wind speed at 2 m height (m s^{-1}).

5.2.3 Drydown identification

Soil moisture drydowns are characterized by periods when θ continuously decreases in the absence of water input (precipitation and/or irrigation), where the transition between energy-limited and water-limited regimes is most likely to occur. This study focuses on drydowns during the growing season when most of the soil surface on the lysimeters is covered by the vegetation. The growing season was defined as April to September for grasslands and as the mid-season stage during April and September for croplands and shrublands, following the FAO guidelines (Allen et al., 1998) .

Following the methodology of McColl et al. (2017), we automate the drydown selection process on a daytime basis according to the following logic:

1) The drydown must begin only after water supply stops, indicating that the water input should be zero on the first day of the drydown period.
2) Water input should not exceed 1mm/day during a drydown event.

3) During a drydown event, θ increments should be negative. However, to account for potential observational noise, any positive θ increment less than 1% of the range of observed θ is excluded, preventing generation of multiple drydown events due to isolated positive increments in a series of negative changes.
4) The drydown must last for at least 5 days.

The drydown selection process was performed separately for surface θ (θ_s) and root zone θ (θ_v). An illustrative example of θ time series is shown in Figure C1. to highlight the drydowns identified by the above procedure based on observations from one lysimeter.

5.2.4 Determination of critical soil moisture

The relationship between the ratio of ET_a to ET_0 (rET_0) and θ was established using all data pairs during drydowns for each lysimeter and then fitted by a linear-plus-plateau model:

$$\mathrm{rET}_0 = \begin{cases} \mathrm{rET}_{0\max} + S(\theta - \theta_{\mathrm{crit}}) & \text{if } \theta \le \theta_{\mathrm{crit}} \\ \mathrm{rET}_{0\max} & \text{if } \theta > \theta_{\mathrm{crit}} \end{cases} \tag{5.2}$$

where θ_{crit} is the critical soil moisture. θ can be either θ_s or θ_v. $\mathrm{rET}_{0\max}$ denotes the maximum rET_0 value in the energy-limited stage where θ is abundant and not the limiting factor for ET. S denotes the slope of the linear increase phase, indicating the sensitivity of rET_0 to θ and thus the impact of θ on atmospheric conditions in the water-limited regime(Fu et al., 2022; Schwingshackl et al., 2017). The model parameters including θ_{crit} and S were estimated via global optimization by minimizing the sum of squared errors using "minpack.lm" package in the R programming language (Elzhov et al., 2015).

Similar to previous studies (Feldman et al., 2019; Z. Fu et al., 2024; Hsu & Dirmeyer, 2023a), two other linear models were considered in this study: one assuming that ET_a is purely water-limited, and another assuming a purely energy-limited regime. The Akaike's Information Criteria (AIC) metric (Akaike, 1974) was used to determine the optimal model with the lowest AIC value. θ_{crit} was identified only when the linear-plus-plateau model was selected. Finally, θ_{crit} values were detected for 101 out of the 179 lysimeters θ_{crit} for either the surface layer, the root zone layer, or both.

The difference between root zone and surface θ_{crit} ($\Delta\theta_{crit}$) is defined as $\theta_{\mathrm{crit,root}} - \theta_{\mathrm{crit,surf}}$. The relative difference is calculated as

$$\text{Relative } \Delta\theta_{\mathrm{crit}} = \frac{\Delta\theta_{\mathrm{crit}}}{\theta_{\mathrm{crit,surf}}} \times 100\% \tag{5.3}$$

5.2.5 Consistency of critical soil moisture between surface and root zone layers

The consistency of ET_a regime identification between surface and root zone θ was evaluated using several diagnostic metrics. First, the persistence of water-limited regime (γ) is defined as the fraction of time spent in the water-limited regime during drydowns for a given soil layer. (Equation 4) (Feldman et al., 2019; Paul et al., 2025). Second, the binary regime similarity (φ) quantifies the agreement between surface and root zone θ in identifying the same ET_a regime (Equation 5) (Dong et al., 2022),

$$\gamma_i = \frac{n_{WL,i}}{n_i} \tag{5.4}$$

$$\varphi = \frac{n_r}{n} \tag{5.5}$$

where $n_{WL,i}$ is the number of days when θ is below θ_{crit} for a given layer i (i refers to surface or root zone layer); n_i is the total duration of drydowns for layer i. n_r is the number of days when both surface and root zone θ identified the same regime (water-limited or energy-limited regimes) and n is the total number of days with valid observations. Both γ and φ range from 0 to 1, where higher values of γ indicate greater persistence of water-limited regime and higher values of φ indicate greater regime similarity.

To determine whether the onset of regime transitions was simultaneous between surface and root zone layers, we computed the conditional expectation $E(\theta_{root} \mid \theta_{surf} = \theta_{crit,surf})$, defined as the mean root zone θ when surface θ approaches its threshold during drydowns (Dong et al., 2022). Specifically, we selected all days on which surface θ fell within a ±3% relative window of surface θ_{crit} and calculated the mean root zone θ for those days. The difference between the root zone θ_{crit} and the conditional expectation was defined as

$$\Delta_{ECSM} = \theta_{crit,root} - E(\theta_{root} \mid \theta_{surf} = \theta_{crit,surf}) \tag{5.6}$$

While φ provides an overall measure of regime similarity, it does not diagnose the ability of surface θ_{crit} to detect root zone water limitation. To address this, we assume that root zone θ_{crit} provides a true approximation of transition onset and that surface θ_{crit} as the detection signal. A two-by-two confusion matrix was then constructed by classifying each valid observation day during drydown into one of four mutually exclusive categories based on whether surface and root zone θ were simultaneously above or below their respective θ_{crit}. This yielded four counts:

1) False alarms counts (FA), defined as days when the surface was in the water-limited regime but the root zone was not ($\theta_{surf} < \theta_{crit,surf}$ and $\theta_{root} \geqslant \theta_{crit,root}$)

2) Missed events counts (ME), defined as days when the root zone was water-limited but the surface was not ($\theta_{root} < \theta_{crit,root}$ and $\theta_{surf} \geqslant \theta_{crit,surf}$)
3) True alarms counts (TA), defined as days when both soil layers were simultaneously water limited ($\theta_{surf} < \theta_{crit,surf}$ and $\theta_{root} < \theta_{crit,root}$).
4) True non-alarms counts (TN), defined as days when both soil layers were simultaneously energy-limited ($\theta_{surf} \geqslant \theta_{crit,surf}$ and $\theta_{root} \geqslant \theta_{crit,root}$).

From the confusion matrix, three performance metrics were derived. False alarm rate (FAR = FA/(FA+TA)), indicates the proportion of days on which surface θ_{crit} falsely warned of root zone water limitation. Missed event rate (MER = ME/(ME+TA)) represents the proportion of root zone water limitations that were not detected by surface θ_{crit}. True alarms rate (TAR = TA/(ME+TA)) represents the proportion of root zone water limitations that were correctly identified by surface θ_{crit}.

A higher FAR indicates that surface θ_{crit} overestimates the frequency of root zone water limitations, while a lower MER accompanied by a higher TAR indicates a greater ability of surface θ_{crit} to capture root zone water limitations.

5.2.6 Drivers of θ_{crit}

A combination of Random Forest and Shapley additive explanation (SHAP) models was utilized to assess the relative importance of variables controlling surface and root zone θ_{crit}. Random forests models were trained to identify key drivers of θ_{crit}. Model performance was evaluated using five-hold cross-validation based on two criteria: RMSE and R^2. The better model has the smaller RMSE and the higher R^2. We first trained a full model including all candidate predictors (all the meteorological variables and soil texture variables available, including sand fraction, clay fraction, AI, mean annual Ta, mean annual P, mean annual RH, mean annual WS, mean annual Rg and mean annual vapor pressure deficit (VPD)), and then iteratively removed the least important variables. If model performance did not improve, the variable was excluded. Finally, the model had six predictors: sand fraction, clay fraction, AI, mean annual Ta, annual Rg, mean annual VPD and mean annual WS .

The selected random forest model was further interpreted using SHAP to quantify the contribution of each predictor to model output. SHAP is a game theory-based approach that assigns an importance value to each predictor for individual predictions, enabling both local and global interpretability. Within this framework, the difference between an individual

prediction and the mean prediction is decomposed into additive contributions from each predictor. Higher SHAP values indicate a stronger positive contribution to θ_{crit}.

5.3 Results

5.3.1 Overall evaluation of surface and root zone θ_{crit}

By deriving rET_0-θ relationship for a total of 179 lysimeters, we identified surface θ_{crit} for 87 lysimeters at 17 sites and root zone θ_{crit} for 86 lysimeters at 16 sites. Not all lysimeters yielded estimates for both layers, resulting in 72 pairs of surface and root zone θ_{crit} at 13 sites (Table C 1, Table C 2).

Among all estimated values, surface θ_{crit} ranged from 0.052 to 0.332 m^3/m^3 and root zone θ_{crit} 0.049 to 0.324 m^3/m^3 (Figures 1a-1d). The highest θ_{crit} was observed at Rietholzbach site for the surface layer and at Rollesbroich site for root zone layers (Table C 1). They are both humid grassland sites. The lowest θ_{crit} for both surface and root zone layers occurred at the humid Stubai site (Table C 1), where a drought experiment was conducted during June-August in 2016.

Overall, root zone θ_{crit} (0.184 ± 0.061 m^3/m^3) was significantly higher than surface θ_{crit} (0.157 ± 0.058 m^3/m^3) ($p < 0.01$, Wilcoxon test; Figure 5.2c). Among the 72 paired estimates, surface and root-zone θ_{crit} were strongly correlated ($r = 0.84$; Figure 5.2d).

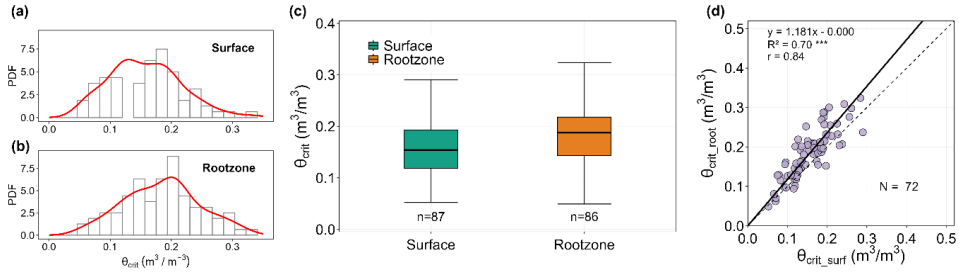


Figure 5.2 (a-b) Probability density functions (PDFs) of θ_{crit} in (a) surface layer and (b) root zone layers, respectively. (c) Comparison of lysimeter-specific θ_{crit} between surface and root zone layers using all valid estimates. (d) Relationship of lysimeter-specific θ_{crit} between surface and root zone layers using all paired values The solid black line represents the reduced major axis (RMA) regression and the dashed line is the 1:1 line. The RMA equation, R^2, two-sided P value for the linear regression slope (regression t-test), and sample size (N) are shown in the panel (***$P < 0.001$).

5.3.2 Comparison surface and root zone θ_{crit} across climates and land covers

We further examined θ_{crit} across different climates and land covers using 72 paired estimates. Surface and root zone θ_{crit} were strongly correlated in both climates, with slightly higher correlation in humid and sub-humid climates (r = 0.88) than in semi-arid climates (r = 0.80, Figure 5.3a, 5.3b). In humid and sub-humid climates, root zone θ_{crit} (0.19 ± 0.073 m^3/m^3) was significantly higher than surface θ_{crit} (0.157 ± 0.056 m^3/m^3, Figure 5.4a), with a difference of 0.034 ± 0.036 m^3/m^3 and a relative difference of 21.4 ± 24.2% (Figure 5.5a, 5.5b). In semi-arid climate, root zone θ_{crit} (0.177 ± 0.039 m^3/m^3) also exceeded surface θ_{crit} (0.158 ± 0.05 m^3/m^3, Figure 4a), but the difference was θaller, as reflected by a lower difference 0.019 ± 0.030 m^3/m^3 and a lower relative difference 16.6 ± 23.2% (Figure 5.5a, Figure 5.5b).

Across land covers, the correlation between surface and root zone θ_{crit} remained high in both grasslands and croplands, 0.89 and 0.84, respectively (Figure 5.3c, 5.3d). Grasslands exhibited a slightly larger offset between root zone (0.191± 0.08 m^3/m^3) and surface θ_{crit} (0.153± 0.058 m^3/m^3) (Figure 5.4b), with a difference of 0.038 ± 0.04 m^3/m^3 and a relative difference of 23.8 ± 27.4% (Figure 5c, 5d). In croplands, root zone θ_{crit} (0.18 ± 0.041 m^3/m^3) is also higher than surface (0.161 ± 0.049 m^3/m^3) (Figure 5.4b), but the difference was smaller. The difference was 0.02 ± 0.027 m^3/m^3 and the relative difference was 15.8 ± 19.6% (Figure 5.5c, 5.5d).

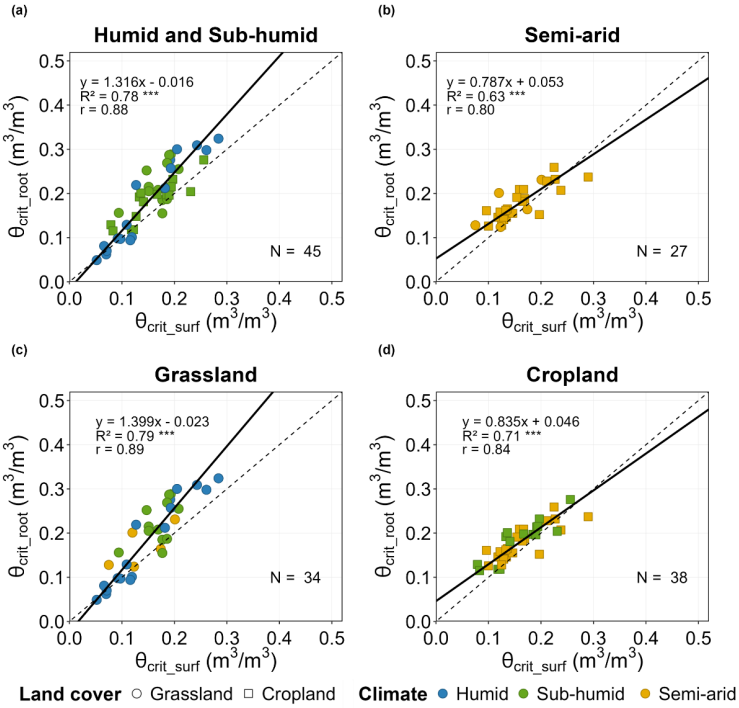


Figure 5.3 Relationship of lysimeter-specific θ_{crit} between surface and root zone layers (a) for humid and sub-humid sites, (b) for semi-arid sites, (c) for grasslands and (d) for croplands. The solid black line represents the reduced major axis (RMA) regression and the dashed line is the 1:1 line. The RMA equation, R^2, two-sided P value for the linear regression slope (regression t-test), and sample size (N) are shown in the panels (***P < 0.001).

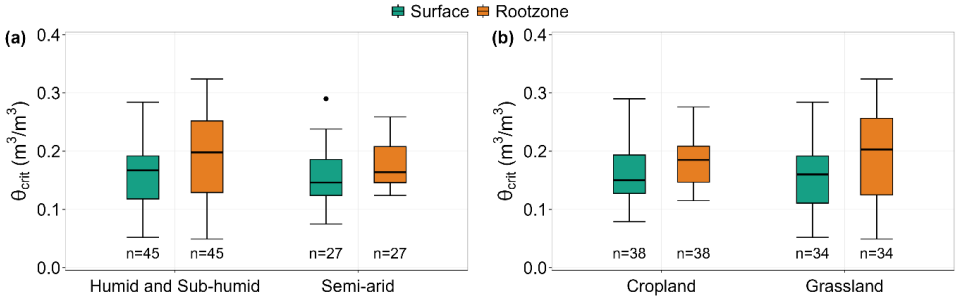


Figure 5.4 Boxplot of lysimeter-specific θ_{crit} for surface and root zone layers using all valid pairs across different (a) climates and (b) land covers.

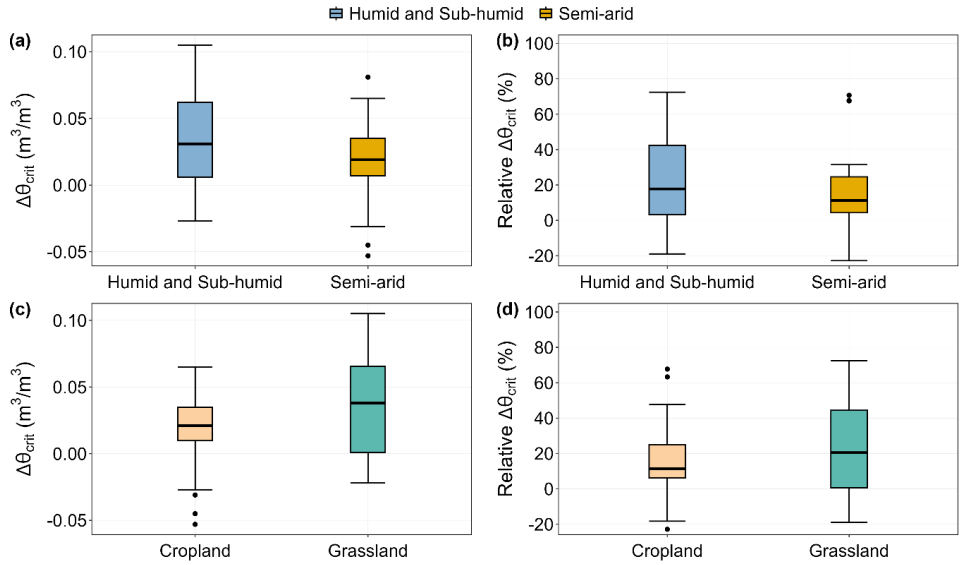


Figure 5.5 Difference and relative difference between surface and root zone θ_{crit} across (a,b) climates and (c,d) land covers.

5.3.3 Consistency between surface and root zone ET_a regime identification

The binary regime similarity (φ) exceeded 0.75 across all lysimeters paired values available, showing consistency between surface and root zone layers in regime identification. However, φ was higher in humid and sub-humid climates than in semi-arid climates and in grasslands than in croplands (Figure 5.6a, 5.6d).

The persistence of water-limited regime (γ) showed generally high correlation between surface and root-zone layers in both humid and sub-humid climates (r = 0.75, Figure 5.6b) and semi-arid climate (r = 0.8, Figure 5.6c). However, γ_{root} was systematically lower than γ_{surf} in semi-arid climate, as evidenced by most points falling below the 1:1 line, whereas the two were more comparable in humid and sub-humid climates. In terms of land covers, γ_{surf} and γ_{root} were strongly correlated and closely aligned with the 1:1 line in grasslands (r = 0.90, Figure 5.6e), but showed a weaker correlation (r = 0.42), where γ_{root} was generally lower than γ_{surf}. This indicates that the root zone spends less time in the water-limited regime than the surface layer does under semi-arid climate and in croplands.

We further examined whether these differences in γ were associated with a temporal offset in the onset of regime transitions between layers. Figure 5.7a shows that the expected root zone

θ when surface θ reaches surface θ_{crit} ($E(\theta_{root} \mid \theta_{surf} = \theta_{crit,surf})$) was highly correlated with root zone θ_{crit} across all lysimeters ($r = 0.94$). However, their difference (Δ_{ECSM}) varied systematically across climates and land cover types. More negative Δ_{ECSM} was observed in semi-arid climate (-0.016 ± 0.02 m^3/m^3) compared to humid and sub-humid climates (-0.001 ± 0.02 m^3/m^3) (Figure 5.7b). Likewise, Δ_{ECSM} was close to zero (0.001 ± 0.02 m^3/m^3) in grasslands, but was more negative (-0.014 ± 0.02 m^3/m^3) in croplands (Figure 5.7c). The near-zero Δ_{ECSM} in humid and sub-humid climates and grasslands indicates that root zone θ generally approached its θ_{crit} when surface θ reached its θ_{crit}. In contrast, the more negative Δ_{ECSM} in semi-arid climate and in croplands indicates that root zone θ generally remained above its θ_{crit} at this point.

We next assessed whether these temporal offsets affected the ability of surface θ_{crit} to identify root zone water limitation. The true alarm rate (TAR) and missed event rate (MER) were comparable across both climates and land cover types (Figure 8). TAR was above 0.9 and MER was around 0.1, indicating that surface θ_{crit} correctly identified more than 90% of the time when the root zone was water limited. However, the false alarm rate (FAR) was significantly higher in semi-arid climate (0.24 ± 0.17) than in humid and sub-humid climate (0.11 ± 0.14, $p<0.01$) and was significantly higher in cropland (0.25 ± 0.15) than in grassland (0.06 ± 0.10, $p<0.01$) (Figure 5.8a, Figure **5.8**d). This indicates that in semi-arid climate and in croplands, surface θ_{crit} was more likely to falsely identify root zone conditions as water limited while the root zone was remained energy limited, as illustrated by lysimeter SE34 (Figure C1).

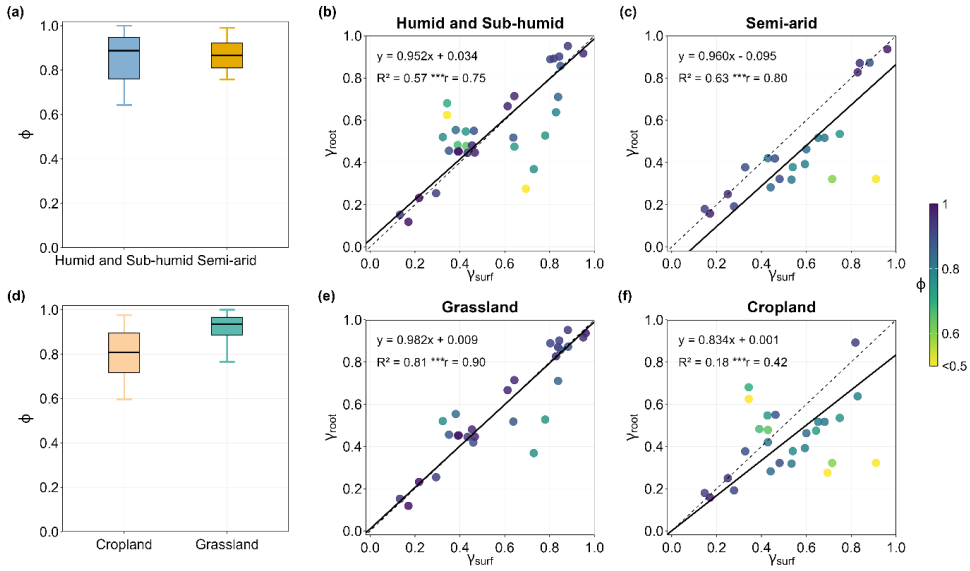


Figure 5.6 Binary regime similarity (φ) between surface and root zone layer across (a) climates and (d) land covers. Scatter plot of the time spent in water-limited regime (γ) for the surface layer (γ_{surf}) against that for the root zone layer (γ_{root}) across different (b-c) climates and (e-f) land covers. The solid black line represents the reduced major axis (RMA) regression and the dashed line is the 1:1 line. The RMA equation, R^2 and two-sided P value for the linear regression slope (regression t-test) are shown in the panels (***P < 0.001).

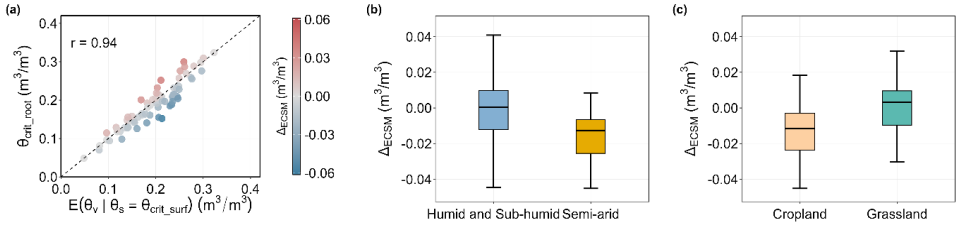


Figure 5.7 (a) Relationship between root zone θ_{crit} and conditionally averaged root zone soil moisture when surface soil moisture reaches surface θ_{crit} ($E(\theta_{root} \mid \theta_{surf} = \theta_{crit,surf})$). (b,c) The differences ($\Delta_{EC\Theta}$) between root zone θ_{crit} and $E(\theta_{root} \mid \theta_{surf} = \theta_{crit,surf})$ across (b) different climates and (c) land cover types.

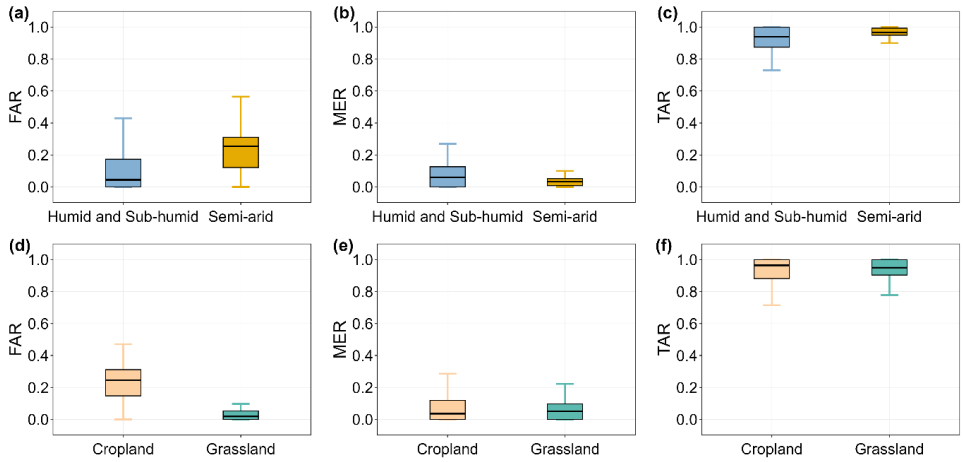


Figure 5.8 Distributions of (a,d) false alarms rate (FAR), (b,e) missed event rate (MER), and (c,f) true alarms rate (TAR) across (a-c) different climates and (d-f) different land covers.

5.3.4 Drivers of surface and root zone θ_{crit}

In this section, we explored whether there are differences in the drivers of surface and root zone θ_{crit}. Soil texture was found to be consistently the dominant factor, with sand fraction ranked as the most important variable controlling θ_{crit} for both surface and root zone layers (Figure 9). Its contribution was greater for root zone than surface θ_{crit} as indicated by higher mean absolute SHAP value in the root zone model. Clay fraction was the second important variable (Figure 9). Both surface and root zone θ_{crit} decreased with increasing sand fraction (Figure 10a, 11a) and increased with increasing clay fraction (Figure 10b. 11b), indicating lower θ_{crit} in coarse-textured soils. Global radiation (Rg) showed similar high mean absolute SHAP values at both depths, followed by air temperature, which contributed more strongly to root zone than to surface θ_{crit} (Figure 9). Both Rg and T_a were positively associated with a higher θ_{crit} for both layers (Figures 10d,f and 11d, f). VPD, wind speed (WS) and aridity index (AI) showed comparatively θaller contributions at both depths (Figure 9). AI was the least important variable for root zone θ_{crit} and the second least important variable for surface θ_{crit}. Nevertheless, both surface and root zone θ_{crit} generally showed a negative dependence on AI, indicating a shift towards lower θ_{crit} under more arid conditions (Figure 10c, 11 c).

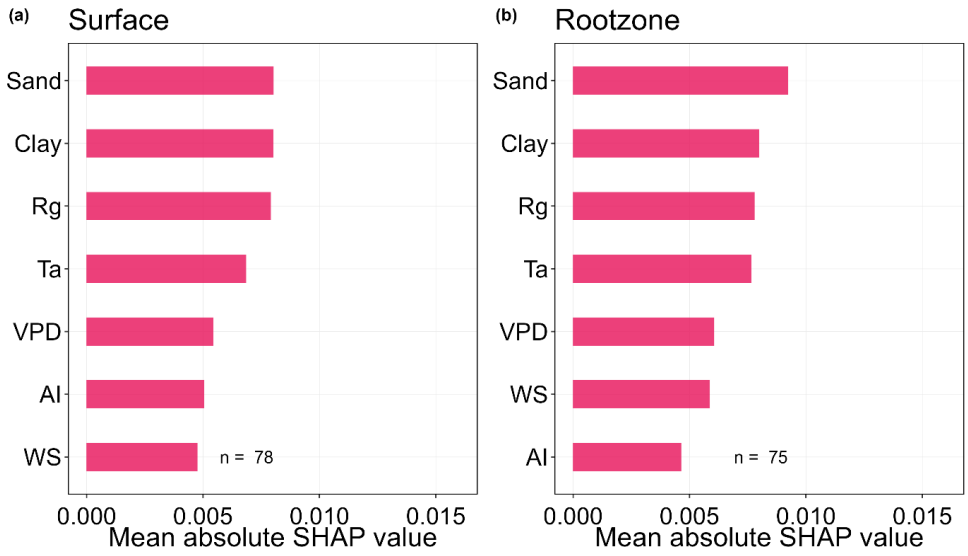


Figure 5.9 Relative importance of factors influencing θ_{crit} for (a) surface layer and (b) root zone layer. The importance was assessed with the mean absolute SHAP value.

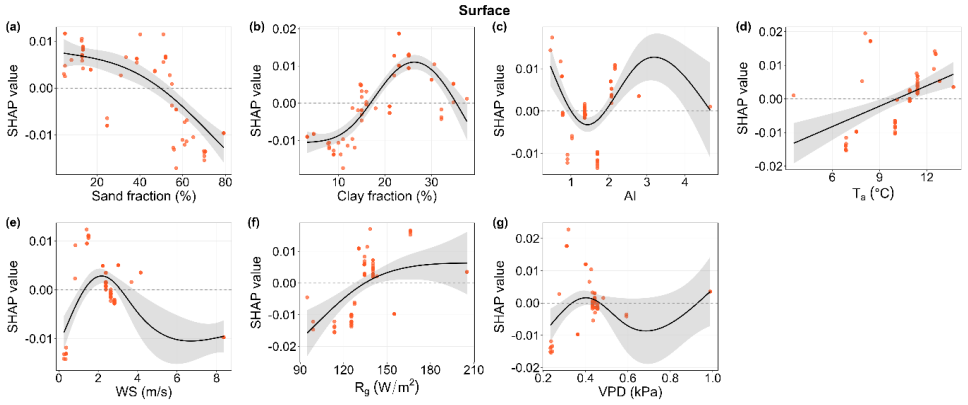


Figure 5.10 Partial dependence plots of the SHAP value for surface θ_{crit} against the seven explanatory variables in (a) sand fraction, (b) clay fraction, (c) aridity index (AI), (d) air temperature (AI), (e) wind speed (WS), (f) global radiation (Rg) and (g) vapor pressure deficit (VPD). Positive and negative SHAP values indicate contributions towards higher and lower predicted θ_{crit}, respectively. The black line shows the fitted line, providing an estimate of the general trend. The shading area indicates the 95% confidence interval.

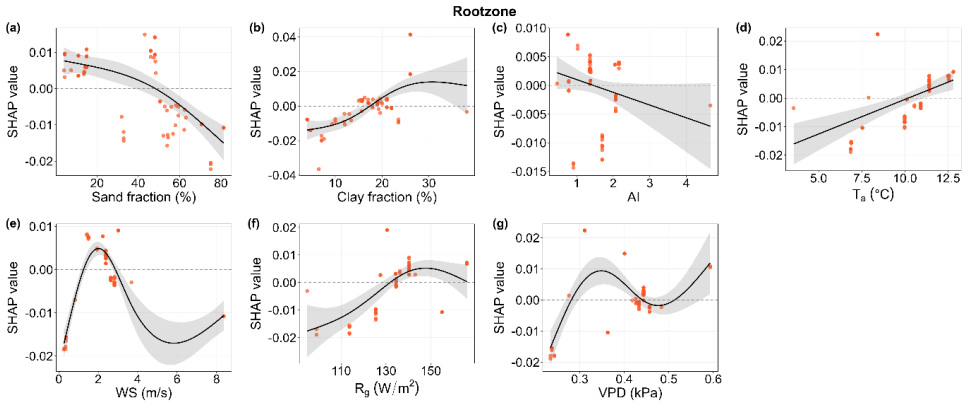


Figure 5.11 Partial dependence plots of the SHAP value for root zone θ_{crit} against the seven explanatory variables in (a) sand fraction, (b) clay fraction, (c) aridity index (AI), (d) air temperature (AI), (e) wind speed (WS), (f) global radiation (Rg) and (g) vapor pressure deficit (VPD). Positive and negative SHAP values indicate contributions towards higher and lower predicted θ_{crit}, respectively. The black line shows the fitted line, providing an estimate of the general trend. The shading area indicates the 95% confidence interval.

5.4 Discussion

In this study, we provided comprehensive insights into surface and root zone θ_{crit} using lysimeter measurements. By integrating in-situ θ observations taken at several depths within the lysimeter profile, we obtained more accurate and reliable root zone θ than the satellite-derived estimates, as the latter require ground validation themselves (Aliyu et al., 2025).

Our study showed that root zone (0-50 to 0-80 cm) θ_{crit} was generally significantly higher than surface (0 - 30 cm) θ_{crit}, yet the two were strongly correlated (r = 0.84), and this correlation held across climates and land covers. This correlation is notably higher than the value of 0.53 reported by Dong et al. (2022), who compared surface (5 cm) and root zone θ_{crit} (0-50 cm) using AmeriFlux data from the continental United States (including 114 sites). Our findings also align with a recent global study based on ERA5 reanalysis data (Paul et al., 2025), which reported a correlation of 0.74 between surface (0-7 cm) and root zone θ_{crit} (0-100 cm). Such high correlation implies a strong spatial consistency between the θ_{crit} of the surface and root zone layers.

However, spatial agreement in θ_{crit} does not necessarily translate into temporal agreement in ET_a regime identification. Although there was a strong overall correlation ($r = 0.94$) between the conditional expectation of root zone θ when surface θ reaches θ_{crit} ($E(\theta root \mid \theta surf = \theta crit,surf)$) and root zone θ_{crit}, which is consistent with previous studies (Dong et al., 2022; Paul et al., 2025), our results revealed that the synchrony between surface and root zone based regime transitions varied substantially across climates and land covers.

In humid and sub-humid climates and grasslands, root zone θ generally approached its threshold when surface θ reached its θ_{crit}, as evidenced by the fact that Δ_{ECSM}, which is the difference between root zone θ_{crit} and $E(\theta_{root} \mid \theta_{surf} = \theta_{crit,surf})$, was close to zero. This indicates that the transition to water-limited regime occurred nearly simultaneously at both layers. Consistent with this, the persistence of water- limited regimes (γ) was comparable between surface and root-zone θ and the false alarm rate (FAR) was low. Under these conditions, surface θ_{crit} can therefore provide a reasonable proxy for identifying the onset and persistence of root zone water limitation.

In contrast, in semi-arid sites and croplands, Δ_{ECSM} was more negative, indicating that root zone θ remained above its threshold when surface θ reached its θ_{crit}. In other words, root zone had not yet transitioned to water-limited regime at the time the surface did. This temporal offset was also reflected in a longer persistence of water-limited conditions at the surface than in the root zone ($\gamma_{surf} > \gamma_{root}$) and a higher FAR. Surface θ more frequently indicated water limitation that were not yet experienced by the root zone. These results highlight that surface θ_{crit} systematically overestimates the frequency and duration of root-zone water limitation in semi-arid climates and croplands.

This contrasting timing patterns among climates may be related to differences in the coupling of surface and root zone θ during drydowns. In humid and sub-humid climates, surface and root zone θ are often strongly hydraulically connected and surface θ variations correlates well with deeper θ variations (Feldman et al., 2023), This leads to more synchronous depletion of surface and root zone θ during drydowns. In semi-arid climates, however, surface and root zone θ may become increasingly decoupled during a drydown. Surface θ can decrease rapidly due to ET losses (McColl et al., 2017; Sehgal et al., 2020), while water remains stored in deeper soil layers after surface θ has been depleted (Pollacco & Mohanty, 2012). Vegetation can access this deeper water through its root system, sustaining transpiration as the surface dries (Fan et al., 2017) and delaying the decline of root zone θ towards root zone θ_{crit} relative to the surface

transition. Notably, the absolute and relative differences between root zone θ_{crit} and surface θ_{crit} were θaller in semi-arid compared to humid and sub-humid climates, which means root zone θ_{crit} is closer to surface θ_{crit} at lower values. Consequently, root zone θ needs to decline further during a drydown before the transition is triggered. This may additionally delay the onset of root zone water limitation.

The land cover differences may partly arise from differences in rooting systems. Grasslands typically develop denser root systems over time, as their roots grow and persist year after year. Whereas in croplands, crops are replanted annually, resulting in less dense root systems (Dupont et al., 2014). The denser grassland roots draw water throughout the profile and help maintain hydraulic connectivity between layers, so surface and root zone θ decline and reach their thresholds at similar times. In croplands, sparser roots weaker vertical coupling, so the surface reaches its θ_{crit} while deeper θ is less efficiently drawn down. In addition, croplands in our dataset only distributed at sub-humid and semi-arid sites, with no humid croplands. Thus climate and land cover are partly confounded. Future studies could include cropland sites in humid climates to disentangle their respective effects on surface and root zone regime transitions.

These findings reveal an important distinction between threshold agreement and regime agreement. While surface θ_{crit} was highly correlated with root zone θ_{crit} across lysimeters, it did not equivalently capture the timing and duration of root zone water-limited ET regimes under all conditions. Surface θ_{crit} can be used as a reliable indicator of root zone water limitation onset in humid and sub-humid climates and grasslands, but tends to systematically overestimate water limitation in semi-arid climates and croplands due to a temporal offset in the onset of water-limited regimes between surface and root zone soil layers. The differences in ET_a regime identification between surface and root zone soil warrants that reliance solely on surface θ_{crit} may lead to biased drought diagnostics. This has implications for satellite-based drought monitoring, where surface θ_{crit} commonly used to infer vegetation water stress (Ahady et al., 2026). It is also consistent with a recent study reporting that Earth System Models can overestimate the frequency of water limitation because of limitations in representing rooting depth, plant water uptake and plant water-use strategies (Giardina et al., 2025). Therefore, knowledge of root zone θ_{crit} is essential for reliable assesθent of ecosystem water limitation. It is worth noting that our dataset captures root zone θ to a maximum depth of 80 cm, whereas many plants can develop their rooting depth considerably deeper, particularly in drier climates

(Stocker et al., 2023). Therefore, the temporal offset between surface and root-zone water limitation observed here may represent a conservative estimate, particularly for deep-rooted vegetation and in more arid climates. In addition, our ability to evaluate this offset under arid climates remains limited. Although our datasets include one arid site, Shapotou station at the southeastern edge of the Tengger Desert in China with AI of 7.3, due to limited data available during drydowns θ_{crit} could not be detected robustly. Therefore, further investigation on root zone θ_{crit} is needed for arid climates.

We further investigated the drivers of surface and root zone θ_{crit}. Soil texture was shown to be the dominant control for both surface and root zone θ_{crit}. Both surface and root zone θ_{crit} showed a negative dependence on sand fraction. In sandy soils, a given soil moisture corresponds to a less negative matric potential than in finer-textured soils, meaning plants can sustain water uptake at lower absolute soil moisture contents. Similar findings have been reported in previous studies, but only for the soil surface layer without focusing on the soil root zone (Denissen et al., 2020; Z. Fu et al., 2024; Shi et al., 2024; Wankmüller et al., 2024).

Increasing AI (i.e., increasing aridity) generally leads to lower θ_{crit}. This can be attributed to the interplay between atmospheric demand and plants. AI represent a long term. Under drier conditions with higher evaporative demand, θ_{crit} should increase as soil water conductivity becomes limiting at higher θ level (Carminati & Javaux, 2020; Feldman et al., 2019).Thus, the observed decrease in θ_{crit} would imply an overcompensation by vegetation, by extending root length, directing root growth towards wetter zones or, in the case of grasslands, changing its composition towards more drought-tolerant plant species (Jarvis et al., 2022).

In contrast to previous findings that suggested a negative relationship between θ_{crit} and vapor pressure deficit (VPD) and a negative relationship between θ_{crit} and global radiation (Feldman et al., 2019; Z. Fu et al., 2024; Paul et al., 2025), we found that higher VPD and higher radiation were both associated with higher θ_{crit}, which is consistent with the demand-side control as mentioned above, whereby greater atmospheric evaporative demand increases the water flux required to sustain ET, causing water limitation to emerge at higher θ level.

As evidenced by recent studies, current Earth System Models still inadequately capture the θ_{crit} variability and show uncertainties in drought projection (Dong et al., 2025; Ji et al., 2024; Ukkola et al., 2016). These biases stem largely from limitations in the model representation of ET_a - θ relationships (Giardina et al., 2025). Earth System Models tend to assume a fixed θ_{crit}

tied to plant functional types (Poulter et al., 2015). However, plants may adopt more water-efficient strategies to survive drought, particularly in arid areas (Anderegg et al., 2013). For example, they may reduce their leaf area index and downregulate stomatal conductance. Such adaptive mechanisms have not been adequately parameterized or fully integrated in the models. Incorporating θ_{crit} as a function of soil, climate and vegetation into models to better capture the ET_a - θ relationships would be a valuable focus for future model development.

5.5 Conclusion

Our study provides a systematic comparison of surface and root zone θ_{crit} and their associated ET_a regimes across a large lysimeter dataset. Surface and root zone θ_{crit} showed strong correlation ($r = 0.84$) and generally similar environmental controls, with soil texture emerging as the dominant driver at both depths. These results demonstrate that surface θ_{crit} contains substantial information on the spatial variability of root zone θ_{crit}.

However, agreement in θ_{crit} did not necessarily imply agreement in when water limitation occurred. In humid and sub-humid climates and grasslands, surface and root zone θ approached their respective thresholds nearly synchronously, resulting in comparable persistence of water-limited conditions. In semi-arid climates and croplands, surface θ more frequently reached its threshold while root zone θ remained above its θ_{crit}. The resulting lag in root zone transition led to greater persistence of water limitation at the surface and a higher frequency of false alarms when surface θ was used to represent root zone status. Thus, the reliability of surface θ_{crit} for diagnosing root zone water limitation depends not only on the correspondence between surface and root zone θ_{crit}, but critically on whether the two layers reach their respective thresholds synchronously.

These findings have direct implications for drought monitoring based on surface θ observations. Surface θ_{crit} can provide a useful proxy for the spatial variation of root zone θ_{crit}, but surface θ_{crit} should not be interpreted as the onset of root-zone water limitation, especially in more arid climates and croplands. Our results highlight the importance of distinguishing agreement in θ_{crit} from agreement in its timing is essential when diagnosing ecosystem water limitation from surface observations

Chapter 6. Conclusions and outlook

6.1 Conclusions

Actual evapotranspiration (ET_a) is a fundamental component of the hydrological cycle and plays a central role in the water, energy and carbon cycles. Weighable lysimeters, regarded as the most precise in situ method for quantifying ET_a, provide essential insights into the complex dynamics of the soil–plant–atmosphere continuum. The overarching objective of this thesis was to explore the potential of weighable lysimeters in improving the understanding of ET_a and the associated critical soil moisture threshold (θ_{crit}), the soil moisture (θ) at which ET_a shifts from an energy-limited to a water-limited regime.

This thesis highlighted that despite the inherently θall surface area of weighable lysimeters (~1 m^2), lysimeter ET_a measurements can provide information at much larger scales, as indicated by comparable spatial correlations of ET_a measured by lysimeters between different locations and those of ET_a measured by eddy covariance (EC) between different locations at the plot scale, landscape scale and larger regional scale. This implies that lysimeter ET_a can potentially be used for upscaling, and therefore for example, for validating land surface models. This also has implications for the design of lysimeter networks. Compared to the EC technique, lysimeters can estimate ET_a more precisely and uniquely quantify other water balance components (rainfall, non-rainfall, percolation, capillary rise), but they require higher maintenance costs. The similar spatial representativity of ET_a measurement by lysimeters and EC suggests that lysimeters could be collocated with EC towers to develop a larger monitoring network at a relatively low cost with higher measurement accuracy. However, the parallel measurements by lysimeters and EC towers are limited in this thesis, particularly the lack of water-limited sites, and the land cover of EC sites and the vegetation on lysimeters are not fully compatible. Future research should therefore further assess the spatial representativity of lysimeter-based ET_a across different landscapes and conditions to confirm their suitability for upscaling and to support the design of efficient, cost-effective monitoring networks.

The thesis further demonstrated the robustness of θ_{crit} estimated from lysimeter measurements with respect to different definitions of ET_a and fitting functions. All three definitions (evaporative fraction, the ratio of ET_a to grass reference ET, the ratio of ET_a to calculated potential ET) and two fitting functions (linear plus plateau function and a spherical variogram function) showed good consistency, indicating the applicability of each of the three definitions

or the two fitting curve frameworks. However, the thesis emphasized that root zone θ_{crit} was found to be higher than surface θ_{crit}, yet they are strongly correlated across all climate regimes, suggesting that while θ_{crit} values corresponding to different measurement depths should not be directly compared to each other, they might still serve as proxies of each other.

The influence of soil, vegetation, climate and environmental conditions on surface and root zone θ_{crit} was also evaluated in this thesis. A multiple linear regression analysis demonstrated that increasing sand fraction was associated with lower θ_{crit}, with a decline of approximately 0.01 m^3/m^3 per 10 % increase in sand fraction. In contrast, increasing aridity index (AI, mean annual grass reference ET divided by mean annual precipitation) led to higher θ_{crit}, with θ_{crit} increasing by about 0.08 - 0.13 m^3/m^3 per unit increase in AI. While θ_{crit} differed between croplands and grasslands, land cover was a less influential driver than sand fraction and aridity index. In addition, higher potential evapotranspiration and higher vapor pressure deficit could lead to lower θ_{crit} in both surface and root zone layers. These findings provide mechanistic insights into θ_{crit}, enabling it to be interpreted as a comprehensive function of soil, vegetation, climate, and environmental conditions and helping to identify the potential tipping points where water stress begins to impair ecosystem functions.

6.2 Outlook

The insights gained from this thesis suggest several promising avenues for future research. As mentioned above, including more concurrent measurements by lysimeters and EC towers is suggested to further assess the spatial representativity of lysimeter-based ET_a across various landscapes and conditions. Additionally, wavelet coherence analysis indicated that lysimeter ET_a can be reliably extended over spatial scales using neighboring site data, especially when considering temporal lags and seasonal dynamics. Accurate prediction of ET_a across locations requires not just knowledge of the strength of correlations between sites, but also about the lag time between their responses, which reflect the timing differences in hydrological or meteorological drivers, such as precipitation, radiation, and soil moisture. Seasonal differences in coherence are also crucial. For example, strong coherence during summer suggests that we can confidently use lysimeter data to estimate ET_a over a wider area during that season, whereas lower coherence in winter suggests more caution is needed in extending site-specific ET_a data to larger scales. Future research can aim to further explore the temporal patterns of the

coherence between sites and the underlying drivers that influence the coherence. Such analysis should not be confined to lysimeter ET_a measurements, but can also include other ET_a observations like measurements from EC or Bowen ratio systems. A deeper understanding of these coherence and factors can ultimately support the development of more efficient and diverse ET_a monitoring strategies, reducing reliance on dense and costly measurement networks.

In parallel, this work derived the lysimeter observation based θ_{crit} for surface and root zone soil as well as their influencing factors using 177 lysimeters, highlighting the potential of lysimeter measurements for estimating θ_{crit}. Future studies could expand the number of lysimeter sites to cover a wider range of climatic, soil, and land cover types. Since the factors considered in this thesis (e.g., sand fraction, AI and land cover types) only explained about 50% of the variance in θ_{crit} based on multiple linear regression analysis, additional climatic, edaphic and biotic variables such as soil hydraulic conductivity, leaf area index, canopy biomass and plant functional type could be included to facilitate a more comprehensive analysis of the drivers. Moreover, more advanced approaches, such as machine learning models or explainable AI methods, could be applied to disentangle and quantify the relative importance of different drivers of θ_{crit}.

The measurements of root zone θ in this thesis were limited to depths less than 80 cm due to the restricted depth of lysimeters, which may not fully capture the actual rooting depth. Global observations indicate that rooting depths vary widely across ecosystems, with some vegetation accessing water from depths exceeding 25 m (Stocker et al., 2023). In situ θ measurements are the only observations that extend into the root zone relevant to vegetation and are therefore considered as the ground truth (Bessenbacher et al., 2023; Gruber et al., 2013). In recent years, a growing number of regional soil moisture networks have measured θ at many sites and several depths, reaching up to 2 m (Mittelbach et al., 2011). For example, International Soil Moisture Network (ISMN) currently represents the most comprehensive global collection of such in situ θ data (Dorigo et al., 2021). Taking advantage of these in situ θ could provide unique insights on the root zone regime dynamics. In addition, given that roots extract water from the soil profile in a non-uniform way (Baldocchi et al., 2004), other approaches to estimating root zone θ from θ measurements at multiple depths, such as weighting θ by the probability distribution of roots by depth, can be applied to offer a more realistic representation of root zone θ.

As evidenced by recent studies, current Earth System Models still inadequately capture the θ_{crit} variability and show uncertainties in drought projection (Dong et al., 2025; Ji et al., 2024; Ukkola et al., 2016). These biases stem largely from limitations in the model representation of ET_a - θ relationships (Giardina et al., 2025). Earth System Models tend to assume a fixed θ_{crit} tied to plant functional types (Poulter et al., 2015). However, plants may adopt more water-efficient strategies to survive drought, particularly in arid areas (Anderegg et al., 2013). For example, they may reduce their leaf area index and downregulate stomatal conductance. Such adaptive mechanisms have not been adequately parameterized or fully integrated in the models. Incorporating θ_{crit} as a dynamic function of soil, climate, vegetation and environmental conditions into models to better capture the ET_a - θ relationships would be a valuable focus for future model development.

Given the demonstrated value of lysimeters in quantifying ET_a and θ_{crit}, establishing a global observational network is needed. Current in situ lysimeter observations remain scarce, especially in “hot spots” regions such as Sahel and Amazon basin. These regions are highly vulnerable in terms of water resources and climate change, yet large discrepancies in ET_a - θ among model simulation were noted in these regions (Hsu & Dirmeyer, 2023b; Lei et al., 2018). As mentioned above, lysimeter ET_a could provide information at spatial scales comparable to ET_a from EC. Strategically designing an observation network that integrates lysimeters with EC towers will enable cross-validation and a broader-scale extension, thereby bridging the gap between site-level observations and regional-to-global modellin

Appendix

Appendix A

Table A.1 Start and end of the snow cover period observed for the lysimeters at the Rollesbroich (RO) site. "/" means no records. The information is from the camera surveillance system near the lysimeters.

Year	Start	End
2015	/	/
2016	14.01.2016	25.01.2016
	09.02.2016	17.02.2016
	04.03.2016	11.03.2016
2017	01.01.2017	29.01.2017
	11.12.2017	30.12.2017
2018	02.02.2018	09.03.2018
	12.12.2018	17.12.2018
2019	08.01.2019	09.01.2019
	17.01.2019	02.02.2019
	12.03.2019	14.03.2019
	07.12.2019	13.12.2019
2020	25.02.2020	01.03.2020
	29.03.2020	30.03.2020
	10.12.2020	13.12.2020
	31.12.2020	31.12.2020

Table A.2 Start and end of the snow cover period observed for the lysimeters at the Wüstebach (WU) site. The information is from the camera surveillance system near the lysimeters.

Year	Start	End
2015	01.01.2015	09.01.2015
	17.01.2015	08.03.2015
2016	13.01.2016	25.01.2016
	09.02.2016	17.03.2016
	24.04.2016	29.04.2016
2017	01.01.2017	03.02.2017
	23.11.2017	30.12.2017
2018	16.01.2018	24.01.2018
	01.02.2018	09.03.2018

2019	12.12.2018	18.12.2018
	08.01.2019	11.01.2019
	17.01.2019	08.02.2019
	11.02.2019	14.02.2019
	11.03.2019	14.03.2019
	07.12.2019	13.12.2019
2020	25.02.2020	04.03.2020
	29.03.2020	30.03.2020
	10.12.2020	13.12.2020
	24.12.2020	31.12.2020

Table A.3 Start and end of the snow cover period observed on the lysimeters at the Graswang (GW) site.

Start	End
01.01.2015	10.04.2015
21.11.2015	31.03.2016
27.11.2016	05.03.2017
10.11.2017	31.03.2018
08.12.2018	20.03.2019
01.12.2019	10.03.2020
01.12.2020	31.12.2020

Table A.4 The percentage of gap-filled hourly data for each month over 2015-2020. The units are "%".

Month	RO		WU		SEro	SEwu	SEse	SE	GW	
	ET-LYS	ET-EC	ET-LYS	ET-EC	ET-LYS	ET-LYS	ET-LYS	ET-EC	ET-LYS	ET-EC
Jan	46.1	45.3	49.3	78.5	11.8	10.8	7.0	22.7	100.0	58.9
Feb	39.8	38.2	46.8	72.2	13.6	15.8	10.0	20.3	100.0	47.4
Mar	21.3	32.9	26.5	58.3	6.8	10.3	5.7	18.0	81.1	38.0
Apr	5.7	18.5	6.4	45.0	5.0	7.7	2.6	19.4	30.1	37.8
May	2.7	20.8	4.0	48.4	4.2	7.4	3.0	12.6	31.5	40.7
Jun	4.1	19.5	2.9	36.1	4.5	6.5	4.9	26.4	31.6	31.7
Jul	9.6	16.3	3.4	38.2	8.5	10.5	6.6	28.0	29.1	29.6
Aug	3.1	22.6	8.6	42.2	6.4	8.8	6.2	16.3	28.8	27.6
Sep	6.6	26.2	5.5	40.3	6.5	8.4	5.6	18.4	30.5	29.3
Oct	7.6	34.7	5.4	62.8	5.6	7.3	3.7	21.0	41.1	34.3
Nov	8.6	40.4	8.4	67.7	5.9	6.9	3.1	23.4	57.0	38.1
Dec	14.3	43.6	22.2	72.6	7.7	8.5	5.9	25.2	98.7	57.2
Sum	14.0	29.9	15.6	55.2	7.2	9.0	5.3	21.0	54.8	39.2

Table A.5 The percentage of gap-filled hourly data during daytime and nighttime for each year over 2015-2020. Daytime and nighttime defined based on sunrise and sunset.

Site	Year		2015	2016	2017	2018	2019	2020	Mean
RO	Gap-filled ET-LYS [%]	daytime	7.5 (±1.19)	5.5 (±0.44)	5.2 (±0.35)	7.7 (±0.32)	8.8 (±4.59)	3.4 (±0.43)	6.3 (±1.99)
		nighttime	8.7 (±1.24)	5.9 (±0.26)	7.6 (±0.12)	9.9 (±0.16)	9.7 (±5.21)	4.4 (±0.53)	7.7 (±2.19)
	Gap-filled ET-EC [%]	daytime	11.1	12.2	11.5	8.9	11.3	9.4	10.7
		nighttime	19.3	20.6	21.7	17.7	17.9	17.9	19.2
WU	Gap-filled ET-LYS [%]	daytime	6.2 (±0.69)	7.9 (±0.66)	6.9 (±0.63)	7.7 (±0.83)	6.7 (±0.71)	5.3 (±1.39)	6.8 (±0.96)
		nighttime	6.0 (±0.30)	8.6 (±0.26)	10.3 (±0.29)	11.1 (±0.62)	9.7 (±0.4)	7.7 (±0.63)	8.9 (±1.88)
	Gap-filled ET-EC [%]	daytime	22.4	21.9	28.1	29.3	21.8	19.9	23.9
		nighttime	29.1	29.1	36.1	36.0	29.1	28.0	31.2
SE	Gap-filled ET-LYS (SEse) [%]	daytime	5.2 (±1.71)	3.2 (±0.61)	3.3 (±1.98)	2.7 (±0.37)	2.9 (±0.66)	1.7 (±0.34)	3.2 (±1.16)
		nighttime	2.7 (±0.33)	2.3 (±0.45)	3.0 (±1.01)	2.6 (±0.28)	1.2 (±0.13)	1.3 (±0.58)	2.2 (±0.76)
	Gap-filled ET-LYS (SEro) [%]	daytime	6.4 (±1.84)	3.8 (±0.56)	2.6 (±0.17)	1.8 (±0.19)	4.0 (±0.36)	2.0 (±0.39)	3.4 (±1.71)
		nighttime	6.1 (±2.83)	4.5 (±1.01)	3.2 (±0.25)	2.3 (±0.73)	4.2 (±0.48)	2.3 (±0.16)	3.8 (±1.45)
	Gap-filled ET-LYS (SEwu) [%]	daytime	6.5 (±4.8)	3.9 (±0.52)	2.5 (±0.75)	2.8 (±0.55)	5.4 (±1.48)	3.1 (±0.63)	4.0 (±1.60)
		nighttime	6.1 (±1.93)	5.1 (±0.56)	3.3 (±0.54)	4.1 (±1.10)	7.0 (±1.16)	4.3 (±0.15)	5.0 (±1.37)
	Gap-filled ET-EC [%]	daytime	7.0	7.3	9.0	6.3	6.6	12.1	8.1
		nighttime	12.5	13.1	13.3	12.2	11.6	14.7	12.9
GW	Gap-filled ET-LYS [%]	daytime	24.2 (±0.13)	19.0 (±0.15)	19.1 (±0.94)	21.9 (±0.73)	28.0 (±1.27)	32.8 (±0.78)	24.2 (±5.41)
		nighttime	25.7 (±0.43)	22.5 (±0.47)	24.0 (±2.06)	23.2 (±0.62)	26.1 (±1.71)	26.9 (±0.94)	24.7 (±1.75)
	Gap-filled ET-EC [%]	daytime	13.9	14.1	13.9	32.3	10.8	10.2	15.9
		nighttime	25.4	25.1	24.5	25.0	19.6	20.6	23.4

Table A.6 Crop information for the lysimeters in Selhausen filled with soil from Selhausen (SEse).

Crop type	Date of sowing	Date of harvest
Winter wheat	15.10.2014	21.07.2015
Winter Barley	07.10.2015	08.07.2016
winter rye	11.10.2016	21.07.2017
summer oat	15.03.2018	24.07.2018
Winter wheat	05.11.2018	24.07.2019
Winter Barley	30.09.2019	07.07.2020
winter rye	20.10.2020	04.08.2021

Table A.7 Crop information for the EC field at Selhausen (SE).

Crop type	Sowing	Harvest
winter wheat	25.10.2014	02.08.2015
winter barley	29.09.2015	20.07.2016
sugar beet	31.03.2017	05.10.2017
winter wheat	25.10.2017	16.07.2018
Potato	26.04.2019	17.10.2019
Winter wheat	26.10.2019	28.07.2020

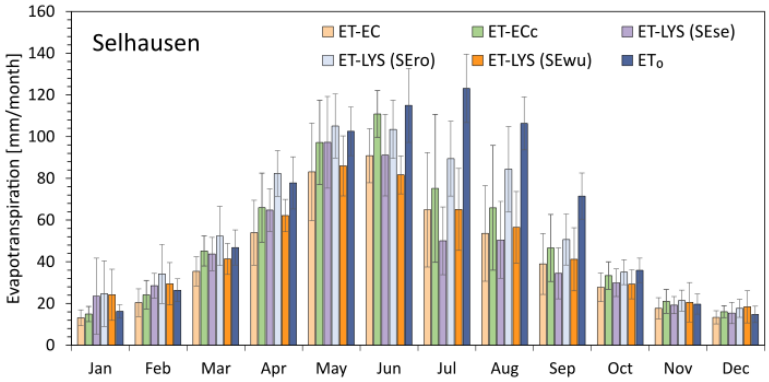


Figure A.1 Average monthly cumulative ET-LYS for different lysimeter groups, ET-EC, ET-ECc and ET_0 at Selhausen (SE) site, calculated over the period 2015-2020. Error bars denote the standard deviations of monthly ET, calculated over the years.

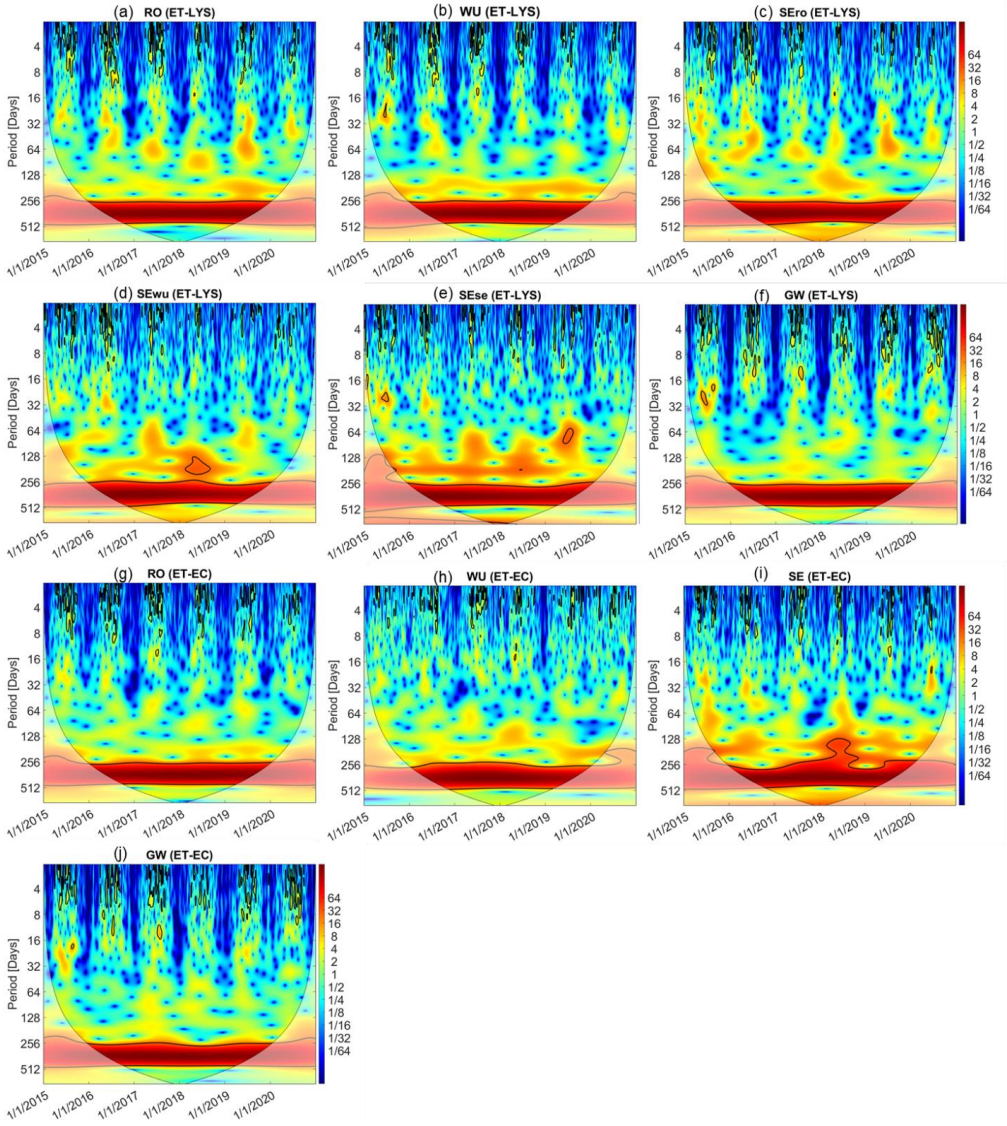


Figure A.2 Continuous wavelet transform (CWT) for the six daily ET-LYS series and four daily ET-EC series for years 2015 – 2020. The contours indicate 95% confidence levels. Thin solid lines delineate the cones of influence. The color denotes the strength of wavelet power.

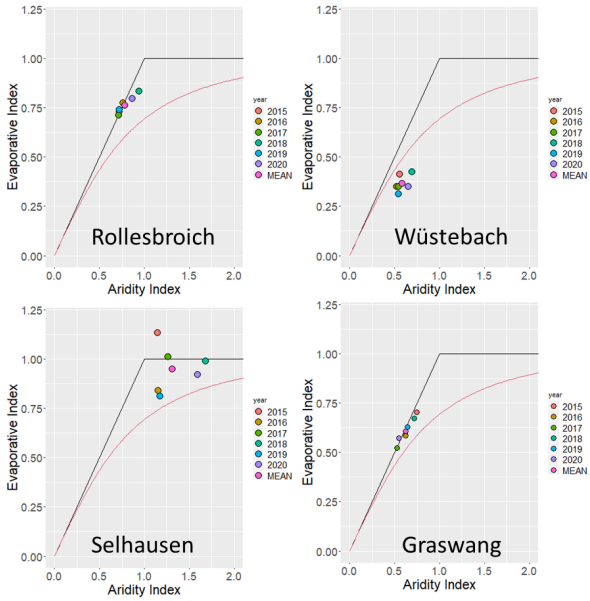


Figure A.3 Budyko plots for the 4 sites during 2015-2020. This was done using the mean daily ET-LYS from multiple lysimeters at the same site.

Appendix B

Appendix B.1

Direct measurement of the soil heat flux at the soil surface (G_0) is difficult because soil heat flux (SHF) plates have to be buried at a certain depth in the soil (Gao et al., 2017). The calorimetric method is a common way to determine G_0 from the in-situ SHF measurements (Liebethal et al., 2005; Ding et al., 2010):

$$G = G_z + \Delta S \tag{B.1}$$

$$\Delta S = \frac{T_{s,i} - T_{s,i-1}}{t} d(\rho_b C_s + \rho_w C_w \theta) \tag{B.2}$$

where G_z is the measured soil heat flux at a depth of z. d is the depth of the layer above the SHF plate and ΔS is the heat storage of this layer. G_0 is equal to G when d is equal to z. t is the time interval (3600s in this study), $T_{s,i} - T_{s,i-1}$ is the difference of soil temperature in the soil layer between time steps i and i-1 during the time interval (K). θ is the volumetric soil moisture content in the soil layer (m^3/m^3). ρ_w is water density (1.0×10^3 kg m^{-3}) and C_w is the specific heats for water (4190 J kg^{-1} K^{-1}). ρ_b is soil dry bulk density (kg m^{-3}), and C_s is the specific heat for soil solid portion (J kg^{-1} K^{-1}) and hence $\rho_b C_s$ is the volumetric heat capacity for the dry part (J K^{-1} m^{-1}).

However, different input data sets may cause uncertainty in the estimation of G_0. Therefore, we conducted a sensitivity analysis of the calorimetric method for G_0 estimation using different input data sets by comparing the calculated G and the measured G.

We selected Rollesbroich site as a test site, because it has the most required measured variables among our study sites and is equipped with six lysimeters and an eddy covariance tower with corresponding conditions. The soil cores in the lysimeters originated from the source area of the nearby EC stations. The vegetation on the lysimeters and EC field is grass. In each lysimeter, one SHF plate was installed at 10 cm depth to measure soil heat flux (G_{10}). In addition, at the same depth (10 cm), soil temperature (T_{s_10}) and soil water content (θ_{10}) were measured by at a temporal resolution of 10 min. At the field, soil temperature and soil water content were measured at 5 cm depth (T_{s_05} and θ_{05}, respectively), and soil heat flux was measured among others at 3 cm depth (G_{03_obs}). Soil properties such as soil texture and organic matter content are also available.

We proposed 4 approaches to calculate G_0 from G_{10} utilizing calorimetric method but with different input data sets considering different scenarios of data availability. The four approaches are described briefly in the following and the required inputs for each approach are provided in Table B.1. In order to compare the estimation with ground truth measurements, G_{03_obs} was deployed as a reference to assess the four approaches. Therefore, soil heat flux at 3 cm (G_{03_est}) was estimated in the testing phase rather than G_0. In this case, d in the Equation B.2 is 0.07m.

Approach 1 (A1): G_{03_est} in this approach was based on the Equations B.1 and B.2. T_{s_05} and θ_{05} were used for the calculation.

There are no measurements on ρ_b, but ρ_b can be calculated from porosity (p):

$$\rho_b = (1 - p) * \rho_s \tag{B.3}$$

where ρ_s is particle density (2.65 kg m^{-3}). p is porosity, which can be deduced from the maximum daily θ_{05}. We assumed that all the soil pores are full of water when θ_{05} is at its maximum. Therefore, p is 0.48 hence ρ_b is 1.38 kg m^{-3}.

No measurements on C_s either. However, Wang et al. (2019) proposed an equation to estimate C_s:

$$C_s = 0.719 + 0.076 f_{clay} + 0.016 OM - 0.023 f_{clay} OM \tag{B.4}$$

where f_{clay} is the clay content (%) and OM is organic matter content (g $100g^{-1}$). In this study, f_{clay} and OM are 16% and 4.46 g $100g^{-1}$ for the 7 cm layer above the SHF plate in the lysimeter, respectively. Therefore C_s is 0.79×10^6 J $K^{-1}m^{-3}$.

Approach 2 (A2): Similar as Approach 1, but $\rho_b C_s$ was assumed to be 1.42×10^6 J $K^{-1}m^{-3}$ instead of estimating ρ_b and C_s separately.

Approach 3 (A3): In this approach, calorimetric method was still applied, while T_{s_10} and θ_{10} are considered, ρ_b and C_s are estimated using Equations B.3 and B.4 as approach 1.

Approach 4 (A4): Similar as approach 3, but $\rho_b C_s$ was assumed as 1.42×10^6 J $K^{-1}m^{-3}$ instead of estimating ρ_b and C_s separately.

Table B.1 Overview of the approaches

Approach	Input variables	Calculation
A1	G_{10}, T_{s_05}, θ_{05}, f_{clay}, OM	Equations B.1, B.2, B.3 and B.4
A2	G_{10}, T_{s_05}, θ_{05}	Equations B.1, B.2 $\rho_b C_s = 1.42 \times 10^6$ J K^{-1}m^{-3}
A3	G_{10}, T_{s_10}, θ_{10}, f_{clay}, OM	Equations B.1, B.2, B.3 and B.4
A4	G_{10}, T_{s_10}, θ_{10}	Equations B.1, B.2 $\rho_b C_s = 1.42 \times 10^6$ J K^{-1}m^{-3}

Our study period focused on daytime (9:00 – 17:00) from April to September from 2013-2021. G_{03_est} was calculated by each approach separately on an hourly basis and then averaged to the daytime values. We evaluated the accuracy of the applied approaches using root mean square error (RMSE) and the normalized mean error (NME). For a data set with N data points:

$$RMSE = \sqrt{\frac{\sum_1^N (G_{03_est} - G_{03_obs})^2}{N}} \quad \text{(B.5)}$$

$$NME = \frac{\sum_1^N |G_{03_obs} - G_{03_est}|}{\sum_1^N |G_{03_obs}|} \times 100\% \quad \text{(B.6)}$$

Figure B.1 presents the scatterplot of G_{03_obs} and G_{03_est} by difference approaches as well as the measured G_{10} in the lysimeter taking one lysimeter (RO11) as an example. Table B.2 reports the performance of the approaches. The results showed that G_{10} and G_{03_obs} deviated significantly from the 1:1 line (Figure B.1) and had the largest NME and RMSE (52.9% and 10.8 W m^{-2}, respectively; Table B.2). This indicates the need to correct G_{10} towards G_0 to avoid systematic bias. From Table B.2 it can be seen that the performance of each lysimeter was similar, indicating the replications work well. The four approaches show similar performance, with Approach 2 achieving the lowest NME (32.7%) and RMSE (7.4 W m^{-2}) and Approach 4 the highest (35.4% and 8.4 W m^{-2}, respectively). In conclusion, the four approaches all can be used to estimate G_0 given their similar performance.

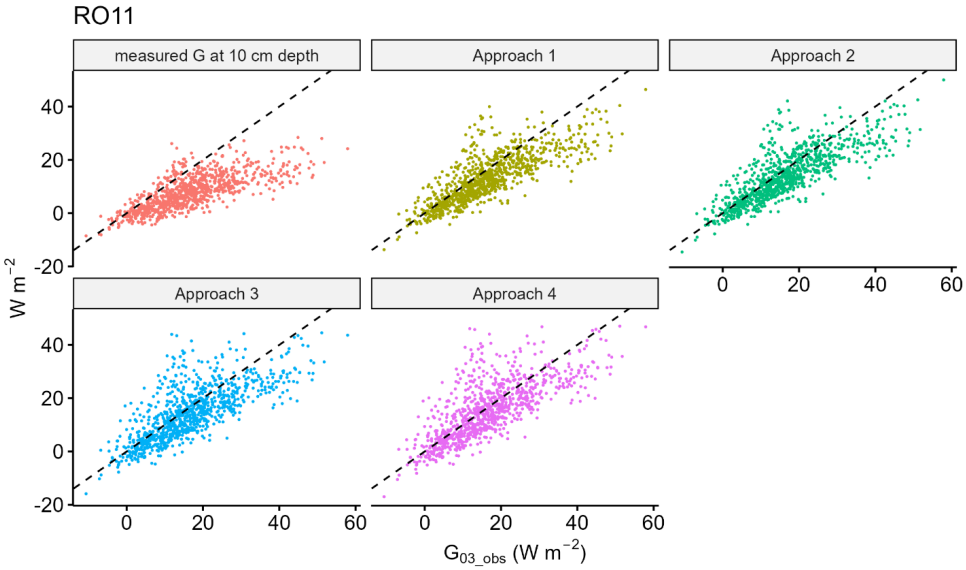


Figure B.1 Scatterplots comparing the measured G at 3 cm depth at the field (G_{03_obs}) and the measured G at 10 cm depth in the lysimeter (G_{10}, upper left panel) as well as the estimated G (G_{03_est}) by the four approaches for daytime from April to September for one lysimeter (RO11) at the Rollesbroich site. The dashed line is a 1:1 line.

Table B.2 Summary of approach performance indicated by the statistical metrics. RO11 to RO16 indicate the statistical metrics for each lysimeter. Mean and Sd refer to the average and standard error for NEM or RMSE for all the lysimeters, respectively. The unit for NME is % and for RMSE is W m^{-2}.

Lysimeter	RO11		RO12		RO13		RO14		RO15		RO16		Mean (Sd)	
Approach	NME	RMSE	NME	RMSE	NME	RMSE	NME	RMSE	NME	RMSE	NME	RMSE	NME	RMSE
G_{10}	55.1	11.5	48.8	9.8	56	11.4	56.8	11.6	48.3	9.8	52.6	10.8	52.9 (±3.7)	10.8 (±0.8)
A1	34.2	7.4	31.1	6.9	34.9	7.7	39	8.4	30.5	6.6	35.1	8	34.1 (±3.1)	7.5 (±0.7)
A2	32.1	7.1	30.4	6.9	33.1	7.5	37.6	8.3	29.2	6.6	33.9	7.9	32.7 (±2.9)	7.4 (±0.6)
A3	36.6	7.9	34.5	8	33.4	7.7	38.6	8.6	31.6	7.5	37.7	8.9	35.4 (±2.7)	8.1 (±0.5)
A4	35.9	8	36.4	8.5	32.7	7.9	38.2	8.8	32.1	7.8	37.3	9.2	35.4 (±2.5)	8.4 (±0.6)

Appendix B.2

Table B.3 Summary of sowing dates of crops at lysimeter sites and the information of similar crop in FAO-56.

Actual crops on the lysimeters		Reference crop in FAO-56					
Crop	Sowing date	Crop	Plant date	Region	Total length	Mid season stage length	Crop coefficient for mid-season stage
winter wheat	Sep/Oct/Nov	Winter Wheat	October	Idaho, USA	335	75	1.15
winter barley	Sep/Oct						
winter canola	Aug/Sep						
winter rye	Sep/Oct						
oats	March/Apr	Barley/Oats/Wheat	March/Apr	35-45 °L	135	60	1.15
Persian clover (first cut)	March	Alfalfa, 1st cutting cycle	Jan Apr (last - 4°C)	Idaho, USA.	75	25	1.2
Persian clover (second cut)	Jun	Alfalfa, other cutting cycles	Jun	Idaho, USA	45	10	0.95

Table B.4 Site-specific crop information including the recorded crop types, sowing dates, harvest dates as well as the estimated start and end dates of the mid-season stage at the Selhausen (SE) site from 2012-2023.

Crop	Observation			Estimation		
	Sowing	Harvest	Duration crop season (days)	Start mid-season stage	End mid-season stage	Duration mid-season stage (days)
winter barley	10/14/2011	7/10/2012	270	4/21/2012	6/20/2012	60
winter canola	9/18/2012	7/26/2013	311	4/24/2013	7/3/2013	70
oats	3/5/2014	6/3/2014	90	4/4/2014	5/14/2014	40
winter wheat	10/15/2014	7/21/2015	279	4/28/2015	6/30/2015	63
winter barley	10/7/2015	7/8/2016	275	4/17/2016	6/18/2016	62
winter rye	10/11/2016	7/21/2017	283	4/27/2017	6/30/2017	64
oats	3/15/2018	7/23/2018	130	5/24/2018	7/3/2018	40
winter wheat	11/5/2018	7/24/2019	261	5/8/2019	7/5/2019	58
winter barley	9/30/2019	7/7/2020	281	4/14/2020	6/16/2020	63
winter rye	10/20/2020	8/4/2021	288	5/11/2021	7/14/2021	64
oats	3/16/2022	8/3/2022	140	5/30/2022	7/12/2022	43
winter wheat	10/24/2022	7/20/2023	269	5/1/2023	6/30/2023	60

Table B.5 Same as Table B.4, but for the Dedelow (DD) site from 2014-2023.

Crop	Observation			Estimation		
	Sowing	Harvest	Duration crop season (days)	Start mid-season stage	End mid-season stage	Duration mid-season stage (days)
Persian clover (first cut)	3/4/2014	6/12/2014	100	4/26/2014	5/30/2014	34
Persian clover (second cut)	6/12/2014	7/24/2014	42	7/6/2014	7/15/2014	9
winter wheat	9/17/2014	7/23/2015	309	4/22/2015	6/30/2015	69
winter wheat	10/2/2015	7/27/2016	299	4/29/2016	7/5/2016	67
winter rye	10/6/2016	8/2/2017	300	5/4/2017	7/11/2017	68
oats	4/11/2018	7/27/2018	107	6/8/2018	7/11/2018	33
winter wheat	10/9/2018	7/25/2019	289	4/30/2019	7/4/2019	65
winter barley	9/30/2019	7/7/2020	281	4/14/2020	6/16/2020	63
winter rye	10/20/2020	7/26/2021	279	5/3/2021	7/5/2021	63
oats	3/18/2022	7/30/2022	134	5/29/2022	7/9/2022	41
winter wheat	10/7/2022	7/27/2023	293	5/1/2023	7/6/2023	66

Table B.6 Same as Table B.4, but for the Bad-Lauchstädt (BL) site from 2014-2018.

Crop	Observation			Estimation		
	Sowing	Harvest	Duration crop season (days)	Start mid-season stage	End mid-season stage	Duration mid-season stage (days)
oats	3/13/2014	6/12/2014	91	4/11/2014	5/21/2014	40
winter wheat	10/13/2014	7/28/2015	288	5/3/2015	7/7/2015	65
winter barley	9/22/2015	6/30/2016	282	4/7/2016	6/9/2016	63
winter rye	10/5/2016	7/17/2017	285	4/23/2017	6/26/2017	64
oats	4/6/2018	7/18/2018	103	5/10/2018	6/25/2018	46

Table B.7 Same as Table B.4, but for the Sauerbach (SB) site from 2012-2020.

Crop	Observation			Estimation		
	Sowing	Harvest	Duration crop season (days)	Start mid-season stage	End mid-season stage	Duration mid-season stage (days)
winter barley	9/28/2011	7/9/2012	285	4/15/2012	6/18/2012	64
winter canola	8/29/2012	7/29/2013	334	4/20/2013	7/4/2013	75
oats	3/13/2014	6/4/2014	83	4/9/2014	5/16/2014	37
winter wheat	10/8/2014	8/12/2015	308	5/12/2015	7/20/2015	69
winter barley	9/24/2015	7/13/2016	293	4/16/2016	6/21/2016	66
winter rye	9/27/2016	7/24/2017	300	4/25/2017	7/2/2017	68
oats	4/4/2018	7/17/2018	104	5/8/2018	6/24/2018	47
winter wheat	10/11/2018	8/5/2019	298	5/8/2019	7/14/2019	67
winter barley	9/20/2019	7/27/2020	311	4/25/2020	7/4/2020	70

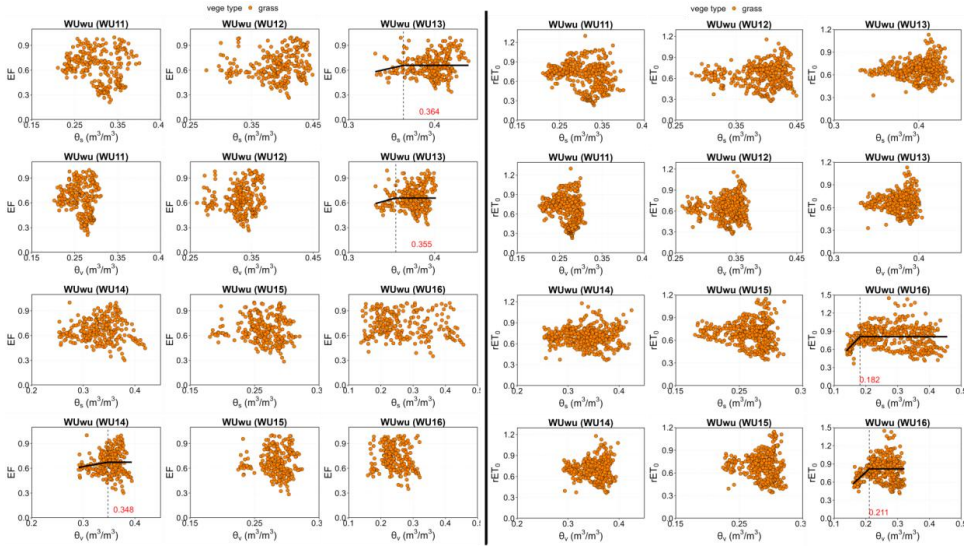


Figure B.2 Critical soil moisture threshold (θ_{crit}) of the surface soil moisture (θ_s) and root zone soil moisture (θ_v) for all lysimeters using the EF and rET_0 method for the WUwu lysimeters. In each plot, the shape of the dots indicates the crop type. The thick black line in each plot indicates the fitted linear-plus-plateau regression. The red numbers in each plot indicate the estimated θ_{crit}.

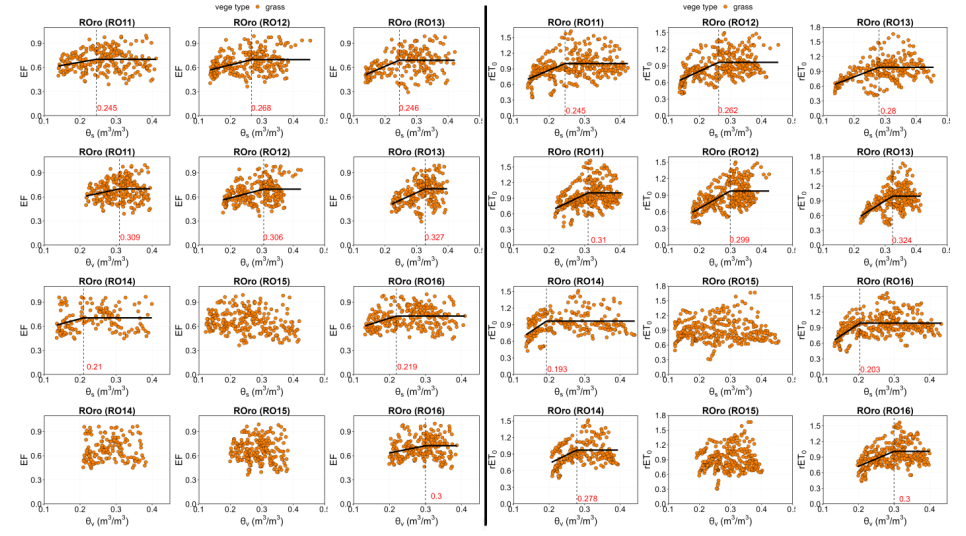


Figure B.3 Critical soil moisture threshold (θ_{crit}) of the surface soil moisture (θ_s) and root zone soil moisture (θ_v) for all lysimeters using the EF and rET_0 method for the ROro lysimeters. In

each plot, the shape of the dots indicates the crop type. The thick black line in each plot indicates the fitted linear-plus-plateau regression. The red numbers in each plot indicate the estimated θ_{crit}.

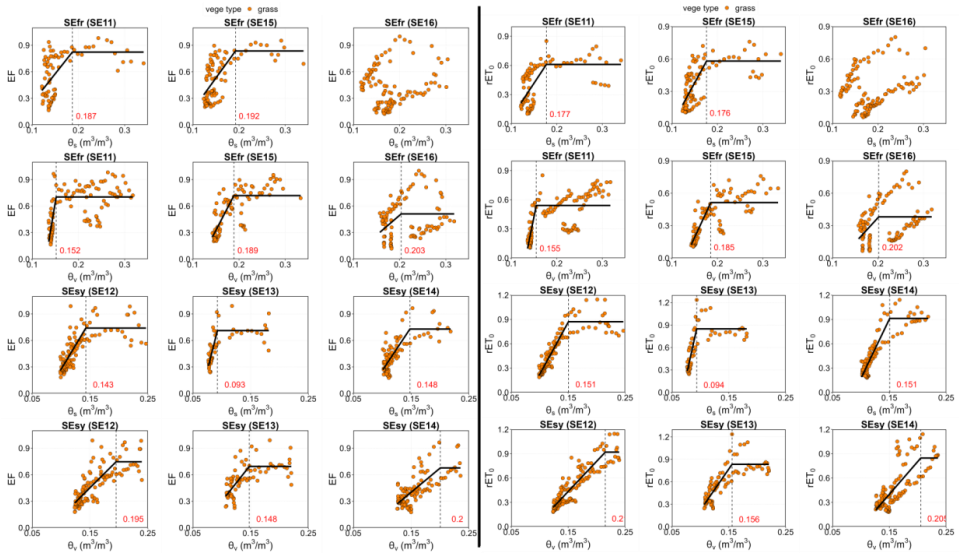


Figure B.4 Critical soil moisture threshold (θ_{crit}) of the surface soil moisture (θ_s) and root zone soil moisture (θ_v) for all lysimeters using the EF and rET_0 method for the SEfr and SEsy lysimeters. In each plot, the shape of the dots indicates the crop type. The thick black line in each plot indicates the fitted linear-plus-plateau regression. The red numbers in each plot indicate the estimated θ_{crit}.

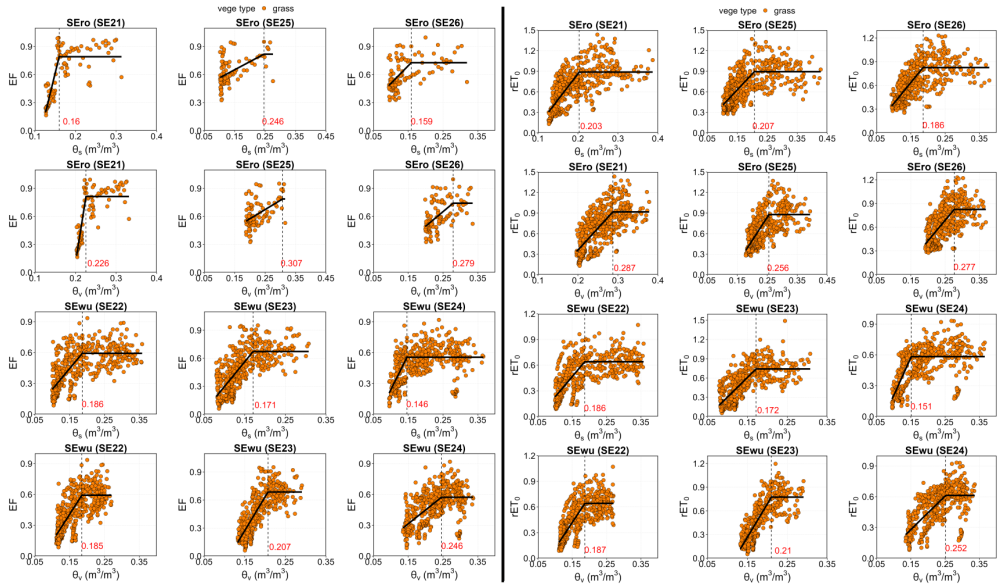


Figure B.5 Critical soil moisture threshold (θ_{crit}) of the surface soil moisture (θ_s) and root zone soil moisture (θ_v) for all lysimeters using the EF and rET_0 method for the SEro and SEwu lysimeters. In each plot, the shape of the dots indicates the crop type. The thick black line in each plot indicates the fitted linear-plus-plateau regression. The red numbers in each plot indicate the estimated θ_{crit}.

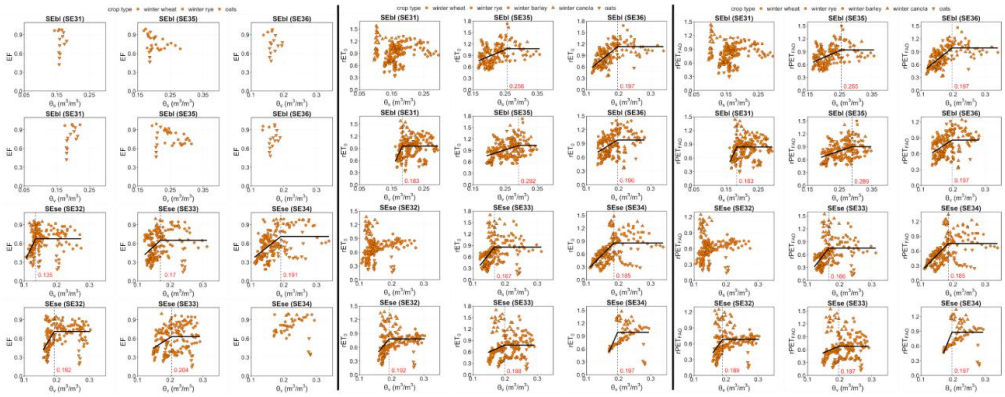


Figure B.6 Critical soil moisture threshold (θ_{crit}) of the surface soil moisture (θ_s) and root zone soil moisture (θ_v) for all lysimeters using the EF, rET_0 and $rPET_{FAO}$ method for the SEro and SEwu lysimeters. In each plot, the shape of the dots indicates the crop type. The thick black

line in each plot indicates the fitted linear-plus-plateau regression. The red numbers in each plot indicate the estimated θ_{crit}.

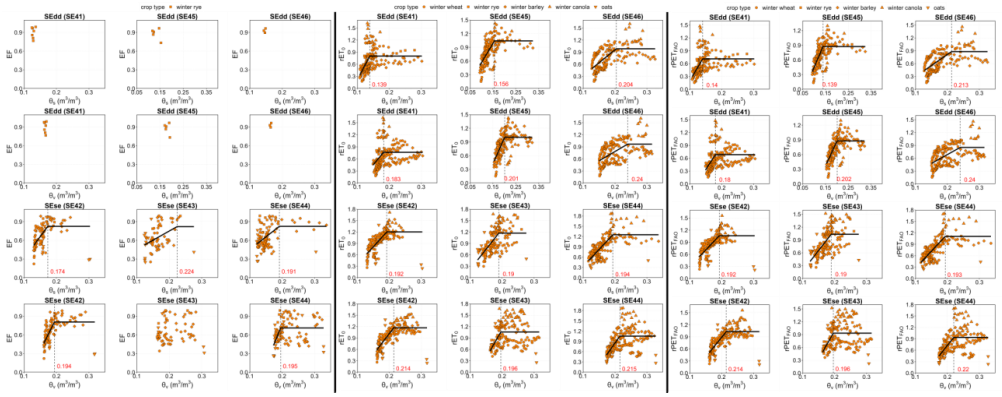


Figure B.7 Critical soil moisture threshold (θ_{crit}) of the surface soil moisture (θ_s) and root zone soil moisture (θ_v) for all lysimeters using the EF, rET_0 and $rPET_{FAO}$ method for the SEdd and SEse lysimeters. In each plot, the shape of the dots indicates the crop type. The thick black line in each plot indicates the fitted linear-plus-plateau regression. The red numbers in each plot indicate the estimated θ_{crit}.

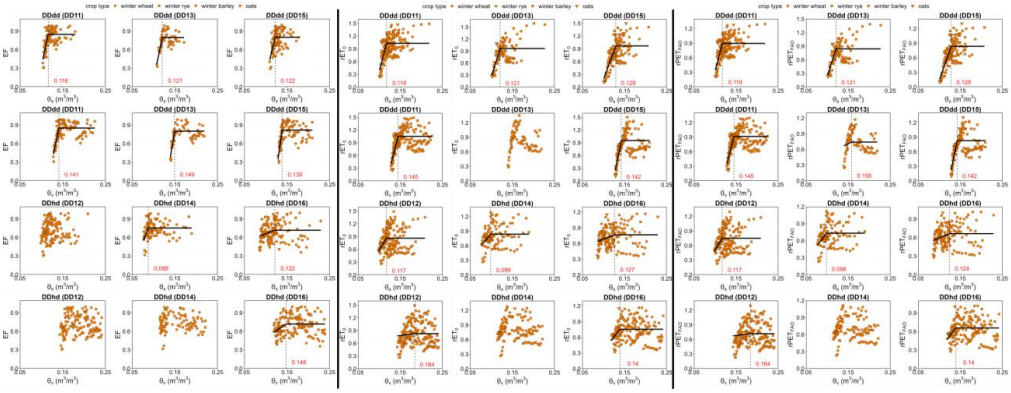


Figure B.8 Critical soil moisture threshold (θ_{crit}) of the surface soil moisture (θ_s) and root zone soil moisture (θ_v) for all lysimeters using the EF, rET_0 and $rPET_{FAO}$ method for the DDdd and DDhd lysimeters. In each plot, the shape of the dots indicates the crop type. The thick black line in each plot indicates the fitted linear-plus-plateau regression. The red numbers in each plot indicate the estimated θ_{crit}.

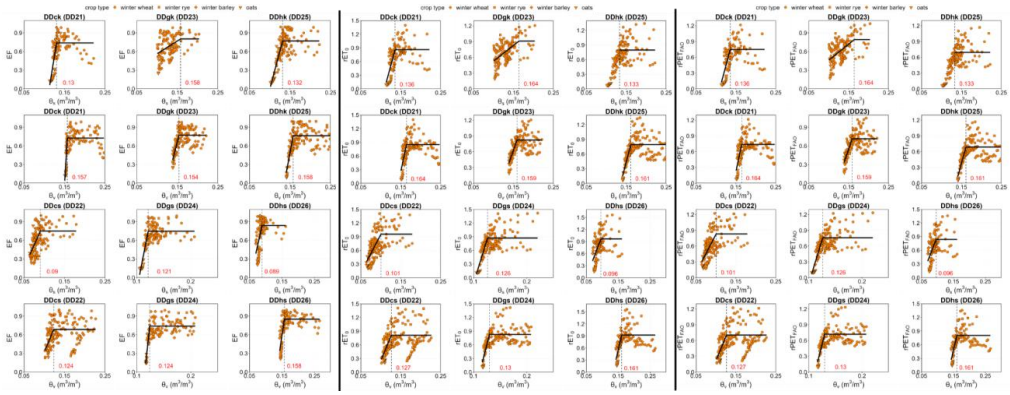


Figure B.9 Critical soil moisture threshold (θ_{crit}) of the surface soil moisture (θ_s) and root zone soil moisture (θ_v) for all lysimeters using the EF, rET_0 and $rPET_{FAO}$ method for the DDk and DDs lysimeters. In each plot, the shape of the dots indicates the crop type. The thick black line in each plot indicates the fitted linear-plus-plateau regression. The red numbers in each plot indicate the estimated θ_{crit}.

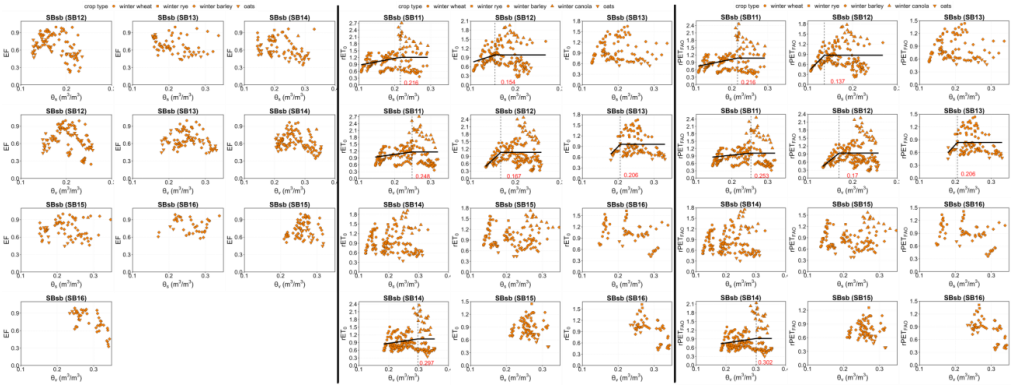


Figure B.10 Critical soil moisture threshold (θ_{crit}) of the surface soil moisture (θ_s) and root zone soil moisture (θ_v) for all lysimeters using the EF, rET_0 and $rPET_{FAO}$ method for the SBsb lysimeters. In each plot, the shape of the dots indicates the crop type. The thick black line in each plot indicates the fitted linear-plus-plateau regression. The red numbers in each plot indicate the estimated θ_{crit}.

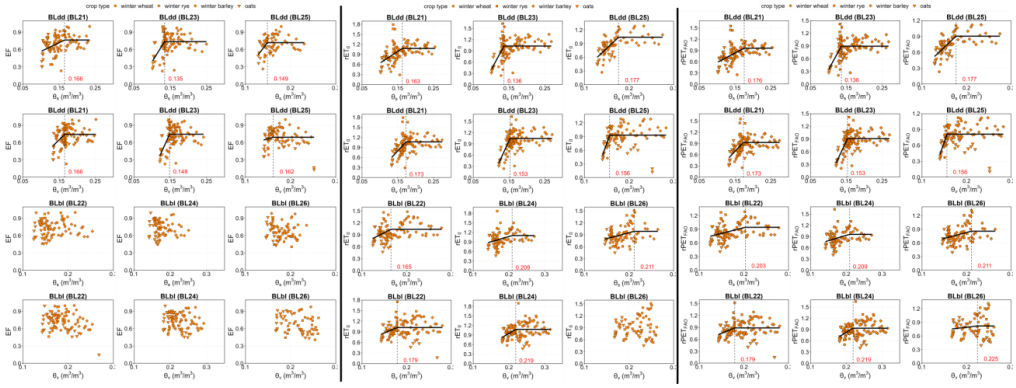


Figure B.11 Critical soil moisture threshold (θ_{crit}) of the surface soil moisture (θ_s) and root zone soil moisture (θ_v) for all lysimeters using the EF, rET_0 and $rPET_{FAO}$ method for the BLbl lysimeters. In each plot, the shape of the dots indicates the crop type. The thick black line in each plot indicates the fitted linear-plus-plateau regression. The red numbers in each plot indicate the estimated θ_{crit}.

Appendix C

Table C 1. Summary of lysimeters details and corresponding critical soil moisture thresholds for both surface and root zone soil.

Site	Lysimeter ID	Lon	Lat	AI	Climate	Land cover	Surface depth (cm)	Surface soil texture	Surface θ_{crit}	Root zone depth (cm)	Root zone soil texture	Root zone θ_{crit}
ClimGrass	L1_C2T0	14.10	47.49	0.68	Humid	Grassland	10	Silt loam	NA[2]	60	Loam	NA[2]
ClimGrass	L2_C0T0	14.10	47.49	0.68	Humid	Grassland	10	Sandy loam	NA[2]	60	Loam	NA[2]
ClimGrass	L3_C0T2	14.10	47.49	0.73	Humid	Grassland	10	Sandy loam	NA[2]	60	Loam	NA[2]
ClimGrass	L4_C2T2	14.10	47.49	0.73	Humid	Grassland	10	Silt loam	NA[1]	60	Loam	NA[1]
ClimGrass	L5_C0T2	14.10	47.49	0.73	Humid	Grassland	10	Silt loam	0.218	60	Loam	NA[1]
ClimGrass	L6_C2T0	14.10	47.49	0.68	Humid	Grassland	10	Silt loam	NA[2]	60	Loam	NA[2]
Stoderzinken	St_L1	13.83	47.46	0.42	Humid	Grassland	5	Silt Loam	NA[2]	60	Clay Loam	NA[2]
Stubai	DDry_L14	11.32	47.12	0.52	Humid	Grassland	5	Sandy loam	0.065	60	NA	NA[2]
Stubai	DDry_L22	11.32	47.12	0.51	Humid	Grassland	5	Sandy loam	NA[1]	60	NA	NA[1]
Stubai	DDry_L23	11.32	47.12	0.52	Humid	Grassland	5	Sandy loam	NA[2]	60	NA	NA[1]
Stubai	DWet_L11	11.32	47.12	0.46	Humid	Grassland	5	Sandy loam	NA[2]	60	NA	NA[3]
Stubai	DWet_L13	11.32	47.12	0.46	Humid	Grassland	5	Sandy loam	NA[2]	60	NA	NA[2]
Stubai	DWet_L24	11.32	47.12	0.46	Humid	Grassland	5	Sandy loam	NA[2]	60	NA	NA[3]
Stubai	HDry_L15	11.32	47.12	0.52	Humid	Grassland	5	Sandy loam	NA[2]	60	NA	0.074
Stubai	HDry_L16	11.32	47.12	0.52	Humid	Grassland	5	Sandy loam	0.092	60	NA	0.098
Stubai	HDry_L21	11.32	47.12	0.52	Humid	Grassland	5	Sandy loam	NA[1]	60	NA	NA[2]
Stubai	HWet_L12	11.32	47.12	0.46	Humid	Grassland	5	Sandy loam	NA[2]	60	NA	NA[3]
Stubai	HWet_L25	11.32	47.12	0.46	Humid	Grassland	5	Sandy loam	NA[2]	60	NA	NA[3]
Stubai	HWet_L26	11.32	47.12	0.46	Humid	Grassland	5	Sandy loam	NA[2]	60	NA	NA[2]
Stubai	ICrl_L13	11.32	47.12	0.02	Humid	Grassland	5	Sandy loam	NA3	60	Sandy loam	NA[3]
Stubai	ICrl_L25	11.32	47.12	0.02	Humid	Grassland	5	Sandy loam	NA[3]	60	Sandy loam	NA[3]
Stubai	ICrl_L45	11.32	47.12	0.02	Humid	Grassland	5	Sandy loam	NA[3]	60	Sandy loam	NA[3]
Stubai	ITr2_L14	11.32	47.12	0.91	Humid	Grassland	5	Sandy loam	0.052	60	Sandy loam	0.049
Stubai	ITr2_L23	11.32	47.12	0.78	Humid	Grassland	5	Sandy loam	0.070	60	Sandy loam	0.062
Stubai	ITr2_L33	11.32	47.12	0.90	Humid	Grassland	5	Sandy loam	0.071	60	Sandy loam	0.07
Stubai	MCrl_L11	11.32	47.12	0.02	Humid	Grassland	5	Clay loam	NA[3]	60	Loam	NA[3]
Stubai	MCrl_L26	11.32	47.12	0.02	Humid	Grassland	5	Clay loam	NA[3]	60	Loam	NA[3]
Stubai	MCrl_L44	11.32	47.12	0.02	Humid	Grassland	5	Clay loam	NA[3]	60	Loam	NA[3]
Stubai	MTr1_L34	11.32	47.12	0.02	Humid	Grassland	5	Clay loam	0.109	60	Loam	0.129
Stubai	MTr1_L41	11.32	47.12	0.02	Humid	Grassland	5	Clay loam	NA[2]	60	Loam	NA[2]
Stubai	MTr1_L43	11.32	47.12	0.02	Humid	Grassland	5	Clay loam	NA[1]	60	Loam	NA[1]
Stubai	MTr2_L16	11.32	47.12	0.91	Humid	Grassland	5	Clay loam	0.119	60	Loam	0.101
Stubai	MTr2_L22	11.32	47.12	0.78	Humid	Grassland	5	Clay loam	0.097	60	Loam	0.097
Stubai	MTr2_L32	11.32	47.12	0.90	Humid	Grassland	5	Clay loam	NA[2]	60	Loam	0.103
Stubai	SCrl_L12	11.32	47.12	0.02	Humid	Grassland	5	Silt loam	NA[3]	60	Silt loam	NA[3]
Stubai	SCrl_L24	11.32	47.12	0.02	Humid	Grassland	5	Silt loam	NA[3]	60	Silt loam	NA[3]
Stubai	SCrl_L46	11.32	47.12	0.02	Humid	Grassland	5	Silt loam	NA[3]	60	Silt loam	NA[3]
Stubai	STr1_L35	11.32	47.12	0.02	Humid	Grassland	5	Silt loam	NA[1]	60	Silt loam	NA[1]

Stubai	STr1_L36	11.32	47.12	0.02	Humid	Grassland	5	Silt loam	NA[2]	60	Silt loam	NA[2]
Stubai	STr1_L42	11.32	47.12	0.02	Humid	Grassland	5	Silt loam	NA[2]	60	Silt loam	NA[1]
Stubai	STr2_L15	11.32	47.12	0.91	Humid	Grassland	5	Silt loam	0.066	60	Silt loam	0.081
Stubai	STr2_L21	11.32	47.12	0.78	Humid	Grassland	5	Silt loam	NA[2]	60	Silt loam	NA[1]
Stubai	STr2_L31	11.32	47.12	0.90	Humid	Grassland	5	Silt loam	0.116	60	Silt loam	0.094
Wagna	BIO	15.55	46.77	0.86	Humid	Cropland	35	NA	NA[2]	60	NA	NA[2]
Wagna	KON	15.55	46.77	0.86	Humid	Cropland	35	NA	NA[1]	60	NA	0.261
Hasselt	HS_L1	5.63	50.98	1.08	Humid	Cropland	10	NA	NA[3]	60	NA	NA[3]
Hasselt	HS_L10	5.63	50.98	1.08	Humid	Cropland	10	NA	0.059	60	NA	NA[1]
Hasselt	HS_L11	5.63	50.98	1.08	Humid	Cropland	10	NA	NA[1]	60	NA	NA[1]
Hasselt	HS_L12	5.63	50.98	1.08	Humid	shrub	10	NA	NA[3]	60	NA	NA[3]
Hasselt	HS_L2	5.63	50.98	1.08	Humid	shrub	10	NA	NA[3]	60	NA	NA[3]
Hasselt	HS_L3	5.63	50.98	1.08	Humid	Cropland	10	NA	NA[2]	60	NA	NA[2]
Hasselt	HS_L4	5.63	50.98	1.08	Humid	Cropland	10	NA	NA[1]	60	NA	NA[1]
Hasselt	HS_L5	5.63	50.98	1.08	Humid	shrub	10	NA	NA[1]	60	NA	NA[2]
Hasselt	HS_L6	5.63	50.98	1.08	Humid	Cropland	10	NA	NA[2]	60	NA	NA[1]
Hasselt	HS_L7	5.63	50.98	1.08	Humid	shrub	10	NA	NA[1]	60	NA	NA[1]
Hasselt	HS_L8	5.63	50.98	1.08	Humid	shrub	10	NA	NA[3]	60	NA	NA[3]
Hasselt	HS_L9	5.63	50.98	1.08	Humid	shrub	10	NA	NA[1]	60	NA	NA[1]
Soil Interpretive health Centre	Cov_C2	-80.38	43.64	1.38	Sub-humid	Cropland	10	Loamy sand	0.079	60	Loamy sand	0.129
Soil Interpretive health Centre	Cov_C6	-80.38	43.64	1.38	Sub-humid	Cropland	10	Loamy sand	0.083	60	Loamy sand	0.115
Soil Interpretive health Centre	Cov_C8	-80.38	43.64	1.38	Sub-humid	Cropland	10	Loamy sand	NA[2]	60	Loamy sand	NA[1]
Soil Interpretive health Centre	Cov_E2	-80.38	43.64	1.38	Sub-humid	Cropland	10	Silt loam	NA[2]	60	Loam	NA[1]
Soil Interpretive health Centre	Cov_E5	-80.38	43.64	1.38	Sub-humid	Cropland	10	Silt loam	NA[2]	60	Loam	NA[2]
Soil Interpretive health Centre	Cov_E9	-80.38	43.64	1.38	Sub-humid	Cropland	10	Silt loam	NA[2]	60	Loam	NA[1]
Soil Interpretive health Centre	Div_C1	-80.38	43.64	1.38	Sub-humid	Cropland	10	Loamy sand	0.118	60	Loamy sand	0.118
Soil Interpretive health Centre	Div_C5	-80.38	43.64	1.38	Sub-humid	Cropland	10	Loamy sand	0.122	60	Loamy sand	0.118
Soil Interpretive health Centre	Div_C7	-80.38	43.64	1.38	Sub-humid	Cropland	10	Loamy sand	0.056	60	Loamy sand	NA[2]
Soil Interpretive health Centre	Div_E3	-80.38	43.64	1.38	Sub-humid	Cropland	10	Silt loam	NA[2]	60	Loam	NA[2]
Soil Interpretive health Centre	Div_E4	-80.38	43.64	1.38	Sub-humid	Cropland	10	Silt loam	NA[2]	60	Loam	NA[2]
Soil Interpretive health Centre	Div_E7	-80.38	43.64	1.38	Sub-humid	Cropland	10	Silt loam	NA[2]	60	Loam	NA[2]
Soil Interpretive health Centre	DivW_C3	-80.38	43.64	1.38	Sub-humid	Cropland	10	Loamy sand	0.125	60	Loamy sand	NA[2]

Soil Interpretive health Centre	DivW_C4	-80.38	43.64	1.38	Sub-humid	Cropland	10	Loamy sand	0.127	60	Loamy sand	0.148
Soil Interpretive health Centre	DivW_C9	-80.38	43.64	1.38	Sub-humid	Cropland	10	Loamy sand	0.112	60	Loamy sand	NA[1]
Soil Interpretive health Centre	DivW_E1	-80.38	43.64	1.38	Sub-humid	Cropland	10	Silt loam	NA[2]	60	Loam	NA[2]
Soil Interpretive health Centre	DivW_E6	-80.38	43.64	1.38	Sub-humid	Cropland	10	Silt loam	NA[2]	60	Loam	NA[2]
Soil Interpretive health Centre	DivW_E8	-80.38	43.64	1.38	Sub-humid	Cropland	10	Silt loam	NA[2]	60	Loam	NA[1]
Shapotou	Sh_L1	105.19	37.52	7.26	Arid	shrub	10	Sand	NA[1]	60	Sand	NA[1]
Shapotou	Sh_L2	105.19	37.52	7.26	Arid	shrub	10	Sand	NA[2]	60	Sand	NA[1]
Shapotou	Sh_L6	105.19	37.52	7.26	Arid	shrub	10	Sand	NA[2]	60	Sand	NA[2]
Zagreb	F_L2	16.01	45.86	1.03	Humid	Grassland	5	Silt loam	0.193	60	Silt loam	0.257
Zagreb	H_L1	16.01	45.86	1.03	Humid	Grassland	5	Silt loam	3.000	60	Silt loam	0.219
Montpellier	M1	3.88	43.68	2.16	Semi-arid	Cropland	13	Silt loam	NA[1]	80	Silt loam	NA[1]
Montpellier	M10	3.88	43.68	2.16	Semi-arid	Cropland	13	Silt loam	0.163	80	Silt loam	NA[2]
Montpellier	M11	3.88	43.68	2.16	Semi-arid	Cropland	13	Silt loam	NA[2]	80	Silt loam	NA[2]
Montpellier	M12	3.88	43.68	2.16	Semi-arid	Cropland	13	Silt loam	NA[2]	80	Silt loam	0.208
Montpellier	M2	3.88	43.68	2.16	Semi-arid	Cropland	13	Silt loam	0.227	80	Silt loam	0.232
Montpellier	M3	3.88	43.68	2.16	Semi-arid	Cropland	13	Silt loam	NA[2]	80	Silt loam	NA[1]
Montpellier	M4	3.88	43.68	2.16	Semi-arid	Cropland	13	Silt loam	NA[1]	80	Silt loam	NA[1]
Montpellier	M5	3.88	43.68	2.16	Semi-arid	Cropland	13	Silt loam	0.238	80	Silt loam	0.207
Montpellier	M6	3.88	43.68	2.16	Semi-arid	Cropland	13	Silt loam	0.290	80	Silt loam	0.237
Montpellier	M7	3.88	43.68	2.16	Semi-arid	Cropland	13	Silt loam	NA[1]	80	Silt loam	0.224
Montpellier	M8	3.88	43.68	2.16	Semi-arid	Cropland	13	Silt loam	NA[1]	80	Silt loam	NA[2]
Montpellier	M9	3.88	43.68	2.16	Semi-arid	Cropland	13	Silt loam	NA[2]	80	Silt loam	NA[1]
Bad-Lauchstädt	BL11	11.88	51.39	2.07	Semi-arid	Cropland	10	Silt loam	0.159	60	Silt loam	0.209
Bad-Lauchstädt	BL12	11.88	51.39	2.07	Semi-arid	Cropland	10	Silt loam	0.169	60	Silt loam	0.188
Bad-Lauchstädt	BL13	11.88	51.39	2.07	Semi-arid	Cropland	10	Silt loam	NA[1]	60	Silt loam	0.181
Bad-Lauchstädt	BL14	11.88	51.39	2.07	Semi-arid	Cropland	10	Silt loam	0.246	60	Silt loam	NA[2]
Bad-Lauchstädt	BL15	11.88	51.39	2.07	Semi-arid	Cropland	10	Silt loam	0.167	60	Silt loam	0.209
Bad-Lauchstädt	BL16	11.88	51.39	2.07	Semi-arid	Cropland	10	Silt loam	0.165	60	Silt loam	0.182
Bad-Lauchstädt	BL21	11.88	51.39	2.07	Semi-arid	Cropland	10	Sandy loam	0.197	60	Loam	0.152
Bad-Lauchstädt	BL22	11.88	51.39	2.07	Semi-arid	Cropland	10	Silt loam	NA[1]	60	Silt loam	0.179
Bad-Lauchstädt	BL23	11.88	51.39	2.07	Semi-arid	Cropland	10	Sandy loam	0.134	60	Sandy clay loam	0.146

Bad-Lauchstädt	BL24	11.88	51.39	2.07	Semi-arid	Cropland	10	Silt loam	0.154	60	Silt loam	0.191
Bad-Lauchstädt	BL25	11.88	51.39	2.07	Semi-arid	Cropland	10	Loam	0.146	60	Loam	0.155
Bad-Lauchstädt	BL26	11.88	51.39	2.07	Semi-arid	Cropland	10	Silt loam	NA[2]	60	Silt loam	NA[1]
Brandis	L74	12.60	51.33	1.38	Sub-humid	Cropland	NA	NA	NA[3]	50	Loam	0.237
Brandis	L86	12.60	51.33	1.38	Sub-humid	Cropland	NA	NA	NA[3]	50	Sandy loam	0.122
Brandis	L91	12.60	51.33	1.38	Sub-humid	Cropland	NA	NA	NA[3]	50	Silt loam	NA[2]
Dedelow	DD11	13.80	53.37	1.70	Semi-arid	Cropland	10	Sandy loam	0.118	60	Sandy loam	0.146
Dedelow	DD12	13.80	53.37	1.70	Semi-arid	Cropland	10	Sandy loam	0.117	60	Sandy loam	NA[1]
Dedelow	DD13	13.80	53.37	1.70	Semi-arid	Cropland	10	Loam	0.122	60	Loam	0.158
Dedelow	DD14	13.80	53.37	1.70	Semi-arid	Cropland	10	Sandy loam	0.098	60	Sandy loam	NA[1]
Dedelow	DD15	13.80	53.37	1.70	Semi-arid	Cropland	10	Loam	0.129	60	Loam	0.142
Dedelow	DD16	13.80	53.37	1.70	Semi-arid	Cropland	10	Sandy loam	0.129	60	Sandy loam	0.141
Dedelow	DD21	13.80	53.37	1.70	Semi-arid	Cropland	10	Sandy loam	0.136	60	Sandy loam	0.165
Dedelow	DD22	13.80	53.37	1.70	Semi-arid	Cropland	10	Sandy loam	0.100	60	Sandy loam	0.126
Dedelow	DD23	13.80	53.37	1.70	Semi-arid	Cropland	10	Sandy loam	NA1	60	Sandy loam	0.159
Dedelow	DD24	13.80	53.37	1.70	Semi-arid	Cropland	10	Sandy loam	0.125	60	Sandy loam	0.128
Dedelow	DD25	13.80	53.37	1.70	Semi-arid	Cropland	10	Sandy loam	0.133	60	Sandy loam	0.162
Dedelow	DD26	13.80	53.37	1.70	Semi-arid	Cropland	10	Sandy loam	0.096	60	Sandy loam	0.161
Graswang	GW13	11.03	47.57	0.62	Humid	Grassland	10	Clay	NA[3]	60	Clay	NA[3]
Rollesbroich	RO11	6.30	50.62	0.76	Humid	Grassland	10	Sandy clay loam	0.243	60	Sandy clay loam	0.309
Rollesbroich	RO12	6.30	50.62	0.76	Humid	Grassland	10	Sandy clay loam	0.261	60	Sandy clay loam	0.298
Rollesbroich	RO13	6.30	50.62	0.76	Humid	Grassland	10	Sandy clay loam	0.284	60	Sandy clay loam	0.324
Rollesbroich	RO14	6.30	50.62	0.76	Humid	Grassland	10	Sandy clay loam	0.192	60	Sandy clay loam	0.276
Rollesbroich	RO15	6.30	50.62	0.76	Humid	Grassland	10	Sandy clay loam	NA[1]	60	Sandy clay loam	NA[1]
Rollesbroich	RO16	6.30	50.62	0.76	Humid	Grassland	10	Sandy clay loam	0.205	60	Sandy clay loam	0.3
Sauerbach	SB11	11.28	52.08	2.05	Semi-arid	Cropland	10	Silt loam	0.211	60	Silt loam	0.228
Sauerbach	SB12	11.28	52.08	2.05	Semi-arid	Cropland	10	Silt loam	NA[1]	60	Silt loam	0.205
Sauerbach	SB13	11.28	52.08	2.05	Semi-arid	Cropland	10	Silt loam	0.158	60	Silt loam	NA[1]
Sauerbach	SB14	11.28	52.08	2.05	Semi-arid	Cropland	10	Silt loam	0.225	60	Silt loam	0.259
Sauerbach	SB15	11.28	52.08	2.05	Semi-arid	Cropland	10	Silt loam	0.243	60	Silt loam	NA[2]
Sauerbach	SB16	11.28	52.08	2.05	Semi-arid	Cropland	10	Silt loam	NA[2]	60	Silt loam	NA[2]
Selhausen	SE11	6.45	50.87	1.36	Sub-humid	Grassland	10	Sandy loam	0.177	60	Sandy loam	0.155
Selhausen	SE12	6.45	50.87	1.36	Sub-humid	Grassland	10	Sandy loam	0.151	60	Sandy loam	0.215
Selhausen	SE13	6.45	50.87	1.36	Sub-humid	Grassland	10	Sandy loam	0.094	60	Sandy loam	0.156
Selhausen	SE14	6.45	50.87	1.36	Sub-humid	Grassland	10	Sandy loam	0.151	60	Sandy loam	0.205
Selhausen	SE15	6.45	50.87	1.36	Sub-humid	Grassland	10	Sandy loam	0.177	60	Sandy loam	0.185
Selhausen	SE16	6.45	50.87	1.36	Sub-humid	Grassland	10	Sandy loam	NA[2]	60	Sandy loam	0.199
Selhausen	SE21	6.45	50.87	1.36	Sub-humid	Grassland	10	Sandy clay loam	0.190	60	Sandy clay loam	0.287
Selhausen	SE22	6.45	50.87	1.36	Sub-humid	Grassland	10	Clay loam	0.186	60	Loam	0.187
Selhausen	SE23	6.45	50.87	1.36	Sub-humid	Grassland	10	Clay loam	0.169	60	Loam	0.208
Selhausen	SE24	6.45	50.87	1.36	Sub-humid	Grassland	10	Clay loam	0.147	60	Loam	0.252

Selhausen	SE25	6.45	50.87	1.36	Sub-humid	Grassland	10	Sandy clay loam	0.208	60	Sandy clay loam	0.255
Selhausen	SE26	6.45	50.87	1.36	Sub-humid	Grassland	10	Sandy clay loam	0.186	60	Sandy clay loam	0.269
Selhausen	SE31	6.45	50.87	1.36	Sub-humid	Cropland	10	Silt loam	NA[1]	60	Silt Loam	0.183
Selhausen	SE32	6.45	50.87	1.36	Sub-humid	Cropland	10	Silt loam	0.133	60	Silt Loam	0.192
Selhausen	SE33	6.45	50.87	1.36	Sub-humid	Cropland	10	Silt loam	0.167	60	Silt Loam	0.198
Selhausen	SE34	6.45	50.87	1.36	Sub-humid	Cropland	10	Silt loam	0.185	60	Silt Loam	0.197
Selhausen	SE35	6.45	50.87	1.36	Sub-humid	Cropland	10	Silt loam	0.256	60	Silt Loam	0.276
Selhausen	SE36	6.45	50.87	1.36	Sub-humid	Cropland	10	Silt loam	0.197	60	Silt Loam	0.232
Selhausen	SE41	6.45	50.87	1.36	Sub-humid	Cropland	10	Sandy loam	0.141	60	Sandy loam	0.181
Selhausen	SE42	6.45	50.87	1.36	Sub-humid	Cropland	10	Silt loam	0.192	60	Silt loam	0.214
Selhausen	SE43	6.45	50.87	1.36	Sub-humid	Cropland	10	Silt loam	0.190	60	Silt loam	0.196
Selhausen	SE44	6.45	50.87	1.36	Sub-humid	Cropland	10	Silt loam	0.194	60	Silt loam	0.215
Selhausen	SE45	6.45	50.87	1.36	Sub-humid	Cropland	10	Sandy loam	0.136	60	Sandy loam	0.201
Selhausen	SE46	6.45	50.87	1.36	Sub-humid	Cropland	10	Loam	0.231	60	Loam	0.204
Spreewald	SP_L1	14.04	51.88	1.57	Semi-arid	Grassland	10	Loam	NA[1]	60	Sandy loam	NA[2]
Wuestebach	WU11	6.33	50.50	0.46	Humid	Grassland	10	Clay loam	NA[2]	60	Loam	NA[2]
Wuestebach	WU12	6.33	50.50	0.46	Humid	Grassland	10	Clay loam	NA[1]	60	Loam	NA[2]
Wuestebach	WU13	6.33	50.50	0.46	Humid	Grassland	10	Clay loam	NA[2]	60	Loam	NA[1]
Wuestebach	WU14	6.33	50.50	0.46	Humid	Grassland	10	Clay loam	NA[1]	60	Loam	NA[1]
Wuestebach	WU15	6.33	50.50	0.46	Humid	Grassland	10	Clay loam	NA[2]	60	Loam	NA[2]
Wuestebach	WU16	6.33	50.50	0.46	Humid	Grassland	10	Clay loam	0.182	60	Loam	0.212
Kazakhstan	G_L2	70.07	51.24	4.66	Semi-arid	Grassland	30	Silty clay loam	0.174	60	Silty clay loam	0.164
Kazakhstan	W_L1	70.07	51.24	4.66	Semi-arid	Cropland	30	Silty clay loam	NA[2]	60	Silty clay	NA[1]
Chichaoua	Mo_L1	-8.65	31.43	6.21	Arid	Cropland	15	NA	NA[2]	60	NA	NA[1]
Petrovce	Pe_L1	21.89	48.79	1.40	Sub-humid	Grassland	20	Silt loam	0.193	60	Silt loam	0.288
ElsPlans	EP_L1	1.63	42.58	3.08	Semi-arid	Grassland	5	Silty clay loam	NA[2]	60	Clay loam	0.151
Majadas	Ma_L1	-5.77	39.94	3.36	Semi-arid	Grassland	10	Sandy loam	0.123	60	Sandy loam	0.124
Majadas	Ma_L2	-5.77	39.94	3.36	Semi-arid	Grassland	10	Sandy loam	0.201	60	Sandy loam	0.231
Majadas	Ma_L5	-5.77	39.94	3.36	Semi-arid	Grassland	10	Sandy loam	0.120	60	Sandy loam	0.201
Majadas	Ma_L6	-5.77	39.94	3.36	Semi-arid	Grassland	10	Sandy loam	0.075	10	Sandy loam	0.128
Mollerussa	ML_L1	0.87	41.62	3.27	Semi-arid	Cropland	8	NA	NA[1]	NA	NA	NA[3]
UPV	NA	-0.49	39.48	3.58	Semi-arid	Cropland	10	Sand	NA[3]	10	Sand	NA[3]
Rietholzbach	RB_L1	8.99	47.38	0.51	Humid	Grassland	5	Clay loam	0.332	60	Clay loam	NA[1]
Bushland	NE	-102.09	35.19	2.78	Semi-arid	Cropland	6	Silty clay loam	NA[2]	NA	NA	NA[3]
Bushland	NW	-102.09	35.19	2.78	Semi-arid	Cropland	6	Silty clay loam	NA[1]	NA	NA	NA[3]
Bushland	SE	-102.09	35.19	2.78	Semi-arid	Cropland	6	Silty clay loam	0.166	NA	NA	NA[3]
Bushland	SW	-102.09	35.19	2.78	Semi-arid	Cropland	6	Silty clay loam	0.204	NA	NA	NA[3]

[1] Critical soil moisture was identified but excluded because the linear-plus-plateau model did not provide the lowest AIC was not the best model

[2] No critical soil moisture was identified because the linear-plus-plateau model failed to converge

3 No data during drydown or no drydown detected

Table C 2. Summary of availability of critical soil moisture.

Status	Description	Surface	Root zone
θ_{crit}	Threshold identified	87	86
NA[1]	Excluded (higher AIC)	27	35
NA[2]	LPP fit failed	47	34
NA[3]	Insufficient data	18	24

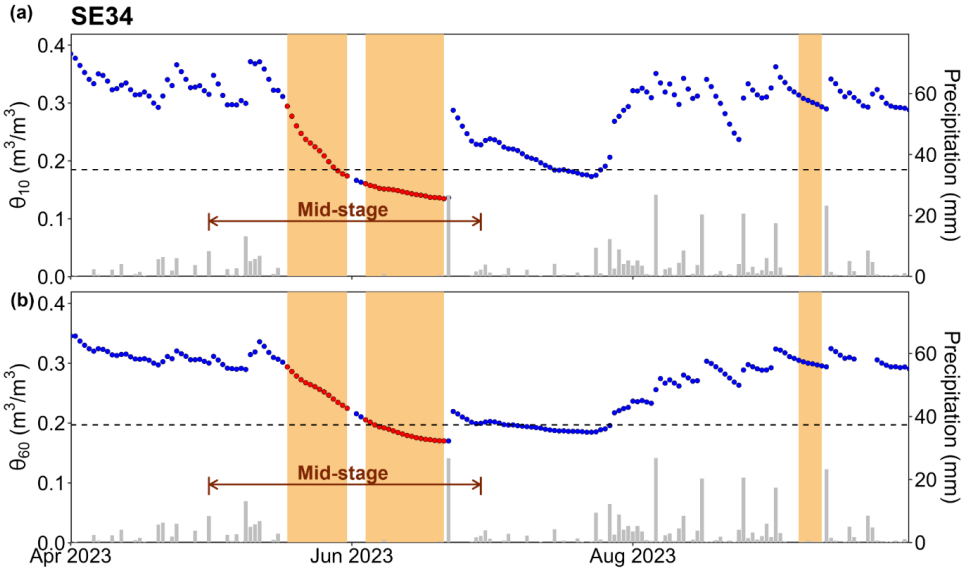


Figure C1. Example time series of (a) surface soil moisture at 10 cm depth and (b) root zone soil moisture integrated over 0-60 cm for a cropland lysimeter (SE34) at the Selhausen site, Germany, during April-September 2023. Drydowns are highlighted in orange. Soil moisture observations during the drydown events are marked as red, whereas observations outside or excluded from the drydown events are shown in blue. Bars represent the daily precipitation.Horizontal dashed line indicates the corresponding critical soil moisture estimated for this lysimeter from 2013-2023.

Bibliography

Ahady, A. B., Wolf, S., & Klopries, E. (2026). Identifying soil moisture thresholds for agricultural drought sensitivity through coupling modeled and satellite data in a humid temperate catchment. *Ecological Indicators*, *186*(April), 114875. https://doi.org/10.1016/j.ecolind.2026.114875

Akaike, H. (1974). A New Look at the Statistical Model Identification. *IEEE Transactions on Automatic Control*, *19*(6), 716–723. https://doi.org/10.1109/TAC.1974.1100705

Akbar, R., Gianotti, D. J. S., McColl, K. A., Haghighi, E., Salvucci, G. D., & Entekhabi, D. (2018). Estimation of landscape soil water losses from satellite observations of soil moisture. *Journal of Hydrometeorology*, *19*(5), 871–889. https://doi.org/fi

Akbar, R., Short Gianotti, D., McColl, K. A., Haghighi, E., Salvucci, G. D., & Entekhabi, D. (2018). Hydrological Storage Length Scales Represented by Remote Sensing Estimates of Soil Moisture and Precipitation. *Water Resources Research*, *54*(3), 1476–1492. https://doi.org/10.1002/2017WR021508

Aliyu, A., Leng, P., Li, Y., Liao, Q., Geng, Y., Ma, J., Sun, Y., Song, X., Duan, S., & Li, Z. (2025). Remote sensing of root zone soil moisture : A review of methods and products. *Journal of Hydrology*, *656*(March), 133002. https://doi.org/10.1016/j.jhydrol.2025.133002

Allen, R. G., Pereira, L. S., Howell, T. A., & Jensen, M. E. (2011). Evapotranspiration information reporting: I. Factors governing measurement accuracy. *Agricultural Water Management*, *98*(6), 899–920. https://doi.org/10.1016/j.agwat.2010.12.015

Allen, R. G., Pereira, L. S., Raes, D., Smith, M., & others. (1998). Crop evapotranspiration-Guidelines for computing crop water requirements-FAO Irrigation and drainage paper 56. *Fao, Rome*, *300*(9), D05109.

Allen, R. G., Pruitt, W. O., Wright, J. L., Howell, T. A., Ventura, F., Snyder, R., Itenfisu, D., Steduto, P., Berengena, J., Yrisarry, J. B., Smith, M., Pereira, L. S., Raes, D., Perrier, A., Alves, I., Walter, I., & Elliott, R. (2006). A recommendation on standardized surface resistance for hourly calculation of reference ETo by the FAO56 Penman-Monteith method. *Agricultural Water Management*, *81*(1–2), 1–22. https://doi.org/10.1016/j.agwat.2005.03.007

Anderegg, W. R. L., Kane, J. M., & Anderegg, L. D. L. (2013). Consequences of widespread tree mortality triggered by drought and temperature stress. *Nature Climate Change*, *3*(1), 30–36. https://doi.org/10.1038/nclimate1635

Awada, H., Ciraolo, G., Maltese, A., Provenzano, G., Moreno Hidalgo, M. A., & Còrcoles, J. I. (2019). Assessing the performance of a large-scale irrigation system by estimations of actual evapotranspiration obtained by Landsat satellite images resampled with cubic convolution. *International Journal of Applied Earth Observation and Geoinformation*,

75(October 2018), 96–105. https://doi.org/10.1016/j.jag.2018.10.016

Baldocchi, D. D. (2003). *Assessing the eddy covariance technique for evaluating carbon dioxide exchange rates of ecosystems : past , present and future*. *October 2002*, 479–492.

Baldocchi, D. D., Xu, L., & Kiang, N. (2004). *How plant functional-type , weather , seasonal drought , and soil physical properties alter water and energy fluxes of an oak – grass savanna and an annual grassland*. *123*, 13–39. https://doi.org/10.1016/j.agrformet.2003.11.006

Berg, A., Findell, K., Lintner, B., Giannini, A., Seneviratne, S. I., Van Den Hurk, B., Lorenz, R., Pitman, A., Hagemann, S., Meier, A., Cheruy, F., Ducharne, A., Malyshev, S., & Milly, P. C. D. (2016). Land-atmosphere feedbacks amplify aridity increase over land under global warming. *Nature Climate Change*, *6*(9), 869–874. https://doi.org/10.1038/nclimate3029

Bessenbacher, V., Gudmundsson, L., & Seneviratne, S. I. (2023). Optimizing Soil Moisture Station Networks for Future Climates. *Geophysical Research Letters*, *50*(4), 1–11. https://doi.org/10.1029/2022GL101667

Blois, J. L., Williams, J. W., Fitzpatrick, M. C., Jackson, S. T., & Ferrier, S. (2013). Space can substitute for time in predicting climate-change effects on biodiversity. *Proceedings of the National Academy of Sciences of the United States of America*, *110*(23), 9374–9379. https://doi.org/10.1073/pnas.1220228110

Bogena, H. R., Bol, R., Borchard, N., Brüggemann, N., Diekkrüger, B., Drüe, C., Groh, J., Gottselig, N., Huisman, J. A., Lücke, A., Missong, A., Neuwirth, B., Pütz, T., Schmidt, M., Stockinger, M., Tappe, W., Weihermüller, L., Wiekenkamp, I., & Vereecken, H. (2015). A terrestrial observatory approach to the integrated investigation of the effects of deforestation on water, energy, and matter fluxes. *Science China Earth Sciences*, *58*(1), 61–75. https://doi.org/10.1007/s11430-014-4911-7

Bogena, H. R., Montzka, C., Huisman, J. A., Graf, A., Schmidt, M., Stockinger, M., von Hebel, C., Hendricks-Franssen, H. J., van der Kruk, J., Tappe, W., Lücke, A., Baatz, R., Bol, R., Groh, J., Pütz, T., Jakobi, J., Kunkel, R., Sorg, J., & Vereecken, H. (2018). The TERENO-Rur Hydrological Observatory: A Multiscale Multi-Compartment Research Platform for the Advancement of Hydrological Science. *Vadose Zone Journal*, *17*(1), 180055. https://doi.org/10.2136/vzj2018.03.0055

Bravo, S., González-chang, M., Dec, D., Valle, S., & Wendroth, O. (2020). Using wavelet analyses to identify temporal coherence in soil physical properties in a volcanic ash-derived soil. *Agricultural and Forest Meteorology*, *285–286*(January), 107909. https://doi.org/10.1016/j.agrformet.2020.107909

Brown, W. G., Cosh, M. H., Dong, J., & Ochsner, T. E. (2023). Upscaling soil moisture from point scale to field scale: Toward a general model. *Vadose Zone Journal*, *22*(2), 1–14. https://doi.org/10.1002/vzj2.20244

Budyko, M. I. (1974). *Climate and life*.

Buitink, J., Swank, A. M., Van Der Ploeg, M., Smith, N. E., Benninga, H. J. F., Van Der Bolt, F., Carranza, C. D. U., Koren, G., Van Der Velde, R., & Teuling, A. J. (2020). Anatomy of the 2018 agricultural drought in the Netherlands using in situ soil moisture and satellite vegetation indices. *Hydrology and Earth System Sciences*, *24*(12), 6021–6031. https://doi.org/10.5194/hess-24-6021-2020

Callejas-Rodelas, J. Á., Knohl, A., van Ramshorst, J., Mammarella, I., & Markwitz, C. (2024). Comparison between lower-cost and conventional eddy covariance setups for CO2 and evapotranspiration measurements above monocropping and agroforestry systems. *Agricultural and Forest Meteorology*, *354*(May). https://doi.org/10.1016/j.agrformet.2024.110086

Cao, M., Wang, W., Xing, W., Wei, J., Chen, X., & Li, J. (2021). Multiple sources of uncertainties in satellite retrieval of terrestrial actual evapotranspiration. *Journal of Hydrology*, *601*(March), 126642. https://doi.org/10.1016/j.jhydrol.2021.126642

Capehart, W. J., & Carlson, T. N. (1997). Decoupling of surface and near-surface soil water content: A remote sensing perspective. *Water Resources Research*, *33*(6), 1383–1395.

Carey, S. K., Tetzlaff, D., Buttle, J., Laudon, H., McDonnell, J., McGuire, K., Seibert, J., Soulsby, C., & Shanley, J. (2013). Use of color maps and wavelet coherence to discern seasonal and interannual climate influences on streamflow variability in northern catchments. *Water Resources Research*, *49*(10), 6194–6207. https://doi.org/10.1002/wrcr.20469

Carminati, A., & Javaux, M. (2020). Soil Rather Than Xylem Vulnerability Controls Stomatal Response to Drought. *Trends in Plant Science*, *25*(9), 868–880. https://doi.org/10.1016/j.tplants.2020.04.003

Charlier, J. B., Ladouche, B., & Maréchal, J. C. (2015). Identifying the impact of climate and anthropic pressures on karst aquifers using wavelet analysis. *Journal of Hydrology*, *523*, 610–623. https://doi.org/10.1016/j.jhydrol.2015.02.003

Cheng, Q., Zhong, F., & Wang, P. (2021). Baseflow dynamics and multivariate analysis using bivariate and multiple wavelet coherence in an alpine endorheic river basin (Northwest China). *Science of the Total Environment*, *772*, 145013. https://doi.org/10.1016/j.scitotenv.2021.145013

Chu, H., Luo, X., Ouyang, Z., Chan, W. S., Dengel, S., Biraud, S. C., Torn, M. S., Metzger, S., Kumar, J., Arain, M. A., Arkebauer, T. J., Baldocchi, D., Bernacchi, C., Billesbach, D., Black, T. A., Blanken, P. D., Bohrer, G., Bracho, R., Brown, S., … Zona, D. (2021). Representativeness of Eddy-Covariance flux footprints for areas surrounding AmeriFlux sites. *Agricultural and Forest Meteorology*, *301–302*, 108350. https://doi.org/10.1016/J.AGRFORMET.2021.108350

Cohen, J. (1988). *Statistical Power Analysis for the Behavioral Sciences, 2nd Edn. Hillsdale, NJ: Erlbaum.*

Corami, A., Eslamian, S., & Eslamian, F. (2024). *Fundamentals of Evapotranspiration*. Taylor

and Francis, CRC Group, USA. https://doi.org/10.1201/9781003467229

Couvreur, V., Vanderborght, J., & Javaux, M. (2012). A simple three-dimensional macroscopic root water uptake model based on the hydraulic architecture approach. *Hydrology and Earth System Sciences*, *16*(8), 2957–2971. https://doi.org/10.5194/hess-16-2957-2012

Cowan, B. Y. I. R. (1965). Transport of water in the soil-plant-atmosphere system. *Journal of Applied Ecology*, *2*(1), 221–239.

Cuxart, J., & Boone, A. A. (2020). Evapotranspiration over Land from a Boundary-Layer Meteorology Perspective. *Boundary-Layer Meteorology*, *177*(2–3), 427–459. https://doi.org/10.1007/s10546-020-00550-9

Denager, T., Looms, M. C., Sonnenborg, T. O., & Jensen, K. H. (2020). Comparison of evapotranspiration estimates using the water balance and the eddy covariance methods. *Vadose Zone Journal*, *19*(1), 1–21. https://doi.org/10.1002/vzj2.20032

Denager, T., Sonnenborg, T. O., Looms, M. C., Bogena, H., & Jensen, K. H. (2023). *Point-scale multi-objective calibration of the Community Land Model (version 5 . 0) using in situ observations of water and energy fluxes and variables*. 2827–2845.

Denissen, J. M. C., Teuling, A. J., Pitman, A. J., Koirala, S., Migliavacca, M., Li, W., Reichstein, M., Winkler, A. J., Zhan, C., & Orth, R. (2022). Widespread shift from ecosystem energy to water limitation with climate change. *Nature Climate Change*, *12*(7), 677–684. https://doi.org/10.1038/s41558-022-01403-8

Denissen, J. M. C., Teuling, A. J., Reichstein, M., & Orth, R. (2020). Critical Soil Moisture Derived From Satellite Observations Over Europe. *Journal of Geophysical Research: Atmospheres*, *125*(6), 1–10. https://doi.org/10.1029/2019JD031672

Dhungel, R., Aiken, R., Evett, S. R., Colaizzi, P. D., Marek, G., Moorhead, J. E., Baumhardt, R. L., Brauer, D., Kutikoff, S., & Lin, X. (2021). Energy Imbalance and Evapotranspiration Hysteresis Under an Advective Environment: Evidence From Lysimeter, Eddy Covariance, and Energy Balance Modeling. *Geophysical Research Letters*, *48*(1), 1–12. https://doi.org/10.1029/2020GL091203

Ding, R., Kang, S., Li, F., Zhang, Y., Tong, L., & Sun, Q. (2010). Evaluating eddy covariance method by large-scale weighing lysimeter in a maize field of northwest China. *Agricultural Water Management*, *98*(1), 87–95. https://doi.org/10.1016/j.agwat.2010.08.001

Dirmeyer, P. A., Zeng, F. J., Ducharne, A., Morrill, J. C., & Koster, R. D. (2000). The sensitivity of surface fluxes to soil water content in three land surface schemes. *Journal of Hydrometeorology*, *1*(2), 121–134. https://doi.org/10.1175/1525-7541(2000)001<0121:TSOSFT>2.0.CO;2

Dong, J., Akbar, R., Feldman, A. F., Gianotti, D. S., & Entekhabi, D. (2023). Land Surfaces at the Tipping-Point for Water and Energy Balance Coupling. *Water Resources Research*, *59*(2), 1–15. https://doi.org/10.1029/2022WR032472

Dong, J., Akbar, R., Short Gianotti, D. J., Feldman, A. F., Crow, W. T., & Entekhabi, D. (2022). Can Surface Soil Moisture Information Identify Evapotranspiration Regime Transitions? In *Geophysical Research Letters* (Vol. 49, Issue 7). https://doi.org/10.1029/2021GL097697

Dong, J., Gao, M., Zhou, J., Wei, L., Zhou, H., Zhang, Y., Gao, H., Duan, Z., & Crow, W. T. (2025). Land Surface Energy Partitioning Dominates Dry-Season Water Availability Uncertainties in Earth System Models. *Water Resources Research*, *61*(5). https://doi.org/10.1029/2024WR038000

Dorigo, W., Himmelbauer, I., Aberer, D., Schremmer, L., Petrakovic, I., Zappa, L., Blöschl, G., Bogena, H., Brocca, L., Calvet, J., Camarero, J. J., & Capello, G. (2021). *The International Soil Moisture Network : serving Earth system science for over a decade*. 5749–5804.

Dupont, S. T., Beniston, J., Glover, J. D., & Hodson, A. (2014). Root traits and soil properties in harvested perennial grassland , annual wheat , and never-tilled annual wheat. *Plant and Soil,* 381(1), 405–420. https://doi.org/10.1007/s11104-014-2145-2

Eagleson, P. S. (1978). Climate, soil, and vegetation: 4. The expected value of annual evapotranspiration. *Water Resources Research*, *14*(5), 731–739. https://doi.org/10.1029/WR014i005p00731

Elzhov, T. V, Mullen, K. M., Spiess, A.-N., & Bolker, B. (2015). minpack. lm: R interface to the Levenberg-Marquardt nonlinear least-squares algorithm found in MINPACK, plus support for bounds. R package version 1.1-8. *CRAN. R-Project. Org/Package= Minpack. Lm*.

Escorihuela, M. J., Chanzy, A., Wigneron, J. P., & Kerr, Y. H. (2010). Remote Sensing of Environment Effective soil moisture sampling depth of L-band radiometry : A case study. *Remote Sensing of Environment*, *114*(5), 995–1001. https://doi.org/10.1016/j.rse.2009.12.011

Evett, S. R., Schwartz, R. C., Howell, T. A., Louis Baumhardt, R., & Copeland, K. S. (2012). Can weighing lysimeter ET represent surrounding field ET well enough to test flux station measurements of daily and sub-daily ET? *Advances in Water Resources*, *50*, 79–90. https://doi.org/10.1016/j.advwatres.2012.07.023

Fan, Y., Miguez-Macho, G., Jobbágy, E. G., Jackson, R. B., & Otero-Casal, C. (2017). Hydrologic regulation of plant rooting depth. *Proceedings of the National Academy of Sciences of the United States of America*, *114*(40), 10572–10577. https://doi.org/10.1073/pnas.1712381114

Feldman, A. F., Short Gianotti, D. J., Dong, J., Akbar, R., Crow, W. T., McColl, K. A., Konings, A. G., Nippert, J. B., Tumber-Dávila, S. J., Holbrook, N. M., Rockwell, F. E., Scott, R. L., Reichle, R. H., Chatterjee, A., Joiner, J., Poulter, B., & Entekhabi, D. (2023). Remotely Sensed Soil Moisture Can Capture Dynamics Relevant to Plant Water Uptake. *Water Resources Research*, *59*(2), 1–17. https://doi.org/10.1029/2022WR033814

Feldman, A. F., Short Gianotti, D. J., Trigo, I. F., Salvucci, G. D., & Entekhabi, D. (2019). Satellite-Based Assessment of Land Surface Energy Partitioning–Soil Moisture Relationships and Effects of Confounding Variables. *Water Resources Research*, *55*(12), 10657–10677. https://doi.org/10.1029/2019WR025874

Ficklin, D. L., Myers, D. T., Null, S. E., & Abatzoglou, J. T. (2022). *Hydrological Intensification Will Increase the Complexity of Water Resource Management Earth ' s Future*. https://doi.org/10.1029/2021EF002487

Finnigan, J. (2004). The footprint concept in complex terrain. *Agricultural and Forest Meteorology,* 127, 117–129. https://doi.org/10.1016/j.agrformet.2004.07.008

Fisher, J. B., Melton, F., Middleton, E., Hain, C., Anderson, M., Allen, R., McCabe, M. F., Hook, S., Baldocchi, D., Townsend, P. A., Kilic, A., Tu, K., Miralles, D. D., Perret, J., Lagouarde, J. P., Waliser, D., Purdy, A. J., French, A., Schimel, D., … Wood, E. F. (2017). The future of evapotranspiration: Global requirements for ecosystem functioning, carbon and climate feedbacks, agricultural management, and water resources. *Water Resources Research*, *53*(4), 2618–2626. https://doi.org/10.1002/2016WR020175

Foken, T. (2008). The energy balance closure problem: An overview. *Ecological Applications*, *18*(6), 1351–1367. https://doi.org/10.1890/06-0922.1

Foken, T., Aubinet, M., Finnigan, J. J., Leclerc, M. Y., Mauder, M., & Paw U, K. T. (2011). Results of a panel discussion about the energy balance closure correction for trace gases. *Bulletin of the American Meteorological Society*, *92*(4), 13–18. https://doi.org/10.1175/2011BAMS3130.1

Foken, T., & Wichura, B. (1996). Tools for quality assessment of surface-based flux measurements. *Agricultural and Forest Meteorology*, *78*(1–2), 83–105. https://doi.org/10.1016/0168-1923(95)02248-1

Foley, J. A., Ramankutty, N., Brauman, K. A., Cassidy, E. S., Gerber, J. S., Johnston, M., Mueller, N. D., Connell, C. O., Ray, D. K., West, P. C., Balzer, C., Bennett, E. M., Sheehan, J., Siebert, S., Carpenter, S. R., Hill, J., Monfreda, C., Polasky, S., Rockstro, J., … Zaks, D. P. M. (2011). Solutions for a cultivated planet. *Nature*. https://doi.org/10.1038/nature10452

Ford, T. W., Harris, E., & Quiring, S. M. (2014). Estimating root zone soil moisture using near-surface observations from SMOS. *Hydrology and Earth System Sciences*, *1994*, 139–154. https://doi.org/10.5194/hess-18-139-2014

Ford, T. W., Wulff, C. O., & Quiring, S. M. (2014). Assessment of observed and model-derived soil moisture-evaporative fraction relationships over the United States southern great plains. *Journal of Geophysical Research*, *119*(11), 6279–6291. https://doi.org/10.1002/2014JD021490

Forstner, V., Groh, J., Vremec, M., Herndl, M., Vereecken, H., Gerke, H. H., Birk, S., & Pütz, T. (2021). Supplementrary Response of water fluxes and biomass production to climate change in permanent grassland soil ecosystems. *Hydrology and Earth System Sciences*,

25(12), 6087–6106. https://doi.org/10.5194/hess-25-6087-2021

Fraenkel, J. R., & Wallen, N. E. (1990). *How to design and evaluate research in education.* ERIC.

Franssen, H. J. H., Stöckli, R., Lehner, I., Rotenberg, E., & Seneviratne, S. I. (2010). Energy balance closure of eddy-covariance data : A multisite analysis for European FLUXNET stations. *Agricultural and Forest Meteorology*. https://doi.org/10.1016/j.agrformet.2010.08.005

Fu, J., Gasche, R., Wang, N., Lu, H., Butterbach-Bahl, K., & Kiese, R. (2017). Impacts of climate and management on water balance and nitrogen leaching from montane grassland soils of S-Germany. *Environmental Pollution*, *229*, 119–131. https://doi.org/10.1016/j.envpol.2017.05.071

Fu, J., Gasche, R., Wang, N., Lu, H., Butterbach-Bahl, K., & Kiese, R. (2019). Dissolved organic carbon leaching from montane grasslands under contrasting climate, soil and management conditions. *Biogeochemistry*, *145*(1–2), 47–61. https://doi.org/10.1007/s10533-019-00589-y

Fu, Z., Ciais, P., Feldman, A. F., Gentine, P., Makowski, D., Prentice, I. C., Stoy, P. C., Bastos, A., & Wigneron, J. P. (2022). Critical soil moisture thresholds of plant water stress in terrestrial ecosystems. *Science Advances*, *8*(44), 1–13. https://doi.org/10.1126/sciadv.abq7827

Fu, Z., Ciais, P., Makowski, D., Bastos, A., Stoy, P. C., Ibrom, A., Knohl, A., Migliavacca, M., Cuntz, M., Šigut, L., Peichl, M., Loustau, D., El-Madany, T. S., Buchmann, N., Gharun, M., Janssens, I., Markwitz, C., Grünwald, T., Rebmann, C., … Wigneron, J. P. (2022). Uncovering the critical soil moisture thresholds of plant water stress for European ecosystems. *Global Change Biology*, *28*(6), 2111–2123. https://doi.org/10.1111/gcb.16050

Fu, Z., Ciais, P., Wigneron, J.-P., Gentine, P., Andrew F. Feldman, Makowski, D., Viovy, N., Kemanian, A. R., DanielS.Goll, PaulC.Stoy, Prentice, I., Yakir, D., Liu, L., Ma, H., Li, X., Huang, Y., Yu, K., Zhu, P., Li, X., … Smith, W. K. (2024). Global critical soil moisture thresholds of plant water stress. *Nature Communications*, *22 May 2024*, 5194. https://doi.org/10.1038/s41467-024-49244-7

Gao, Z., Russell, E. S., Missik, J. E. C., Huang, M., Chen, X., Strickland, C. E., Clayton, R., Arntzen, E., Ma, Y., & Liu, H. (2017). A novel approach to evaluate soil heat flux calculation: An analytical review of nine methods. *Journal of Geophysical Research*, *122*(13), 6934–6949. https://doi.org/10.1002/2017JD027160

Garcia-Vila, M., dos Santos Vianna, M., Harrison, M. T., Liu, K., de S. Nóia-Júnior, R., Weber, T. K. D., Zhao, J., Acutis, M., Archontoulis, S., Asseng, S., Aubry, P., Balkovic, J., Basso, B., Chen, X., Chen, Y., de Jong van Lier, Q., Delandmeter, M., de Wit, A., Dumont, B., … Palosuo, T. (2025). Gaps and strategies for accurate simulation of waterlogging impacts on crop productivity. *Nature Food*, *6*(6), 553–562. https://doi.org/10.1038/s43016-025-

01179-y

Gebler, S., Hendricks Franssen, H. J., Pütz, T., Post, H., Schmidt, M., & Vereecken, H. (2015). Actual evapotranspiration and precipitation measured by lysimeters: A comparison with eddy covariance and tipping bucket. *Hydrology and Earth System Sciences*, *19*(5), 2145–2161. https://doi.org/10.5194/hess-19-2145-2015

Giambelluca, T. W., Scholz, F. G., Bucci, S. J., Meinzer, F. C., Goldstein, G., Hoffmann, W. A., Franco, A. C., & Buchert, M. P. (2009). Evapotranspiration and energy balance of Brazilian savannas with contrasting tree density. *Agricultural and Forest Meteorology*, *149*(8), 1365–1376. https://doi.org/10.1016/j.agrformet.2009.03.006

Giardina, F., Padrón, R. S., Stocker, B. D., Schumacher, D. L., & Seneviratne, S. I. (2025). Large biases in the frequency of water limitation across Earth system models. *Communications Earth and Environment*, *6*(1), 1–9. https://doi.org/10.1038/s43247-025-02426-7

Giraud, M., Groh, J., Gerke, H. H., Brüggemann, N., Vereecken, H., & Pütz, T. (2021). Soil Nitrogen Dynamics in a Managed Temperate Grassland Under Changed Climatic Conditions. *Water*, 1–23. https://doi.org/10.3390/w13070931

Goss, M. J., & Ehlers, W. (2009). The role of lysimeters in the development of our understanding of soil water and nutrient dynamics in ecosystems. *Soil Use and Management*, *25*(3), 213–223. https://doi.org/10.1111/j.1475-2743.2009.00230.x

Graf, A., Bogena, H. R., Drüe, C., Hardelauf, H., & Pütz, T. (2014). Spatiotemporal relations between water budget components and soil water content in a forested tributary catchment. *Water Resources Research*, 5375–5377. https://doi.org/10.1002/2013WR014979.Reply

Graf, A., Klosterhalfen, A., Arriga, N., Bernhofer, C., Bogena, H., Bornet, F., Brüggemann, N., Brümmer, C., Buchmann, N., Chi, J., Chipeaux, C., Cremonese, E., Cuntz, M., Dušek, J., El-Madany, T. S., Fares, S., Fischer, M., Foltýnová, L., Gharun, M., … Vereecken, H. (2020). Altered energy partitioning across terrestrial ecosystems in the European drought year 2018: Energy partitioning in the drought 2018. *Philosophical Transactions of the Royal Society B: Biological Sciences*, *375*(1810). https://doi.org/10.1098/rstb.2019.0524

Green, J. K., Zhang, Y., Luo, X., & Keenan, T. F. (2024). Systematic Underestimation of Canopy Conductance Sensitivity to Drought by Earth System Models. *AGU Advances*, *5*(1). https://doi.org/10.1029/2023AV001026

Green, S. R., & Clothier, B. E. (1995). Root water uptake by kiwifruit vines following partial wetting of the root zone. *Plant and Soil*, 317–328.

Grinsted, A., Moore, J. C., & Jevrejeva, S. (2004). Application of the cross wavelet transform and wavelet coherence to geophysical time series. *Nonlinear Processes in Geophysics*, *11*(4), 515–533. https://doi.org/10.5194/npg-11-515-2004

Groh, J., Diamantopoulos, E., Duan, X., Ewert, F., Heinlein, F., Herbst, M., Holbak, M., Kamali, B., Kersebaum, K. C., Kuhnert, M., Nendel, C., Priesack, E., Steidl, J., Sommer,

M., Pütz, T., Vanderborght, J., Vereecken, H., Wallor, E., Weber, T. K. D., … Gerke, H. H. (2022). Same soil, different climate: Crop model intercomparison on translocated lysimeters. *Vadose Zone Journal*, *21*(4), 1–25. https://doi.org/10.1002/vzj2.20202

Groh, J., Diamantopoulos, E., Duan, X., Ewert, F., Herbst, M., Holbak, M., Kamali, B., Kersebaum, K.-C., Kuhnert, M., Lischeid, G., & others. (2020). Crop growth and soil water fluxes at erosion-affected arable sites: Using weighing lysimeter data for model intercomparison. *Vadose Zone Journal*, *19*(1), e20058. https://doi.org/10.1002/vzj2.20058

Groh, J., Pütz, T., Gerke, H. H., Vanderborght, J., & Vereecken, H. (2019). Quantification and Prediction of Nighttime Evapotranspiration for Two Distinct Grassland Ecosystems. *Water Resources Research*, *55*(4), 2961–2975. https://doi.org/10.1029/2018WR024072

Groh, J., Slawitsch, V., Herndl, M., Graf, A., Vereecken, H., & Pütz, T. (2018). Determining dew and hoar frost formation for a low mountain range and alpine grassland site by weighable lysimeter. *Journal of Hydrology*, *563*(November 2017), 372–381. https://doi.org/10.1016/j.jhydrol.2018.06.009

Groh, J., Vanderborght, J., Pütz, T., Gründling, R., Rupp, H., Rahmati, M., Sommer, M., Sommer, M., Vereecken, H., & Gerke, H. H. (2020). Responses of soil water storage and crop water use efficiency to changing climatic conditions: A lysimeter-based space-for-time approach. *Hydrology and Earth System Sciences*, *24*(3), 1211–1225. https://doi.org/10.5194/hess-24-1211-2020

Groh, J., Vanderborght, J., Pütz, T., & Vereecken, H. (2016). How to Control the Lysimeter Bottom Boundary to Investigate the Effect of Climate Change on Soil Processes? *Vadose Zone Journal*, *15*(7), vzj2015.08.0113. https://doi.org/10.2136/vzj2015.08.0113

Gruber, A., Dorigo, W. A., Zwieback, S., Xaver, A., & Wagner, W. (2013). Characterizing Coarse-Scale Representativeness of in situ Soil Moisture Measurements from the International Soil Moisture Network. *Vadose Zone Journal*, *12*(2), 1–16. https://doi.org/10.2136/vzj2012.0170

Grumm, R. H., & Hart, R. (2001). Standardized Anomalies Applied to Significant Cold Season Weather Events : Preliminary Findings. *Weather and Forecasting*, 736–754.

Gu, L., Meyers, T., Pallardy, S. G., Hanson, P. J., Yang, B., Heuer, M., Hosman, K. P., Riggs, J. S., Sluss, D., & Wullschleger, S. D. (2006). Direct and indirect effects of atmospheric conditions and soil moisture on surface energy partitioning revealed by a prolonged drought at a temperate forest site. *Journal of Geophysical Research Atmospheres*, *111*(16). https://doi.org/10.1029/2006JD007161

Haghighi, E., Short Gianotti, D. J., Akbar, R., Salvucci, G. D., & Entekhabi, D. (2018). *Soil and Atmospheric Controls on the Land Surface Energy Balance: A Generalized Framework for Distinguishing Moisture-Limited and Energy-Limited Evaporation Regimes*. 1831–1851. https://doi.org/10.1002/2017WR021729

Han, Q., Wang, T., Wang, L., Smettem, K., Mai, M., & Chen, X. (2021). Comparison of

Nighttime With Daytime Evapotranspiration Responses to Environmental Controls Across Temporal Scales Along a Climate Gradient. *Water Resources Research*, *57*(7), 1–18. https://doi.org/10.1029/2021WR029638

Hanson, R. L. (1991). Evapotranspiration and droughts. *National Water Summary 1988--89: Hydrologic Events and Floods and Droughts (US Geological Survey Water-Supply Paper 2375)*, 99–104.

Heinrich, I., Balanzategui, D., Bens, O., Blume, T., Böttcher, F., Borg, E., Brauer, A., Conrad, C., Dräger, N., Fiener, P., Gerke, H. H., Güntner, A., Heine, I., Helle, G., Harfenmeister, K., Heußner, K., Hohmann, C., Itzerott, S., Jurasinski, G., … Wilken, F. (2018). *Interdisciplinary Geo-ecological Research across Time Scales in the Northeast German Lowland Observatory (TERENO-NE)*. https://doi.org/10.2136/vzj2018.06.0116

Herbrich, M., & Gerke, H. H. (2017). Scales of Water Retention Dynamics Observed in Eroded Luvisols from an Arable Postglacial Soil Landscape. *Vadose Zone Journal*, *16*(10), 1–17. https://doi.org/10.2136/vzj2017.01.0003

Hirschi, M., Michel, D., Lehner, I., & Seneviratne, S. I. (2017). A site-level comparison of lysimeter and eddy covariance flux measurements of evapotranspiration. *Hydrology and Earth System Sciences*, *21*(3), 1809–1825. https://doi.org/10.5194/hess-21-1809-2017

Hirschi, M., Mueller, B., Dorigo, W., & Seneviratne, S. I. (2014). Using remotely sensed soil moisture for land – atmosphere coupling diagnostics : The role of surface vs . root-zone soil moisture variability. *Remote Sensing of Environment*, *154*, 246–252. https://doi.org/10.1016/j.rse.2014.08.030

Hollinger, D. Y., & Richardson, A. D. (2005). Uncertainty in eddy covariance measurements and its application to physiological models. *Tree Physiology*, *25*(7), 873–885. https://doi.org/10.1093/treephys/25.7.873

Hsu, H., & Dirmeyer, P. A. (2023a). Soil moisture-evaporation coupling shifts into new gears under increasing CO2. *Nature Communications*, *14*(1). https://doi.org/10.1038/s41467-023-36794-5

Hsu, H., & Dirmeyer, P. A. (2023b). Uncertainty in Projected Critical Soil Moisture Values in CMIP6 Affects the Interpretation of a More Moisture-Limited World. *Earth's Future*, *11*(6), 1–15. https://doi.org/10.1029/2023ef003511

Hu, W., & Si, B. (2021). Technical Note: Improved partial wavelet coherency for understanding scale-specific and localized bivariate relationships in geosciences. *Hydrology and Earth System Sciences*, *25*(1), 321–331. https://doi.org/10.5194/hess-25-321-2021

Hu, W., & Si, B. C. (2016). Technical note: Multiple wavelet coherence for untangling scale-specific and localized multivariate relationships in geosciences. *Hydrology and Earth System Sciences*, *20*(8), 3183–3191. https://doi.org/10.5194/hess-20-3183-2016

Hu, W., Si, B. C., Biswas, A., & Chau, H. W. (2017). Temporally stable patterns but seasonal

dependent controls of soil water content: Evidence from wavelet analyses. *Hydrological Processes*, *31*(21), 3697–3707. https://doi.org/10.1002/hyp.11289

Humphrey, V., Berg, A., Ciais, P., Gentine, P., Jung, M., Reichstein, M., Seneviratne, S. I., & Frankenberg, C. (2021). Soil moisture – atmosphere feedback dominates land carbon uptake variability. *Nature*, *592*(April). https://doi.org/10.1038/s41586-021-03325-5

Iwema, J., Rosolem, R., Rahman, M., Blyth, E., & Wagener, T. (2017). Land surface model performance using cosmic-ray and point-scale soil moisture measurements for calibration. *Hydrology and Earth System Sciences*, *21*(6), 2843–2861. https://doi.org/10.5194/hess-21-2843-2017

Jarvis, N., Groh, J., Lewan, E., Meurer, K. H. E., Durka, W., Baessler, C., Pütz, T., Rufullayev, E., & Vereecken, H. (2022). Coupled modelling of hydrological processes and grassland production in two contrasting climates. *Hydrology and Earth System Sciences*, *26*(8), 2277–2299. https://doi.org/10.5194/hess-26-2277-2022

Ji, Y., Fu, J., Liu, B., Huang, Z., & Tan, X. (2024). Uncertainty separation of drought projection in the 21st century using SMILEs and CMIP6. *Journal of Hydrology*, *628*(November 2023), 130497. https://doi.org/10.1016/j.jhydrol.2023.130497

Karbalaye, A., Rao, S., Hessels, T., Bastiaanssen, W., & Kisekka, I. (2025). Enhancing evapotranspiration estimates in composite terrain through the integration of satellite remote sensing and eddy covariance measurements. *Science of the Total Environment*, *963*(December 2024).

Kauwe, M. G. De, Medlyn, B. E., Knauer, J., & Williams, C. A. (2017). Ideas and perspectives : how coupled is the vegetation to the boundary layer ? *Biogeosciences*, *14*(19), 4435-4453. https://doi.org/10.5194/bg-14-4435-2017

Kessomkiat, W., Franssen, H. J. H., Graf, A., & Vereecken, H. (2013). Estimating random errors of eddy covariance data: An extended two-tower approach. *Agricultural and Forest Meteorology*, *171–172*, 203–219. https://doi.org/10.1016/j.agrformet.2012.11.019

Kiese, R., Fersch, B., Baessler, C., Brosy, C., Butterbach-Bahl, K., Chwala, C., Dannenmann, M., Fu, J., Gasche, R., Grote, R., Jahn, C., Klatt, J., Kunstmann, H., Mauder, M., Rödiger, T., Smiatek, G., Soltani, M., Steinbrecher, R., Völksch, I., … Schmid, H. P. (2018). The TERENO Pre-Alpine Observatory: Integrating Meteorological, Hydrological, and Biogeochemical Measurements and Modeling. *Vadose Zone Journal*, *17*(1), 180060. https://doi.org/10.2136/vzj2018.03.0060

Kim, D., Choi, M., & Chun, J. A. (2022). Linking the complementary evaporation relationship with the Budyko framework for ungauged areas in Australia. *Hydrology and Earth System Sciences*, *26*(23), 5955–5969. https://doi.org/10.5194/hess-26-5955-2022

Kljun, N., Calanca, P., Rotach, M. W., & Schmid, H. P. (2015). A simple two-dimensional parameterisation for Flux Footprint Prediction (FFP). *Geoscientific Model Development*, *8*(11), 3695–3713. https://doi.org/10.5194/gmd-8-3695-2015

Kohfahl, C., Molano-Leno, L., Martínez, G., Vanderlinden, K., Guardiola-Albert, C., & Moreno, L. (2019). Determining groundwater recharge and vapor flow in dune sediments using a weighable precision meteo lysimeter. *Science of the Total Environment*, *656*, 550–557. https://doi.org/10.1016/j.scitotenv.2018.11.415

Kool, D., Agam, N., Lazarovitch, N., Heitman, J. L., Sauer, T. J., & Ben-Gal, A. (2014). A review of approaches for evapotranspiration partitioning. *Agricultural and Forest Meteorology*, *184*, 56–70. https://doi.org/10.1016/j.agrformet.2013.09.003

Korres, W., Koyama, C. N., Fiener, P., & Schneider, K. (2010). Analysis of surface soil moisture patterns in agricultural landscapes using Empirical Orthogonal Functions. *Hydrology and Earth System Sciences*, *14*(5), 751–764. https://doi.org/10.5194/hess-14-751-2010

Korres, W., Reichenau, T. G., Fiener, P., Koyama, C. N., Bogena, H. R., Cornelissen, T., Baatz, R., Herbst, M., Diekkrüger, B., Vereecken, H., & Schneider, K. (2015). Spatio-temporal soil moisture patterns - A meta-analysis using plot to catchment scale data. *Journal of Hydrology*, *520*, 326–341. https://doi.org/10.1016/j.jhydrol.2014.11.042

Koster, R. D., Feldman, A. F., Holmes, T. R. H., Anderson, M. C., Crow, W. T., & Hain, C. (2024). Estimating Hydrological Regimes from Observational Soil Moisture , Evapotranspiration , and Air Temperature Data. *Journal of Hydrometeorology*, 495–513. https://doi.org/10.1175/JHM-D-23-0140.1

Koster, R. D., Guo, Z., Yang, R., Dirmeyer, P. A., Mitchell, K., & Puma, M. J. (2009). On the nature of soil moisture in land surface models. *Journal of Climate*, *22*(16), 4322–4335. https://doi.org/10.1175/2009JCLI2832.1

Koster, R. D., Schubert, S. D., & Suarez, M. J. (2009). Analyzing the concurrence of meteorological droughts and warm periods, with implications for the determination of evaporative regime. *Journal of Climate*, *22*(12), 3331–3341. https://doi.org/10.1175/2008JCLI2718.1

Labat, D. (2005). Recent advances in wavelet analyses: Part 1. A review of concepts. *Journal of Hydrology*, *314*(1), 275–288. https://doi.org/https://doi.org/10.1016/j.jhydrol.2005.04.003

Lei, F., Crow, W. T., Holmes, T. R. H., Hain, C., & Anderson, M. C. (2018). Global Investigation of Soil Moisture and Latent Heat Flux Coupling Strength. *Water Resources Research*, *54*(10), 8196–8215. https://doi.org/10.1029/2018WR023469

Levy, P., Clement, R., Cowan, N., Keane, B., Myrgiotis, V., van Oijen, M., Smallman, T. L., Toet, S., & Williams, M. (2022). Challenges in Scaling Up Greenhouse Gas Fluxes: Experience From the UK Greenhouse Gas Emissions and Feedbacks Program. *Journal of Geophysical Research: Biogeosciences*, *127*(5), 1–22. https://doi.org/10.1029/2021JG006743

Li, W., Hendricks Franssen, H. J., Brunner, P., Li, Z., Wang, Z., Wang, Y., & Wang, W. (2022). The role of soil texture on diurnal and seasonal cycles of potential evaporation over

saturated bare soils – Lysimeter studies. *Journal of Hydrology*, *613*(December 2021). https://doi.org/10.1016/j.jhydrol.2022.128194

Liebethal, C., Huwe, B., & Foken, T. (2005). Sensitivity analysis for two ground heat flux calculation approaches. *Agricultural and Forest Meteorology*, *132*(3–4), 253–262. https://doi.org/10.1016/j.agrformet.2005.08.001

Liu, Q., Hao, Y., Stebler, E., Tanaka, N., & Zou, C. B. (2017). Impact of Plant Functional Types on Coherence Between Precipitation and Soil Moisture: A Wavelet Analysis. *Geophysical Research Letters*, *44*(24), 12,197-12,207. https://doi.org/10.1002/2017GL075542

Liu, Y., Xiao, J., Li, X., & Li, Y. (2024). Critical soil moisture detection and water-energy limit shift attribution using satellite-based water and carbon fluxes over China. *Hydrology and Earth System Sciences*, *April*, 1–30. https://doi.org/10.5194/hess-29-1241-2025

Lo, M. H., Wu, W. Y., Tang, L. I., Ryu, D., Rashid, M., & Wu, R. J. (2021). Temporal changes in land surface coupling strength: An example in a semi-arid region of Australia. *Journal of Climate*, *34*(4), 1503–1513. https://doi.org/10.1175/JCLI-D-20-0250.1

Long, D., Longuevergne, L., & Scanlon, B. R. (2014). Uncertainty in evapotranspiration from land surface modeling, remote sensing, and GRACE satellites. *Water Resources Research*, *Vic*, 1131–1151. https://doi.org/10.1002/2013WR014581

Lu, X., Groh, J., Graf, A., Pütz, T., Schneider, K., Si, B., Vereecken, H., & Franssen, H. J. H. (2024). Analysis of scale-dependent spatial correlations of actual evapotranspiration measured by lysimeters. *Agricultural and Forest Meteorology*, *359*(October), 110288. https://doi.org/10.1016/j.agrformet.2024.110288

Mahmood, R., & Hubbard, K. G. (2007). Relationship between soil moisture of near surface and multiple depths of the root zone under heterogeneous land uses and varying hydroclimatic conditions. *Hydrological Processes: An International Journal*, 21(25), 3449-3462. https://doi.org/10.1002/hyp.6578

Mälicke, M., Hassler, S. K., Weiler, M., Blume, T., & Zehe, E. (2018). Exploring hydrological similarity during soil moisture recession periods using time dependent variograms. *Hydrology and Earth System Sciences Discussions*, *2018*, 1-25. https://doi.org/10.5194/hess-2018-396

Manabe, S. (1969). Climate and the Ocean Circulation: The Atmospheric Circulation and the Hydrology of the Earth's Surface. *Monthly Weather Review*, *97*(11), 739–774. http://journals.ametsoc.org/doi/abs/10.1175/1520-0493(1969)097%3C0739:CATOC%3E2.3.CO;2

Maraun, D., & Kurths, J. (2004). Cross wavelet analysis: significance testing and pitfalls D. *Nonlinear Processes in Geophysics*, *11*(3), 363–370. https://doi.org/10.5194/npg-11-363-2004

Martens, B., Miralles, D. G., Lievens, H., Van Der Schalie, R., De Jeu, R. A. M., Fernández-

Prieto, D., Beck, H. E., Dorigo, W. A., & Verhoest, N. E. C. (2017). GLEAM v3: Satellite-based land evaporation and root-zone soil moisture. *Geoscientific Model Development*, *10*(5), 1903–1925. https://doi.org/10.5194/gmd-10-1903-2017

Mauder, M., Cuntz, M., Drüe, C., Graf, A., Rebmann, C., Schmid, H. P., Schmidt, M., & Steinbrecher, R. (2013). A strategy for quality and uncertainty assessment of long-term eddy-covariance measurements. *Agricultural and Forest Meteorology*, *169*, 122–135. https://doi.org/10.1016/j.agrformet.2012.09.006

Mauder, M., & Foken, T. (2011). Documentation and Instruction Manual of the Eddy-Covariance Software Package TK3. *Arbeitsergebnisse*, *3*(46), 60, ISSN 1614-8916. http://nbn-resolving.de/urn/resolver.pl?urn:nbn:de:bvb:703-opus-8665%5Cnhttp://opus4.kobv.de/opus4-ubbayreuth/frontdoor/index/index/docId/681

Mauder, M., Foken, T., & Cuxart, J. (2020). Surface-Energy-Balance Closure over Land: A Review. In *Boundary-Layer Meteorology* (Vol. 177, Issues 2–3). Springer Netherlands. https://doi.org/10.1007/s10546-020-00529-6

Mauder, M., Genzel, S., Fu, J., Kiese, R., Soltani, M., Steinbrecher, R., Zeeman, M., Banerjee, T., De Roo, F., & Kunstmann, H. (2018). Evaluation of energy balance closure adjustment methods by independent evapotranspiration estimates from lysimeters and hydrological simulations. *Hydrological Processes*, *32*(1), 39–50. https://doi.org/10.1002/hyp.11397

Mauder, M., Ibrom, A., Wanner, L., Roo, F. De, Brugger, P., & Kiese, R. (2021). Options to correct local turbulent flux measurements for large-scale fluxes using an approach based on large-eddy simulation. *Atmospheric Measurement Techniques*, 14(12), 7835-7850. https://doi.org/10.5194/amt-14-7835-2021

Maxwell, R. M., & Condon, L. E. (2016). Connections between groundwater flow and transpiration partitioning. *Science*, *353*(6297), 377-380. https://doi.org/10.1126/science.aaf7891

McColl, K. A., Wang, W., Peng, B., Akbar, R., Short Gianotti, D. J., Lu, H., Pan, M., & Entekhabi, D. (2017). Global characterization of surface soil moisture drydowns. *Geophysical Research Letters*, *44*(8), 3682–3690. https://doi.org/10.1002/2017GL072819

Meng, L., Chambers, J., Koven, C., Pastorello, G., & Gimenez, B. (2022). Soil moisture thresholds explain a shift from light- limited to water-limited sap velocity in the Central Amazon during the 2015 – 16 El Niño drought OPEN ACCESS Soil moisture thresholds explain a shift from light-limited to water-limited sap velocity in. *Environmental Research Letters*. https://doi.org/10.1088/1748-9326/ac6f6d

Miralles, D. G., Gentine, P., Seneviratne, S. I., & Teuling, A. J. (2019). Land – atmospheric feedbacks during droughts and heatwaves : state of the science and current challenges. *Annals of the New York Academy OfSciences*, *1436*, 19–35. https://doi.org/10.1111/nyas.13912

Mittelbach, H., Casini, F., Lehner, I., Teuling, A. J., & Seneviratne, S. I. (2011). Soil moisture

monitoring for climate research: Evaluation of a low-cost sensor in the framework of the Swiss soil moisture experiment (SwissSMEX) campaign. *Journal of Geophysical Research Atmospheres*, *116*(5), 1–11. https://doi.org/10.1029/2010JD014907

Mondal, S., & Mishra, A. (2024). Quantifying the Precipitation, Evapotranspiration, and Soil Moisture Network's Interaction Over Global Land Surface Hydrological Cycle. *Water Resources Research*, *60*(2). https://doi.org/10.1029/2023WR034861

Mu, Q., Zhao, M., & Running, S. W. (2011). Improvements to a MODIS global terrestrial evapotranspiration algorithm. *Remote Sensing of Environment*, *115*(8), 1781–1800. https://doi.org/10.1016/j.rse.2011.02.019

Mueller, B., Seneviratne, S. I., Jimenez, C., Corti, T., Hirschi, M., Balsamo, G., Ciais, P., Dirmeyer, P., Fisher, J. B., Guo, Z., Jung, M., Maignan, F., McCabe, M. F., Reichle, R., Reichstein, M., Rodell, M., Sheffield, J., Teuling, A. J., Wang, K., … Zhang, Y. (2011). Evaluation of global observations-based evapotranspiration datasets and IPCC AR4 simulations. *Geophysical Research Letters*, *38*(6), 1–7. https://doi.org/10.1029/2010GL046230

Negm, A., Jabro, J., & Provenzano, G. (2017). Assessing the suitability of American National Aeronautics and Space Administration (NASA) agro-climatology archive to predict daily meteorological variables and reference evapotranspiration in Sicily, Italy. *Agricultural and Forest Meteorology*, *244–245*(October 2016), 111–121. https://doi.org/10.1016/j.agrformet.2017.05.022

Newman, B. D., Wilcox, B. P., Archer, S. R., Breshears, D. D., Dahm, C. N., Duffy, C. J., Mcdowell, N. G., Phillips, F. M., Scanlon, B. R., & Vivoni, E. R. (2006). Ecohydrology of water-limited environments : A scientific vision. *Water Resources Research*, *42*, 1–15. https://doi.org/10.1029/2005WR004141

Odorico, P. D., Davis, K. F., Rosa, L., Carr, J. A., Chiarelli, D., Angelo, J. D., Gephart, J., Macdonald, G. K., Seekell, D. A., Suweis, S., & Rulli, M. C. (2018). The Global Food-Energy-Water Nexus. *Reviews of Geophysics*, 456–531. https://doi.org/10.1029/2017RG000591

Oki, T., & Kanae, S. (2006). Global Hydrological Cycles and World Water Resources. *Science*, *August*, 1068–1072. https://doi.org/10.1126/science.1128845

Oliveira, R. S., Davidson, E. A., Klink, C. A., & Moreira, A. (2005). Deep root function in soil water dynamics in cerrado savannas of central Brazil. *Functional Ecology*, *1996*, 574–581. https://doi.org/10.1111/j.1365-2435.2005.01003.x

Oliver, M. A., Webster, R., & others. (2015). *Basic steps in geostatistics: the variogram and kriging*. . Cham, Switzerland: Springer International Publishing.

Paul, S., Feldman, A. F., & Karthikeyan, L. (2025). Are rootzone soil moisture dynamics and thresholds associated with surface layer? *Environmental Research Letters*, *20*(1), 014037. https://doi.org/10.1088/1748-9326/ad9293

Paulus, S. J., El-Madany, T. S., Orth, R., Hildebrandt, A., Wutzler, T., Carrara, A., Moreno, G., Perez-Priego, O., Kolle, O., Reichstein, M., & Migliavacca, M. (2022). Resolving seasonal and diel dynamics of non-rainfall water inputs in a Mediterranean ecosystem using lysimeters. *Hydrology and Earth System Sciences*, *26*(23), 6263–6287. https://doi.org/10.5194/hess-26-6263-2022

Paulus, S. J., Orth, R., Lee, S., Hildebrandt, A., Jung, M., Nelson, J. A., El-madany, S., Carrara, A., Moreno, G., Mauder, M., Groh, J., & Graf, A. (2024). Interpretability of negative latent heat fluxes from eddy covariance measurements in dry conditions. *Biogeosciences*, 21(8), 2051-2085. https://doi.org/10.5194/bg-21-2051-2024

Peltola, O., Aslan, T., Aurela, M., Lohila, A., & Mammarella, I. (2025). Towards an enhanced metric for detecting vertical flow decoupling in eddy covariance flux observations. *Agricultural and Forest Meteorology*, *362*(December 2024), 110326. https://doi.org/10.1016/j.agrformet.2024.110326

Peng, L., Zeng, Z., Wei, Z., Chen, A., Wood, E. F., & Sheffield, J. (2019). Determinants of the ratio of actual to potential evapotranspiration. *Global Change Biology*, *25*(4), 1326–1343. https://doi.org/10.1111/gcb.14577

Peters, A., Groh, J., Schrader, F., Durner, W., Vereecken, H., & Pütz, T. (2017). Towards an unbiased filter routine to determine precipitation and evapotranspiration from high precision lysimeter measurements. *Journal of Hydrology*, *549*, 731–740. https://doi.org/10.1016/j.jhydrol.2017.04.015

Peters, A., Nehls, T., Schonsky, H., & Wessolek, G. (2014). Separating precipitation and evapotranspiration from noise - A new filter routine for high-resolution lysimeter data. *Hydrology and Earth System Sciences*, *18*(3), 1189–1198. https://doi.org/10.5194/hess-18-1189-2014

Pitman, A. J. (2003). The evolution of, and revolution in, land surface schemes designed for climate models. *International Journal of Climatology*, *510*, 479–510. https://doi.org/10.1002/joc.893

Pollacco, J. A. P., & Mohanty, B. P. (2012). *Uncertain Θ es of Water Fluxes in Soil – Vegeta Θ on – Atmosphere Transfer Models : Inver ng Surface Soil Moisture and Evapotranspira on Retrieved from Remote Sensing*. https://doi.org/10.2136/vzj2011.0167

Post, H., Hendricks Franssen, H. J., Graf, A., Schmidt, M., & Vereecken, H. (2015). Uncertainty analysis of eddy covariance CO2 flux measurements for different EC tower distances using an extended two-tower approach. *Biogeosciences*, *12*(4), 1205–1221. https://doi.org/10.5194/bg-12-1205-2015

Poulter, B., Macbean, N., Hartley, A., Khlystova, I., Arino, O., Betts, R., Bontemps, S., & Boettcher, M. (2015). *Plant functional type classification for earth system models : results from the European Space Agency ' s Land Cover*. 2315–2328. https://doi.org/10.5194/gmd-8-2315-2015

Purdy, A. J., Fisher, J. B., Goulden, M. L., Colliander, A., Halverson, G., Tu, K., & Famiglietti,

J. S. (2018). SMAP soil moisture improves global evapotranspiration. *Remote Sensing of Environment*, *219*(October), 1–14. https://doi.org/10.1016/j.rse.2018.09.023

Pütz, T., & Groh, J. (2023). Lysimetry. In M. J. Goss & M. Oliver (Eds.), *Encyclopedia of Soils in the Environment (Second Edition)* (Second Edition, pp. 667–679). Academic Press. https://doi.org/https://doi.org/10.1016/B978-0-12-822974-3.00272-X

Pütz, T., Kiese, R., Wollschläger, U., Groh, J., Rupp, H., Zacharias, S., Priesack, E., Gerke, H. H., Gasche, R., Bens, O., Borg, E., Baessler, C., Kaiser, K., Herbrich, M., Munch, J.-C., Sommer, M., Vogel, H.-J., Vanderborght, J., & Vereecken, H. (2016). TERENO-SOILCan: a lysimeter-network in Germany observing soil processes and plant diversity influenced by climate change. *Environmental Earth Sciences*, *75*(18), 1242. https://doi.org/10.1007/s12665-016-6031-5

Qiu, J., Crow, W. T., Dong, J., & Nearing, G. S. (2020). Model representation of the coupling between evapotranspiration and soil water content at different depths. *Hydrology and Earth System Sciences*, *24*(2), 581–594. https://doi.org/10.5194/hess-24-581-2020

Qiu, J., Crow, W. T., & Nearing, G. S. (2016). The impact of vertical measurement depth on the information content of soil moisture for latent heat flux estimation. *Journal of Hydrometeorology*, *17*(9), 2419–2430. https://doi.org/10.1175/JHM-D-16-0044.1

Rabbel, I. (2018). *Analyzing feedbacks in a forest soil-vegetation-atmosphere system*. (Doctoral dissertation, Universitäts-und Landesbibliothek Bonn).

Radolinski, J., Vremec, M., Wachter, H., Birk, S., Brüggemann, N., Herndl, M., Kahmen, A., Nelson, D. B., Kübert, A., Schaumberger, A., Stumpp, C., Tissink, M., Werner, C., & Bahn, M. (2025). Drought in a warmer, CO2-rich climate restricts grassland water use and soil water mixing. *Science*, *296*(January), 290–296. https://doi.org/10.1126/science.ado0734

Raes, D., Steduto, P., Hsiao, T. C., & Fereres, E. (2023). Chapter 2: Users guide. AquaCrop version 7.1. Reference Manual. *Food and Agriculture Organization of the United Nations Rome, August*.

Rahmati, M., Groh, J., Graf, A., Pütz, T., Vanderborght, J., & Vereecken, H. (2020). On the impact of increasing drought on the relationship between soil water content and evapotranspiration of a grassland. *Vadose Zone Journal*, *19*(1), 1–20. https://doi.org/10.1002/vzj2.20029

Raoult, N., Ruscica, R. C., Salvia, M. M., & Sörensson, A. A. (2022). Soil Moisture Drydown Detection Is Hindered by Model-Based Rescaling. *IEEE Geoscience and Remote Sensing Letters*, *19*, 1–5. https://doi.org/10.1109/LGRS.2022.3178685

Reba, M. L., Link, T. E., Marks, D., & Pomeroy, J. (2009). An assessment of corrections for eddy covariance measured turbulent fluxes over snow in mountain environments. *Water Resources Research*, *46*(4). https://doi.org/10.1029/2008WR007045

Rodriguez-Iturbe, I. (2000). Ecohydrology: A hydrologic perspective of climate-soil-

vegetation dynamics. *Water Resources Research*. https://doi.org/10.1029/1999WR900210

Sánchez, J. M., López-Urrea, R., Valentín, F., Caselles, V., & Galve, J. M. (2019). Lysimeter assessment of the Simplified Two-Source Energy Balance model and eddy covariance system to estimate vineyard evapotranspiration. *Agricultural and Forest Meteorology*, *274*(September 2018), 172–183. https://doi.org/10.1016/j.agrformet.2019.05.006

Schneider, J., Groh, J., Pütz, T., Helmig, R., Rothfuss, Y., Vereecken, H., & Vanderborght, J. (2021). Prediction of soil evaporation measured with weighable lysimeters using the FAO Penman–Monteith method in combination with Richards' equation. *Vadose Zone Journal*, *20*(1), 1–20. https://doi.org/10.1002/vzj2.20102

Schnepper, T., Groh, J., Gerke, H. H., Reichert, B., & Pütz, T. (2023). Evaluation of precipitation measurement methods using data from a precision lysimeter network. *Hydrol. Earth Syst. Sci*, *27*, 3265–3292. https://doi.org/10.5194/hess-27-3265-2023

Schrader, F., Durner, W., Fank, J., Gebler, S., Pütz, T., Hannes, M., & Wollschläger, U. (2013). Estimating Precipitation and Actual Evapotranspiration from Precision Lysimeter Measurements. *Procedia Environmental Sciences*, *19*, 543–552. https://doi.org/10.1016/j.proenv.2013.06.061

Schwingshackl, C., Hirschi, M., & Seneviratne, S. I. (2017). Quantifying spatiotemporal variations of soil moisture control on surface energy balance and near-surface air temperature. *Journal of Climate*, *30*(18), 7105–7124. https://doi.org/10.1175/JCLI-D-16-0727.1

Sehgal, V., Gaur, N., & Mohanty, B. P. (2020). Global Surface Soil Moisture Drydown Patterns. *Water Resources Research*, 1–26. https://doi.org/10.1029/2020WR027588

Seneviratne, S. I., Corti, T., Davin, E. L., Hirschi, M., Jaeger, E. B., Lehner, I., Orlowsky, B., & Teuling, A. J. (2010). Investigating soil moisture-climate interactions in a changing climate: A review. *Earth-Science Reviews*, *99*(3–4), 125–161. https://doi.org/10.1016/j.earscirev.2010.02.004

Seneviratne, S. I., Lehner, I., Gurtz, J., Teuling, A. J., Lang, H., Moser, U., Grebner, D., Menzel, L., Schroff, K., Vitvar, T., & Zappa, M. (2012). Swiss prealpine Rietholzbach research catchment and lysimeter: 32 year time series and 2003 drought event. *Water Resources Research*, *48*(6), 1–20. https://doi.org/10.1029/2011WR011749

Shellito, P. J., Small, E. E., & Livneh, B. (2018). Controls on surface soil drying rates observed by SMAP and simulated by the Noah land surface model. *Hydrology and Earth System Sciences*, *22*(3), 1649–1663. https://doi.org/10.5194/hess-22-1649-2018

Shi, L., Zhou, Y., He, W., Dong, Z., Jiang, Z., Wang, Y., Liu, Y., Ju, W., & Duan, Z. (2024). Mapping critical soil moisture thresholds of water stress for global grasslands. *Journal of Hydrology*, 132090. https://doi.org/10.1016/j.jhydrol.2024.132090

Sörensson, A. A., & Ruscica, R. C. (2018). Intercomparison and Uncertainty Assessment of

Nine Evapotranspiration Estimates Over South America. *Water Resources Research*, *54*(4), 2891–2908. https://doi.org/10.1002/2017WR021682

Spinoni, J., Vogt, J., Naumann, G., Carrao, H., & Barbosa, P. (2015). Towards identifying areas at climatological risk of desertification using the Köppen-Geiger classification and FAO aridity index. *International Journal of Climatology*, *35*(9), 2210–2222. https://doi.org/10.1002/joc.4124

Stocker, B. D., Tumber-dávila, S. J., Konings, A. G., Anderson, M. C., Hain, C., & Jackson, R. B. (2023). *Global patterns of water storage in the rooting zones of vegetation*. *16*(March). https://doi.org/10.1038/s41561-023-01125-2

Stoy, P. C., Mauder, M., Foken, T., Marcolla, B., Boegh, E., Ibrom, A., Arain, M. A., Arneth, A., Aurela, M., Bernhofer, C., Cescatti, A., Dellwik, E., Duce, P., Gianelle, D., Gorsel, E. Van, Kiely, G., Knohl, A., Margolis, H., Mccaughey, H., … B, A. V. (2013). A data-driven analysis of energy balance closure across FLUXNET research sites : The role of landscape scale heterogeneity. *Agricultural and Forest Meteorology*, *171–172*, 137–152. https://doi.org/10.1016/j.agrformet.2012.11.004

Straaten, A., & Weber, S. (2021). Measurement report: Three years of size-resolved eddy-covariance particle number flux measurements in an urban environment. *Atmospheric Chemistry and Physics*, *21*(24), 18707–18726. https://doi.org/10.5194/acp-21-18707-2021

Su, L., Miao, C., Duan, Q., Lei, X., & Li, H. (2019). Multiple-Wavelet Coherence of World's Large Rivers With Meteorological Factors and Ocean Signals. *Journal of Geophysical Research: Atmospheres*, *124*(9), 4932–4954. https://doi.org/10.1029/2018JD029842

Sun, Z., Gebremichael, M., Ardö, J., Nickless, A., Caquet, B., Merboldh, L., & Kutschi, W. (2012). Estimation of daily evapotranspiration over Africa using MODIS / Terra and SEVIRI / MSG data. *Atmospheric Research*, *112*, 35–44. https://doi.org/10.1016/j.atmosres.2012.04.005

Tadesse, T., Senay, G. B., Berhan, G., & Regassa, T. (2015). International Journal of Applied Earth Observation and Geoinformation Evaluating a satellite-based seasonal evapotranspiration product and identifying its relationship with other satellite-derived products and crop yield : A case study for Ethiopia. *Int J Appl Earth Obs Geoinformation*, *40*, 39–54. https://doi.org/10.1016/j.jag.2015.03.006

Teuling, A. J. (2018). A Forest Evapotranspiration Paradox Investigated Using Lysimeter Data. *Vadose Zone Journal*, *17*(1), 1–7. https://doi.org/10.2136/vzj2017.01.0031

Thompson, S. E., Harman, C. J., Konings, A. G., Sivapalan, M., Neal, A., & Troch, P. A. (2011). Comparative hydrology across AmeriFlux sites: The variable roles of climate, vegetation, and groundwater. *Water Resources Research*, *47*(7), 1–17. https://doi.org/10.1029/2010WR009797

Tian, J., & Zhang, Y. (2023). *Comprehensive validation of seven root zone soil moisture products at 1153 ground sites across*. *8947*.

https://doi.org/10.1080/17538947.2023.2261902

Torrence, C., & Compo, G. P. (1998). A practical guide to wavelet analysis. *Bulletin of the American Meteorological Society*, *79*(1), 61–78. https://doi.org/10.1175/1520-0477(1998)079%3C0061:APGTWA%3E2.0.CO;2

Tran, B. N., Kwast, J. Van Der, Seyoum, S., Uijlenhoet, R., & Jewitt, G. (2023). Uncertainty assessment of satellite remote-sensing-based evapotranspiration estimates : a systematic review of methods and gaps. *Hydrology and Earth System Sciences*, 4505–4528. https://doi.org/10.5194/hess-27-4505-2023

Tran, B., Van Der Kwast, J., Seyoum, S., Uijlenhoet, R., Jewitt, G., & Mul, M. (2023). Uncertainty Assessment of Satellite Remote Sensing-based Evapotranspiration Estimates: A Systematic Review of Methods and Gaps. *EGUsphere Preprint Repository*, *https://doi.org/10.5194/egusphere-2023-725*, 1–40. https://doi.org/10.5194/egusphere-2023-725

Trenberth, K. E., Fasullo, J. T., & Kiehl, J. (2009). Earth's global energy budget. *Bulletin of the American Meteorological Society*. https://doi.org/10.1175/2008BAMS2634.I

Trenberth, K. E., Smith, L., Qian, T., Dai, A., & Fasullo, J. (2006). Estimates of the Global Water Budget and Its Annual Cycle Using Observational and Model Data. *Journal of Hydrometeorology*, 758–769. https://doi.org/10.1175/JHM600.1

Trigo, I. F., de Bruin, H., Beyrich, F., Bosveld, F. C., Gavilán, P., Groh, J., & López-Urrea, R. (2018). Validation of reference evapotranspiration from Meteosat Second Generation (MSG) observations. *Agricultural and Forest Meteorology*, *259*(September 2017), 271–285. https://doi.org/10.1016/j.agrformet.2018.05.008

Troch, P. A., Lahmers, T., Meira, A., Mukherjee, R., Pedersen, J. W., Roy, T., & Valdés-Pineda, R. (2015). Catchment coevolution: A useful framework for improving predictions of hydrological change? *Water Resources Research*, *51*(7), 4903–4922.

Twine, T. E., Kustas, W. P., Norman, J. M., Cook, D. R., Houser, P. R., Meyers, T. P., Prueger, J. H., Starks, P. J., & Wesely, M. L. (2000). Correcting eddy-covariance flux underestimates over a grassland. *Agricultural and Forest Meteorology*, *103*(3), 279–300. https://doi.org/10.1016/S0168-1923(00)00123-4

Ukkola, A. M., De Kauwe, M. G., Pitman, A. J., Best, M. J., Abramowitz, G., Haverd, V., Decker, M., & Haughton, N. (2016). Land surface models systematically overestimate the intensity, duration and magnitude of seasonal-scale evaporative droughts. *Environmental Research Letters*, *11*(10). https://doi.org/10.1088/1748-9326/11/10/104012

Unold, G. Von, & Fank, J. (2008). Modular Design of Field Lysimeters for Specific Application Needs. *Water Air Soil Pollut: Focus*, 233–242. https://doi.org/10.1007/s11267-007-9172-4

van Groenigen, J. W. (2000). The influence of variogram parameters on optimal sampling schemes for mapping by kriging. *Geoderma*, *97*(3), 223–236.

https://doi.org/https://doi.org/10.1016/S0016-7061(00)00040-9

Vereecken, H., Huisman, J. A., Bogena, H., Vanderborght, J., Vrugt, J. A., & Hopmans, J. W. (2008). On the value of soil moisture measurements in vadose zone hydrology: A review. *Water Resources Research*, *46*(4), 1–21. https://doi.org/10.1029/2008WR006829

Wadoux, A. M.-C., Marchant, B. P., & Lark, R. M. (2019). Efficient sampling for geostatistical surveys. *European Journal of Soil Science*, *70*(5), 975–989.

Wang, J., Franc, B., & Lambert, P. (2017). Equations for hydraulic conductivity estimation from particle size distribution: A dimensional analysis. *Water Resources Research*. https://doi.org/10.1002/2017WR020888

Wang, K., & Dickinson, R. E. (2012). A review of global terrestrial evapotranspiration: Observation, modeling, climatology, and climatic variability. *Reviews of Geophysics*, *50*(2). https://doi.org/10.1029/2011RG000373

Wang, Y., Lu, Y., Horton, R., & Ren, T. (2019). Specific Heat Capacity of Soil Solids: Influences of Clay Content, Organic Matter, and Tightly Bound Water. *Soil Science Society of America Journal*, *83*(4), 1062–1066. https://doi.org/10.2136/sssaj2018.11.0434

Wankmüller, F. J. P., Delval, L., Lehmann, P., Baur, M. J., Cecere, A., Wolf, S., Or, D., Javaux, M., & Carminati, A. (2024). Global influence of soil texture on ecosystem water limitation. *Nature*, *635*(November). https://doi.org/10.1038/s41586-024-08089-2

Widmoser, P., & Michel, D. (2021). Partial energy balance closure of eddy covariance evaporation measurements using concurrent lysimeter observations over grassland. *Hydrology and Earth System Sciences*, *25*(3), 1151–1163. https://doi.org/10.5194/hess-25-1151-2021

Widmoser, P., & Wohlfahrt, G. (2018). Attributing the energy imbalance by concurrent lysimeter and eddy covariance evapotranspiration measurements. *Agricultural and Forest Meteorology*, *263*(March), 287–291. https://doi.org/10.1016/j.agrformet.2018.09.003

Wilson, K. B., Hanson, P. J., Mulholland, P. J., Baldocchi, D. D., & Wullschleger, S. D. (2001). A comparison of methods for determining forest evapotranspiration and its components: sap-flow, soil water budget, eddy covariance and catchment water balance. *Agricultural and Forest Meteorology*, *106*(2), 153–168. https://doi.org/10.1016/S0168-1923(00)00199-4

Wollschläger, U., Attinger, S., Borchardt, D., Brauns, M., Cuntz, M., Dietrich, P., Fleckenstein, J. H., Friese, K., Friesen, J., Harpke, A., Hildebrandt, A., Jäckel, G., Kamjunke, N., Knöller, K., Kögler, S., Kolditz, O., Krieg, R., Kumar, R., Lausch, A., … Zacharias, S. (2017). The Bode hydrological observatory: a platform for integrated, interdisciplinary hydro-ecological research within the TERENO Harz/Central German Lowland Observatory. *Environmental Earth Sciences*, *76*(1). https://doi.org/10.1007/s12665-016-6327-5

Wu, D., Di, C., Wang, T., Wang, L., & Chen, X. (2021). Characterization of the Coherence

Between Soil Moisture and Precipitation at Regional Scales. *Journal of Geophysical Research: Atmospheres*, *126*(8), 1–14. https://doi.org/10.1029/2020JD034340

Xiang, K., Li, Y., Horton, R., & Feng, H. (2020). Similarity and difference of potential evapotranspiration and reference crop evapotranspiration – a review. *Agricultural Water Management*, *232*, 106043. https://doi.org/10.1016/J.AGWAT.2020.106043

Xiao, H., Meissner, R., Seeger, J., Rupp, H., & Borg, H. (2009). Effect of vegetation type and growth stage on dewfall , determined with high precision weighing lysimeters at a site in northern Germany. *Journal of Hydrology*, *377*(1–2), 43–49. https://doi.org/10.1016/j.jhydrol.2009.08.006

Yao, A. Y. M. (1974). Agricultural potential estimated from the ratio of actual to potential evapotranspiration. *Agricultural Meteorology*, *13*(3), 405–417. https://doi.org/https://doi.org/10.1016/0002-1571(74)90081-8

Zacharias, S., Bogena, H., Samaniego, L., Mauder, M., Fuß, R., Pütz, T., Frenzel, M., Schwank, M., Baessler, C., Butterbach-Bahl, K., & others. (2011). A network of terrestrial environmental observatories in Germany. *Vadose Zone Journal*, *10*(3), 955–973.

Zacharias, S., Loescher, H. W., Bogena, H., Kiese, R., Schrön, M., Attinger, S., Blume, T., Borchardt, D., Borg, E., Bumberger, J., Chwala, C., Dietrich, P., Fersch, B., Frenzel, M., Gaillardet, J., Groh, J., Hajnsek, I., Itzerott, S., Kunkel, R., … Vereecken, H. (2024). Fifteen Years of Integrated Terrestrial Environmental Observatories (TERENO) in Germany: Functions, Services, and Lessons Learned. *Earth's Future*, *12*(6), 1–30. https://doi.org/10.1029/2024EF004510

Zaitchik, B. F., Rodell, M., Biasutti, M., & Seneviratne, S. I. (2023). Wetting and drying trends under climate change. *Nature Water,* 1(6), 502-513. https://doi.org/10.1038/s44221-023-00073-w

Zeeman, M. J., Mauder, M., Steinbrecher, R., Heidbach, K., Eckart, E., & Schmid, H. P. (2017). Reduced snow cover affects productivity of upland temperate grasslands. *Agricultural and Forest Meteorology*, *232*, 514–526. https://doi.org/10.1016/j.agrformet.2016.09.002

Zhang, L., Marshall, M., Vrieling, A., & Nelson, A. (2023). The divergence of energy- and water-balance evapotranspiration estimates in humid regions. *Journal of Hydrology*, *624*(May), 129971. https://doi.org/10.1016/j.jhydrol.2023.129971

Zhang, P., Jeong, J. H., Yoon, J. H., Kim, H., Simon Wang, S. Y., Linderholm, H. W., Fang, K., Wu, X., & Chen, D. (2020). Abrupt shift to hotter and drier climate over inner East Asia beyond the tipping point. *Science*, *370*(6520), 1095–1099. https://doi.org/10.1126/science.abb3368

Zhang, W., Jung, M., Migliavacca, M., Poyatos, R., Miralles, D., El-Madany, T. S., Galvagno, M., Carrara, A., Arriga, N., Ibrom, A., Mammarella, I., Papale, D., Cleverly, J., Liddell, M. J., Wohlfahrt, G., Markwitz, C., Mauder, M., Paul-Limoges, E., Schmidt, M., … Nelson, J. A. (2022). The Effect of Relative Humidity on Eddy Covariance Latent Heat Flux Measurements and its Implication for Partitioning into Transpiration and

Evaporation. *Agricultural and Forest Meteorology*, *January*. https://doi.org/10.2139/ssrn.4106267

Zhang, Z., Fan, B., Song, C., Zhang, X., Zhao, Q., & Ye, B. (2023). Advances in Root System Architecture: Functionality, Plasticity, and Research Methods. *Journal of Resources and Ecology*, *14*(1), 15–24. https://doi.org/10.5814/j.issn.1674-764x.2023.01.002

Zhang, Z., Tian, F., Hu, H., & Yang, P. (2014). A comparison of methods for determining field evapotranspiration: Photosynthesis system, sap flow, and eddy covariance. *Hydrology and Earth System Sciences*, *18*(3), 1053–1072. https://doi.org/10.5194/hess-18-1053-2014

Zhu, S., Olde, L., Lewis, K., Quaife, T., Cardenas, L., Loick, N., Xu, J., & Hill, T. (2023). Eddy covariance fluxes over managed ecosystems extrapolated to field scales at fine spatial resolutions. *Agricultural and Forest Meteorology*, *342*, 109675. https://doi.org/10.1016/J.AGRFORMET.2023.109675

Zomer, R. J., Jianchu, X., & Tr, A. (2022). *Version 3 of the Global Aridity Index and Potential Evapotranspiration Database*. 1–15. https://doi.org/10.1038/s41597-022-01493-1

Band / Volume 725
Synthese und Bewertung hochaktiver Katalysatoren zur Herstellung höherer Alkohole aus Methanol als Kraftstoff
J. Häusler (2026), xiii, 265 Seiten
ISBN: 978-3-95806-962-6 (Print)
ISBN: 978-3-95806-963-3 (E-Book)

Band / Volume 726
Development and Characterization of Ni_3Fe Layered Double Hydroxide-Based Oxygen-Evolution Electrodes for Anion Exchange Membrane Water Electrolysis
I.Galkina (2026), vii, 173, xxxiii Seiten
ISBN: 978-3-95806-966-4 (Print)
ISBN: 978-3-95806-967-1 (E-Book)

Band / Volume 727
Surface Regeneration of Plasma-Facing Components by Wire-Based Laser Metal Deposition
J. Tweer (2026), XX, 186 pp
ISBN: 978-3-95806-970-1 (Print)
ISBN: 978-3-95806-971-8 (E-Book)

Band / Volume 728
Reducing the noble metal and titanium content of anode PTLs in PEM water electrolysis – performance and degradation
S. Zerressen (2026), XIII, 235 pp
ISBN: 978-3-95806-972-5 (Print)
ISBN: 978-3-95806-973-2 (E-Book)

Band / Volume 729
Gasfernleitungsnetze und deren Umstellung auf Wasserstoff
T. A. Triesch (2026), 364 pp
ISBN: 978-3-95806-978-7 (Print)
ISBN: 978-3-95806-979-4 (E-Book)

Band / Volume 730
Land-Atmosphere Coupling in a Changing Climate: Understanding Variability, Extremes, and Human Influence through Regional Climate Modeling
Y. Zhang (2026), 135 pp
ISBN: 978-3-95806-980-0 (Print)
ISBN: 978-3-95806-981-7 (E-Book)

Band / Volume 731
Abbildung gekoppelter Infrastrukturen in Energiesystemmodellen
P. Freitag (2026), XIX, 322 pp
ISBN: 978-3-95806-984-8 (Print)
ISBN: 978-3-95806-985-5 (E-Book)

Band / Volume 732
Cost-reduced and Sustainable Interconnects and their Coatings for Solid Oxide Cells
M. Hilger (2026), viii, 185 pp
ISBN: 978-3-95806-988-6 (Print)
ISBN: 978-3-95806-989-3 (E-Book)

Band / Volume 733
Liquid-Phase Synthesis of Silicon and Silicon Carbide Thin-Films via Atmospheric Pressure Chemical Vapor Deposition
B. Fischer (2026), xxii, 211, A15 pp
ISBN: 978-3-95806-990-9 (Print)
ISBN: 978-3-95806-991-6 (E-Book)

Band / Volume 734
Modellgestützte Transformationspfade des deutschen Energiesystems
R. Maier (2026), xxvii, 331 pp
ISBN 978-3-95806-994-7 (Print)
ISBN 978-3-95806-995-4 (E-Book)

Band / Volume 735
Dynamical drivers of deep and shallow branches in the stratospheric circulation and transport
R.-A. Baikhadzhaev (2026), 120 pp
ISBN 978-3-95806-996-1 (Print)
ISBN 978-3-95806-997-8 (E-Book)

Band / Volume 736
Silicon heterojunction solar cells on thin wafers – prospects in different utilization scenarios
U. K. Chime (2026), 151 pp
ISBN 978-3-95806-998-5 (Print)
ISBN 978-3-95806-999-2 (E-Book)

Band / Volume 737
Advancing the understanding of actual evapotranspiration and critical soil moisture thresholds using lysimeter networks
X. Lu (2026), XXX, 159 pp
ISBN 978-3-69367-000-2 (Print)
ISBN 978-3-69367-001-9 (E-Book)

Weitere ***Schriften des Verlags im Forschungszentrum Jülich*** unter
http://wwwzb1.fz-juelich.de/verlagextern1/index.asp

Energie & Umwelt / Energy & Environment
Band / Volume 737
ISBN 978-3-69367-001-9

Mitglied der Helmholtz-Gemeinschaft

JÜLICH
Forschungszentrum